AAA Workshop Series Vol. 10
Asociación Argentina de Astronomía

First Workshop on

Chemical Abundances in Gaseous Nebulae

Campos do Jordão, Brasil, 2-5 November 2016

Proceedings

Edited by
Guillermo F. Hägele, Mónica V. Cardaci & Enrique Pérez-Montero

ASOCIACIÓN ARGENTINA DE ASTRONOMÍA
WORKSHOP SERIES

Vol. 10

CHEMICAL ABUNDANCES IN GASEOUS NEBULAE

Proceedings of the 1st Workshop held at
Universidade do Vale do Paraíba, Campos do Jordão, Brasil
November 2-5, 2016

Edited by

Guillermo F. Hägele
Instituto de Astrofísica de La Plata, CONICET-UNLP, Argentina

Mónica V. Cardaci
Instituto de Astrofísica de La Plata, CONICET-UNLP, Argentina

and

Enrique Pérez-Montero
Instituto de Astrofísica de Andalucía, Granada, Spain

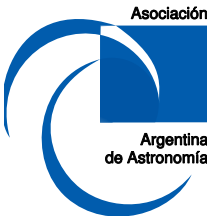

Published by:
ASOCIACIÓN ARGENTINA DE ASTRONOMÍA

ISBN: 978-987-24948-5-8

Credits:
Cover picture: Detail of the Carina Nebula taken with the Hubble Space Telescope. Copyright: NASA, ESA, M. Livio and the Hubble 20th Anniversary Team (STScI)
http://sci.esa.int/jump.cfm?oid=46914
Cover design: Mónica V. Cardaci
Logo design: Lilia C. Rodrigues & UNIVAP Marketing Department
Conference photo: Sarita Pereira de Carvalho
LaTeX editor: Mónica V. Cardaci
using LaTeX's 'confproc' package, version 0.8

Only electronic format — Jul. 2018

Hägele, Guillermo F.
First Workshop on Chemical Abundances in Gaseous Nebulae / Guillermo F. Hägele ; Mónica V. Cardaci ; Enrique Pérez-Montero. - 1a ed . - La Plata : Asociación Argentina de Astronomía, 2018.
Libro digital, PDF - (Asociación Argentina de Astronomía Workshop Series ; 10)
Archivo Digital: online
ISBN 978-987-24948-5-8
1. Astrofísica. 2. Química. I. Cardaci, Mónica V. II. Pérez-Montero, Enrique III. Título
CDD 520

Universidade do Vale do Paraíba

FAPESP
FUNDAÇÃO DE AMPARO À PESQUISA DO ESTADO DE SÃO PAULO

CAPES

S A B

Asociación Argentina de Astronomía

ASOCIACIÓN ARGENTINA DE ASTRONOMÍA

Fundada en 1958

Personería Jurídica (Legajo 21.459 - Matr. 1.421), Pcia. de Buenos Aires

Comisión Directiva

(2014 – 2017)

PRESIDENTE:	Guillermo Bosch
VICEPRESIDENTE:	Andrea Costa
SECRETARIO:	Roberto Venero
TESORERA:	Mónica Cardaci
VOCAL 1RO:	Javier Ahumada
VOCAL 2DO:	Jorge Combi
VOCAL SUP. 1RO:	Sergio Dasso
VOCAL SUP. 2DO:	Federico González

Comisión Revisora de Cuentas

TITULARES:	Cristina Cappa
	Gabriela Castelletti
	Alejandro Córsico

Comité Nacional de Astronomía

SECRETARIA:	Estela Reynoso
MIEMBROS:	Andrea Torres
	Christian Giuppone
	Rene Rohrmann
	Mariano Domínguez

1st Workshop on

Chemical Abundances in Gaseous Nebulae (CAGN2016)

Campos do Jordão, Brasil, November 2-5, 2016

Scientific Organizing Committee

Oli Dors (UNIVAP/Brazil) *co-chair*
Guillermo Hägele (IALP/Argentina) *co-chair*
Rogemar Riffel (UFSM/Brazil)
Mónica Cardaci (IALP/Argentina)
Dinalva Sales (UFRGS/Brazil)
Enrique Pérez-Montero (IAA/Spain)
Christophe Morisset (UNAM/Mexico)
Leonid Pilyugin (MAO/Ukraine)
Cesar Esteban (IAC/Spain)

Local Organizing Committee

Oli Dors (UNIVAP)
Rogemar Riffel (UFSM)
Lilia Rodrigues (UNIVAP)
Jacqueline Huayanca (UNIVAP)
Dinalva Sales (FURG)
Ângela Krabbe (UNIVAP)
Lucimara Martins (UNICSUL)
Walter Maciel (USP)

Editorial Committee

Guillermo F. Hägele
Mónica V. Cardaci
Enrique Pérez-Montero

Foreword

The determination of the abundance of heavy elements (e.g. O, N, S, Ar) in gaseous nebulae is fundamental to understand the formation and the chemical evolution of galaxies and of the Universe. Despite recent surveys (e.g. Califa, Sloan Digital Sky Survey) have provided advances in the knowledge of gaseous nebulae and their host galaxies, important aspects in the study of these objects remain ill-defined. In particular, the abundance discrepancy problem in HII regions and planetary nebulae, generally interpreted as being caused by the presence of temperature fluctuation, calling into question the nebular abundance scale of the Milk Way and extragalactic objects. In order to address this problem this workshop brought together a group of scientists and students to stimulate extensive discussions about crucial questions related to the study of the chemical abundances in gaseous nebulae.
The present volume contains the set of contributions presented at the workshop.

Oli Dors & Guillermo Hägele
Campos do Jordão, São Paulo, Brazil, November 2016

Words of the editors

The editors wish to thank Oli Dors for all his work in organizing this wonderful meeting and hope that it is only the first of a series of useful workshops. They also want to thank the hospitality of the Universidade do Vale do Paraíba for providing a homely place in Campos do Jordão to carry out the meeting, and the hospitality of its *Instituto de Pesquisa e Desenvolvimento - IP&D* - where part of this book was edited.

G. Hägele, M. Cardaci and E. Pérez-Montero
Editors.


UNIVERSIDADE DO VALE DO PARAÍBA
CAMPUS PLATANUS
04/11/2016
11:52

CONTENTS

Invited

Contributed

Posters

Invited Contributions

Chemical Abundances in Gaseous Nebulae
AAA Workshop Series 10, 2016
G. Hägele, M. Cardaci & E. Pérez-Montero, eds.

Invited Review

Chemical Abundances in AGNs

Oli Dors[1]

[1] *Universidade do Vale do Paraíba (UNIVAP), SP, Brazil*

Abstract. In this paper I analyse the chemical abundance determinations based on optical emission-lines in Seyfert 2 type Active Galactic Nuclei (AGNs) located at low redshifts ($z < 0.1$). I show that oxygen abundance determinations based on the classical T_e-method underestimate the oxygen abundances in Sy2 objects by up to ∼2 dex (with averaged value of ∼ 0.8 dex) compared to the abundances derived through the strong-line method and central intersect abundances estimated from the radial abundance gradients. I also show that oxygen, nitrogen and sulphur abundances in AGNs seem to be similar to those derived for HII regions with high metallicity. This suggests that there is no extraordinary chemical enrichment in Sy2 AGNs.

1. Introduction

Active galactic nuclei (AGNs) present prominent emission lines of heavy elements that can be easily measured, even for objects at large redshifts. The intensity of these emission lines depends on the metallicity, which makes them convenient tracers of the chemical evolution of the Universe.
The first determination of abundance of heavy elements in AGNs, by using emission-lines observed in the optical range, seems to have been carried out by Osterbrock & Miller (1975). These authors, using the Lick telescope, obtained spectrophotometric measurements of the radio galaxy 3C 405 (Cygnus A), in which was possible to obtain the intensity of the emission-line ratios sensitive to the electron temperature RO3=([OIII](λ4959+λ5007)/λ4363)=77 and RN2=([NII](λ6548+λ6584)/λ5755)=90, corresponding to electron temperature values of 15 000 ± 1000 K and 10 000 ± 1000 K, respectively. Also, these authors found for the ratio [SII]λ6716/λ6731 a value of 1.10, corresponding to a electron density of ∼800 cm^{-3}. Using the values of these parameters, the intensity of the emission-lines [OI]λ6300, [OII]λλ3726+29 (hereafter [OII]λ3727), [OIII]λ5007 relative to intensity of Hβ, and assuming

$$\frac{\mathrm{O}}{\mathrm{H}} = \frac{\mathrm{O}^0}{\mathrm{H}^+} + \frac{\mathrm{O}^+}{\mathrm{H}^+} + \frac{\mathrm{O}^{2+}}{\mathrm{H}^+}, \quad (1)$$

Osterbrock & Miller (1975) derived the value 12+log(O/H)∼8.70 for Cygnus A,

or a metallicity $Z \sim Z_{\odot}$[1]. Other important work in this epoch was carried out by Koski (1978), who obtained spectrophotometric data of 20 Sy2 galaxies. Also, it is important to cite the work published by Storchi-Bergmann et al. (1998, hereafter SB98), who proposed the first (and unique) two calibrations between narrow strong emission-lines of AGNs with the oxygen abundance, i.e. calibrations between the emission-line ratios [NII]$\lambda\lambda$6548,6584/Hα, [OIII]$\lambda\lambda$4959,5007/Hβ and [OII]λ3727/[OIII]$\lambda\lambda$4959,5007 with O/H (or Z). Using these calibrations, SB98 derived for a sample of seven Seyfert galaxies 12+log(O/H) values in the range 8.90-9.40 dex ($1.60 \lesssim (Z/Z_{\odot}) \lesssim 4.50$), i.e. oversolar abundances. High O/H or Z values have been also derived by other authors for AGNs at low redshifts. In fact, Groves et al. (2006), using photoionization models to examine the effects of metallicity variations on the narrow emission-lines taken from the Sloan Digital Sky Survey (Adelman-McCarthy et al., 2006), found that models assuming $(Z/Z_{\odot}) = 4.0$ or 12+log(O/H)=9.30 describe the observational data.
However, an opposite support against the results that Sy2 AGNs have very high metallicity, is obtained from chemical studies of HII regions. For example, Pilyugin et al. (2004), by using the P-method (Pilyugin, 2001, 2000) and observational data of disk HII regions, derived the oxygen abundance gradients for a sample of 54 spiral galaxies. Considering the extrapolated oxygen value for the central part of the disk obtained by Pilyugin et al. (2004), an average oxygen value of 12+log(O/H)$\approx$8.8 or $Z/Z_{\odot} \approx 1.20$ is derived. Also, Dors et al. (2008) derived the metallicity of circumnuclear star forming regions (CNSFRs) located in the spiral galaxies NGC 6951 and NGC 1097 and found an oxygen abundance of 12 + log(O/H)$\approx$8.8. Thus, if we assume the same metallicity derived in CNSFRs for AGNs, no overabundance is derived for these objects.
Concerning other elements (e.g. N, S, Ne, Ar), their abundances are poorly known in AGNs. In fact, Storchi-Bergmann & Pastoriza (1990) compared the intensity of the [NII]$\lambda\lambda$6548,6584/Hα and [SII]($\lambda\lambda$6716,31)/Hα ratios predicted by photoionization models with observational data of a sample of 177 Sy2 AGNs. These authors found that models assuming N and S abundances ranging from 0.5 to 3 times the solar values reproduce the observational data. Although this is a qualitative result, it seems to be the first N and S abundance determinations in AGNs (see also Yu & Hwang, 2011; Bradley et al., 2004). With the above in mind, the main goals of this paper are: i) verify if Sy2 AGNs present oversolar metallicity; ii) calculate the nitrogen abundance in Sy2 AGNs; and iii) calculate the sulphur abundance in Sy2 AGNs.

2. Have AGNs Sy2 high metallicity?

The metallicity in AGNs originates from the past and ongoing star formation near to the black hole (Collin & Zahn, 1999, 2008; Wang et al., 2011). Therefore, the knowledge of this metallicity (and of elemental abundances) becomes possible to determine star formation parameters in the central part of galaxies, e.g. Initial Mass Function (IMF), star formation mass limits, etc. On this

[1]Along the paper the solar oxygen abundance of $12 + \log(\mathrm{O/H})_{\odot} = 8.69$, derived by Allende Prieto et al. (2001), will be adopted.

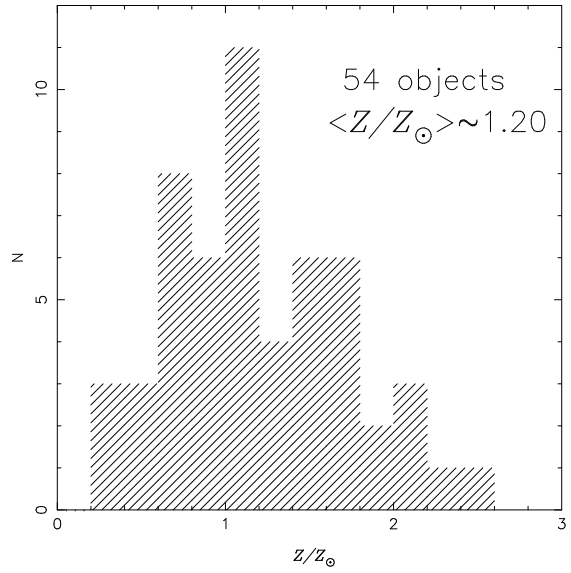

Figure 1. Histogram showing the metallicity values obtained from the extrapolated oxygen abundance ($\log(\mathrm{O/H})_0$) for the central part of the disk of a sample of spiral galaxies taken from Pilyugin et al. (2004). The Z values were obtained using the Eq. 2. The number of objects considered and the average metallicity value obtained are indicated.

scenario, considering that spiral galaxies are formed according to the classical inside-out scheme (Mollá & Díaz, 2005) and the IMF is universal (see, for example, Elmegreen, 2006; Kroupa, 2014, 2001; Bastian et al., 2010; Massey et al., 1995), it is expected that AGNs exhibit similar elemental abundances than the ones in the innermost disk HII regions located in spiral galaxies.
Pilyugin et al. (2007) used the luminosity versus metallicity relation of galaxies in order to search for the maximum oxygen abundance in spiral galaxies, These authors found 12 + $\log(\mathrm{O/H})\approx 8.95$. Now, lets consider the extrapolated value of the oxygen abundance $\log(\mathrm{O/H})_0$ for the central part of the disk of spirals obtained by Pilyugin et al. (2004). In Fig. 1, it is shown a histogram containing the metallicity in relation to the solar one, defined by

$$(Z/Z_\odot) = 10^{\log(\mathrm{O/H})_0 - \log(\mathrm{O/H})_\odot}, \tag{2}$$

In this figure it can be seen that the oxygen abundance predictions for the central part of the majority of the objects is about solar, with an average value of $(Z/Z_\odot) \approx 1.20$. Thus, from this result, we can conclude that AGNs or galaxy nuclei have metallicities near to the solar value.
Recently, Dors et al. (2015) calculated the oxygen abundances in the narrow-line regions (NLRs) of Sy2 through the three methods describe below.

1. T_e-method– To use this method, we must calculate the electron temperature in the high ionization zone (referred to as t_3) from the observed ratio

R_{O3}=[OIII](λ4959 + λ5007)/λ4363 and from the expression

$$t_3 = 0.8254 - 0.0002415 R_{O3} + \frac{47.77}{R_{O3}}, \quad (3)$$

with t_3 in units of 10^4K. The electron temperature of the low ionization zone (referred to as t_2) is derived from the theoretical relation:

$$t_2^{-1} = 0.693\, t_3^{-1} + 0.281. \quad (4)$$

The O^{++} and O^{+} ionic abundances are compute through the relations:

$$12 + \log(\frac{O^{++}}{H^{+}}) = \log(\frac{I(4959) + I(5007)}{I(H\beta)}) + 6.144 + \frac{1.251}{t_3} - 0.55 \log t_3. \quad (5)$$

and

$$12 + \log(\frac{O^{+}}{H^{+}}) = \log(\frac{I(3727)}{I(H\beta)}) + 5.992 + \frac{1.583}{t_2} - 0.681 \log t_2 + \log(1 + 2.3 n_e). \quad (6)$$

Finally, the total oxygen abundance is obtained assuming

$$\frac{O}{H} = \frac{O^{+}}{H^{+}} + \frac{O^{++}}{H^{+}}. \quad (7)$$

2. Strong-line method– SB98 carried out NLR model calculations using the photoionization code CLOUDY and suggested two relations for the abundance determinations in the NLRs of AGNs. The first one is

$$\begin{aligned} (O/H)_{SB98,1} &= 8.34 + (0.212\, x) - (0.012\, x^2) - (0.002\, y) \\ &+ (0.007\, xy) - (0.002\, x^2 y) + (6.52 \times 10^{-4}\, y^2) \\ &+ (2.27 \times 10^{-4}\, xy^2) + (8.87 \times 10^{-5}\, x^2 y^2), \end{aligned} \quad (8)$$

where x = [N II]$\lambda\lambda$6548,6584/Hα and y = [O III]$\lambda\lambda$4959,5007/Hβ.

The dependence of these relations on the density should be taken into account. This dependence is given by the expression considered by SB98

$$(O/H)_{final} = O/H - 0.1\ \log(N_e/300), \quad (9)$$

where N_e is the electron density in cm^{-3} and the correction is valid for 100 cm^{-3} $\lesssim N_e \lesssim$ 10^4 cm^{-3}. It should be noted that the value of this correction exceeds 0.1 dex for high-density objects only, i.e., for objects with electron densities $N_e \gtrsim 3{\times}10^3$ cm^{-3}.

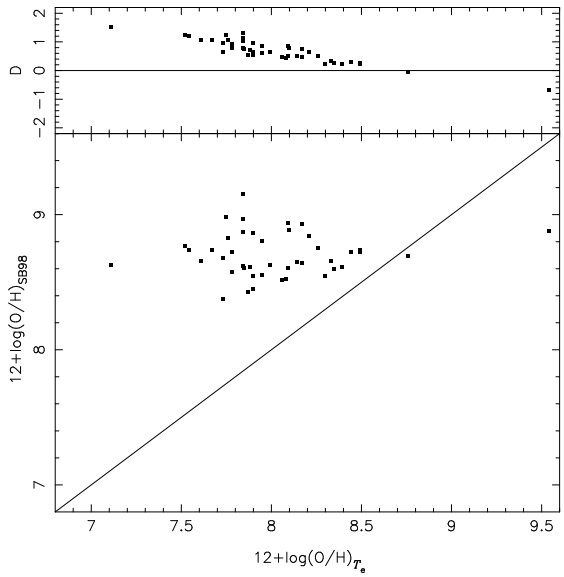

Figure 2. The bottom panel shows the comparison between the oxygen abundance obtained through the T_e-method and through the calibration of SB98. The upper panel shows the differences between estimations based on SB98 and on T_e-method. Figure based on Fig. 1 from Dors et al. (2015).

3. Extrapolated O/H method– Such as reported above, it is possible to infer a metallicity (or an elemental abundance) for the central region of a given galaxy through the extrapolation of the derived metallicity gradient generally found along the disk of spiral galaxies. For that, it is necessary to calculate the oxygen abundance for a number "N" ($N \gtrsim 10$) of HII regions with a large range of galactocentric distances. In general, this gradient is represented by

$$12 + \log(\mathrm{O/H}) = \mathrm{a}\, R + \mathrm{b}, \tag{10}$$

being $\mathrm{b} = 12 + \log(\mathrm{O/H})_0$, "a" the slope of the gradient and R the galactocentric distance.

Firstly, Dors et al. (2015) compared the oxygen abundance of a sample of AGNs Sy2 calculated through the T_e-method and Strong-line method (SB98 calibration), described above. In Fig. 2 this comparison is presented. It can be seen that O/H values via T_e-method are lower than the ones via SB98 calibration by up to $\sim$ 2 dex, with an average value of $\sim$ 0.8 dex. From this result it arises the question, what is the correct method? The answer can be obtained from independent and indirect O/H determinations, i.e. from extrapolated O/H method.

The radial abundance gradients in the disks of nearby late-type galaxies were recently determined by Pilyugin et al. (2015, 2014). The extrapolation of the radial abundance gradient to the zero galactocentric distance gives the central intersect abundance $(\mathrm{O/H})_0$ in galaxies. On the other hand, Ho et al. (1997) obtained emission-line spectra of the central regions of many nearby galaxies.

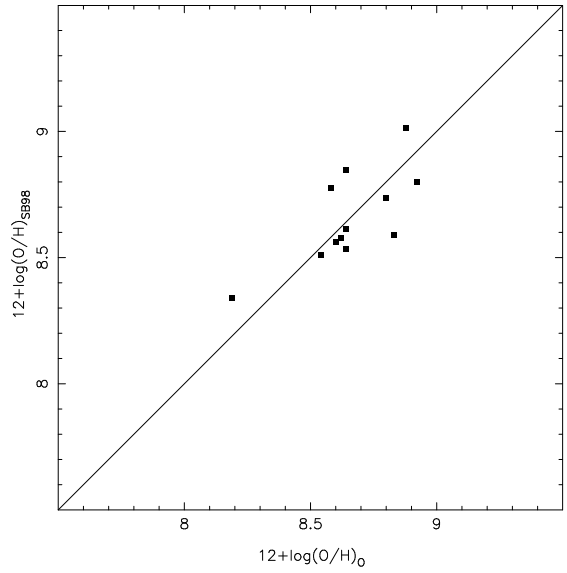

Figure 3. Comparison between central intersect oxygen abundances derived from the radial abundance gradients [$(O/H)_0$] and the central abundances determined from the spectra of AGNs obtained by Ho et al. (1997) and using the SB98 calibration [$(O/H)_{SB98}$].

This provides a possibility to estimate the oxygen abundances at the center of those galaxies.

Thus, for a given AGN, we compare the central O/H abundance estimated from the spectra of Ho et al. (1997) and using the SB98 calibration with the central intersect abundances obtained by Pilyugin et al. (2015, 2014). We selected from the sample of Ho et al. (1997) only the galaxies with central spectra classified by these authors as Seyfert and which are also in the Pilyugin et al. (2015, 2014) list. Our selected sample contains 12 AGNs. In Fig. 3 we show the comparison between the central intersect abundances in the selected galaxies $(O/H)_0$ obtained from the radial abundance gradients and central abundances $(O/H)_{SB98}$. This figure shows that the $(O/H)_{SB98,}$ abundances in the NLRs are close to central intersect abundances in the host galaxies. Thus, we concluded the T_e-method yields very low and unrealistic O/H (or metallicity) values for AGNs. This fact could be attributed to the presence of gas shock waves propagating at supersonic velocities through the NLRs, which does to enhance the intensity of [OIII]λ4363 producing larger electron temperature values and, consequently, low (unrealistic) O/H values when using the T_e-method (see Dors et al., 2015).

3. Nitrogen and sulphur abundance in AGNs

Such as reported in the Introduction, N and S abundances are poorly known in AGNs and the most part of the abundance determinations of these elements are qualitative ones, i.e. values for N/H and S/H for a given AGN are not derived (see, for example, Storchi-Bergmann & Pastoriza, 1990). Thus, in order

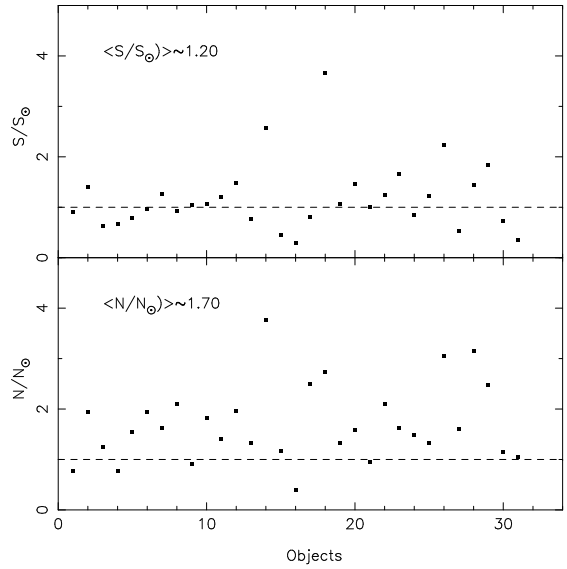

Figure 4. Nitrogen and sulphur abundances in relation to the solar value for a sample of Sy2 objects. The x-axis represents the objects considered in the sample. The points represent results of detailed photoionization models built in order to reproduce optical emission-line intensities of a sample of Sy2 objects (see Sect. 3). The dashed lines represent the N/H and S/H solar values. We assumed $12+\log(\mathrm{N/H})_{\odot}=7.93$ and $12+\log(\mathrm{S/H})_{\odot}=7.27$ taken from Holweger (2001) and Grevesse & Sauval (1998), respectively.

to obtain elemental abundance for the N and S in AGNs Sy2, we built detailed photoionization models to reproduce the intensity of optical emission lines of a sample of these objects.

For that, we selected from the literature narrow emission-lines of AGNs Sy2. Our selection criterion was the presence of flux measurements of the narrow optical emission-lines [OII]λ3727, Hβ, [OIII]λ5007, Hα, [NII]λ6584, and [SII]$\lambda\lambda$6717,31. Observational data of 31 Sy2 compiled by Dors et al. (2015) and observed by Dopita et al. (2015) were considered. For each object, we calculated the metallicity using the following calibration

$$(Z/Z_{\odot}) = 1.08(\pm0.19) \times N2O2^2 + 1.78(\pm0.07) \times N2O2 + 1.24(\pm0.01), \quad (11)$$

proposed by Castro et al. (2017), where

$$N2O2 = \log([\mathrm{NII}]\lambda6584/[\mathrm{OII}]\lambda3727). \quad (12)$$

Also, for each object, we calculated the N_{e} using the relation of this parameter with the observed ratio [SII]$\lambda\lambda$6717/6731 presented by Hägele et al. (2008). The obtained $(Z/Z_{\odot})$ and N_{e} values as well as the logarithm of the number of ionization photons $\log Q(\mathrm{H}) = 51$, nitrogen and sulphur abundances equal to 2 and 1 times the respective solar values, ionizing source as being a power law with the flux $F \sim \nu^{\alpha=-1.4}$ were used as initial parameters in individual photoionization

models built in order to reproduce all emission-line intensities of each object of our sample. The models were built with the Cloudy code version 13.04 (Ferland et al., 2013). We run models ranging $Z/Z_{\odot}$, N/H, S/H, Q(H), and α using the PHYMIR method (van Hoof, 1997) until the models reproduce all emission-line intensities of each AGN of our sample.
In Fig. 4, the nitrogen and sulphur abundances in relation to the solar values[2] predicted by the detailed models, representing each AGN of the sample of objects, are plotted. We can see that nitrogen abundances are generally higher than the solar value, with an average value $< (N/N_{\odot}) >\sim 1.70$, while sulphur abundances are similar to the solar abundance, with $< (S/S_{\odot}) >\sim 1.20$.

4. Final remarks

Along the decades, several works have been addressed to the study of chemical abundances in HII regions. Unfortunately, an opposite situation is found for AGNs, in which the most part of the studies have determined only the metallicity, considered to be oversolar. However, if we consider extrapolations of the radial abundance gradients in spiral galaxies to zero galactocentric distances as being the AGN metallicity (indirect estimations), we conclude that this result is somewhat incorrect. This fact produces important constraints to chemical evolution models, where the AGN metallicity (or the central part of galaxies) represent the upper limit for the metallicity.
Also, few authors have determined calibrations between metallicity and strong emission-lines of AGNs. Since the pioneer work of Pagel et al. (1979), several authors have proposed different calibrations to be applied in chemical abundance studies of HII regions (for a review see López-Sánchez & Esteban, 2009). However, for AGNs, practically there are only three calibrations based on optical lines in the literature (see above) and a calibration considering ultraviolet emission-lines proposed by Dors et al. (2014).
Moreover, the worst situation is found for the elements nitrogen, sulphur, argon, etc, in which, despite the efforts of some authors (e.g. Gary Ferland, Jack Baldwin, Kirk Korista, Thaisa Storchi-Bergmann, Thierry Contini, among others), it seems that the majority of the studies have only produced qualitative estimations for these elements.
In summary, despite a large number of observational data of AGNs are available in the literature, in my opinion, there are lacking theoretical efforts to determine the elemental abundances in these objects.

Acknowledgments. I would like to thank to Universidade do Vale do Paraíba (UNIVAP) administration to became possible the Workshop Chemical Abundances in Gaseous Nebular. Many thanks to my collaborators Mónica Cardaci, Guillermo Hägele, Leonid Pilyugin, Karla Z. Arellano-Córdova, Enrique Pérez-Montero, Ângela C. Krabbe and for my PHD students Claudio Castro and Sarita Pereira de Carvalho by the support during the workshop organization. All my little contribution in the knowledge of the chemical abundance of AGNs and

[2]We assumed $12+\log(N/H)_{\odot}=7.93$ and $12+\log(S/H)_{\odot} = 7.27$ taken from Holweger (2001) and Grevesse & Sauval (1998), respectively.

HII regions is dedicated to Donald Osterbrock, Bob Rubin and Bernard Pagel. I also thank Dr. Gary Ferland and Dr. Peter van Hoof for making available the Cloudy program. I also grateful to the FAPESP for support under grant 2016/04728-7.

References

Adelman-McCarthy J. K., Agüeros M. A., Allam S. S., et al., 2006, *ApJS*, **162**, 38
Allende Prieto C., Lambert D. L., Asplund M., 2001, *ApJL*, **556**, L63
Bastian N., Covey K. R., Meyer M. R., 2010, *ARA&A*, **48**, 339
Bradley L. D., Kaiser M. E., Baan W. A., 2004, *ApJ*, **603**, 463
Castro C. S., Dors O. L., Cardaci M. V., Hägele G. F., 2017, *MNRAS*, **467**, 1507
Collin S., Zahn J.-P., 1999, *Ap&SS*, **265**, 501
Collin S., Zahn J.-P., 2008, *A&A*, **477**, 419
Dopita M. A., Shastri P., Davies R., et al., 2015, *ApJS*, **217**, 12
Dors O. L., Cardaci M. V., Hägele G. F., Krabbe Â. C., 2014, *MNRAS*, **443**, 1291
Dors O. L., Cardaci M. V., Hägele G. F., Rodrigues I., Grebel E. K., Pilyugin L. S., Freitas-Lemes P., Krabbe A. C., 2015, *MNRAS*, **453**, 4102
Dors Jr. O. L., Storchi-Bergmann T., Riffel R. A., Schimdt A. A., 2008, *A&A*, **482**, 59
Elmegreen B. G., 2006, *ApJ*, **648**, 572
Ferland G. J., Porter R. L., van Hoof P. A. M., et al., 2013, *RevMexAA*, **49**, 137
Grevesse N., Sauval A. J., 1998, *Space Sci.Rev.*, **85**, 161
Groves B. A., Heckman T. M., Kauffmann G., 2006, *MNRAS*, **371**, 1559
Hägele G. F., Díaz A. I., Terlevich E., et al., 2008, *MNRAS*, **383**, 209
Ho L. C., Filippenko A. V., Sargent W. L. W., 1997, *ApJS*, **112**, 315
Holweger H., 2001, R. F. Wimmer-Schweingruber (ed.), *Joint SOHO/ACE workshop "Solar and Galactic Composition"*, Vol. 598 of *American Institute of Physics Conference Series*, pp 23–30
Koski A. T., 1978, *ApJ*, **223**, 56
Kroupa P., 2001, *MNRAS*, **322**, 231
Kroupa P., 2014, D. Stamatellos, S. Goodwin, and D. Ward-Thompson (eds.), *The Labyrinth of Star Formation*, Vol. 36 of *Astrophysics and Space Science Proceedings*, p. 335
López-Sánchez A. R., Esteban C., 2009, *A&A*, **508**, 615
Massey P., Johnson K. E., Degioia-Eastwood K., 1995, *ApJ*, **454**, 151
Mollá M., Díaz A. I., 2005, *MNRAS*, **358**, 521
Osterbrock D. E., Miller J. S., 1975, *ApJ*, **197**, 535
Pagel B. E. J., Edmunds M. G., Blackwell D. E., et al., 1979, *MNRAS*, **189**, 95
Pilyugin L. S., 2000, *A&A*, **362**, 325
Pilyugin L. S., 2001, *A&A*, **369**, 594
Pilyugin L. S., Grebel E. K., Kniazev A. Y., 2014, *AJ*, **147**, 131
Pilyugin L. S., Grebel E. K., Zinchenko I. A., 2015, *MNRAS*, **450**, 3254
Pilyugin L. S., Thuan T. X., Vílchez J. M., 2007, *MNRAS*, **376**, 353
Pilyugin L. S., Vílchez J. M., Contini T., 2004, *A&A*, **425**, 849

Storchi-Bergmann T., Pastoriza M. G., 1990, *PASP*, **102**, 1359
Storchi-Bergmann T., Schmitt H. R., Calzetti D., Kinney A. L., 1998, *AJ*, **115**, 909
van Hoof P. A. M., 1997, *Ph.D. thesis*, Utrecht University
Wang J. M., Ge J. Q., Hu C., Baldwin J. A., Li Y. R., Ferland G. J., Xiang F., Yan C. S., Zhang S., 2011, *ApJ*, **739**, 3
Yu P. C., Hwang C. Y., 2011, *AJ*, **142**, 14

Chemical Abundances in Gaseous Nebulae
AAA Workshop Series 10, 2016
G. Hägele, M. Cardaci & E. Pérez-Montero, eds.

Invited Review

Empirical calibrations for abundance determinations in HII regions

Leonid S. Pilyugin[1]

[1] *Main Astronomical Observatory of National Academy of Sciences of Ukraine, 27 Zabolotnogo str., 03680 Kiev, Ukraine*

Abstract. The calibrations of different types for the oxygen abundance determinations in the HII regions are reviewed. The validity of the metallicity scale for HII regions is discussed.

1. Introduction

The determination of the chemical compositions of cosmic bodies is based on the spectral analysis discovered by Gustav Kirchhoff in 1859. He established that each atom or ion has a unique set of emission (or absorption) lines (spectral fingerprins of chemical element). Kirchhoff also found that the intensities of the emission lines of a given element in the spectra are dependent on its abundance as well as depend strongly on the physical conditions (electron temperature T_e and density N_e) in the line emitting gas. The element (ion)-to-hydrogen abundance ratios $N_{El}/N_{\rm H}$ are traditionally used to describe the chemical composition. Then the statement of Kirchhoff is given by the expression

$$F_{El}/F_{{\rm H}\beta} = f(N_{El}/N_{\rm H}, T_e, N_e) \quad (1)$$

or

$$N_{El}/N_{\rm H} = f(F_{El}/F_{{\rm H}\beta}, T_e, N_e) \quad (2)$$

where $F_{El}/F_{{\rm H}\beta}$ is the flux in some emission line of a given ion element (ion) normalised to the flux in the hydrogen emission line Hβ, T_e is the electron temperature in the line emitting gas, and N_e the electron density. The equation (2) is at the base of the abundance determinations in HII regions. The oxygen abundance determination in HII regions is discussed here.

Collisionally excited lines are used for the determinations of the electron temperature and oxygen abundance in HII regions. The relations used to convert the values of the line fluxes to the electron temperatures and to the ion abundances are derived through the five-level atom solution. The bulk of extragalactic HII regions are in the low density regime ($N_e \lesssim$ 100-200 cm^{-3}). In this case, the influence of the density on the emission line intensities is weak and can be neglected. The simplified equation

$$N_{\rm O}/N_{\rm H} = f(F_{\rm O}/F_{{\rm H}\beta}, T_e) \quad (3)$$

is adequate at low densities. The two ionization stages in oxygen O^+ and O^{++} are significant in HII regions. A two zone model for the temperature structure

within HII region is usually adopted. The ratio of the nebular to auroral oxygen line intensities [OIII]λ4959 + λ5007/[OIII]λ4363 is used for the determination of the electron temperature within the [OIII] zone, while the ratio of the nebular to auroral nitrogen line intensities [NII]λ6548 + λ6584/[NII]λ5755 is used for the determination of the electron temperature within the [OII] zone.
Abundance determinations through the direct T_e-method require high-precision spectroscopy of HII regions in order to detect the weak auroral lines such as [OIII]λ4363 or/and [NII]λ5755. Unfortunately, these auroral lines are often rather faint and thus may be detected only in the spectra of a limited number of HII regions. The abundances in other HII regions are then usually estimated through the method suggested by Pagel et al. (1979) and Alloin et al. (1979). The idea of this method (traditionally called the strong-line method) is to establish the relation between the (oxygen) abundance in an HII region and some combination of the intensities of strong emission lines in its spectrum, i.e., the combination of the intensities of these strong lines is calibrated in terms of the metallicity of the HII region. Therefore, such a relation is usually called a "calibration" and serves to convert metallicity-sensitive emission-line combinations into metallicity estimations.
Below, we will use the following standard notations for the line intensities:
$R_2 = F_{[\mathrm{O\,II}]\lambda3727+\lambda3729}/F_{\mathrm{H}\beta}$,
$N_2 = F_{[\mathrm{N\,II}]\lambda6548+\lambda6584}/F_{\mathrm{H}\beta}$,
$S_2 = F_{[\mathrm{S\,II}]\lambda6717+\lambda6731}/F_{\mathrm{H}\beta}$,
$R_3 = F_{[\mathrm{O\,III}]\lambda4959+\lambda5007}/F_{\mathrm{H}\beta}$,
$R_{23} = R_2 + R_3$.
Based on these definitions, the excitation parameter P is expressed as $P = R_3/R_{23} = R_3/(R_2 + R_3)$.

2. Simple calibrations

Each calibration for the abundance determinations can be specified by two ingredients: a sample of the calibrating data points and the set of strong emission lines used as the abundance index.
Different combinations of emission lines of different ions (of oxygen, nitrogen, sulphur, argon, neon) were suggested as oxygen abundance indicators:
R_{23} = ([OII]$\lambda\lambda$3727,3729 + [OIII]$\lambda\lambda$4959,5007)/H_β by Pagel et al. (1979),
N_2 = [NII]λ6584/H_α and
O_3N_2 = ([OIII]λ5007/H_α)/([NII]λ6584/H_α) by Alloin et al. (1979),
S_{23} = ([SII]$\lambda\lambda$6717,6731 + [SIII]$\lambda\lambda$9069,9532)/H_β by Vílchez & Esteban (1996),
A_3O_3 = [ArIII]λ7135/[OIII]λ5007 and
S_3O_3 = [SIII]λ9069/[OIII]λ5007 by Stasińska (2006),
Ne_3O_2 = [NeIII]λ3869/[OII]λ3727 by Shi et al. (2007).

2.1. Calibrating data points: theoretical versus empirical calibrations

An important characteristic of the calibration is the sample of calibrating data points used in the construction of the calibration relation. Grids of photoionization models of HII regions can be used to establish a relation between strong-line intensities and oxygen abundances (e.g. McCall et al., 1985; Vale Asari et al.,

2016). Such calibrations are usually referred to as theoretical or model calibrations. On the other hand, a sample of HII regions in which the oxygen abundances are determined through the direct T_e-method can serve as basis of a calibration (e.g. Pilyugin, 2000; Marino et al., 2013). Such calibrations are called empirical calibrations. There are also a hybrid calibrations where both the HII regions with directly measured abundances and the photoionization models of HII regions are used (Pettini & Pagel, 2004).

There are large systematic discrepancies between the abundance values produced by different published calibrations. The theoretical (or model) calibrations generally produce oxygen abundances that are by factors of 1.5 to 5 higher than those derived through the direct T_e-method or through empirical calibrations (see Kewley & Ellison, 2008). Thus, at the present time there is no absolute scale for metallicities of HII regions. The empirical calibrations have advantages as compared to the theoretical calibrations. The empirical metallicity scale is well defined in terms of the abundances in HII regions derived through the direct T_e-method, i.e., in that sense the empirical metallicity scale is absolute. The abundances in HII regions obtained through the different empirical calibrations are compatible with each other as well as with the direct T_e-based abundances. The empirical metallicity scale is likely the preferable metallicity scale at present.

2.2. Simple calibrations based on the oxygen lines: approach of Pagel et al.

Since the temperature-sensitive lines are often too weak to be detected, for such HII regions one has to resort to abundance indicators based on more readily observable lines. The oxygen abundance indicator R_{23} = ([OII]$\lambda\lambda$3727,3729 + [OIII]$\lambda\lambda$4959,5007)/H_β suggested by Pagel et al. (1979) has found widespread acceptance and use. Left panel of Fig. 1 shows the recent O/H – R_{23} diagram for the compiled sample of the HII regions (Pilyugin & Grebel, 2016). Fig. 1 well demonstrates that the relation between the oxygen abundance and the R_{23} index is double-valued, with two distincts parts traditionally known as the upper and lower branches of the O/H – R_{23} diagram. Two distinct relations between the oxygen abundance and the R_{23} index should be established, one for the upper branch (the high-metallicity calibration) and one for the lower branch (the low-metallicity calibration). One should delimited the upper and lower branches and the transition zone (see right panel of Fig. 1). These delimitations are somewhat arbitrary.

The earliest calibrations were one-dimensional (Edmunds & Pagel, 1984; McCall et al., 1985, among others), i.e. they had the functional form O/H = $f(R_{23})$ where O/H depends on the unique parameter R_{23}. It has been argued (Pilyugin, 2000, 2001) that oxygen abundances derived with such a one-dimensional calibration are systematically in error. Indeed, the intensities of the oxygen emission lines generally do not depend only on the oxygen abundance of the HII region, but also on its physical conditions. These physical conditions are taken directly into account in the T_e-method through the very use of T_e, but they are ignored in one-dimensional calibrations. Following the suggestion of McGaugh (1991) that the strong oxygen lines may contain the necessary information to determine the oxygen abundance in low-metallicity HII regions, Pilyugin (2000, 2001) has shown that the physical conditions in a HII region can be estimated and taken

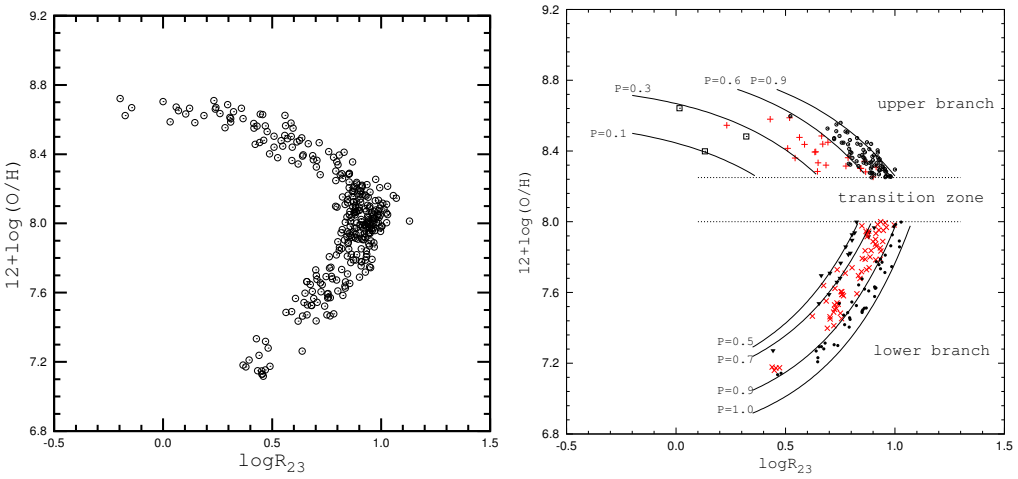

Figure 1. Left panel. The O/H – R_{23} diagram for the compiled sample of HII regions with T_e-based abundances (Pilyugin & Grebel, 2016). Right panel. A family of O/H = f(R23,P) curves labeled by different values of the excitation parameter P, superimposed on the then available observational data (Figure taken from Pilyugin & Thuan, 2005). The high-metallicity HII regions with 0.0 < P < 0.3 are shown by open squares, those with 0.3 < P < 0.6 by plus signs, and those with 0.6 < P < 0.9 by open circles. The low-metallicity HII regions with 0.5 < P < 0.7 are shown by filled triangles, those with 0.7 < P < 0.9 by crosses, and those with 0.9 < P < 1.0 by filled circles.

into account via the excitation parameter P. A more general two-dimensional parametric calibration of the functional form O/H = f(P, R_{23}) called the parametric method or the P-method. Right panel of Fig. 1 shows a family of O/H = f(R23,P) curves for different values of the excitation parameter P obtained by Pilyugin & Thuan (2005). The two-dimensional parametric calibration represents a significant improvement over the one-dimensional one.

The abundance determinations through the R_{23} calibrations meet two significant problems. First. Oxygen abundances in HII regions of the transition zone cannot be estimated through this calibration. Second. Since the relationship between oxygen abundance and R_{23} index is double-valued then one has to know apriori on which of the two branches the HII region lies. An unjustified use of the upper branch relationship in the determination of the oxygen abundance in low-metallicity HII regions (transition zone and below) would result in overestimated oxygen abundances.

2.3. Simple calibrations based on nitrogen lines: approach of Alloin et al.

Starting from the work by Alloin et al. (1979), the values of N_2 = [NII]λ6584/H_α and O_3N_2 = ([OIII]λ5007/H_α)/([NII]λ6584/H_α) are used as indicators of the oxygen abundance in HII regions. Why the nitrogen line N_2 can be use as oxygen

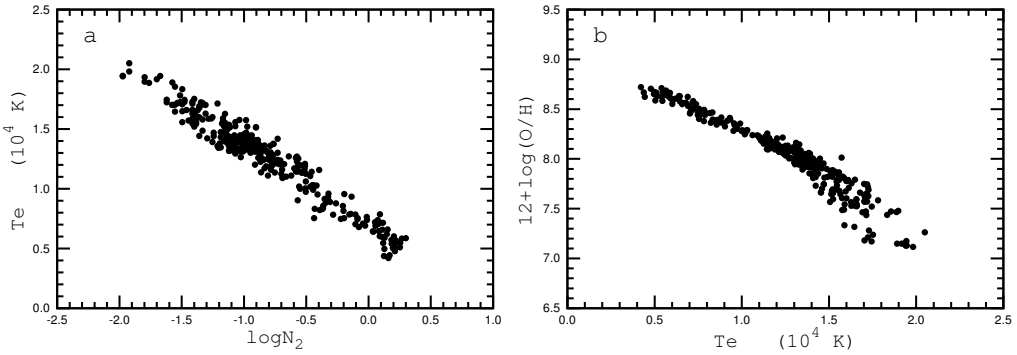

Figure 2. The electron temperature as a function of $\log N_2$ (left panel, Figure taken from Pilyugin & Grebel 2016) and the oxygen abundance as a function of electron temperature (right panel) for the compiled sample of HII regions with T_e-based abundances (Pilyugin & Grebel, 2016).

abundance index? The left panel of Fig. 2 shows the electron temperature in the HII region as a function of the nitrogen line N_2 flux (normalized to the Hα flux) in its spectrum for the sample of HII regions with measured electron temperatures T_e (compilation in Pilyugin & Grebel, 2016). The right panel shows the oxygen abundance as a function of electron temperature for the same objects. Inspection of the left panel of Fig. 2 shows that there is a rather tight correlation between the electron temperature and the nitrogen line N_2 flux. In turn, there is rather tight correlation between the oxygen abundance and electron temperature in the HII region (right panel of Fig. 2). As a result, the nitrogen line N_2 is an index of the oxygen abundance in the HII region.

Pettini & Pagel (2004) have suggested two calibrations based on the nitrogen lines $O/H = f(N_2)$ and $O/H = f(O_3N_2)$. Those calibrations are widely used in abundance determinations. The solid line on the left panel of Fig. 3 shows the relationship $O/H = f(N_2)$ of Pettini & Pagel (2004) superimposed on the observational data for the compiled sample of extragalactic HII regions with T_e-based abundances (Pilyugin & Grebel, 2016). The dashed line shows the $O/H = f(N_2)$ relationship obtained by Marino et al. (2013). The right panel of Fig. 3 shows the same but for the relationship $O/H = f(O_3N_2)$.

Examination of Fig. 3 shows that the $O/H = f(N_2)$ and $O/H = f(O_3N_2)$ calibrations produce a realistic oxygen abundances in high-metallicity HII regions but they are not workable at low-metallicities.

3. "Counterpart" method and combined calibrations

A new approach to the abundance determinations is developed in the last years (Pilyugin et al., 2012; Pérez-Montero, 2014; Vale Asari et al., 2016). This approach is based on the standard assumption that HII regions with similar intensities of strong emission lines have similar physical properties and abundances. If there were a suitable sample of reference HII regions with well-measured electron

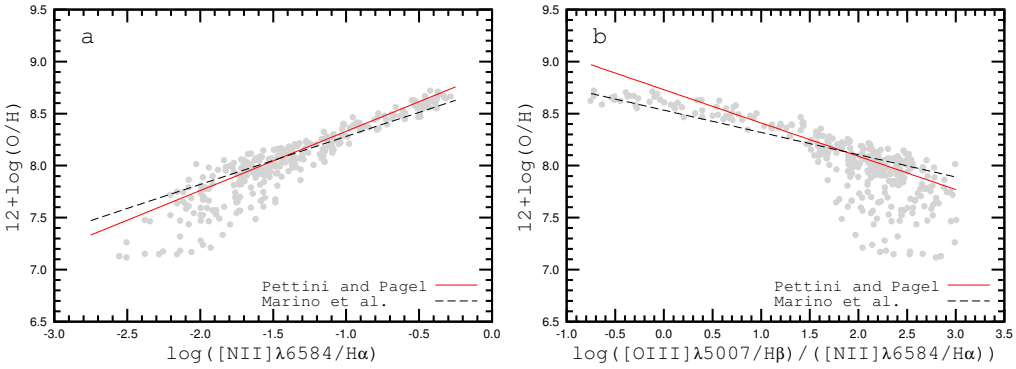

Figure 3. Left Panel. The oxygen abundance against the N_2 index for the compiled sample of extragalactic HII regions with T_e-based abundances (Pilyugin & Grebel, 2016). The solid line is the linear relationship $O/H = f(N_2)$ obtained by Pettini & Pagel (2004). The dashed line is the relationship from Marino et al. (2013). The right panel shows the same as the left panel but for the index O_3N_2.

temperatures and abundances, then one can choose among those reference HII regions the ones that have the smallest difference in strong line intensities compared to the studied HII region, i.e., one can find a corresponding, "counterpart" HII region. Then the oxygen and nitrogen abundances and electron temperatures in the investigated HII region can be assumed to be the same as in its counterpart. To obtain more reliable abundances, one may select several reference HII regions (counterparts) and then estimate the abundance in the target HII region through extrapolation. We will refer to this method as the "counterpart method". Pilyugin et al. (2012) have used a sample of real HII regions with well-measured electron temperatures and abundances (with T_e-based abundances) as reference HII regions while Pérez-Montero (2014) and Vale Asari et al. (2016) have used a set of HII region models.

A number of different emission lines can be used in the counterpart method. Therefore, one can expect that the abundances in HII regions obtained within the framework of this approach are more reliable than that obtained through the simple calibrations. It is very important that this method be workable over the whole metallicity scale for HII regions.

Generally speaking, it is not necessary to compare a number of emission lines in the target HII region and in the reference HII regions if the expression relating the oxygen abundance with the intensities of those emission lines would be established. Simple relations for deriving the oxygen abundances in HII regions with intensities of the three strong emission lines R_2, R_3, and N_2 in their spectra, $O/H = f(R_2, R_3, N_2)$, were suggested by Pilyugin & Grebel (2016). From one side, those calibration relations can be considered as an analytical form of the counterpart method since the same set of the emission lines is used. From another side, those calibration relations can be considered as a combined calibration since the oxygen- and nitrogen-line-based abundance indicators are simultaneously used. Relations for the determination of nitrogen abundances are also constructed.

There are many measurements of HII regions where the line R_2 is not available, for instance in the spectra of nearby galaxies in the Sloan Digital Sky Survey (SDSS). In this case, the sulphur line S_2 instead of the oxygen line R_2 can be used. The calibration relations of the type $\mathrm{O/H} = f(S_2, R_3, N_2)$ were also constructed. The abundances produced by the R_2-based and the S_2-based calibrations are in agreement to each other.

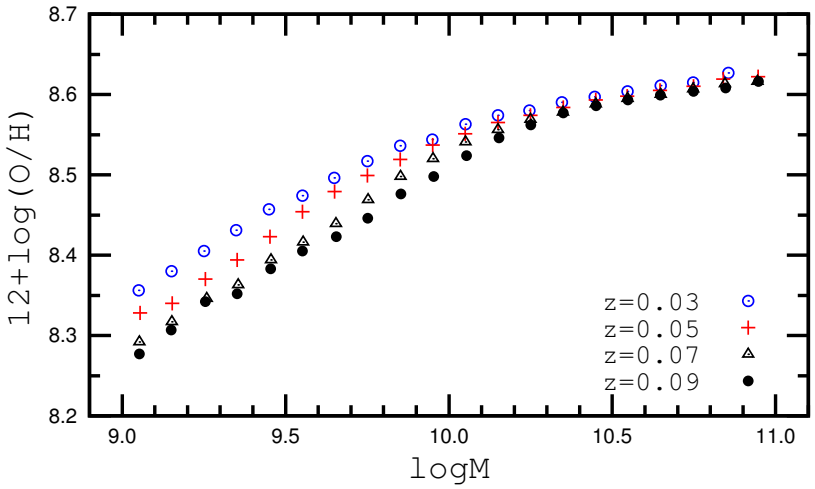

Figure 4. Oxygen abundance vs. stellar mass diagram for a sample of 77659 SDSS galaxies. The O/H – M relations for galaxies in four redshift intervals of $z \pm 0.01$ are presented. Symbols indicate the mean values for the bins of 0.1 dex in stellar masses. Figure taken from Pilyugin et al. (2017).

The validity and accuracy of the abundances obtained via the combined calibration can be illustrated in the following manner. Fig. 4 shows the O/H – M diagram for the sample of 77,659 SDSS galaxies. The O/H – M relations for galaxies in four redshift bins $z_j \pm 0.01$ (where $z_j = 0.03$, 0.05, 0.07, and 0.09) are presented. The symbols in Fig. 4 show the mean values in bins of 0.1 dex of the stellar masses. The O/H – M relations at low redshifts are more reliable for the low-mass galaxies than for the massive galaxies because the low-mass galaxies are numerous at low redshifts in our sample while the number of massive galaxies is rather low. Conversely, the O/H – M relations for large (near $z \sim 0.1$) redshifts are more reliable for massive galaxies than for the low-mass galaxies. Since only a sample of galaxies within a rather small interval of redshifts (ages) are considered, the evolutionary changes in oxygen abundances are small, around 0.05 dex. Nevertheless, our $\mathrm{O/H} = f(z, M)$ relations reproduce the known trends in galactic abundances. This suggests that the precision of the derived abundances derived through the combined calibration is high enough, i.e. the changes in abundances of the order of ∼0.05 dex can be detected.

4. On the metallicity scale for HII regions

The validity and reliability of the calibration-based abundances can be addressed on three levels.

First level, how well do the calibration-based abundances agree with the original abundances in the calibrating objects? The accuracy of the calibration relations depends on the number and quality of the calibrating data points. The number of the reference HII regions at high metallicities is relatively small. New high precision measurements of HII regions, especially at high metallicities, would be desirable to increase the reliability of the calibration-based abundances. The abundances in HII regions provided by the suggested calibration relations are in agreement with the T_e-based abundances, the mean difference for the 313 calibrating HII regions is 0.049 dex Pilyugin & Grebel (2016). There is no systematic discrepancy between calibration-based and T_e-based abundances. Therefore, the validity of the absolute calibration-based abundances (the potential systematic error) is, in fact, determined by the validity of the T_e-based metallicity scale for HII regions.

Second level, how well do the calibration-based abundances agree with the abundances determined through the other methods (model calibrations) using the same kind of the abundance indicators (collisionally excited lines)? It was noted above that the model calibrations generally produce oxygen abundances that are significantly higher than those derived through the empirical calibrations (see Kewley & Ellison, 2008), i.e. there is a discrepancy between the values of the abundance of a given HII region derived through the T_e-method and via the model fitting using the same collisionally excited lines. The validity and reliability of abundances obtained both through model fitting as well as through the T_e-method can be questioned. On the one hand, it is pertinent to quote a passage from a review paper written by an HII region modeller Stasińska (2004): "A widely spread opinion is that photoionization model fitting provides the most accurate abundances. This would be true if the constraints were sufficiently numerous (not only on emission line ratios, but also on the stellar content and on the nebular gas distribution) and if the model fit were perfect (with a photoionization code treating correctly all the relevant physical processes and using accurate atomic data). These conditions are never met in practice." On the other hand, there are a number of factors that can affect T_e-based abundance determinations. It should be stressed that the underlying logic of the classical T_e-method is irreproachable. However, the practical realization of the T_e-method relies on some assumptions that can be questioned. Indeed, the equations of the T_e-method correlate the intensities of the emission lines with the electron temperature and abundances within a volume with constant conditions (electron temperature and chemical composition). In reality, possible spatial variations of the physical conditions inside an HII region can affect the T_e-based abundance determinations.

Third level, how well do the calibration-based abundances agree with the abundances determined through the methods using another kind of abundance (and/or physical conditions) indicators (optical recombination lines, the Balmer and/or Paschen jumps)? Usually collisionally excited lines are used for the determination of the electron temperature and abundance in HII regions, e.g., in the T_e-method. The electron temperature of an HII region can be also derived from the Balmer

(or Paschen) jump Peimbert (1967), whereas the abundance of an HII region can also be determined from optical recombination lines. Guseva et al. (2006, 2007) determined the Balmer and/or Paschen jump temperatures in a large sample of low-metallicity ($12 + \log(O/H) \lesssim 8.36$) HII regions. They found that the temperatures of the O^{++} zones determined through the equation of the T_e-method (from collisionally excited lines) do not differ, in a statistical sense, from the temperatures of the H^+ zones determined from the Balmer and Paschen jumps although small temperature differences of the order of 3%–5% cannot be ruled out. The O^{++} abundances obtained from the optical recombination lines are systematically higher (by a factor of 1.3 – 3) than the ones determined through the equation of the T_e-method from collisionally excited lines (García-Rojas & Esteban, 2007; Esteban et al., 2014, and references therein).

Different hypotheses were used to explain the discrepancy between the abundances determined from the collisionally excited lines and from the optical recombination lines. Peimbert (1967) assumed that the temperature field within the HII region is not uniform but that there are instead small-scale spatial temperature fluctuations inside an HII region. If they are important then the $(O/H)_{T_e}$ abundance would be a lower limit and the abundances determined from the optical recombination lines remain unaltered. Tsamis & Péquignot (2005) suggest a dual-abundance model incorporating small-scale chemical inhomogeneities in the form of hydrogen-deficient inclusions. Neither abundances determined from the collisionally excited lines nor from the optical recombination lines are reliable in this case. Nicholls et al. (2012) and Dopita et al. (2013) argue that the energy distribution of electrons in HII regions does not follow a Maxwell distribution. In this case, abundances determined from optical recombination lines are more reliable.

Thus, at the present time there is no absolute scale for the metallicities of HII regions. Until the problem of the discrepancy between the abundances determined in different ways is resolved, doubts about the validity and reliability of the T_e-based (and any other) metallicity scale will remain. If at some point irrefutable proof will established that the T_e-based abundances should be adjusted then our calibration relations should be also reconsidered.

Finally, it should be noted that the T_e-method (and, consequently, our calibrations) produces the gas-phase oxygen abundance in HII regions. Some fraction of oxygen may be embedded in dust grains. Peimbert & Peimbert (2010) have concluded that the depletion of the oxygen abundance in HII regions can be around 0.1 dex increasing from ~ 0.08 dex in low-metallicity HII regions to ~ 0.12 dex in high-metallicity HII regions. When this effect is taken into account the total (gas + dust) oxygen abundance in an HII region is higher by ~ 0.1 dex than the one produced by the T_e-method and our calibrations.

Acknowledgments. This review is based on a number of original papers by the author and his collaborators J. M. Vílchez, T. X. Thuan, E. K. Grebel, and L. Mattsson. I am grateful to them for the contributions to those works.

I thank Oli Dors for invitation to take part in this Workshop. I acknowledge the Universidade do Vale do Paraíba for support of my visit to Campos do Jordão.

References

Alloin D., Collin-Souffrin S., Joly M., Vigroux L., 1979, *A&A*, **78**, 200
Dopita M. A., Sutherland R. S., Nicholls D. C., Kewley L. J., Vogt F. P. A., 2013, *ApJS*, **208**, 10
Edmunds M. G., Pagel B. E. J., 1984, *MNRAS*, **211**, 507
Esteban C., García-Rojas J., Carigi L., et al., 2014, *MNRAS*, **443**, 624
García-Rojas J., Esteban C., 2007, *ApJ*, **670**, 457
Guseva N. G., Izotov Y. I., Papaderos P., Fricke K. J., 2007, *A&A*, **464**, 885
Guseva N. G., Izotov Y. I., Thuan T. X., 2006, *ApJ*, **644**, 890
Kewley L. J., Ellison S. L., 2008, *ApJ*, **681**, 1183
Marino R. A., Rosales-Ortega F. F., Sánchez S. F., et al., 2013, *A&A*, **559**, A114
McCall M. L., Rybski P. M., Shields G. A., 1985, *ApJS*, **57**, 1
McGaugh S. S., 1991, *ApJ*, **380**, 140
Nicholls D. C., Dopita M. A., Sutherland R. S., 2012, *ApJ*, **752**, 148
Pagel B. E. J., Edmunds M. G., Blackwell D. E., et al., 1979, *MNRAS*, **189**, 95
Peimbert A., Peimbert M., 2010, *ApJ*, **724**, 791
Peimbert M., 1967, *ApJ*, **150**, 825
Pérez-Montero E., 2014, *MNRAS*, **441**, 2663
Pettini M., Pagel B. E. J., 2004, *MNRAS*, **348**, L59
Pilyugin L. S., 2000, *A&A*, **362**, 325
Pilyugin L. S., 2001, *A&A*, **369**, 594
Pilyugin L. S., Grebel E. K., 2016, *MNRAS*, **457**, 3678
Pilyugin L. S., Grebel E. K., Mattsson L., 2012, *MNRAS*, **424**, 2316
Pilyugin L. S., Grebel E. K., Zinchenko I. A., Nefedyev Y. A., Mattsson L., 2017, *MNRAS*, **465**, 1358
Pilyugin L. S., Thuan T. X., 2005, *ApJ*, **631**, 231
Shi F., Zhao G., Liang Y. C., 2007, *A&A*, **475**, 409
Stasińska G., 2004, C. Esteban, R. García López, A. Herrero, and F. Sánchez (eds.), *Cosmochemistry. The melting pot of the elements*, pp 115–170
Stasińska G., 2006, *A&A*, **454**, L127
Tsamis Y. G., Péquignot D., 2005, *MNRAS*, **364**, 687
Vale Asari N., Stasińska G., Morisset C., Cid Fernandes R., 2016, *MNRAS*, **460**, 1739
Vílchez J. M., Esteban C., 1996, *MNRAS*, **280**, 720

Chemical Abundances in Gaseous Nebulae
AAA Workshop Series 10, 2016
G. Hägele, M. Cardaci & E. Pérez-Montero, eds.

Invited Review

The abundance discrepancy in HII regions

C. Esteban[1,2], L. Toribio San Cipriano[1,2] and J. García-Rojas[1,2]

[1]*Instituto de Astrofísica de Canarias, E-38200 La Laguna, Tenerife, Spain*
[2]*Departamento de Astrofísica, Universidad de La Laguna, E-38206, La Laguna, Tenerife, Spain*

Abstract. In this paper we discuss some results concerning the abundance discrepancy problem in the context of HII regions. We discuss the behavior of the abundance discrepancy factor (ADF) for different objects and ions. There are evidences that stellar abundances seem to agree better with the nebular ones derived from recombination lines in high-metallicity environments and from collisionally excited lines in the low-metallicity regime. Recent data point out that the ADF seems to be correlated with the metallicity and the electron temperature of the objects. These results open new ways for investigating the origin of the abundance discrepancy problem in HII regions and in ionized nebulae in general.

1. Introduction

The emission-line spectrum of HII regions can be detected and analyzed even at very large distances. They are essential probes to measure distances of extragalactic objects, the intensity and properties of star formation processes and the chemical composition of the interstellar medium. In fact, HII regions provide most of our current knowledge about the chemical composition of the Universe. The spectra of nebulae contain emission lines of several ionization species of chemical elements that are present in the ionized gas. The analysis of emission-lines permits to determine the abundance – the ratio of the number of atoms of a given element with respect to those of H – of important elements as He, C, N, O, Cl, α-elements as Ne, S and Ar and iron-peak elements as Fe and Ni. In the next decade, the use of 30-50m aperture telescopes will probably permit to derive abundances of some neutron-capture s-elements as Se or Kr in the brightest HII regions.

The O abundance determined from nebular spectra is the most widely used proxy of metallicity for galaxies at different redshifts. A proper determination of the physical conditions – electron temperature, T_e, and density, n_e – is necessary for obtaining reliable and accurate metallicities. Many of the emission lines in nebular spectra are excited by collisions with free electrons – the so-called collisionally excited lines (CELs) – and are forbidden by the selection rules. CELs can be very bright due to the high electron temperatures and low densities of ionized nebulae. In addition, there are also bright recombination lines of HI

– Balmer series in the optical – and HeI. In the last two decades, our group has developed a long-term research project devoted to measure very faint pure recombination lines (RLs) of heavy-element ions in HII regions from high- and intermediate-resolution spectroscopical data. The optical-NIR spectral range contains RLs of OI, OII, CII and NeII, whose intensities are of the order of 0.0001 to 0.001 times that of Hβ. Due to their faintness, these lines can only be detected and measured in bright nebulae using large aperture telescopes.
For several decades it has turned out that abundances of heavy-element ions determined from the standard method based on the intensity ratios of collisionally excited lines (CELs) are systematically lower than those derived from the faint RLs emitted by the same ions. This fact, usually known as the *abundance discrepancy* (AD) problem is quantified by the abundance discrepancy factor (hereafter ADF), defined as the difference between the logarithmic abundances derived from RLs and CELs:

$$\mathrm{ADF(X^i)} = \log(\mathrm{X^i/H^+})_{\mathrm{RLs}} - \log(\mathrm{X^i/H^+})_{\mathrm{CELs}}. \quad (1)$$

In Galactic and extragalactic HII regions, the ADF of O^{2+} – ADF(O^{2+}) – is between 0.10 and 0.35 dex (e.g. García-Rojas & Esteban, 2007; López-Sánchez et al., 2007; Esteban et al., 2009, 2014; Toribio San Cipriano et al., 2016, 2017) and can be even much larger in some planetary nebulae (PNe, see paper by García-Rojas in these proceedings). It is important to remark that other ions with optical RLs: C^{2+}, Ne^{2+}, and O^+ give values of their ADFs similar to those obtained for the ADF(O^{2+}) for the same object (García-Rojas & Esteban, 2007; Toribio San Cipriano et al., 2017), although the data for those ions are more limited and difficult to obtain (see Table 1). It is clear that changes or uncertainties in the face value of metallicity we adopt for celestial bodies may have a major impact in many fields of Astrophysics as the ingredients of chemical evolution models and predicted stellar yields (e.g. Carigi et al., 2005), the luminosity –and mass– metallicity relations for local and high-redshift star-forming galaxies (e.g. Tremonti et al., 2004), the calibration of strong-line methods for deriving the abundance scale of extragalactic HII regions and star-forming galaxies at different redshifts (e.g. Peña-Guerrero et al., 2012; López-Sánchez et al., 2012) or the determination of the primordial helium (e.g. Peimbert, 2008), among others.

Table 1. ADF for different ions and several HII regions (in dex).

	Milky Way	LMC	SMC		
Ion	Orion Neb.	M8	30 Dor	N66C	NGC 5253
O^+	+0.39±0.20	+0.14±0.09	+0.26±0.13	...	...
O^{2+}	+0.14±0.01	+0.37±0.04	+0.21±0.02	+0.35±0.13	+0.25±0.16
C^{2+}	+0.40±0.15	+0.54±0.21	+0.25±0.21	+0.45±0.15	+0.41±0.25
Ne^{2+}	+0.26±0.10	...	...	...	...
Ref.	1	2	3	4	5

1–Esteban et al. (2004); 2–García-Rojas et al. (2007); 3–Peimbert (2003); 4–Toribio San Cipriano et al. (2017); 5–López-Sánchez et al. (2007).

The origin of the AD is still unknown, but several hypotheses have been proposed. In this paper we will limit our discussion to the case of HII regions. For PNe the situation is more complex because they can contain material with different physical conditions and composition (see Peimbert & Peimbert, 2006, García-Rojas, these proceedings). The first hypothesis for explaining the AD was formulated by Torres-Peimbert et al. (1980). They propose that the AD is produced by spatial fluctuations of electron temperature, t^2, in the ionized gas, in the form originally proposed by Peimbert (1967). However, these temperature variations cannot be reproduced by chemically homogeneous photoionization models and different mechanisms have been invoked to explain their presence in ionized nebulae (see Esteban, 2002; Peimbert & Peimbert, 2006). According to this scenario, RLs should provide the true abundances because their emissivities are much less dependent on temperature than those of CELs. In fact, in the typical range of T_e of HII regions, the emissivities of the RLs of heavy-element ions are almost identical to that of Hβ and therefore abundances derived from RLs are practically independent on T_e. Nicholls et al. (2012) have proposed that a κ-distribution of electron energies – departure from the Maxwell-Boltzmann distribution – can be operating in nebulae and produce the AD, being also the determinations based on RLs the most reliable ones. However, some recent works have seriously questioned this hypothesis (e.g. Zhang et al., 2016; Ferland et al., 2016). A third hypothesis was proposed by Stasińska et al. (2007) and is based on the existence of semi-ionized clumps embedded in the ambient gas of HII regions. These hypothetical clumps – unmixed supernova ejecta – would be strong RL emitters, denser, cooler and more metallic than the ambient nebular gas. Assuming this scenario, abundances derived from RLs and CELs should be upper and lower limits, respectively, to the true ones, though those from CELs should be more reliable. There is even a last scenario outlined by Tsamis et al. (2011), which involves the presence of high-density clumps but without abundance contrast between the components.

Until now, the only work where the AD problem in a sample of HII regions has been discussed in length is that by García-Rojas & Esteban (2007). They found that the ADF is fairly constant and of order 2 in a limited sample of Galactic and extragalactic HII regions. In addition, they did not find correlations between the ADF(O^{2+}) and the O/H, O^{2+}/H^+ ratios, the ionization degree, T_e, FWHM of several bright emission-lines, and the effective temperature of the main ionizing stars within the observational uncertainties. On the contrary, they found that ADF seems to be slightly dependent on the excitation energy of the levels that produce the RLs, a fact that is consistent with the predictions of the classical temperature fluctuations or κ-distributions hypotheses.

2. Comparisons between nebular and stellar abundances

If CELs and RLs give different abundances, in which lines shall we trust? There are some observational evidences that can give us clues about this important question. In Fig. 1 we represent the abundances of 4 representative elements – C, N, O, and Ne – for which abundances have been derived from different kinds of lines in the Orion Nebula: CELs in the ultraviolet (UV, Walter et al., 1992; Tsamis et al., 2011), optical (Esteban et al., 2004) and far infrared (FIR; Simpson

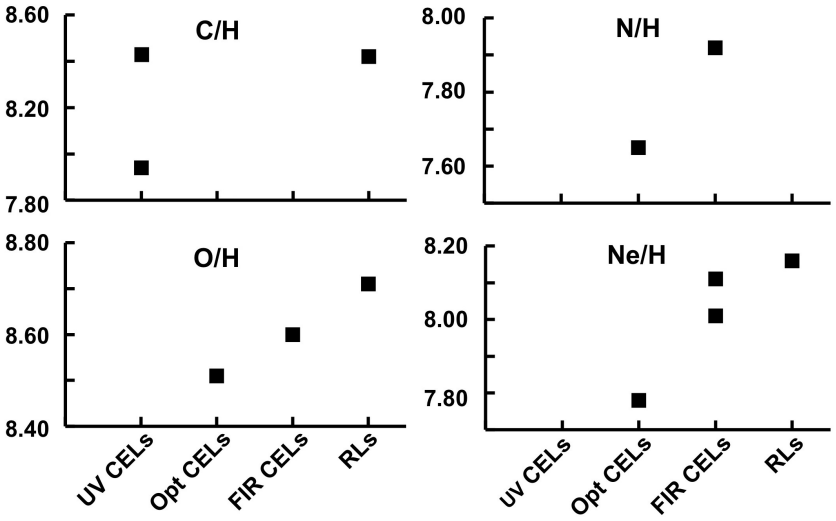

Figure 1. Abundances of C, N, O, and Ne in the Orion Nebula obtained using different kinds of emission-lines. We represent ultraviolet, optical and far infrared (UV, Opt and FIR, respectively) collisionally excited lines (CELs) and optical recombination lines (RLs). See text for references.

et al., 1986; Rubin et al., 2011), and optical RLs (Esteban et al., 2004). Except in the case of C – for which there are two discrepant independent abundance determinations from UV CELs – there is a tendency to increase the abundance when we move to the right in the diagrams, in the sense that the lines whose intensities are less dependent on T_e give higher abundances. This tendency agrees qualitatively with the predictions if the AD is produced by temperature fluctuations or κ-distribution hypotheses.

In Fig. 2 we compare the abundances of C, O and Ne of the Orion Nebula – using UV or optical CELs and RLs – with those of other objects of the Solar Neighborhood for which absolute abundances can be derived. We include the Sun (Asplund et al., 2009; Caffau et al., 2008, 2009), young F&G stars (Sofia & Meyer, 2001), and B-type stars (Nieva & Simón-Díaz, 2011). The size of the bars is proportional to their uncertainty. For C/H we can see that the solar and stellar values are quite consistent with the values obtained for the Orion Nebula using RLs, a similar trend is also found for O/H. However, we would expect some depletion into dust for both elements in the Orion Nebula, of the order of about 0.1 dex according to Esteban et al. (2004). Ne is a noble gas and no dust depletion is expected for this element and the results also indicate that the stellar and solar Ne abundances are more consistent with the Ne/H ratios determined from RLs in the Orion Nebula. It is interesting to note that the accurate determination of Ne/H obtained by Rubin et al. (2011) from FIR CELs observed with *Spitzer* is consistent with the RLs values. This result is also consistent with the predictions of the temperature fluctuations or κ-distribution hypotheses considering the low temperature dependence of the emissivity of FIR

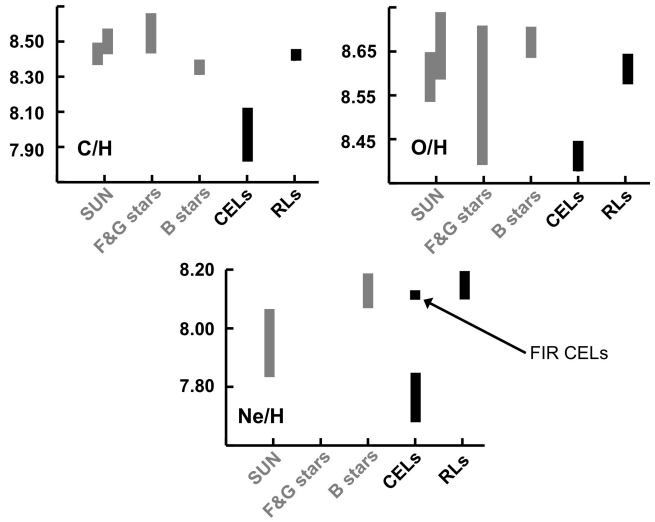

Figure 2. Comparison of abundances of C, O, and Ne in the Orion Nebula determined from CELs and RLs and those of the Sun and young F&G and B-type stars of the Solar Neighborhood (the data for non-nebular objects are represented with grey symbols). The size of the bars is proportional to their uncertainty. See text for references.

CELs. From the results presented in Figs. 1 and 2, one can conclude that nebular abundances determined from RLs are more consistent with those of the Sun and other stellar objects of the Solar Neighborhood than those determined from CELs.

Since 2002, our group has measured CII and OII RLs in several tens of extragalactic HII regions (Esteban et al., 2002, 2009, 2014; López-Sánchez et al., 2007; Toribio San Cipriano et al., 2016, 2017). In several of those papers we have compared our nebular abundances derived from CELs and RLs with those determined in early B-type stars located in their vicinity. The O abundance of early B-type stars –which is not expected to be affected by stellar evolution effects– should reflect the present-day chemical composition of the interstellar material in the regions where they are located. The results for extragalactic objects are not always consistent with the aforementioned ones discussed for the Orion Nebula. Toribio San Cipriano et al. (2016) compared O abundances derived from CELs and RLs in HII regions of the spiral galaxies M33 and NGC300 with the O abundances derived in B supergiants by Urbaneja et al. (2005a,b). These authors found that the stellar O/H ratios are in better agreement with the nebular abundances calculated using RLs in the case of M33, while in the case of NGC 300 the agreement is better with CELs. More recently, Toribio San Cipriano et al. (2017) make a similar comparison in the case of the Magellanic Clouds. They find that the O abundances determined by Hunter et al. (2009) for B-type stars in young clusters of the LMC and SMC are more consistent with the values obtained from CELs for the associated HII regions.

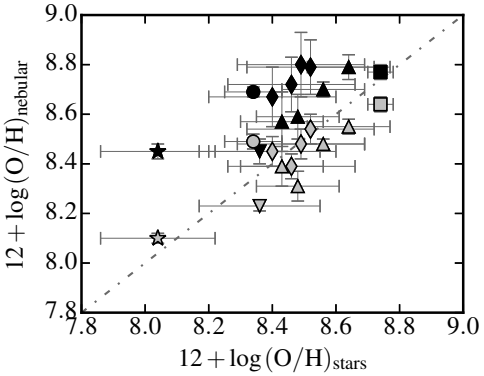

Figure 3. Comparison of the O abundance determined from young supergiant stars with those obtained from HII regions located in the same star-forming region or at the same galactocentric distance in the same galaxy. Squares: Orion Nebula and its associated cluster; circles: N11 in the LMC; stars: N66 in the SMC; down-facing triangles: NGC6822; triangles: M33; diamonds: NGC 300. Grey and black symbols represent nebular CELs-based and RLs-based O/H ratios, respectively. The dot-dashed line represents the 1:1 relation. Figure taken from Toribio San Cipriano et al. (2017).

Bresolin et al. (2016) suggested that nebular abundances determined either from CELs or RLs can display different levels of agreement with the B supergiant determinations in different galaxies, depending on the metallicity regime. They proposed that the RL-based nebular metallicities agree with the stellar metallicities better than the CELs in the high-abundance regime, but that this situation reverses at low abundance values. In Fig. 3 we have made a similar exercise than in figure 11 of Bresolin et al. (2016) but including data for individual HII regions with high quality nebular CELs and RLs determinations and compare with O/H ratios determined from young supergiant stars located in the same star-forming regions or galactocentric distance in the same galaxy. The squares correspond to data for the Orion Nebula and B-type stars of its associated cluster (Simón-Díaz & Stasińska, 2011; Esteban et al., 2004). For the MCs we include data for the ionized gas (Toribio San Cipriano et al., 2017) and B-type stars (Hunter et al., 2009) of the star- forming regions N11 (LMC, circles) and N66 (SMC, stars). We have considered data points of several HII regions of M33 (triangles) and NGC300 (diamonds) taken from Toribio San Cipriano et al. (2016) and Esteban et al. (2009), the stellar abundances have been estimated from the radial O abundance gradients determined by Urbaneja et al. (2005a,b) from the spectra of B-type supergiants, evaluated at the galactocentric distances of each HII region. The down-facing triangles represent values for the dwarf irregular galaxy NGC 6822, the nebular data are taken from Esteban et al. (2014) and the stellar ones from the spectral analysis performed by Venn et al. (2001). Nebular data have been increased 0.1 dex to correct for dust depletion in all the objects. From the figure, one can conclude that while in the case of M33 and NGC 6822 both kinds

of lines give nebular abundances consistent with the stellar ones, in the other cases we obtain contradictory results. The nebular O abundances determined from RLs in the Orion Nebula are the ones consistent with stellar determinations while in the MCs and NGC 300 the determinations based on CELs are the only ones consistent with the stellar abundances. This seems to be qualitatively consistent with the result obtained by Bresolin et al. (2016). We need further high-quality data – specially in the higher- and lower-metallicity regimes – to confirm this tendency.

3. ADF *versus* some nebular parameters

García-Rojas & Esteban (2007) explored the dependence of the ADF with different properties of HII regions. Those authors reported that the ADF seems to be independent of metallicity however, their sample was rather limited in both, the number of objects and metallicity. In Fig. 4, we present the behavior of the ADF(O^{2+}) with respect to O/H ratio, T_e, and ionization degree (O^{2+}/O ratio). Green squares correspond to Galactic HII regions (García-Rojas & Esteban, 2007; Esteban et al., 2004, 2013); red circles and blue stars represent objects in the LMC and SMC, respectively (Toribio San Cipriano et al., 2017); orange triangles correspond to HII regions in M33 (Toribio San Cipriano et al., 2016); cyan pentagons to objects in M101 (Esteban et al., 2009); and pink down-facing triangles to star-forming dwarf galaxies (López-Sánchez et al., 2007; Esteban et al., 2014). Let's focus our attention on panel a) of Fig. 4, although the ADF(O^{2+}) values of many objects have large uncertainties, the distribution of the points indicates a complex behavior in the ADF(O^{2+}) *versus* O/H diagram. The ADF distribution shows a minimum at 12 + log(O/H) $\sim$ 8.5 and seems to increase when the O/H becomes higher or lower. This apparent "seagull" shape, if real, is difficult to explain. In the case of Galactic HII regions we obtain a high dispersion of ADFs and a tendency to larger values when O/H becomes higher. Considering the closeness of the Galactic nebulae, their dispersion may be due to aperture effects because we tend to observe bright small areas in these objects and their ADF could not be representative of the whole nebula. As it has been proven in several works (e.g. Mesa-Delgado et al., 2012, and references therein) the presence of localized high-velocity flows and/or high density clumps can produce large ADFs. The trend of the low-metallicity wing of the "seagull" shape of Fig. 4, seems to be clearer than the high-metallicity wing. The low-metallicity objects correspond to more distant objects, their spectra are obtained from apertures that encompass a large fraction of the nebula and, therefore, their observed areas are more representative of the global emission. Toribio San Cipriano et al. (2017) also find that the ADF(C^{2+}) seems to increase toward lower metallicities, reinforcing the validity of the apparent correlation between ADF(O^{2+}) and O/H shown in panel a).

Panel b) of Fig. 4 shows the ADF(O^{2+}) *versus* T_e for the high-ionization species, basically T_e([OIII]). We can see a similar seagull shape in this relation but inverted with respect to that shown in panel a) –. This result is not unexpected, as T_e and metallicity are related because O is one of the most important coolants in ionized nebulae. The trend of a decrease of ADF with increasing of T_e([OIII])

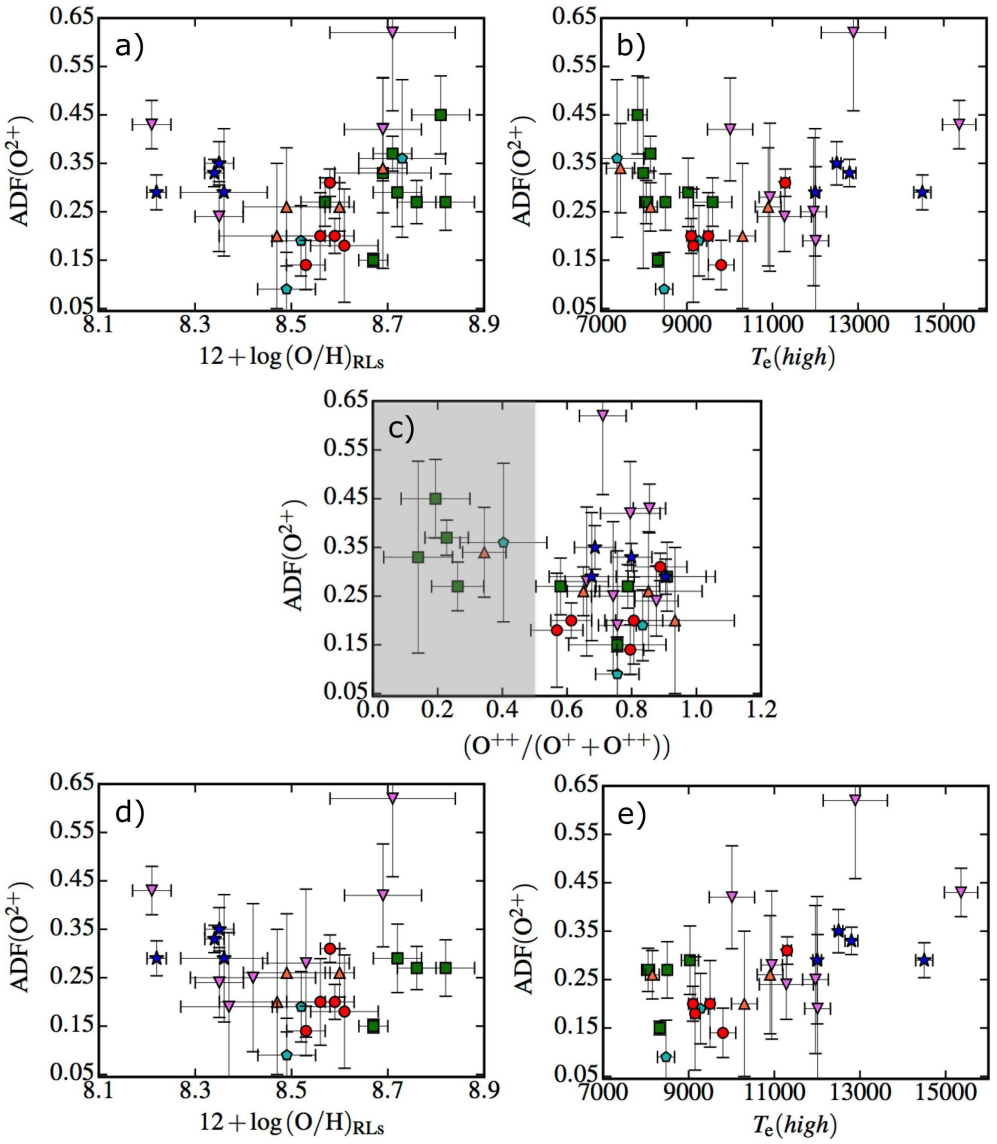

Figure 4. Panels a) and b): ADF(O^{2+}) vs. O/H ratio determined from RLs and vs. T_e for high ionization species for different HII regions in different host galaxies. Panel c): ADF(O^{2+}) vs. O^{2+}/O ratio – iization degree– for the same HII regions. The grey area contains low-ionization objects, with $O^{2+}/O \leq 0.5$. Panels d) and e): The same as panels a) and b) but removing the low-ionization HII regions lying in the grey area of panel c). See text for description of the symbols. Panel a) has been taken from Toribio San Cipriano et al. (2017).

in HII regions of near-solar metallicity and T_e([OIII]) $< 10^4$ K was previously reported by Rodríguez & Manso Sainz (2014).

Panel c) of Fig. 4 represents the ADF(O^{2+}) *versus* O^{2+}/O ratio – ionization degree – of the objects. The panel shows two main groups of objects. Most of them lie around $O^{2+}/O \sim 0.8$ and a small band is located at $O^{2+}/O < 0.5$, these last objects – most of them Galactic HII regions – show the lowest ionization degrees as well as ADFs higher than the average. It is interesting to note that, in panels a) and b), this group of low-ionization objects lie precisely in the zones of high O/H ratio and low T_e where we find the apparent trend of increasing ADFs. Panels d) and e) of Fig. 4 show the same relations than panels a) and b) but removing the low-ionization objects (those with $O^{2+}/O < 0.5$). In these new panels we can see that the trends of the ADF towards high metallicity and low T_e are practically washed out. The interpretation of this behavior is not easy. In low-ionization nebulae with $O^{2+}/O < 0.5$, the O/H ratio is dominated by O^+, and therefore the physical conditions of the O^{2+} zone – specially T_e – may be not representative of the whole HII region. We will further investigate this interesting result.

Another interesting aspect of Fig. 4 is the large ADF(O^{2+}) values reported in some giant HII regions belonging to star-forming dwarf galaxies (pink down-facing triangles). Esteban et al. (2016) speculate that large ADFs in HII regions might be produced by the presence of shocks due to large-scale interaction between the ionized gas and of stellar winds. A process that may dominate the kinematics of these complex and huge nebulae. This suggestion is based on the results obtained by Mesa-Delgado et al. (2014) and Esteban et al. (2016), who determined the ADF(O^{2+}) in several Galactic ring nebulae associated with evolved massive stars. These objects show mean ADF(O^{2+}) between 0.38 and 0.50 dex, values larger than the ADFs of normal HII regions with the same O abundance but similar to the high ADF(O^{2+}) values found in star-forming dwarf galaxies.

Acknowledgments. CE thanks Oli Dors Jr. and the rest of the members of the LOC for their kind invitation and financial support to participate in this enjoyable workshop. LTSC is supported by the FPI Program by MINECO under grant AYA2011-22614. This work was also partially funded by MINECO under grant AYA2015-65205-P.

References

Asplund M., Grevesse N., Sauval A. J., Scott P., 2009, *ARA&A*, **47**, 481
Bresolin F., Kudritzki R.-P., Urbaneja M. A., Gieren W., Ho I.-T., Pietrzyński G., 2016, *ApJ*, **830**, 64
Caffau E., Ludwig H.-G., Steffen M., et al., 2008, *A&A*, **488**, 1031
Caffau E., Maiorca E., Bonifacio P., et al., 2009, *A&A*, **498**, 877
Carigi L., Peimbert M., Esteban C., García-Rojas J., 2005, *ApJ*, **623**, 213
Esteban C., 2002, W. J. Henney, J. Franco, and M. Martos (eds.), *RevMexAA (SC)*, Vol. 12, pp 56–61
Esteban C., Bresolin F., Peimbert M., et al., 2009, *ApJ*, **700**, 654
Esteban C., Carigi L., Copetti M. V. F., et al., 2013, *MNRAS*, **433**, 382
Esteban C., García-Rojas J., Carigi L., et al., 2014, *MNRAS*, **443**, 624
Esteban C., Mesa-Delgado A., Morisset C., et al., 2016, *MNRAS*, **460**, 4038

Esteban C., Peimbert M., García-Rojas J., et al., 2004, *MNRAS*, **355**, 229
Esteban C., Peimbert M., Torres-Peimbert S., et al., 2002, *ApJ*, **581**, 241
Ferland G. J., Henney W. J., O'Dell C. R., et al., 2016, *RevMexAA*, **52**, 261
García-Rojas J., Esteban C., 2007, *ApJ*, **670**, 457
García-Rojas J., Esteban C., et al., 2007, *RevMexAA*, **43**, 3
Hunter I., Lennon D. J., Dufton P. L., et al., 2009, *A&A*, **504**, 211
López-Sánchez A. R., Dopita M. A., Kewley L. J., et al., 2012, *MNRAS*, **426**, 2630
López-Sánchez A. R., Esteban C., García-Rojas J., et al., 2007, *ApJ*, **656**, 168
Mesa-Delgado A., Esteban C., García-Rojas J., et al., 2014, *ApJ*, **785**, 100
Mesa-Delgado A., Núñez-Díaz M., Esteban C., et al., 2012, *MNRAS*, **426**, 614
Nicholls D. C., Dopita M. A., Sutherland R. S., 2012, *ApJ*, **752**, 148
Nieva M.-F., Simón-Díaz S., 2011, *A&A*, **532**, A2
Peña-Guerrero M. A., Peimbert A., Peimbert M., 2012, *ApJL*, **756**, L14
Peimbert A., 2003, *ApJ*, **584**, 735
Peimbert M., 1967, *ApJ*, **150**, 825
Peimbert M., 2008, *Current Science*, **95**, 1165
Peimbert M., Peimbert A., 2006, M. J. Barlow and R. H. Méndez (eds.), *Planetary Nebulae in our Galaxy and Beyond*, Vol. 234 of *IAU Symposium*, pp 227–234
Rodríguez M., Manso Sainz R., 2014, *RevMexAA (SC)*, Vol. 44, pp 22–22
Rubin R. H., Simpson J. P., O'Dell C. R., et al., 2011, *MNRAS*, **410**, 1320
Simón-Díaz S., Stasińska G., 2011, *A&A*, **526**, A48
Simpson J. P., Rubin R. H., Erickson E. F., Haas M. R., 1986, *ApJ*, **311**, 895
Sofia U. J., Meyer D. M., 2001, *ApJL*, **554**, L221
Stasińska G., Tenorio-Tagle G., Rodríguez M., et al., 2007, *A&A*, **471**, 193
Toribio San Cipriano L., Domínguez-Guzmán G., Esteban C., et al., 2017, *MNRAS*, **467**, 3759
Toribio San Cipriano L., García-Rojas J., Esteban C., et al., 2016, *MNRAS*, **458**, 1866
Torres-Peimbert S., Peimbert M., Daltabuit E., 1980, *ApJ*, **238**, 133
Tremonti C. A., Heckman T. M., Kauffmann G., et al., 2004, *ApJ*, **613**, 898
Tsamis Y. G., Walsh J. R., Vílchez J. M., et al., 2011, *MNRAS*, **412**, 1367
Urbaneja M. A., Herrero A., Bresolin F., et al., 2005a, *ApJ*, **622**, 862
Urbaneja M. A., Herrero A., Kudritzki R.-P., et al., 2005b, *ApJ*, **635**, 311
Venn K. A., Lennon D. J., Kaufer A., et al., 2001, *ApJ*, **547**, 765
Walter D. K., Dufour R. J., Hester J. J., 1992, *ApJ*, **397**, 196
Zhang Y., Zhang B., Liu X.-W., 2016, *ApJ*, **817**, 68

Chemical Abundances in Gaseous Nebulae
AAA Workshop Series 10, 2016
G. Hägele, M. Cardaci & E. Pérez-Montero, eds.

Invited Review

Photoionization models of CALIFA HII regions. Genetic method.

Christophe Morisset

Instituto de Astronomía
Universidad Nacional Autónoma de México
email: chris.morisset@gmail.com

Abstract. I present recent and forthcoming works to model the CALIFA HII regions using photoionization models. The first results are obtained with ad-hoc models (combining parameter determination by model fitting and strong line methods) while the next ones will use a Genetic Algorithm to fit the observations in a multi-dimensional space.

1. Introduction

The determination of the composition of HII regions is a challenge that has consequences on our understanding on the chemical evolution of our Universe, through the determination of the evolution of galaxies. Numerous methods have been developed during the last decades to determine chemical abundances. They are barely compatibles, especially when comparing strong line methods and photoionization model based methods (e.g. Fig. 2 of Kewley & Ellison, 2008).
In a recent paper, Morisset et al. (2016, hereafter Paper I) presented photoionization models for the CALIFA[1] survey of HII regions (Sánchez et al., 2012) obtained with the Cloudy code (Ferland et al., 2013) driven by pyCloudy (Morisset, 2013, 2014). The main idea is to obtain models for each one of $\sim$ 9,000 HII regions that reproduce the observed line ratio. We used the stellar population determined by the analysis of the underlying emission to compute the ionizing Spectral Energy Distribution (SED). The O/H abundance was determined from strong line method (from here the name of "hybrid models"). We finally kept only the ionization parameter U[2] and the N/O abundance ratio as free parameters.
In the following I will first briefly describe the method used in Paper I and secondly concentrate on the genetic method that we will apply in a forthcoming work.

[1]Calar Alto Legacy Integral Field spectroscopy Area survey.

[2]The ionization parameter U being $Q_0/4.\pi.r^2.n_H.c$, where Q_0 is the number of ionizing photons emitted by the source per time unit, r is the distance source-gas, n_H is the hydrogen density and c the light speed.

2. Hybrid models from Paper I

A photoionization code is a numerical way to transform a description of the object to be modeled (in terms of a set of input parameters including the SED shape and intensity, the gas distribution and composition and the description of the dust content) into a set of properties of the object that can be compared to observations: typically emission line intensities. Images, continuum spectra and absolute fluxes can also be considered. This operation can be schematically represented by a link between a point from the multiple dimension parameter space (P-space) into the multiple dimensions observable space (O-space), see e.g. Morisset (2009). This transformation is highly no-linear, as seen for example when comparing the regular shape of a input Cartesian grid and the corresponding non regular grid in the O-space (see Fig. 2 from Stasińska et al., 2006, and Fig. 1 below). This implies that the reverse transformation (determination of the parameters values from the observations) is not trivial and that the solution may even not exist or not being unique.
When the number of observables is small, we need to reduce the number of free parameters (i.e. adapt the dimension of the P-space to the dimension of the O-space). This is for example achieved by hiding the stellar luminosity, the distance between the ionizing source and the ionized gas, and the gas density into the single variable U. In our modeling process of the CALIFA HII regions described in Paper I, we have only [NII], [OII], and [OIII] emission lines (with of course Hα and Hβ, used to correct from reddening). We choose in a first step to only let log(U) and N/O as free parameters, and setting the O/H abundance using the diagnostic from Marino et al. (2013). The values of these two free parameters are obtained by fitting [NII]/Hα, and [OIII]/Hβ while [OII]/Hβ is used as an *a posteriori* test to select the final set of successful models. Each region needs an ad-hoc process, as the ionizing SED is defined accordingly to the underlying corresponding stellar population. This leads to running close to 2 millions of models for only fitting two parameters; allowing a third parameter (O/H) to be free would increase this number to an indecent value for the computational power we currently have. At the end of the process, we obtain $\sim$ 3,200 ad-hoc models that fit the 3 line ratios simultaneously. All these models are store and publicly available from the 3MdB database[3] (Morisset et al., 2015).
New relations are obtained between observables and parameters. We found that our models predict the [OIII]4363/5007 line ratio to be close to (and a little bit smaller than) the observed values from Marino et al. (2013). This result contrasts with Dopita et al. (2013) who obtain models hotter than the observations. We suspect the ionizing SED softness to be responsible for this discrepancy between the two kinds of models. Further investigations are on the way. One of the most puzzling results we obtained is from the comparison between the observed and theoretical Hβ equivalent widths. The discrepancies between observations and models are associated to photon leaking and neighbor contamination, see Paper I for more details.

[3] `https://sites.google.com/site/mexicanmillionmodels/`

3. Finding solutions in a 3D space: Genetic method

In a second work (Morisset et al., in prep.), we explore the full 3D parameter space defined by log(U), O/H and N/O, by fitting the [NII]/Hα, [OII]/Hβ, and [OIII]/Hβ line ratio simultaneously. To converge to the solution(s) we apply a genetic method (sort of Evolutionary Algorithm) based on the work by Cantó et al. (2009) and already described by Morisset (2009)). The genetic algorithm is based on successive grids of models (generations) following two basic rules of selection and evolution (crossover and mutation) to go from one generation to the next one:

- The selection is obtained by defining a distance to a target in the O-space (in our case the observed line ratios) and criteria that a model needs to fit to be selected. It can be a minimum distance (defining a selection hypervolume in the O-space) or a maximum number of objects to be selected after sorting them by increasing distance.
- The evolution phase applies to the previously selected models to obtain the parameters for the next generation. We choose to only apply mutations (no crossover), following Canto et al. (2009). The values of the free parameters are modified by applying a Mutation Operator; in our case adding random values to the parameters. This Operator corresponds to a shift of the point corresponding to the model. The shift is defined by a vector of random size and direction in the P-space. The size of the vector defines the hypervolume of the P-space that will be explored. This volume is supposed to decrease at each the generation to refine the quality of the fit.

We will only apply this new procedure to a selected amount of regions (the representative ones that cover most of the O-space and for which the data are of the best quality).
I present in Figs. 1 and 2 the process (in its current preliminary state) for the region 14 of NGC5947.
In Fig. 1, the red dots are the models of the first generation. The upper panels show the O-space projected on 2 planes: [OIII]/Hβ vs. [NII]/Hα on the left and [OIII]/Hβ vs. [OII]/Hβ on the right; each red dot corresponds to the result of a model. The lower panels show the P-space projected on 2 planes: log(U) vs. O/H on the left and N/O vs. O/H on the right; each red dot corresponds to the values of the parameters for a model. The yellow diamond at the crossing of the two dotted lines on the upper panels corresponds to the observations of region 14 of NGC5947. We can appreciate the non linearity of the modeling process, considering the almost regular grid in the P-space, transformed into a messy grid in the O-space. Some *locii* in the O-space correspond to two points in the P-space due to the double value of the abundance for a given [OIII]/Hβ ratio.
In Fig. 2, the models of the generations 6 to 9 are presented, each generation corresponding to a different color. The models are converging to the position of the observed value symbolized by the yellow diamond at the crossing of the dotted lines (panels a and b). The panels c and d show the locations of the models in the P-space; the convergence is also clear. An interesting point here is that the results are bi-valuated: two clouds of different values in the P-space (especially for O/H) lead to the same locations in the O-space: this is the illustration of

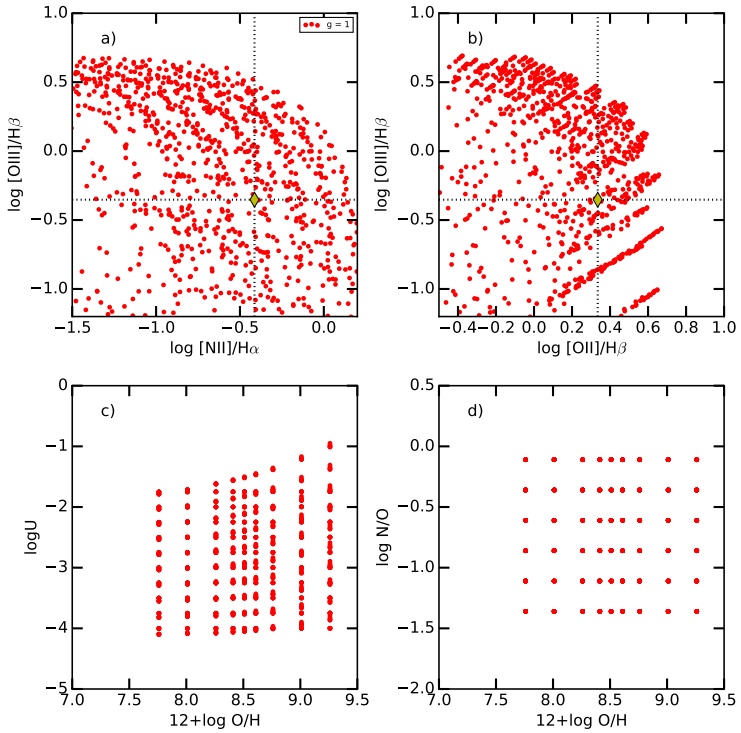

Figure 1. Distribution of the models for the first generation. See text for details.

the degeneracy of the solution and the difficulties to determine O/H in lack of other information. The 4 lower panels show the prediction of the models in other dimensions of the O-space, that could be compared to observations if available. Panels e and f show classical electron temperature diagnostics ([OIII]λ4363/5007 and [NII]λ5755/6584 resp.). The two solutions differ by 1 and 0.5 dex respectively for these line ratios. But the auroral lines are almost impossible to observe for extra-galactic objects. The panel g shows the [ArIII]λ7135/[NeIII]λ3869 line ratio, used by the Bayesian Oxygen and Nitrogen abundance Determinations (BOND) method (Vale Asari et al., 2016) to differentiate the two branches of solutions. We see that this line ratio is discriminant by 0.5 dex; but we have to notice that this line ratio is very dependent on observational constraints (huge range of wavelengths is necessary to obtain both lines at the same time). The HeI/Hβ line ratio (in panel h) is mainly determined by the ionizing SED and is then the same for both solutions.

In our example, at generation 9 (green dots), one of the solutions is excluded from the process (the one corresponding to the higher O/H). It is actually an artifact of the method and will be corrected, as both solutions are valid at that stage. More astrophysical information is needed to choose the "right" solution, using for example N/O vs. O/H empirical relations.

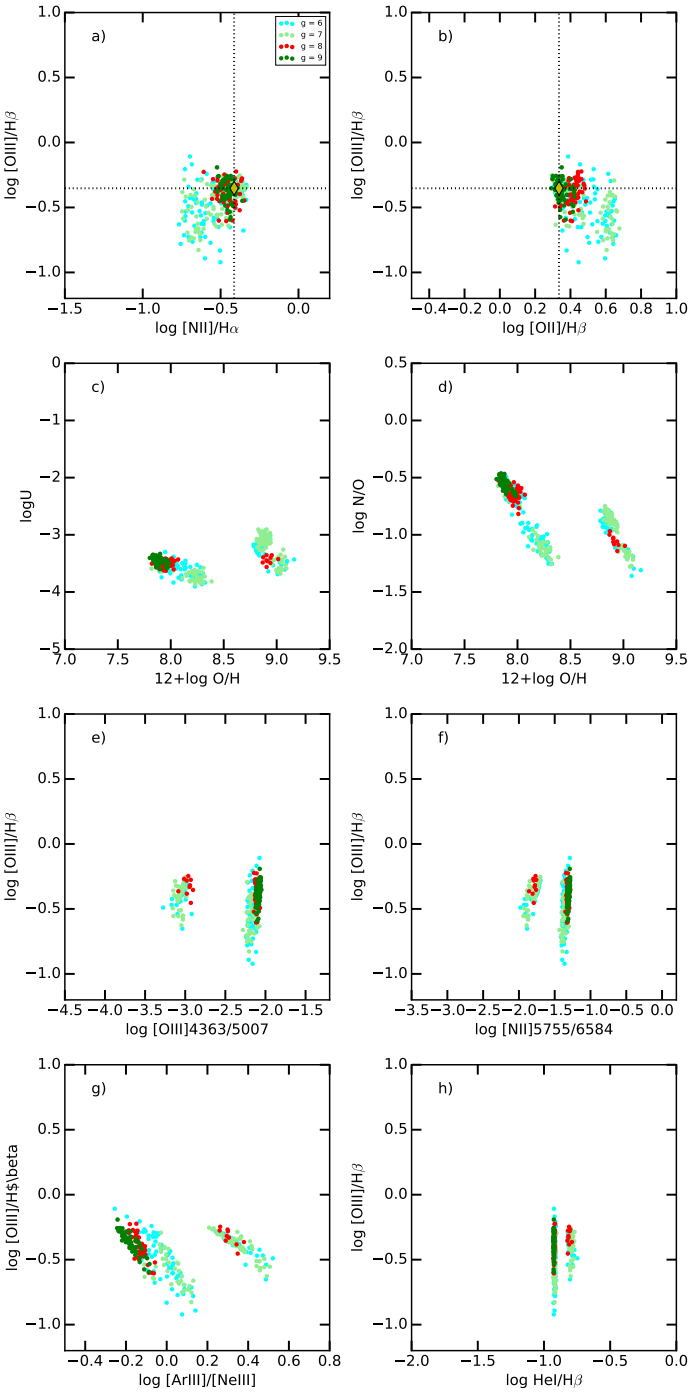

Figure 2. Upper 4 panels: same as Fig. 1 for the generations 6, 7, 8 and 9. The lower 4 panels show predictions of the models in other dimensions of the O-space. See text for details.

4. Conclusions

Stay tuned for the paper II to appear.

Acknowledgments. I would like to thank Oli Dors for this wonderful meeting. Many thanks to the editors for succeeding to join all our work in a coherent way. Thanks to Jorge Garcia-Rojas for reading the draft of this paper. And a very special thanks to Federico for the *asado*.

References

Cantó J., Curiel S., Martínez-Gómez E., 2009, *A&A*, **501**, 1259
Dopita M. A., Sutherland R. S., Nicholls D. C., Kewley L. J., Vogt F. P. A., 2013, *ApJS*, **208**, 10
Ferland G. J., Porter R. L., van Hoof P. A. M., et al., 2013, *RevMexAA*, **49**, 137
Kewley L. J., Ellison S. L., 2008, *ApJ*, **681**, 1183
Marino R. A., Rosales-Ortega F. F., Sánchez S. F., et al., 2013, *A&A*, **559**, A114
Morisset C., 2009, *Memorie della Società Astronomica Italiana*, **80**, 397
Morisset C., 2013, *pyCloudy: Tools to manage astronomical Cloudy photoionization code*, Astrophysics Source Code Library
Morisset C., 2014, *Asymmetrical Planetary Nebulae VI Conference*, p. 62
Morisset C., Delgado-Inglada G., Flores-Fajardo N., 2015, *RevMexAA*, **51**, 103
Morisset C., Delgado-Inglada G., Sánchez S. F., et al., 2016, *A&A*, **594**, A37
Sánchez S. F., Rosales-Ortega F. F., Marino R. A., et al., 2012, *A&A*, **546**, A2
Stasińska G., Cid Fernandes R., Mateus A., et al., 2006, *MNRAS*, **371**, 972
Vale Asari N., Stasińska G., Morisset C., Cid Fernandez R., 2016, *MNRAS*, **460**, 1739

Chemical Abundances in Gaseous Nebulae
AAA Workshop Series 10, 2016
G. Hägele, M. Cardaci & E. Pérez-Montero, eds.

Invited Review

Chemodynamics of Star-Forming Regions

G. F. Hägele[1,2], V. Firpo[3,4], G. Bosch[2,1], A. Díaz[5], N. Morrell[6], F. Campuzano-Castro[1] and M. Cardaci[1,2]

[1]*Instituto de Astrofísica de La Plata (CONICET-UNLP), Argentina*
[2]*Facultad de Ciencias Astronómicas y Geofísicas, Universidad Nacional de La Plata, Paseo del Bosque s/n, 1900 La Plata, Argentina*
[3]*Departamento de Física y Astronomía, Universidad de La Serena, Chile*
[4]*Gemini Observatory*
[5]*Universidad Autónoma de Madrid, E-28049 Madrid, Spain*
[6]*Las Campanas Observatory, Carnegie Observatories, Casilla 601, La Serena, Chile*

Abstract. The large number of massive stars belonging to regions with violent star formation dominates the morphology of the gas, the evolution of the different generations of stars and the physical conditions of their surrounding gaseous nebulae through the photoionization of the gas, strong stellar winds, super-bubble formation and material flows. The analysis of these processes between a starburst and its environment requires the complete study of the gaseous component, from its kinematical structure to its physical properties. Using different observational techniques, low-intermediate and high-spectral resolution spectroscopy, the physical conditions (electron density and temperatures), ionic and total chemical abundances of several atoms, reddening and ionization structure, for the global flux and for the different kinematical components can be derive. Applying the direct method or empirical relationships for abundance determination, we are able to perform a comparative analysis between different star-forming regions belonging to the same galaxy. The relative abundances of N/O, S/O, Ne/O and Ar/O for the different kinematical components give us clues for a common or very similar chemical evolution for the different kinematical components of each knot. It could also be indicative that the different kinematical components are different phases of the same gas. Similarities between the ionization structure of the different kinematical components could imply that the effective temperatures of the ionizing radiation fields are very similar for all the components, in spite of some small differences in the ionization state of different elements. The ionizing star clusters that excite the gas associated to each star-forming knot that produces the different kinematical components could therefore be the same.

1. Introduction

Gas content, masses, bar structure, and dynamical environment can strongly influence the large-scale star formation rate (SFR) along the Hubble sequence (Kennicutt, 1998). The variation of young stellar content and star formation activity is one of the most conspicuous characteristic along this sequence, and this variation in the young stellar population is part of the basis of the morphological classification made by Hubble (1926). Due to their different average SFR, the integrated spectra of galaxies vary considerably along the Hubble sequence.
The star formation processes depend strongly on the physical conditions of the media in which they take place. Among these conditions, the most important are the density of the molecular and gaseous material, and its spatial distribution and metallicity. These conditions restrict the effectiveness and the star formation rate as well as the initial mass function. In particular, the metallicity is a key parameter that controls many aspects in the formation and evolution of stars and galaxies. There are many processes that control the metallicity in a galaxy or a gaseous nebula, such as the galaxy formation and evolution, massive star formation, stellar winds, chemical yields, outflows and inflows (Kunth & Östlin, 2000).
Due to the nature of the galaxies (except for the nearest systems) almost all the information about their star formation properties is collected from integrated light measurements of the ultraviolet continuum, far-infrared and nebular emission recombination lines. In particular, the study of the gas ionized by the most massive stars can provide information about their masses, temperatures and evolutionary state. Photoionized gas shows a characteristic emission line spectrum, and the emission line intensities are controlled by the energy distribution of the ionizing photons, the spatial configuration of the ionized gas and its local properties, essentially its density and metal content. For example, in low metallicity environments, weak auroral lines of [OII]λ7325Å and [SII]λ4068Å are detectable and measurable (see e.g. Hägele et al., 2006, 2008, 2011), making possible the application of what is called the "direct method" or Te-method for abundance determination (see Pagel et al., 1992). For high metallicity regions, the high oxygen content provides a very efficient cooling of the region and therefore the emission lines are, in general, weaker, and no intrinsically weak lines are detected and the "direct method" is not applicable (see e.g. Díaz et al., 2007). In principle, the spectra of Blue Compact Dwarf galaxies (BCDs), galactic HII regions, giant extragalactic HII regions (GEHRs), circumnuclear and even nuclear regions, can be analyzed in the same way.
HII galaxies are low mass irregular galaxies with, at least, a recent episode of violent star formation concentrated in a few parsecs close to their cores. The ionizing fluxes originated by these young massive stars dominate the light, the ionization degree and temperature of their interstellar gas. Thus, these systems have emission line spectra very similar to those of the extragalactic giant HII regions. HII galaxies are a subclass of BCDs, which, in general, are characterized by their compact aspect, very low metallicities, gas richness and blue colors (Kunth & Östlin, 2000). With the improvement of telescopes it was found that not always HII galaxies are so compact as believed (see e.g. Hägele et al., 2011, 2012). Spectrophotometry of bright BCDs in the Local Universe allows the determination of abundances from methods that rely on the measurement of

emission line intensities and atomic physics (the "direct method"). In the case of more distant or intrinsically fainter galaxies, the low signal-to-noise obtained with current telescopes precludes the application of this method and empirical ones based on the strongest emission lines are required. The accuracy of the results however depends on the goodness of their calibration which in turn depends on a well sampled set of precisely derived abundances by the "direct method" so that interpolation procedures are reliable.

Unexpectedly, Gaussian fittings revealed the presence of more than one component in the Hβ and [OIII] emission line profile in high resolution spectra of circumnuclear star-forming regions (Hägele et al., 2007). The optimal fit was found for, at least, two different components for all the regions (see also Hägele, 2008; Hägele et al., 2009, 2010). Amorín et al. (2012) performed a kinematical study in a sample of six Green Pea galaxies (Cardamone et al., 2009), which probably are HII galaxies at intermediate redshifts (z$\sim$0.1-0.5), finding very complex emission-line profiles, consisting of the superposition of different kinematical components on a spatial extent of few kiloparsecs: a very broad line emission underlying more than one narrower component. We also found multi kinematical components in five star-forming knots of the Haro 15 galaxy using high-resolution spectroscopy (Firpo et al., 2011). Already in the original list of blue galaxies with emission lines by Haro (1956) who described this object as a 'minute cometary nebula', Haro 15 was later included in several compilations of BCDs. Haro 15 meets the criteria for a luminous compact blue galaxy (Hoyos et al., 2004), although some authors suggest that it may represent the final outcome of a merger between a dwarf elliptical and a gas-rich dwarf galaxy or HI cloud (Cumming et al., 2008). The interactions taking place during the merging process would act as the starburst trigger. From the morphological point of view, Haro15 has been classified as a (R)SB0 peculiar galaxy by de Vaucouleurs et al. (1991) and in fact, in the deep images taken with the 2.2-m CAHA telescope shown by López-Sánchez & Esteban (2008), the spiral morphology of the galaxy can easily be appreciated.

"Chemodynamics" is a term adopted by Esteban & Vílchez (1992) for the study of Wolf-Rayet nebulae and that our group has adopted for our detailed study of the physical properties of the emitting gas in BCDs taking into account the kinematical components of their emission lines observed using high spectral resolution echelle data.

In Section 2 we summarize the observational data and the technique used to perform the emission line profile decompositions, while in Section 3, we describe the implemented procedure to derived the physical conditions and chemical abundances of the emitting gas. In Section 4 we discuss our results and present our conclusions.

2. Observational data and profile decompositions

We need a wide spectral range to measure simultaneously the [OII]λ3727Å and [SIII]$\lambda\lambda$9069,9532Å nebular emission lines. Besides, we need to measure other important lines such as [OIII]$\lambda\lambda$4363,4959,5007Å, [SII]$\lambda\lambda$4068,6717,6731Å, and [SIII]λ6312Å. Our high-resolution spectroscopic data (R$\simeq$25000, $\Delta\lambda$=0.25Å at λ 6000Å) covering from 3400 to 10000Å were acquired using an echelle spectrograph attached to the 100-inch du Pont Telescope, LCO, in 2006 July 19 and

20. The effective slit width and length were 1 and 4 arcsec. The spectra were obtained as single exposures of 1800 s each. Observing conditions were good with an average seeing of 1 arcsec and photometric nights. Flux calibration was performed by observing, with an exposure time of 1200 s, the CALSPEC spectrophotometric standard star Feige 110 (Bohlin, Dickinson & Calzetti 2001). This star flux is tabulated every 2Å, which is ideal for calibrating high-resolution echelle spectra.
A detailed description about the echelle data and the reduction procedure can be found in Firpo et al. (2011) and Hägele et al. (2012). It must be noted that data obtained for the fainter knot F studied by Firpo et al. (2011) have not sufficient signal-to-noise ratio (S/N) to allow flux measurements with the accuracy needed to perform an analysis of the physical conditions of the gas and have therefore been excluded from this work.
The multiplicity of the kinematical components present in the emission line profiles and their positions and widths were verified in different intense emission lines (see Fig. 3 in Firpo et al., 2011). The kinematical fittings were performed using the ngauss task of IRAF[1] (see a detailed description of the procedure in Firpo et al. 2011 and Hägele et al. 2012). Although no reliable complex profile can be derived from weak lines, we have been able to fit them using as the profile templates the solutions of the stronger lines (which have S/N above 200) adjusting only their amplitudes, since their kinematical solutions (positions and widths) must be the same for different lines of the same atomic ion (or very similar for lines with similar ionization). In Fig. 1 we show an example of the fittings performed for the [OIII] emission lines for knot B. For [OIII]λ4363Å(right panel), we used as initial approximation that shown in the left panel. It was the first time that the study of the kinematical components of the auroral oxygen emission was performed in BCDs (Hägele et al., 2008).

3. Procedure

3.1. Physical conditions

We have studied the physical conditions of the emitting gas in four star-forming regions of Haro 15, analyzing the conditions in each region from the global and kinematical decomposition measurements. In what follows we will explain the different methods used to estimate the electron temperatures (T_e) and densities [$N_e \approx$ n([SII]6717/6731)] (see the detailed discussion in Hägele et al., 2012).
(i) When the weak auroral lines needed to implement the direct method could be measured we have derived the physical conditions using the direct method as described in Hägele et al. (2008,2011; see also Pérez-Montero 2017). This procedure is based on the five-level statistical equilibrium atom approximation in the task `temden`, of the software package IRAF (De Robertis et al., 1987; Shaw & Dufour, 1995).

[1]IRAF: the Image Reduction and Analysis Facility is distributed by the National Optical Astronomy Observatories, which is operated by the Association of Universities for Research in Astronomy, Inc. (AURA) under cooperative agreement with the National Science Foundation (NSF).

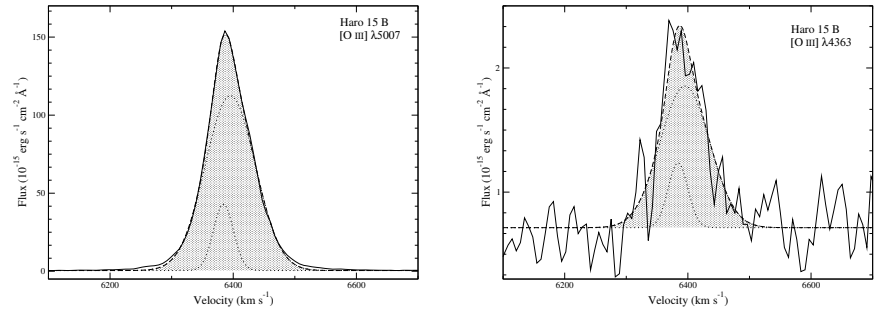

Figure 1. [OIII] λ5007Å (left panel) and [OIII]λ4363Å (right panel) emission line profiles of knot B in the Flux-Velocity plane with their kinematical decomposition and the sum (hatched area) of the different components superposed. Figure taken from Hägele et al. (2012).

(ii) When some of the weak auroral lines were not detected in the spectrum of an observed region, and the line temperatures could not be computed using the direct method, we have used relations between temperatures derived using photoionization models (Pérez-Montero & Díaz, 2003, 2005), or empirical and semi-empirical relations (Hägele et al., 2006; Díaz et al., 2007; Pilyugin, 2007), and the relation by Pérez-Montero & Díaz (2003) to estimate T_e([OII]) from T_e([OIII]). When it was necessary, we assumed the 'classical' approximation $T_e([OII]) \approx T_e([SII]) \approx T_e([NII])$.
(iii) When no auroral emission line was able to be measure in the spectrum, we have used empirical methods to estimate the electron temperatures: (a) If the strong emission lines of [SII], [SIII], [OII], and [OIII] were available in the spectrum of the studied region, we could use the relation between the empirical parameter SO_{23} ($= S_{23}/O_{23}$; defined by Díaz & Pérez-Montero (2000) and the [SIII] line temperature developed by Díaz et al. (2007). We used this T_e([SIII]) to estimate T_e([OIII]) using the relation between these two line temperatures derived by Hägele et al. (2006). (b) If the [SIII] emission lines were not detected with enough quality, we have used the relation between the [NII] nebular-to-auroral line intensities as a function of the intensities of the strong nebular oxygen lines for the determination of the [NII] electron temperature (t_2) applying the empirical relation by Pilyugin (2007).
(iv) When we are not able to measure either any auroral emission line, or any intense lines to derive the electron temperatures from empirical methods, we considered T_e([OIII]) equal to 10^4 K, since it is a typical value for this kind of objects. Theoretical and empirical relations were therefore used to derive the other line temperatures from the adopted value for T_e([OIII]).

3.2. Chemical abundances

The precise derivation of elemental abundances is not a straightforward matter. Firstly, accurate measurements of the emission lines are needed. Secondly, a certain knowledge of the ionization structure of the region is required in order to derive ionic abundances of the different elements and in some cases photoion-

ization models are needed to correct for unseen ionization states. An accurate diagnostic requires the measurement of faint auroral lines (usually about 1% of the Hβ intensity) covering a wide spectral range (see discussion in Hägele et al., 2006).

To study the global and kinematical component abundances in each knot, we have derived the ionic chemical abundances of different species: He^+, O^+, O^{2+}, S^+, S^{2+}, N^+, Ne^{2+}, Ar^{2+}. We have used the strongest available emission lines detected in the analyzed echelle spectra and the task `ionic` of the STSDAS package in IRAF, based on the five-level statistical equilibrium atom approximation, as described in Hägele et al. (2008).

The total abundances of He, O, S, N, Ne and Ar have been derived taking into account, when required, the unseen ionization stages of each element, resorting to the most widely accepted ionization correction factors (ICFs) for each species derived for HII like objects, $X/H = ICF(X^{+i})\, X^{+i}/H^+$ (see Pérez-Montero et al. 2007, and also see Dors et al. 2013, 2016).

4. Discussion and conclusions

In this paper we presented the chemodynamical results derived using echelle data from four star-forming regions belonging to the Blue Compact Dwarf galaxy Haro 15 and some conclusions obtained from them.

For all observed knots, and for all the global measurements and kinematical components, the electron densities were found to be well below the critical density for collisional de-excitation ($N_e \leq 500 cm^{-3}$), as is well known to occur in the star-forming processes belonging to HII galaxies. The errors in the electron densities are large enough so as to consider our estimate as an order of magnitude.

A large number of recombination and forbidden lines was detected in our echelle spectrum of knot A, although we were not able to measure any auroral emission line. We therefore used the relation between the SO_{23} parameter and the [SIII] temperature derived by Díaz et al. (2007) to estimate T_e([SIII]), and the empirical and theoretical relations to estimated the other temperatures from T_e([SIII]) (see Section 3). From the echelle spectra of knot B, we measured T_e([OIII]) and T_e([SIII]) applying the direct method, and estimated the other temperatures using the empirical and theoretical relations. The precision obtained for T_e([OIII]) and T_e([SIII]) is of the order of 5 and 13 per cent for the global measure, 15 and 18 per cent for the narrow component and 4 and 14 per cent for the broad component, respectively, for each temperature.

Using the estimated values for the electron densities and temperatures and a careful and realistic treatment of observational errors, we have estimated ionic and total abundances of several atomic species (O, S, N, Ne, Ar and He). We have also been able to carry out a chemodynamical analysis applying the direct method to the kinematical component decomposition of the emission-line profiles. The global measure presents a total oxygen abundance of 8.17±0.05, 0.3 times the solar value, while for the different kinematical components we obtained 8.04±0.05 (narrow1), 8.11±0.08 (narrow2) and 8.31±0.13 (broad), 0.22, 0.26 and 0.42 times the solar abundance, respectively. There seems to be a difference between broad and narrow components above 1σ level, but since the errors in the calibration of the relations based on photoionization models are not quan-

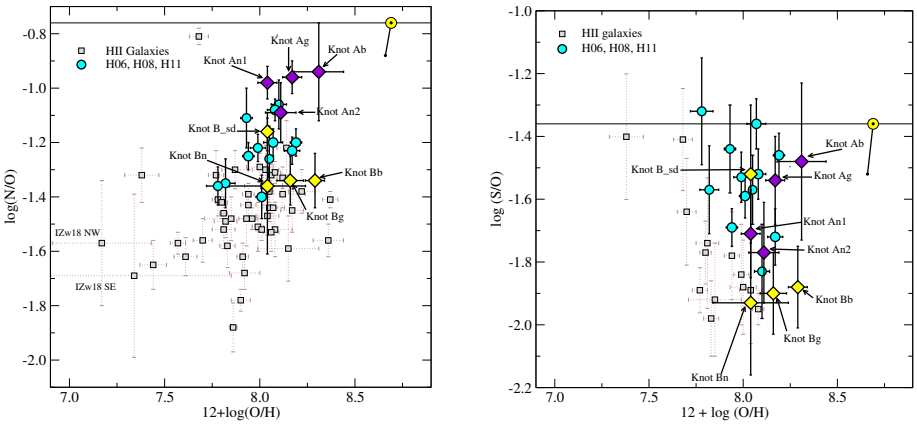

Figure 2. N/O (left-hand panel) and S/O (right-hand panel) as a function of 12+log(O/H) for knots A and B (violet and yellow diamonds, respectively), and the objects from Hägele et al. (2006, 2008, 2011, turquoise circles). The open squares are the HII galaxies from table 13 of Hägele et al. (2008). The observed knots are marked in the plot with their names plus a letter which denote the kinematic component measure ('g': global, 'n': narrow and 'b': broad). The solar values are shown with the usual sun symbol: oxygen from Allende Prieto et al. (2001), nitrogen from Holweger (2001) and sulfur from Grevesse & Sauval (1998). These values are linked by a solid line with the solar ratios from Asplund et al. (2005). Figure taken from Hägele et al. (2012).

titatively established, we can consider the total abundances in agreement for all components. The derived total oxygen abundances for the different kinematical components and for the global measure in this knot present the characteristic low values, within the errors, that are found for HII galaxies: 12+log(O/H) between 7.94 and 8.19 (Terlevich et al., 1991; Hoyos & Díaz, 2006). For knot B, the ionic abundances in the low-ionization zone (O^+, S^+, N^+) are higher for the narrow component, while the ions in the medium- and high- ionization zones (S^{2+}, Ar^{2+} and O^{2+}, Ne^{2+}, respectively) show the opposite behavior, i.e. lower values for the narrow component (see Hägele et al., 2012, for details). Taking into account the observational errors, the total oxygen abundances derived for these four star-forming knots are very similar among themselves, including the estimations for the different kinematical components. The total abundances of O, S, N, Ne and Ar are in the typical range found for HII galaxies (see e.g. Hägele et al., 2008). The total oxygen abundance derived for knots A and B are in good agreement with the values estimated by López-Sánchez & Esteban (2009).

The N/O ratios derived from the different components of knot A and the global measure of knot E are in very good agreement and show an excess with respect to the typical values found for HII galaxies (see left-hand panel of Fig. 2), in agreement with the values previously found by Amorín et al. (2010) and Pérez-Montero et al. (2011) for similar objects. For knots A and B, the relative

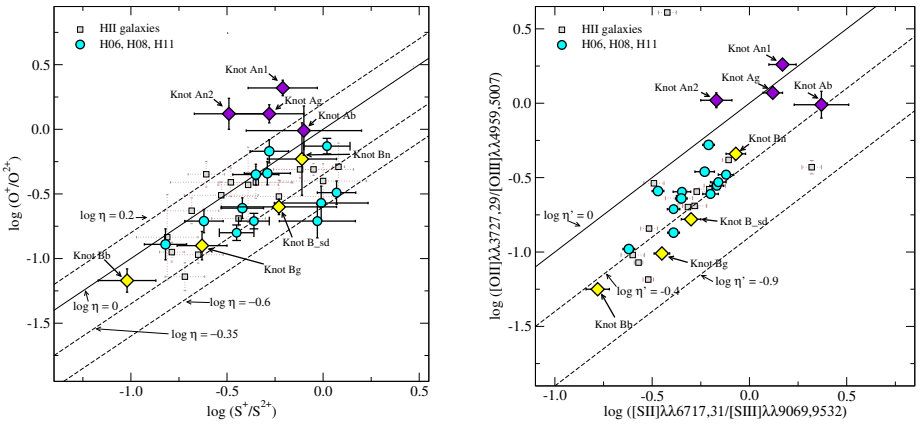

Figure 3. Idem as Fig. 2 for Ne/O (left-hand panel) and Ar/O (right-hand panel).

abundances of N, S, Ne and Ar with respect to the O for the different kinematical components are very similar (see Figs. 2 and 3). These could be evidence for a common or very similar chemical evolution for the different kinematical components of each knot. It could also be indicative that the different kinematical components are different phases of the same gas, which is in agreement with the scenarios proposed, for example, by Tenorio-Tagle et al. (1996) or Westmoquette et al. (2009). The turbulent mixing layer could be the origin of the broad component while the static photoionized layer could be the origin of the narrow one (see Fig. 16 in Westmoquette et al., 2009).

The quotients of O^+/O^{2+} and S^+/S^{2+}, called the 'softness parameter' and denoted by η, and its purely observational counterpart parametrized by the ratio between [OII]/[OIII] and [SII]/[SIII] (the η' parameter), are intrinsically related to the shape of the ionizing continuum and depends only slightly on the geometry (Vílchez & Pagel, 1988). Fig. 4 shows the logarithmic relations between these two ratios, the η and η' diagrams (left- and right-hand panel, respectively) derived for knots A and B. The diagonals in these diagrams correspond to constant values of η and η', which implies the same effective temperature of the radiation field of the ionizing star cluster (Vílchez & Pagel, 1988). The ionization structure of knots A and B mapped through the use of these diagrams shows very similar values, within the errors, for the different components of each of these regions. Only the broad component of knot A seems to have slightly higher effective temperature (lower value of the parameters) than the other components of this knot, showing similar values to those of knot B.

These similarities between the ionization structure of the different kinematical components of each region imply that the effective temperatures of the ionizing radiation fields are very similar for all the different kinematical components, in spite of some small differences in the ionization state of different elements. The ionizing star clusters that excite the gas belonging to each star-forming knot that produces the different kinematical components could therefore be the same. The difference in the ionizing structure of these two knots suggests a

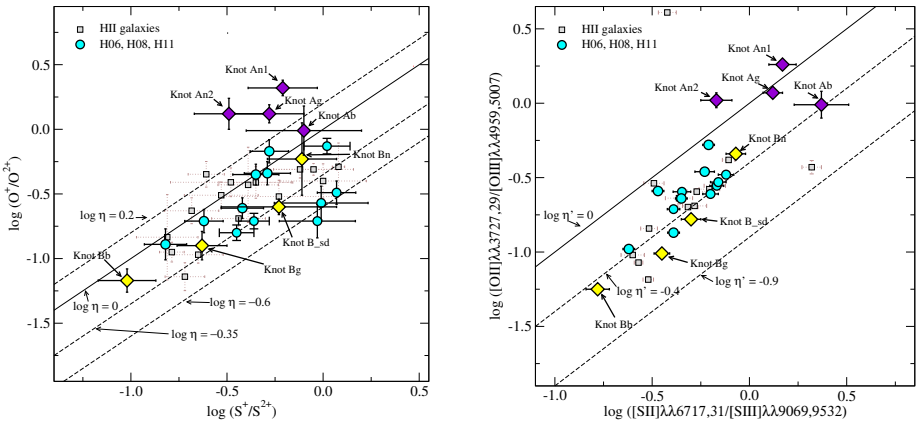

Figure 4. Left-hand panel: $\log(O^+/O^{2+})$ vs. $\log(S^+/S^{2+})$ (η diagram) for knots A and B (filled violet and yellow diamonds, respectively), the objects studied in Hägele et al. (2006, 2008, 2011, turquoise circles), and HII galaxies from the literature as described in Hägele et al. (2008, open squares). Right-hand panel: log([OII]/[OIII]) vs. log([SII]/[SIII]) (η' diagram), symbols as in the left-hand panel. As in Fig. 4, the letter added to the name of each knot denotes the kinematical components fitted in the emission line profiles. Figure taken from Hägele et al. (2012)

different evolutionary stage, with knot A located in a region with lower effective temperature. This is in agreement with the presence of an older and more evolved stellar population in knot A, as suggested by López-Sánchez & Esteban (2010).

Acknowledgments. This research has made use of the NASA/IPAC Extragalactic Database (NED) which is operated by the Jet Propulsion Laboratory, California Institute of Technology, under contract with the National Aeronautics and Space Administration.

References

Allende Prieto C., Lambert D. L., Asplund M., 2001, *ApJL*, **556**, L63
Amorín R., Vílchez J. M., Hägele G. F., et al., 2012, *ApJL*, **754**, L22
Amorín R. O., Pérez-Montero E., Vílchez J. M., 2010, *ApJL*, **715**, L128
Asplund M., Grevesse N., Sauval A. J., 2005, T. G. Barnes, III and F. N. Bash (eds.), *Cosmic Abundances as Records of Stellar Evolution and Nucleosynthesis*, Vol. 336 of *Astronomical Society of the Pacific Conference Series*, p. 25
Cardamone C., Schawinski K., Sarzi M., et al., 2009, *MNRAS*, **399**, 1191
Cumming R. J., Fathi K., Östlin G., et al., 2008, *A&A*, **479**, 725
De Robertis M. M., Dufour R. J., Hunt R. W., 1987, *JRASC*, **81**, 195
de Vaucouleurs G., de Vaucouleurs A., Corwin Jr. H. G., et al., 1991, *Third Reference Catalogue of Bright Galaxies*
Díaz A. I., Pérez-Montero E., 2000, *MNRAS*, **312**, 130

Díaz A. I., Terlevich E., Castellanos M., et al., 2007, *MNRAS*, **382**, 251
Dors O. L., Hägele G. F., Cardaci M. V., et al., 2013, *MNRAS*, **432**, 2512
Dors O. L., Pérez-Montero E., Hägele G. F., et al., 2016, *MNRAS*, **456**, 4407
Esteban C., Vílchez J. M., 1992, *ApJ*, **390**, 536
Firpo V., Bosch G., Hägele G. F., et al., 2011, *MNRAS*, **414**, 3288
Grevesse N., Sauval A. J., 1998, *Space Sci.Rev.*, **85**, 161
Hägele G. F., 2008, *Ph.D. thesis*, Universidad Autónoma de Madrid
Hägele G. F., Díaz A. I., Cardaci M. V., et al., 2007, *MNRAS*, **378**, 163
Hägele G. F., Díaz A. I., Cardaci M. V., et al., 2009, *MNRAS*, **396**, 2295
Hägele G. F., Díaz A. I., Cardaci M. V., et al., 2010, *MNRAS*, **402**, 1005
Hägele G. F., Díaz A. I., Terlevich E., et al., 2008, *MNRAS*, **383**, 209
Hägele G. F., Firpo V., Bosch G., et al., 2012, *MNRAS*, **422**, 3475
Hägele G. F., García-Benito R., Pérez-Montero E., et al., 2011, *MNRAS*, **414**, 272
Hägele G. F., Pérez-Montero E., Díaz A. I., et al., 2006, *MNRAS*, **372**, 293
Haro G., 1956, *Boletin de los Observatorios Tonantzintla y Tacubaya*, **2**, 8
Holweger H., 2001, R. F. Wimmer-Schweingruber (ed.), *Joint SOHO/ACE workshop "Solar and Galactic Composition"*, Vol. 598 of *American Institute of Physics Conference Series*, pp 23–30
Hoyos C., Díaz A. I., 2006, *MNRAS*, **365**, 454
Hoyos C., Guzmán R., Bershady M. A., et al., 2004, *AJ*, **128**, 1541
Hubble E. P., 1926, *ApJ*, 64
Kennicutt Jr. R. C., 1998, *ApJ*, **498**, 541
Kunth D., Östlin G., 2000, *A&A Rev.*, **10**, 1
López-Sánchez A. R., Esteban C., 2008, *A&A*, **491**, 131
López-Sánchez A. R., Esteban C., 2009, *A&A*, **508**, 615
López-Sánchez A. R., Esteban C., 2010, *A&A*, **516**, A104
Pagel B. E. J., Simonson E. A., Terlevich R. J., et al., 1992, *MNRAS*, **255**, 325
Pérez-Montero E., 2017, *PASP*, **129(4)**, 043001
Pérez-Montero E., Díaz A. I., 2003, *MNRAS*, **346**, 105
Pérez-Montero E., Díaz A. I., 2005, *MNRAS*, **361**, 1063
Pérez-Montero E., Hägele G. F., Contini T., et al., 2007, *MNRAS*, **381**, 125
Pérez-Montero E., Vílchez J. M., Cedrés B., et al., 2011, *A&A*, **532**, A141
Pilyugin L. S., 2007, *MNRAS*, **375**, 685
Shaw R. A., Dufour R. J., 1995, *PASP*, **107**, 896
Tenorio-Tagle G., Munoz-Tunon C., Cid-Fernandes R., 1996, *ApJ*, **456**, 264
Terlevich R., Melnick J., Masegosa J., et al., 1991, *A&AS*, **91**, 285
Vílchez J. M., Pagel B. E. J., 1988, *MNRAS*, **231**, 257
Westmoquette M. S., Gallagher J. S., Smith L. J., et al., 2009, *ApJ*, **706**, 1571

Chemical Abundances in Gaseous Nebulae
AAA Workshop Series 10, 2016
G. Hägele, M. Cardaci & E. Pérez-Montero, eds.

Invited Review

Extremely metal-poor galaxies: Chemical laboratories of the Early Universe

E. Pérez-Montero[1], J. Sánchez Almeida[2,3], R. Amorín[4,5,6], J. M. Vílchez[1], A. B. Morales-Luis[2,3], C. Muñoz-Tuñón[2,3] and R. García-Benito[1]

[1]*Instituto de Astrofísica de Andalucía - CSIC. Apdo. 3004. E-18080. Granada, Spain*
[2]*Instituto de Astrofísica de Canarias. C/ Vía Lactea s/n. La Laguna, Tenerife, Spain*
[3] *Departamento de Astrofísica, Universidad de La Laguna, Tenerife, Spain.*
[4]*INAF-Osservatorio Astronomico di Roma, via di Frascati 33, I-00078, Monte Porzio Catone, Italy.*
[5]*Cavendish Laboratory, University of Cambridge, 19 JJ Thomson Avenue, Cambridge, CB3 0HE, UK.*
[6]*Kavli Institute for Cosmology, University of Cambridge, Madingley Road, Cambridge CB3 0HA, UK*

Abstract. Extremely metal-poor galaxies (XMPs) are objects whose gas-phase metallicity is smaller than one tenth than the solar value, so they are thought to be unevolved objects and hence to be analogs to the primeval galaxies when they are found in the Local Universe. In this contribution, we review results from several studies of our group to search for XMPs at low- (SDSS) and mid-redshift (zCOSMOS), focused on improving the methods to identify them. Our analysis of the metal content of these objects includes the derivation of abundances of elements with both primary and secondary nucleosynthetic origin. The chemical analysis combined with the use of spatially resolved observations allow us to discriminate true primitive galaxies from other objects rejuvenated by the fall of pristine gas, helping to perform a better analysis of the analogs to the objects in the primitive Universe.

1. Extremely metal-poor galaxies

Local extremely metal poor galaxies (XMPs) can be analyzed in the Local Universe as possible analogs of very primitive galaxies based on the assumption that their very low metallicities (i.e. $12+\log(\mathrm{O/H}) < 7.69 \approx 1/10 \cdot 12+\log(\mathrm{O/H})_\odot$, taking the solar value from Asplund et al. 2009) evidences of a retarded evolution. However, the very low metal content of these objects can be due either to a very quiescent stellar and chemical evolution or to a more recent interaction with pristine extragalactic gas reservoirs.

XMPs are dwarf galaxies so their identification is not easy, as they tend to be faint. Only those Blue Compact Dwarfs (BCDs) dominated by strong emission lines produced by on-going star formation are targets that can be used for the search and study of metal-poor environments. According to Papaderos et al. (2008), most of the XMPs found can be considered as BCDs, but they present some morphological differences as compared with other dwarf galaxies. For instance XMPs present stepper surface brightness profiles hosts and with conspicuous morphological disruptions, what could be evidences of interactions with the environment.
For this reason it is necessary to complement the derivation of metallicity in XMPs with the study of other chemical species and star formation history that help to unveil the formation and evolution of these objects, prior to be considered as analogs to primitive galaxies.

2. Derivation of chemical abundances in XMPs

A proper determination of O/H in BCDs to identify XMPs relies on the measurement of the electron temperature (e.g. using the [OIII] 4363/5007 emission-line ratio). Once the O^{2+} ionic abundance is derived, the total O/H can be calculated with [OII] 3727 Å and measuring or assuming the temperature in the low-excitation region (e.g. Pérez-Montero & Díaz, 2003). Hence, the number of XMPs in large surveys (e.g. in the Sloan Digital Sky Survey, SDSS) has not been very large because some of the required lines may not be present in the observed spectrum. One alternative is to derive O^{+} ionic abundances using the [OII] auroral emission lines (7319,7330 Å, e.g. Kniazev et al., 2003) but these auroral lines are faint and contaminated with emission from recombination lines.
Strong-line methods based on [NII] emission lines have been widely used as a cheap alternative to derive abundances because it is easy to measure the [NII] 6583/Hα emission-line ratio N2. However, the number of XMPs identified using N2 is not very large (0.011 % of star forming galaxies in SDSS). The main reason is that [NII] emission lines are very faint in XMPs and, at same time, the N2 ratio presents a large dispersion in the low-metallicity regime (Morales-Luis et al., 2014, see Fig. 1) owing to the variation in the ionization parameter ($\log U$) and the nitrogen-to-oxygen ratio.
One example that strong-line methods based on [NII] are not adequate to study metal-poor galaxies is the analysis of the so- called green-pea galaxies (GPs). GPs are compact and their light is dominated by emission lines. Their specific star formation rate (sSFR) is very high, with high UV-luminosity and low extinction. They are metal-poor objects, but they present at same time higher N/O values than expected for their metallicities. Nevertheless, as discussed by Amorín et al. (2010) and can be seen in Fig. 2, the N/O values of the GPs are consistent with their stellar masses when they are compared to the other star-forming galaxies in SDSS, while they look O deficient.
From the mass-N/O relation of GPs, we see that the production of secondary N is the one expected for their mass. In addition, when GPs are observed with very deep optical spectroscopy using OSIRIS in the 10.4 m GTC (Amorín et al., 2012), it is possible to find the continuum emission from very old (several Gyr)

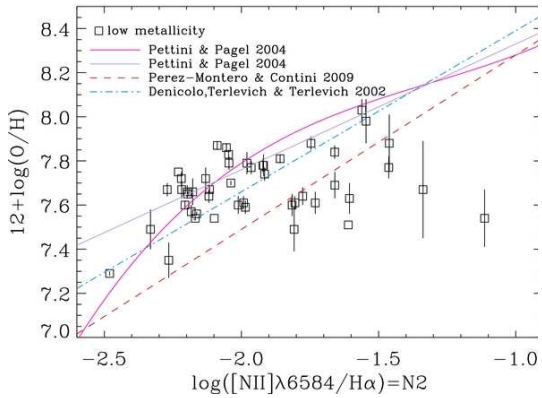

Figure 1. Relation between the N2 emission line ratio and total oxygen abundance for a sample of XMPs (Morales-Luis et al. 2014). The lines show different calibrations of the relationship between the oxygen abundance and N2 parameter. Figure 1 from Morales-Luis et al. (2014).

stellar populations that can be responsible for the production of the observed secondary N.

3. Searching for XMPs in SDSS

Aiming at the identification of a larger number of XMPs in SDSS, Sánchez Almeida et al. (2016) applied a new approach based on the use of the [OIII] emission-line ratio 4363/5007, sensitive to the electron temperature. As metals are the main cooling agent in the gas-phase of these objects, very high values of this ratios could be evidences of high electron temperatures and hence a lower metal abundances.

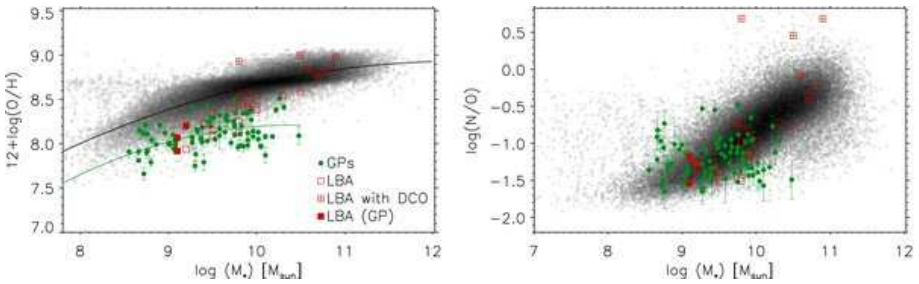

Figure 2. Relation between total stellar mass and total oxygen abundance (left panel) and nitrogen-to-oxygen ratio (right panel) for the star-forming galaxies in SDSS (grey) and GPs (green) taken from Amorín et al. (2010).

A pre-selection was performed classifying all the spectra in the SDSS-DR7 using the algorithm k-means (Sánchez Almeida et al., 2010), and then selecting those classes where the line [OIII] 4363 Å was prominent. An automatic python-based routine was applied to the resulting 1281 candidates to perform stellar continuum subtraction and measurement of the emission line fluxes.

The code HII-CHI-MISTRY [1] (HCM, Pérez-Montero, 2014) was used for the calculation of the total abundances. This method calculates O/H, N/O and log$U$ as the average values of a χ^2-weighted distribution calculated comparing the reddening-corrected intensities of the most representative emission lines with the predictions of a large grid of photoionization models covering a large range of possible abundances and excitations. This method allows us to derive chemical abundances consistent with the direct method using [NII] lines to derive O/H abundances because it constrains N/O in a first iteration using appropriate emission-line ratios (e.g. N2O2 and N2S2, Pérez-Montero & Contini, 2009). The code can also use the emission-line ratio [OIII] 5007/4363 even in the absence of [OII] 3727 Å to derive total oxygen abundances. This results very convenient for the search of XMPs in SDSS, where the spectral blue cut-off at 3800 Å prevents us from measuring the [OII] line for redshift < 0.02. The left panel of Fig. 3 shows a comparison between the O/H values derived from the direct method and using HCM for those XMP candidates with all the necessary lines. Although for very low O/H values HCM over-predicts the metallicity, there is a very good agreement between these two methods, and the code identifies all XMPs present in the list of candidates.

Using this procedure, Sánchez Almeida et al. (2016) selected 196 XMPs when using spectra where all the emission lines have S/N > 3, which almost doubles the number of previously known XMPs. For S/N > 2 the list of candidates has 136 additional objects, as the [OIII] 4363 Å line could be used in a larger number of objects. The right panel of Fig. 3 shows the O/H and N/O distribution of all candidates and those selected as secure XMPs. Most of them tend to have very low N/O ratios, consistently with a primary N production, but there is also a somehow large dispersion above the expected plateau for their regime of metallicity.

It is possible to study other properties of the sample of secure XMPs using the SDSS catalogues (e.g. stellar mass from MPA-JHU catalogue). Fig. 4 shows the relation between stellar mass and O/H (left panel) and stellar mass and N/O (right panel). Although most of the found XMPs are dwarfs, it is possible to see the relation in an extended range of masses. Likewise GPs, there is only an evident correlation in the case of N/O, while O/H do not present any correlation with all values much below than the relation parametrized by Andrews & Martini (2013). A similar behavior is obtained when the correlation with other integrated properties is studied, as it is the case of extinction. This can be indicative that N/O traces much better the previous chemical enrichment history of the galaxy than O/H that, in turn, can be affected by the interactions between the galaxies and the surrounding metal-poor gas. This is confirmed by the analysis of the stellar continuum, which indicates that light is dominated by young stellar populations, while stellar mass is dominated by very old stars.

[1] Publicly available at `http://www.iaa.es/~epm/HII-CHI-mistry.html`.

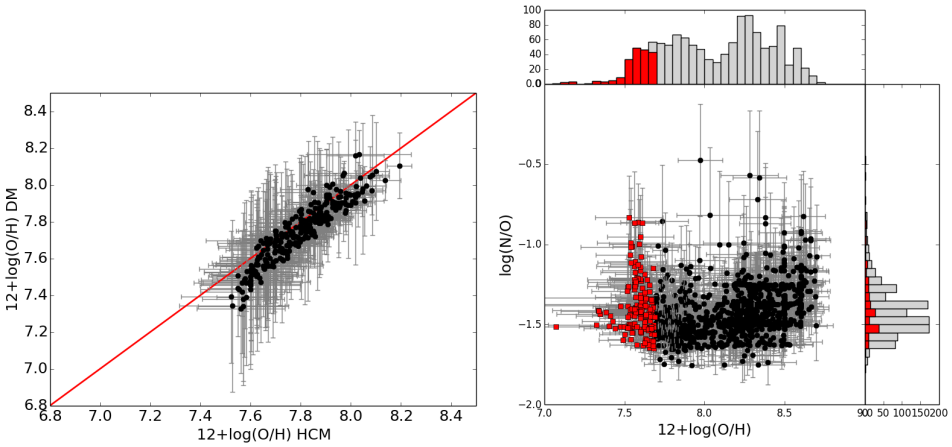

Figure 3. In left panel, relation between O/H derived from the direct method and from HCM when all emission lines were available with S/N > 3. In right panel relation between O/H and N/O and histograms for the sample of XMP-candidates in SDSS taken from Sánchez Almeida et al. (2016). Red squares represent the confirmed XMPs of the sample.

Filho et al. (2013) morphologically classified the XMPs, using SDSS color images, into symmetric, tadpole-like, two knots or multi-knots (see Fig. 5). The analysis reveals that a 71% of the selected XMPs show lack of symmetry as they belong to the three last categories and more than one half have cometary or tadpole-lie morphology.

4. XMPs at high redshift

At high redshift the search for XMPs is mainly based on deep photometric catalogues followed-up by multi-object spectroscopy (MOS). As an example, Amorín et al. (2015) selected in the zCOSMOS 20k survey a sample of 149 Extreme Emission Line Galaxies (EELGs, i.e. galaxies with an equivalent width of [OIII] 5007 Å larger than 100 Å). The optical spectra taken with the VIMOS instrument at the VLT were analyzed and their chemical abundances were derived. Among them, 6 XMPs were found at different redshifts between 0.3 and 0.8. Owing to the limited spectral range, O/H could only be derived using the [OIII] 5007/4363 emission-line ratio in three of the objects, shown in Fig. 6. For the other three, at $z < 0{,}4$, O/H was derived using the [NII]/Hα emission line ratio. These three objects at lower redshift present at same time very low N/O values, compatible with a production of primary nitrogen.
All of them have low masses and disrupted or cometary morphology, as can be also seen in Fig. 6. Most of the galaxies observed at high-redshift in the Hubble Ultra-Deep Field (e.g. Elmegreen et al., 2013) often show this tadpole-lie

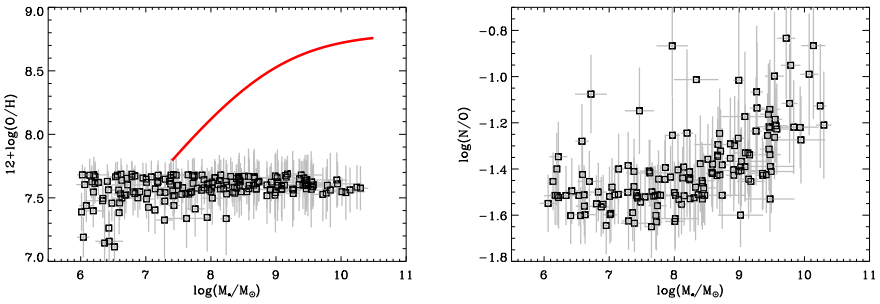

Figure 4. Relation between stellar mass and oxygen abundance (left panel) and between stellar mass and nitrogen-to-oxygen ratio (right panel) for the XMP candidates as taken from Sánchez Almeida et al. (2016). The solid line in left panel represents the parametrization of the mass-metallicity relation given by Andrews & Martini (2013).

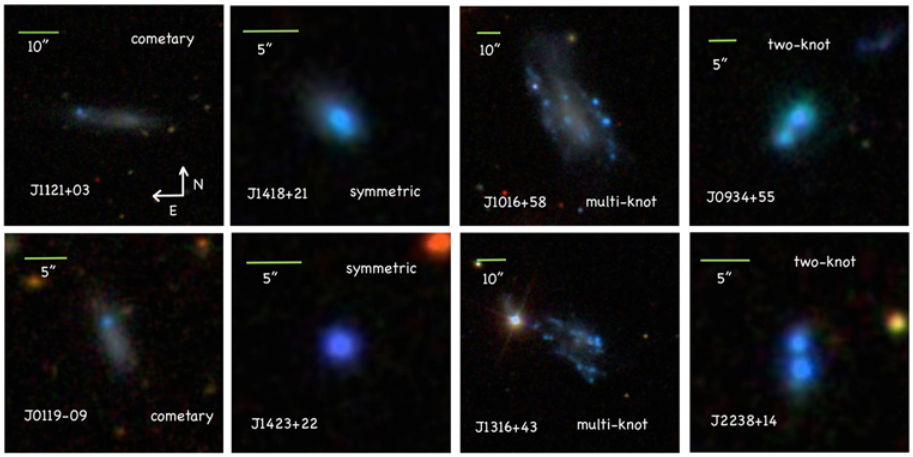

Figure 5. Examples of the various morphological types found among the XMPs; from left to right cometary, symmetric, multi-knot, and two-knot (Sánchez Almeida et al., 2016).

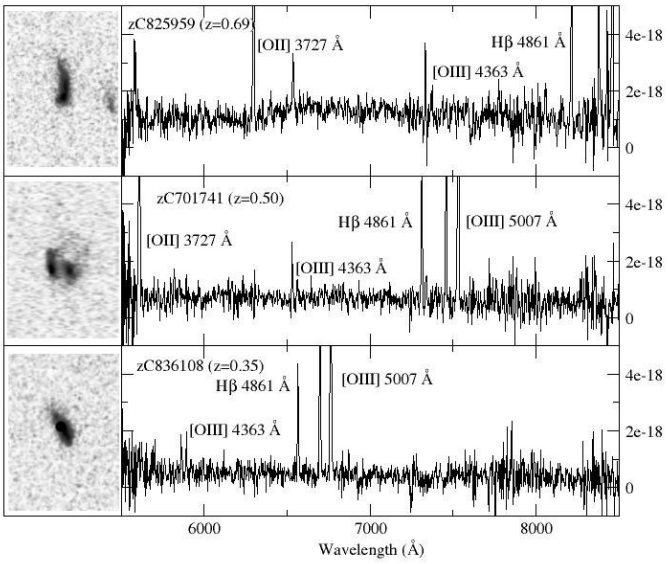

Figure 6. HST images and VLT optical spectra of three EELG-XMP galaxies at different redshifts selected from the zCOSMOS 20k survey (Amorín et al., 2015).

morphology, that could be related to the process of the mass assembly in early stages of galaxy disk formation.
In any case, only by means of near-IR spectroscopy is possible to find XMPs at z > 1. This is even more critical if N/O values for these objects are required, what would allow us to distinguish between real unevolved galaxies and metal-poor star-forming galaxies rejuvenated by the inflow of pristine gas.

5. Chemical inhomogeneities in XMP tadpoles

Given the disrupted or cometary morphology of most of the studied XMPs and the enhanced N/O abundance ratios found in many of them, it is interesting to perform spatially resolved spectroscopic observations of these galaxies. This allows us to separate the analysis of the very bright star forming knots from low surface brightness regions of the same galaxies to investigate the effect of interactions between the galaxies and the surrounding medium in different regions.
In this way, Sánchez Almeida et al. (2015) selected a sample of 10 cometary XMPs in the Local Universe. These objects were observed using deep long-slit OSIRIS-GTC optical spectroscopy observations. The slits were situated to cover the bright star-forming knots and the low-surface brightness tails to explore the metallicity pattern along the major-axis direction. These observations were complemented with long-slit high-resolution spectroscopy using the ISIS instrument at the William Herschel Telescope (WHT) to cover Hα, [NII], and [SII] emission lines (Olmo-García et al., 2017).

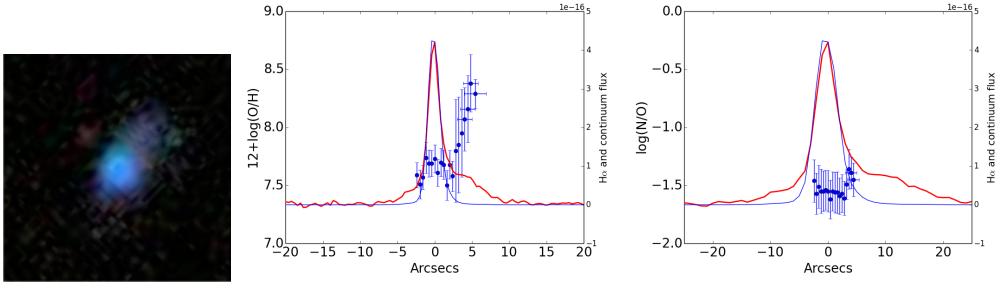

Figure 7. Left panel: SDSS color image of the XMP tadpole galaxy HS 0822+3542. The symbols in the central and right panels show the variation along the slit of O/H and N/O, respectively. These panels also contain the variation of the Hα flux (the red solid line) and the continuum (the blue solid line) along the slit.

The chemical abundances were derived in each extracted spectrum using HCm, what leads to a consistent derivation in the bright star-forming knots where [OIII] 4363 Å is detected and in the weak emission line regions where the direct method cannot be applied. The code overcomes the non detection of the [OIII] auroral line assuming an empirical law between O/H and ionization parameter in the grid of models in such a way that low metallicities are only compatible with high values of log U and vice versa. This assumption also leads to chemical abundances consistent with the direct method, although with a larger uncertainty.

As can be seen for one object of the observed sample in Fig. 7, there is a clear metallicity inhomogeneity correlated with the Hα flux, which is a tracer of the surface star formation rate. The bright star forming knots are metal-poor while the low-surface tails show higher O/H values. At same time, N/O looks much more homogeneous and there is not noticeable difference between the values measured in the knots and the tails. This observation is consistent with the fall of pristine gas in the galaxy heads, producing only in certain regions of the galaxies the triggering of the star formation and the drop of metallicity in these regions.

Fig. 8 shows the relation between total stellar mass and the oxygen abundances found in the starburst regions and in the tails of the analyzed XMP galaxies for the 10 analyzed XMPs. The high O/H values found in the low-surface brightness tails are above the relation found from other low-mass star-forming galaxies in SDSS from Lee et al. (2006). On the other hand, the very low values measured in the knots are clearly below this relation. For integrated observations of these objects, as the knots are much more luminous, these galaxies can be wrongly interpreted as young and unevolved.

6. Summary and conclusions

XMPs are usually identified as analogs to primitive galaxies because of their very low metallicities. However, in order to unveil the main mechanisms involved in the building-up of these galaxies, it is necessary to have a complete chemical char-

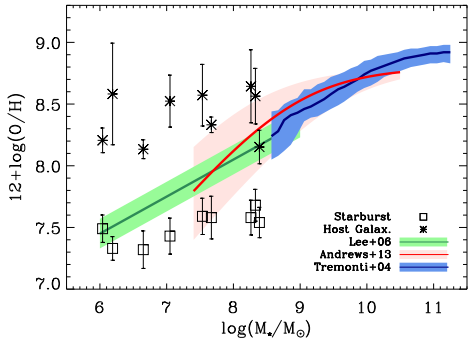

Figure 8. Relation between oxygen abundance and total stellar mass in the hosts (asterisks) and the starbursts (squares) of the 10 cometary XMPs observed with GTC (Sánchez Almeida et al., 2015). The green line represents the low-mass fitting in the SDSS from Lee et al. (2006).

acterization and the knowledge of their stellar masses and their star formation histories.

The identification of a galaxy as an XMP requires measuring its metallicity, which mainly relies on the ratio [OIII] 5007/4363 to determine the electron temperature. In addition, the measurement of other lines emitted by secondary elements, such as [NII] can help to depict a more complete chemical description of these objects. The procedure becomes more difficult at high redshift, since near-IR spectral observations are necessary to measure all these emission lines.

The study carried out by Sánchez Almeida et al. (2016) provides the largest sample of XMPs found in the SDSS so far. This work reveals that XMPs present a large dispersion in the O/H vs. N/O relation, with very low correlation between metallicity and stellar mass. In addition, more than one half of the sample presents cometary morphology.

These facts, as in the case of GPs, are consistent with the inflow driving star formation and being responsible for the low metallicities. This scenario is also consistent with the presence of chemical inhomogeneities found by Sánchez Almeida et al. (2015) in some selected tadpole XMPs. These spatial variations of the metallicity are correlated with the surface star formation rate. A probable origin for this metal-poor gas reservoir in infall to galaxy disks is the cosmic web, what is consistent with the results from numerical simulations (e.g. Sánchez Almeida et al., 2014).

Acknowledgments. This work has been partly funded by the Spanish MINECO projects Estallidos 5 AYA2013-47742-C04 and Estallidos 6 AYA2016-79724-C4.

References

Amorín R., Pérez-Montero E., Contini T., et al., 2015, *A&A*, **578**, A105
Amorín R., Pérez-Montero E., Vílchez J. M., Papaderos P., 2012, *ApJ*, **749**, 185

Amorín R. O., Pérez-Montero E., Vílchez J. M., 2010, *ApJL*, **715**, L128
Andrews B. H., Martini P., 2013, *ApJ*, **765**, 140
Asplund M., Grevesse N., Sauval A. J., Scott P., 2009, *ARA&A*, **47**, 481
Denicoló G., Terlevich R., Terlevich E., 2002, *MNRAS*, **330**, 69
Elmegreen B. G., Elmegreen D. M., Sánchez Almeida J., et al., 2013, *ApJ*, **774**, 86
Filho M. E., Winkel B., Sánchez Almeida J., et al., 2013, *A&A*, **558**, A18
Kniazev A. Y., Grebel E. K., Hao L., et al., 2003, *ApJL*, **593**, L73
Lee H., Skillman E. D., Cannon J. M., et al., 2006, *ApJ*, **647**, 970
Morales-Luis A. B., Pérez-Montero E., Sánchez Almeida J., Muñoz-Tuñón C., 2014, *ApJ*, **797**, 81
Olmo-García A., Sánchez Almeida J., Muñoz-Tuñón C., Filho M. E., Elmegreen B. G., Elmegreen D. M., Pérez-Montero E., Méndez-Abreu J., 2017, *ApJ*, **834**, 181
Papaderos P., Guseva N. G., Izotov Y. I., Fricke K. J., 2008, *A&A*, **491**, 113
Pérez-Montero E., 2014, *MNRAS*, **441**, 2663
Pérez-Montero E., Contini T., 2009, *MNRAS*, **398**, 949
Pérez-Montero E., Díaz A. I., 2003, *MNRAS*, **346**, 105
Pettini M., Pagel B. E. J., 2004, *MNRAS*, **348**, L59
Sánchez Almeida J., Aguerri J. A. L., Muñoz-Tuñón C., de Vicente A., 2010, *ApJ*, **714**, 487
Sánchez Almeida J., Elmegreen B. G., Muñoz-Tuñón C., Elmegreen D. M., 2014, *A&A Rev.*, **22**, 71
Sánchez Almeida J., Elmegreen B. G., Muñoz-Tuñón C., et al., 2015, *ApJL*, **810**, L15
Sánchez Almeida J., Pérez-Montero E., Morales-Luis A. B., et al., 2016, *ApJ*, **819**, 110

Chemical Abundances in Gaseous Nebulae
AAA Workshop Series 10, 2016
G. Hägele, M. Cardaci & E. Pérez-Montero, eds.

Invited Review

Metal content in the central region of galaxies

M.V. Cardaci[1,2], G.F. Hägele[1,2], A.I. Díaz[3], P. Rodríguez-Pascual[4], M. Santos-Lleó[4] and O.L. Dors[5]

[1]*Instituto de Astrofísica de La Plata (CONICET-UNLP), Argentina*
[2]*Facultad de Ciencias Astronómicas y Geofísicas, Universidad Nacional de La Plata, Paseo del Bosque s/n, 1900 La Plata, Argentina*
[3]*Facultad de Ciencias, Universidad Autónoma de Madrid, C/Francisco Tomás y Valiente 7, Ciudad Universitaria de Cantoblanco, 28049 Madrid, Spain.*
[4]*XMM-Newton Science Operations Center, ESAC, ESA, POB 78, 28691 Villanueva de la Cañada, Madrid, Spain*
[5]*Universidade do Vale do Paraíba, Av. Shishima Hifumi, 2911, Cep12244-000, Saõ José dos Campos, SP, Brazil*

Abstract. Accurate abundance determinations for the central regions of a great amount of galaxies would be necessary to improve the calibration of abundances in the over solar regime. Circumnuclear Star Forming Regions (CNSFRs) in early type galaxies, being close to the galactic nuclei, are expected to be of high metal content and in fact empirical abundance indicators constructed with strong optical emission lines point to over-solar abundances up to 3 times solar. Due to the difficulty in deriving abundances directly the calibrations have to be provided by theoretical photoionization models which require several assumptions to be made. Different models/assumptions provide different calibrations. The optical observational analysis of the warm ionized gas of CNSFRs yields oxygen abundances lower than expected from empirical abundance indicators. These findings point to a deficiency of light alpha elements (O, Ne) in the central regions of M 82. If this is common among regions dominated by recent star formation, the estimated oxygen abundances might not be representative of the true metal content of these regions. This could have a profound effect on abundance calibrations leading to fundamental relations like the Mass-Metallicity and Luminosity-Metallicity relations. X-ray emission analysis can provide abundances for the hot gas phase. This hot plasma is thought to be mainly heated by the supernovae explosions so that the X-ray gas should trace the current abundances of the galaxies. These alternative estimations of the metal content of the central region of galaxies would provide new observational constrains for models of chemical evolution.

1. Introduction

Metallicity studies are intended to disentangle the chemical evolution of the Universe. Stars convert H into heavier elements that enrich their environments as the stars evolve and die. Being the third most abundant element (after H and He) the oxygen is a good metallicity tracer in the interstellar medium. HII regions, planetary nebulae, and supernova remnants usually display prominent emission lines of oxygen.

Metallicities of galaxies have been mainly derived by measuring nebular optical emission-lines associated with their giant HII regions. More used elements to determine metallicities in HII regions are oxygen and neon. In spiral galaxies negative gradients with higher abundances towards the galactic centers were found (e.g. Vílchez et al., 1988; Vila-Costas & Edmunds, 1992; Sánchez et al., 2014).

The method applied on each region depends on the intensity of the diagnostic lines. The direct method (Te-method) consist in the determination of O and N abundances through the electron temperature (Te). The major diagnostic Te line is the weak auroral [OIII]λ4363Å emission-line. In high metallicity environments the cooling carried on by some elements makes this [OIII]λ4363Å line, no longer observable. In these cases semi-empirical strong-lines methods were proposed to derive abundances. Semi-empirical methods are based on model assumptions for the geometry and nature of the ionizing source, and the determination of a large number of correlated physical parameters (e.g. U, Teff, Z) that have to be calibrated through the comparison between some strong-line ratios predicted by the models with the ones estimated from observational data. Depending on the adopted calibrations quite different abundances are able to reproduce the observed strong-lines ratios.

Díaz et al. (1989) reported metallicity estimations through the CaII and MgI near-IR lines. They conclude that in the low metallicity regime the strength of the CaII triplet is only a function of the metal abundance and hence it is a useful metallicity indicator in such metal poor systems. These absorption lines are produced by the stars in the HII region, hence they provide a way to estimate stellar abundances. Stellar metallicities trace the galactic enrichment at the time of the stars birth i.e. prior to the last burst of star formation, while hot gas metallicities trace the enrichment produced by the ongoing burst as elements are carried to the interstellar medium (ISM) by stellar winds and supernova explosions.

Star forming regions also emit in X-rays. A recent star formation event is characterized by the presence of diffuse X-ray emission associated with the hot gas, and compact sources associated with massive X-ray binaries and supernova remnants (e.g. Fabbiano, 1989). The interaction of supernovae with the ionized shells formed by winds from massive stars is an efficient producer of X-ray emission in star-forming regions (Chu & Mac Low, 1990; Shull & Saken, 1995; Tenorio-Tagle et al., 2006). This hot plasma is thought to be mainly heated by the supernovae explosions so that the X-ray gas should trace the current abundances of the galaxies. Therefore, the analysis of the X-ray emission would provide abundances for the hot gas phase.

2. Why the central region of galaxies?

The inner parts of some near barred spiral galaxies, as for example NGC 3351 and NGC 3310, show intense star-forming regions frequently arranged in a roughly anular pattern of about 1 kpc in diameter around their nuclei. This regions are called Circumnuclear Star Forming Regions (CNSFRs). These star forming complexes have sizes ranging between a few tens to a few hundreds of pcs (see e.g. Díaz & Pérez-Montero, 2000) and seem to be made up of several HII regions ionized by luminous compact stellar clusters of only a few pc in size, as measured from high spatial resolution HST images (Hägele et al., 2007, 2009, 2010b; Hägele, 2008).

In general, the circumnuclear HII regions are similar to the giant HII regions found in the disks of galaxies, although the circumnuclears are more compact and present a higher peak surface brightness Kennicutt et al. (1989) than their disks counterparts. Their large Hα luminosities, typically higher than 10^{39} erg s^{-1} point to relatively massive star clusters as their ionization source (10^5 - 10^6 M$_\odot$), which minimizes the uncertainties due to small number statistics when applying population synthesis techniques (see e.g. Cerviño et al., 2002). The present of multiple components in their emission-line profiles showing different kinematical behaviours (Hägele et al., 2007, 2009, 2010b) regards important doubts about the properties of the ionized gas derived from global emission-line measurements (Hägele et al., 2013). The lack of detection at radio wavelengths in the central region of NGC 3351 could imply that the ionizing population of their CNSFRs are too young (less than a few Myr) to host supernovae (Hägele et al., 2010a).

Being close to the galactic nuclei, CNSFRs are expected to be of high metal abundance and, in fact, empirical abundance indicators constructed with strong emission lines, point to oversolar abundances up to three times solar. Therefore these regions are very interesting labs since the star-formation is taking place in a high metallicity environment and could provide clues for the understanding of star formation phenomena at large metallicities and, due to its position in the galaxies, for the determination of metallicity gradients in spiral galaxies. For example, for NGC 3310, the abundances of the CNSFR were derived by Pastoriza et al. (1993) from direct measurements of the electron temperature and were found to be under solar while the nucleus showed twice solar abundances.

A dozen of these structures in three other galaxies (NGC 3351, NGC 2903 and NGC 3504) have been studied by Hägele during his PhD Thesis Hägele (2008) and by Díaz et al. (2007). These authors estimated the abundances were found using a new semi-empirical method including emission lines from the far blue to the far red (3600 to 10000 Å). Some of the relevant results that these authors found are that the oxygen abundances of these regions are consistent with solar values; only one of the analyzed CNSFRs shows a metallicity higher than solar (by a factor of 1.5); their ionization structure, as mapped by the [OII]/[OIII] ratios as a function of the [SII]/[SIII] ratios point to relatively hard ionizing sources, contrary to what is expected in high metallicity environments. Hence, no three times oversolar abundances as predicted by abundance empirical indicators were found. A similar result was found later by Sánchez et al. (2014) in 26 over the 193 galaxies ($\sim$ 13.5%) of the sample selected for the CALIFA project.

Regarding the X-ray emission as metallicity tracer of the hot ISM gas, no much was done but in a handful of objects (e.g. N 253, Ptak et al. 1997; NGC 1569,

Martin et al. 2002; NGC 1365, Pagel et al. 1979). The most detailed abundance derivations from emission line analyses of hot gas in this band has been done for the starburst galaxy M 82 using XMM-Newton data.
Read & Stevens (2002) modelled the XMM-Newton high resolution spectra (RGS) using MEKAL models (Mewe et al., 1995) with a sixth order Chebyshev polynomial. They found near solar abundances of O and Fe, and oversolar abundances of Mg ($X/X_{\odot} \sim$ 2.3-5.2), Si($X/X_{\odot}>4.6$) and Ne($X/X_{\odot}>1.4$). Relative OVII(r,f,i) intensities are consistent with collisionnally ionized gas in equilibrium.
Origlia et al. (2004) compared stellar-abundances from near-IR absorption spectra with hot gas abundances from X-rays spectra of M 82. They found a solar abundance of O and half solar of Fe from the stellar component; and half hot gas phase metallicities than the ones reported by Read & Stevens (2002) with the same XMM-Newton observation (RGS+EPIC). It is noteworthy that these authors found different solar abundances of the elements than those found by Read & Stevens, but similar abundance ratios between these elements than them. The low O abundance found by Origlia and collaborators ($X/X_{\odot} \sim 0.3$) is difficult to explain in the framework of the α-element enhancement by SN II explosions.
Ranalli et al. (2008) analysed (in a comprehensive way) a long X-rays observation (110 ks) of M 82. They also compared two of the more often used X-rays models to characterize the hot plasma: MEKAL (Mewe et al., 1995) and APEC (Smith et al., 2001). They found that part of the Optical-to-Xrays difference found by Origlia et al. in the O abundance could be attributed to the charge-exchange emission. This effect was not taken into account previously and is produced when the hot wind encounters with cold neutral gas, ions from the wind diffuse through the interface into the cold gas where electrons are transferred from neutrals to ions. Both the resulting ions can be highly excited and re-arrange their electrons by emitting photons in the extreme UV and the X-ray bands. From the comparison between MEKAL and APEC X-rays models Ranalli and collaborators concluded that there is still needed a fine-tuning between them since they provided different abundances of the elements, but similar abundance ratios between them. These authors also found that the O and N abundances in M 82 are lower/equal to the solar ones.
The detailed abundance study performed in the X-ray band for M 82 has provided unexpected results. In the inner $\sim$ 1 kpc of the galaxy both the hot gas and the stars trace a very similar Fe abundance. Nevertheless, while the ratios of the heavier α-elements (Mg, S) over Fe are enhanced in the hot gas, the lighter α-elements (O, Ne) are not; in fact, they are depressed. If this behavior is common in the central regions of galaxies, the oxygen abundances derived from the ionized gas might not be representative of the true metal content of these regions.

3. Discussion

The fact that the optical analysis of the warm ionized gas in CNSFRs yields an oxygen abundance lower than expected from empirical abundance indicators points to an effect similar to what found in M 82, that is a deficiency of light α-elements (O, Ne) in these central regions.
Our aim is to analyze the X-ray emission of the central zone hosting circumnuclear ring of the two spiral galaxies: NGC 3310 and NGC 2903 for which we have

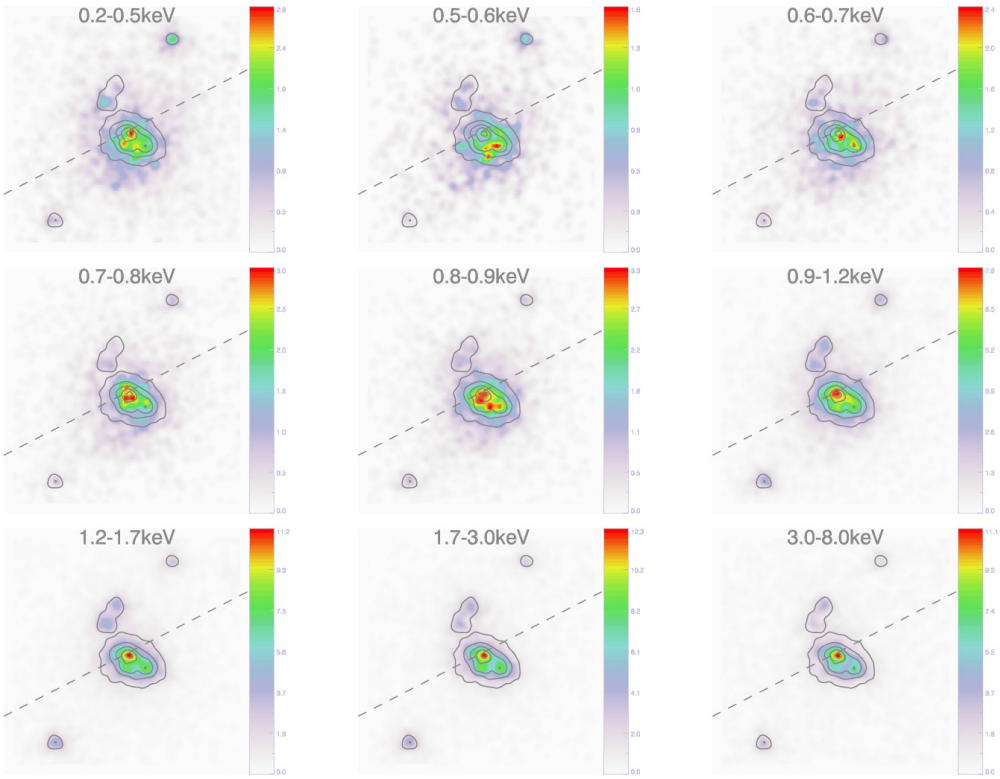

Figure 1. EPIC-MOS images in nine energy intervals selected to compare the distribution of the X-rays from the softness to the hardness ranges.

derived abundances (Pastoriza et al., 1993; Díaz et al., 2007) and gas and star kinematical information as much as estimations of the dynamical masses of the CNSFRs and the ionizing clusters (Hägele et al., 2009, 2010b), and for which X-ray emission has already been detected.

At the objects distances (∼8-15 Mpc) the integrated RGS spectra would encompass the central galaxy region with the circumnuclear ring. This is suitable for us since all the CNSFRs in a given galaxy show comparable (optical) abundances and we are interested in the average abundance of the hot gas associated with the collection of individual star-forming structures.

A previous XMM-Newton observation of NGC 3310, of about 11 ks of effective exposure time, shows hints for the presence of emission lines giving the appropriate scientific case to achieve time for a longer observation. NGC 3310 was re-observed using the XMM-Newton satellite on 2008-2009. The allocated 110 ks observation was performed in two runs of about 55 ks each with an year between them. After the first run, the signal-to-noise improvement was already significant. Comparing the first short observation with data of our first run it shows up clearly that the signal-to-noise improvement is significant.

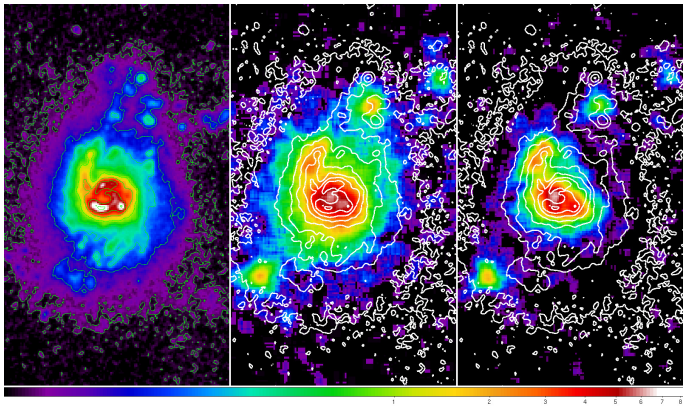

Figure 2. Right: UV image acquired during the first run of our observation using the OM camera on-board the XMM-Newton satellite (UVW1 filter with $\lambda_{\rm eff}$ = 2910Å). Middle: soft X-rays EPIC camera data with the UV contours over-plotted. Right: hard X-rays EPIC camera data with the UV contours over-plotted.

Using the lower resolution EPIC data cubes acquired simultaneously with the RGS spectra we were able to analyze the morphology of the observed field as a function of the energy. In Fig. 1 we can see that in the soft X-ray band the emission is extended and that the emitting zone turns out more compact as the radiation turns harder. Comparing the morphology of the central region of this galaxy in UV, soft and hard X-rays we see that, in general, the X-rays spatial distribution follows the UV emission, in spite of there are strong X-rays emitters that have not an UV counterpart (see Fig. 2).
NGC3310 has also been observed using the ACIS-S camera on board the Chandra satellite. This camera has a spatial resolution of 1 arcsec and a moderate spectral resolution similar to the EPIC-MOS cameras on board the XMM-Newton satellite. The high spatial resolution of the Chandra satellite allows the identification of punctual sources and broad spectral features, but ACIS-S spectral resolution is not enough to identify narrow features in the soft band as the ones needed to perform an abundance study. Comparing contours from our XMM-Newton EPIC-pn camera data (with a spatial resolution of 6 arcsec) with Chandra data we can see a perfect match in the identification of the emitting regions (see, Fig. 3).
Once the whole observation ($\sim$ 110 ks) was performed, we have combined the RGSs data from both data set cleaning high background periods and correcting for effective exposure times. Fig. 4 shows the RGS data displayed as being a long slit. In this figure we see well identified high excitation emission lines (e.g. NeIX, FeXVII and OVIII). As the gas physical properties in X-rays are derived performing model fitting, the more significant lines we have, the more accurate model parameter values we can obtain.

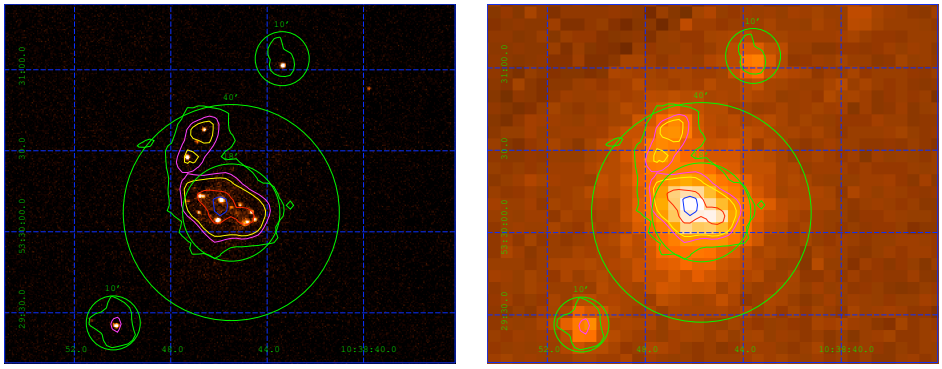

Figure 3. XMM-Newton EPIC-pn contours over-plotted on the Chandra ACIS-S image (left) and the EPIC-pn image (right).

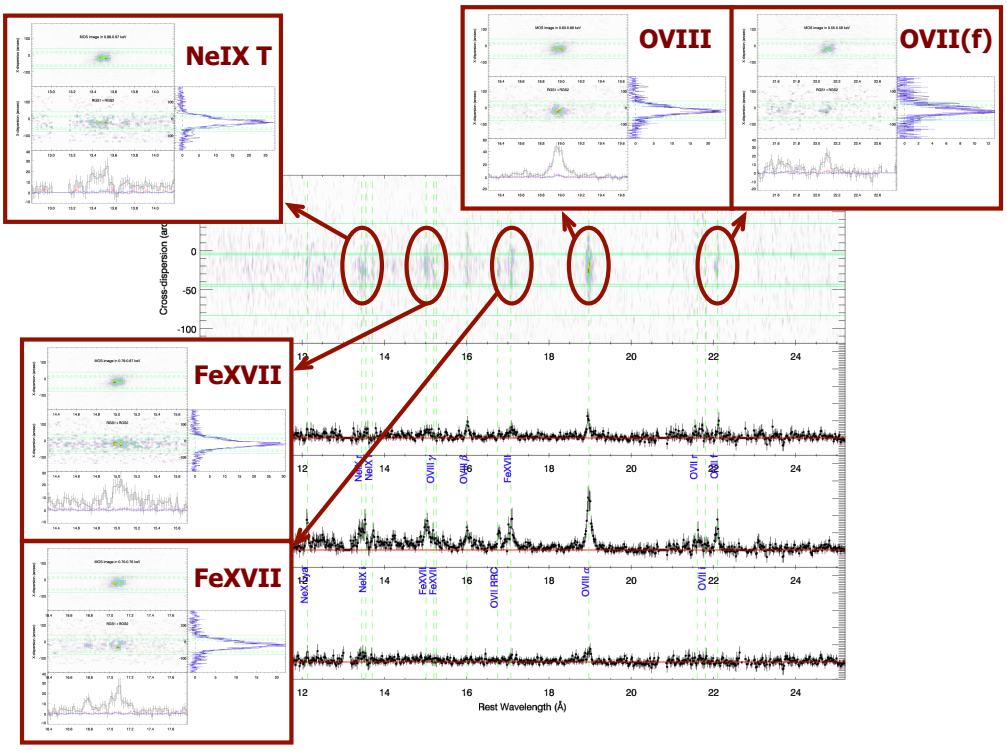

Figure 4. Combined RGSs data from the two runs cleaned for high background periods and corrected by effective exposure times displayed as RGSs be long slit spectrographs. Most prominent features are identify and for each one we obtained spatial profiles. In the remarked boxes RGS and EPIC spatial distribution for these features are compared.

4. Summary

The central regions of some spiral galaxies have metallicities lower than predicted by abundance empirical indicators. This is also the case for a group of spirals hosting Circumnuclear Star Forming Regions. From optical data it has been found that these regions, located at about 1 kpc from the nucleus, show about solar abundances, what makes them good places to study with the aim of disentangling the enrichment process.
It is possible to obtain metallicities using data in the X-rays band to compare it with the ones obtained in other bands. The method is still new and needs to be fine tuned. Our aim is to perform the metallicity study using very good X-rays data of NGC 3310 and NGC 2903. In our RGS spectra significant high excitation lines are clearly identified. The relative intensities between the components of the NeIX$\lambda\lambda$13.4, 13.6, 13.7 Å and OVII$\lambda\lambda$ 21.6, 21.8, 22.1 Å triplets are sensitive to the temperature and density of the plasma (e.g. Porquet & Dubau, 2000), hence they could be used to characterize the media where they are formed.

Acknowledgments. The scientific work reported in this article involves observations obtained with XMM-Newton, an ESA science mission with instruments and contributions directly funded by ESA Member States and NASA. The scientific work reported in this article made use of data obtained from the Chandra Data Archive.

References

Cerviño M., Valls-Gabaud D., Luridiana V., et al., 2002, *A&A*, **381**, 51
Chu Y.-H., Mac Low M.-M., 1990, *ApJ*, **365**, 510
Díaz A. I., Pérez-Montero E., 2000, *MNRAS*, **312**, 130
Díaz A. I., Terlevich E., Castellanos M., et al., 2007, *MNRAS*, **382**, 251
Díaz A. I., Terlevich E., Terlevich R., 1989, *MNRAS*, **239**, 325
Fabbiano G., 1989, *ARA&A*, **27**, 87
Hägele G. F., 2008, *Ph.D. thesis*, Universidad Autónoma de Madrid
Hägele G. F., Ascasibar Y., Richards A. M. S., et al., 2010a, *MNRAS*, **406**, 1675
Hägele G. F., Díaz A. I., Cardaci M. V., et al., 2007, *MNRAS*, **378**, 163
Hägele G. F., Díaz A. I., Cardaci M. V., et al., 2009, *MNRAS*, **396**, 2295
Hägele G. F., Díaz A. I., Cardaci M. V., et al., 2010b, *MNRAS*, **402**, 1005
Hägele G. F., Díaz A. I., Terlevich R., et al., 2013, *MNRAS*, **432**, 810
Kennicutt Jr. R. C., Keel W. C., Blaha C. A., 1989, *AJ*, **97**, 1022
Martin C. L., Kobulnicky H. A., Heckman T. M., 2002, *ApJ*, **574**, 663
Mewe R., Kaastra J. S., Liedahl D. A., 1995, *Legacy*, **6**, 16
Origlia L., Ranalli P., Comastri A., Maiolino R., 2004, *ApJ*, **606**, 862
Pagel B. E. J., Edmunds M. G., Blackwell D. E., et al., 1979, *MNRAS*, **189**, 95
Pastoriza M. G., Dottori H. A., Terlevich E., et al., 1993, *MNRAS*, **260**, 177
Porquet D., Dubau J., 2000, *A&AS*, **143**, 495
Ptak A., Serlemitsos P., Yaqoob T., et al., 1997, *AJ*, **113**, 1286
Ranalli P., Comastri A., Origlia L., Maiolino R., 2008, *MNRAS*, **386**, 1464
Read A. M., Stevens I. R., 2002, *MNRAS*, **335**, L36
Sánchez S. F., Rosales-Ortega F. F., Iglesias-Páramo J., et al., 2014, *A&A*, **563**, A49

Shull J. M., Saken J. M., 1995, *ApJ*, **444**, 663
Smith R. K., Brickhouse N. S., Liedahl D. A., Raymond J. C., 2001, *ApJL*, **556**, L91
Tenorio-Tagle G., Muñoz-Tuñón C., Pérez E., Silich S., Telles E., 2006, *ApJ*, **643**, 186
Vila-Costas M. B., Edmunds M. G., 1992, *MNRAS*, **259**, 121
Vílchez J. M., Pagel B. E. J., Díaz A. I., Terlevich E., Edmunds M. G., 1988, *MNRAS*, **235**, 633

Chemical Abundances in Gaseous Nebulae
AAA Workshop Series 10, 2016
G. Hägele, M. Cardaci & E. Pérez-Montero, eds.

Invited Review

Spatially resolved properties for extremely metal-poor star-forming galaxies with Wolf-Rayet features and high-ionization lines

C.Kehrig[1]

[1]*Instituto de Astrofísica de Andalucía, CSIC, Apartado de correos 3004, E-18080 Granada, Spain*

Abstract.
Extremely metal-poor, high-ionizing starbursts in the local Universe provide unique laboratories for exploring in detail the physics of high-redshift systems. Also, their ongoing star-formation and haphazard morphology make them outstanding proxies for primordial galaxies. Using integral field spectroscopy, we spatially resolved the ISM properties and massive stars of two first-class low metallicity galaxies with Wolf-Rayet features and nebular HeII emission: Mrk178 and IZw18. In this review, we summarize our main results for these two objects.

1. Introduction

Local extremely metal-poor [i.e., 12+log (O/H) $\leq$ 7.7][1] starburst galaxies are among the least chemically evolved objects in the nearby Universe, and are considered to be analogues to the first star-forming (SF) systems (e.g. Izotov et al., 1994, 2009; Hunter & Hoffman, 1999; Kehrig et al., 2006; Sánchez Almeida et al., 2017). Studying these metal-deficient starbursts is needed to learn more about the evolution and feedback from massive stars [e.g. Wolf-Rayet (WR) stars] in high-z galaxies, and for exploring in detail the physics of the farway Universe.
The presence of WR signatures (most commonly a broad feature centered at $\sim$4680 Å or "blue bump") in the spectra of some metal-poor SF galaxies [e.g. Legrand et al. 1997; Guseva, Izotov & Thuan 2000; Cairós et al. 2010; Kehrig et al. 2016 (hereafter K16)] challenges current single star (rotating/non-rotating) stellar evolution models that fail in reproducing the WR content in low metallicity (Z) environments (see Brinchmann, Kunth, & Durret 2008 and references therein; Leitherer et al. 2014). Thus, investigating the WR content and radiative feedback from WR stars in metal-poor starbursts is crucial to test the models at low metallicity. The study on formation and thereabouts of gamma-ray bursts and Type Ib/c SN progenitors, believed to be WRs in metal-poor galaxies, may also benefit from the investigation presented here (e.g. Woosley & Bloom, 2006).

[1]The precise value of the metallicity defining extremely metal-poor galaxies varies in the literature (see Guseva et al., 2017, and references therein)

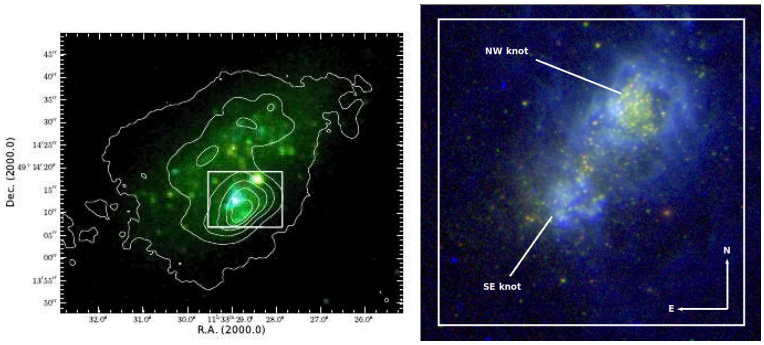

Figure 1. *Left panel*: Colour-composite SDSS image of Mrk178 overlaid with the observed FOV of WHT/INTEGRAL ($\sim$ 16"×12") represented by the white box. *Right panel*: Colour-composite HST image of IZw18. The observed FOV of PMAS (16"×16") is represented by the white box. Figure adapted from K13 and K16.

The spectra of SF galaxies are dominated by strong nebular emission lines which are mainly formed via the photoionization by hot massive stars. High-ionization lines, like HeII, are often seen in the spectra of low metallicity SF galaxies at both low and high redshift [e.g. Kehrig et al. 2004; Thuan & Izotov 2005; Shirazi & Brinchmann 2012; Cassata et al. 2013; Kehrig et al. 2013, 2015 (hereafter K13, K15)]. The expected harder spectral energy distribution (SED) and higher nebular gas temperatures at low metallicities should boost the supply of hard ionizing photons. While the presence of hard radiation is well established in some nearby metal-deficient SF galaxies, the origin of this radiation is much less clear, in spite of several attempts to account for it (e.g. Thuan & Izotov 2005; K15). Overall, several mechanisms for producing hard ionizing radiation have been proposed, such as WR stars, primordial zero-metallicity stars, high-mass X-ray binaries and fast radiative shocks. However, no mechanism has emerged clearly as the leading candidate. Reconsidering the underlying assumptions in the analysis of high-ionization nebular emission in metal-poor galaxies is key to advance our understanding of their properties.

We have used integral field spectroscopy (IFS) to obtain a more believable view of extremely metal-poor, high-ionizing starbursts in the local Universe (see Fig. 1; K13, K15, K16). IFS has many advantages in comparison with long-slit spectroscopy (e.g. Cairós et al., 2009; Kehrig et al., 2012; Pérez-Montero et al., 2013; James et al., 2013; Duarte Puertas et al., 2017). IFS allows a more precise spatial correlation between massive stars and nebular properties through a 2D analysis. IFS is a powerful technique to probe and solve issues related with aperture effects too. Long-slit observations may fail in detecting WR features due to their faintness with respect to the stellar continuum emission and spatial distribution of WR stars across the galaxy. In particular in low-Z objects, the dilution of WR features and the difficulty in spectroscopically identifying WR stars is even stronger owing to the steeper Z dependence of WR star winds which lowers the line luminosities of such stars (e.g. Crowther & Hadfield, 2006). Kehrig et al. (2008) demonstrated for the first time the power of IFS in minimizing the

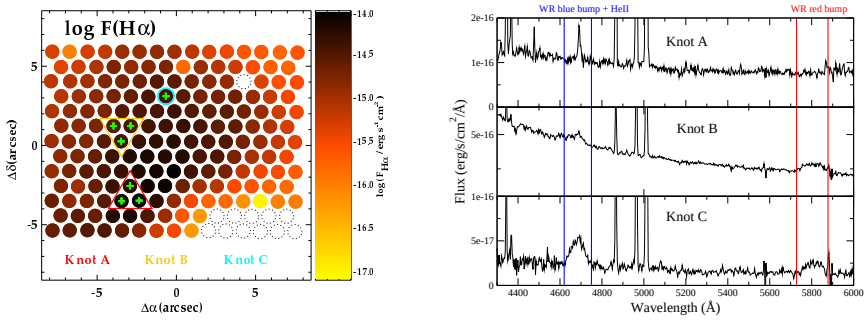

Figure 2. *Left panel*: Map of Hα emission line. The diameter of each spaxel is $\sim$ 1" ($\sim$ 20 pc, our resolution element size). The three WR knots (A, B and C) are labelled on the Hα flux map, and the spaxels where we detect WR features are marked with green crosses. *Right panel*: Integrated spectrum for the 3 knots in which WR features are detected. The spectral range for both blue and red WR bumps are marked. Figure adapted from K13.

WR bump dilution and finding WR stars in extragalactic systems where they were not detected before (see also Cairós et al., 2010; James et al., 2013).
Here, we summarize the main results from the analysis of our new integral field unit (IFU) data of two extremely metal-poor, high-ionizing SF galaxies: Mrk178, *the closest metal-poor WR galaxy* (see K13), and IZw18, *the most metal-deficient* HeII*-emitting SF galaxy known in the local Universe* (see K15, K16).

2. Results

2.1. Mrk178: the closest metal-poor WR galaxy

In K13 we present the first optical IFS study of Mrk 178 based on IFU data obtained with the INTEGRAL IFU at the 4.2m WHT, Roque de los Muchachos observatory (see Fig. 1). The proximity of Mrk 178 (distance $\sim$ 3.9 Mpc) combined with the IFS technique allow us to locate and resolve SF knots hosting a few WRs, and also to characterize the WR content. In addition, we are able to probe the spatial correlation between massive stars and the properties of the surrounding ISM.
We defined three WR knots from which two (knots A and C) are identified for the first time in K13. The WR knot spectra reveal the presence of nitrogen-type and carbon-type WR stars in Mrk 178 (see Fig. 2). By comparing the observed spectra of the WR knots with SMC/LMC template WRs, we empirically estimate a lower limit for the number of WRs ($\geq$ 20) in our Mrk178 FOV that is already higher than that currently found in the literature ($\sim$ 2-3 WRs from Guseva et al., 2000). Regarding the ISM properties, our statistical analysis suggests that spatial variations in the gaseous T_e[OIII] exist and that the scatter in T_e[OIII] can be larger than that in O/H within the observed FOV. Thus, caution should be exercised when analyzing integrated spectra of SF systems which do not necessarily represent the "local" ISM properties around massive

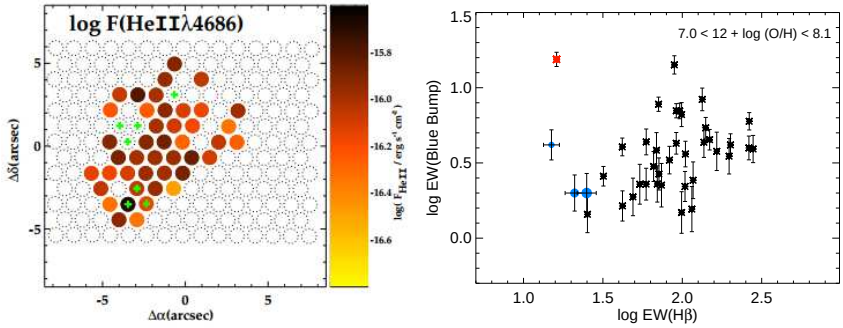

Figure 3. *Left panel*: map of nebular HeIIλ4686 line; spaxels where we detect WR features are marked with green crosses. *Right panel*: EW(WR blue bump) vs. EW(Hβ). Asterisks show values from SDSS DR7 for metal-poor WR galaxies; the red one represents Mrk178. The three blue circles, from the smallest to the biggest one, represent the 5", 7" and 10" diameter apertures from our IFU data centered at the SDSS fiber of Mrk178. Figure adapted from K13.

star clusters. The nebular chemical abundance in Mrk 178 is homogeneous over spatial scales of hundreds of parsecs. The representative metallicity of Mrk 178 derived is 12+log(O/H) = 7.72 ± 0.01 (error-weighted mean value of O/H and its corresponding statistical error). To probe the presence of small-scale ($\sim$ 20 pc) localized chemical variations, we performed a close inspection of the chemical abundances for the WR knots from which we find a possible localized N and He enrichment, spatially correlated with WR knot C (see also James et al., 2013). Nebular HeIIλ4686 emission is shown to be spatially extended reaching well beyond the location of the WRs (see HeIIλ4686 map in Fig. 3). Shock ionization and X-ray binaries are unlikely to be significant ionizing mechanisms since Mrk178 is not detected in X-rays, and measured values of [SII]/Hα ($<$ 0.20) are lower than the typical ones observed in SNRs. The main excitation source of HeII in Mrk178 is still unknown.

From SDSS spectra of metal-poor WR galaxies, we found a too high EW(WR bump)/EW(Hβ) value for Mrk178, which is the most deviant point in the sample (see Fig. 3). Using our IFU data, we showed that this curious behavior is caused by aperture effects, which actually affect, to some degree, the EW(WR bump) measurements for all galaxies in right panel of Fig. 3. Also, we demonstrated that using too large an aperture, the chance of detecting WR features decreases. This result indicates that WR galaxy samples constructed on single fiber/long-slit spectrum basis may be biased in the sense that WR signatures can escape detection depending on the distance of the object and on the aperture size.

2.2. IZw18: the most metal-deficient HeII-emitting SF galaxy in the nearby Universe

We performed new IFS observations of IZw18 using the PMAS IFU on the 3.5m telescope at CAHA (see K15, K16). IZw18 is a high-ionization galaxy which

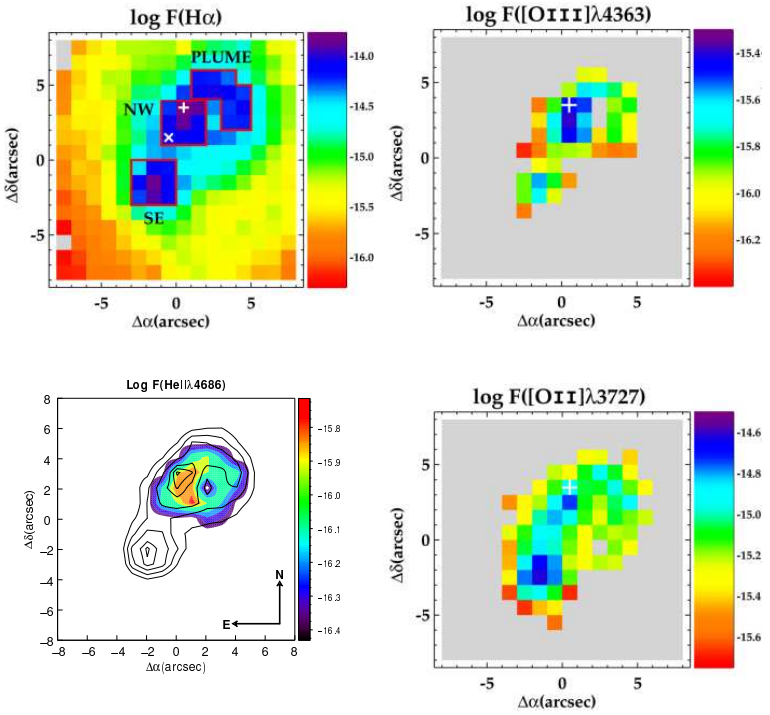

Figure 4. Emission line flux maps: Hα, [OIII]λ4363, HeIIλ4686, and [OII]λ3727. Spaxels with no measurements available are left grey. Each spaxel corresponds to 1" ($\sim$88 pc at the distance of 18.2 Mpc). The peak of Hα emission is marked with a plus (+) sign on all maps. The cross on the Hα map marks the spaxel where we detect the WR feature (see K16). The Hα map also shows the boundaries of the areas that we use to create the 1D spectra of the NW and SE knots, and of the "plume" region (see K16 for details). The HeII map is presented as color-filled contour plot and isocontours of the Hα emission line are shown overplotted for reference. Figure adapted from K15 and K16.

is among the most metal-poor (Z$\sim$ 1/40 Z$_\odot$; e.g. Pagel et al. 1992; Vílchez & Iglesias-Páramo 1998) starbursts in the local Universe. This makes IZw18 an excellent analog for primeval systems. Our IFU aperture samples the entire IZw18 main body and an extended region of its ionized gas (see Fig. 1); the two main SF regions of IZw18 are usually referred to as the north-west (NW) and southeast (SE) components. We have created and analyzed maps for relevant emission lines, line ratios and physical-chemical properties of the ionized gas.

Fig. 4 reveals that the spatial distribution of the emission in Hα, HeIIλ4686 and [OIII]λ4363 is peaked towards the NW component while the [OII]λ3727 emission reaches its maximum at the SE component. By inspecting the maps of [OIII]λ5007/Hβ, [NII]λ6584/Hα and [OIII]/[OII] (Fig. 5), there is a clear tendency for the gas excitation to be higher at the location of the NW knot and thereabouts. The spatial distribution of the abundance indicator R$_{23}$ is found

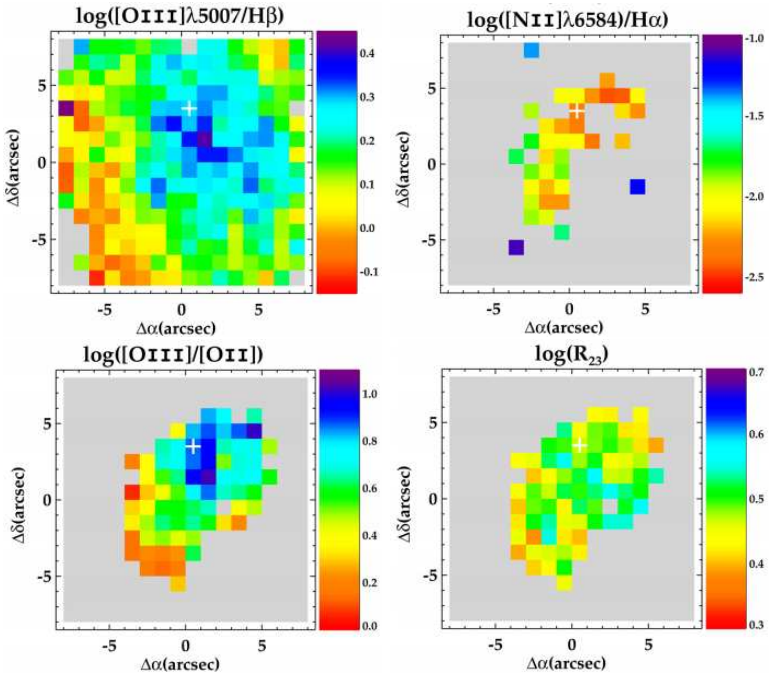

Figure 5. Emission line ratio maps: [OIII]λ5007/Hβ, [NII]λ6584/Hα, [OIII]/[OII], and R_{23}. Spaxels with no measurements available are left grey. Each spaxel corresponds to 1" ($\sim$88 pc at the distance of 18.2 Mpc). The peak of Hα emission is marked with a plus (+) sign on all maps. Figure adapted from K13.

to be relatively flat without any significant peak (see the R_{23} map in Fig. 5). However, the ionization parameter diagnostic [OIII]/[OII] does not show a homogeneous distribution with the highest values of [OIII]/[OII] found within the NW knot, as mentioned above. Our spaxel-by-spaxel analysis shows that there is no dependence between R_{23} and the ionization parameter across IZw18 (see right panel in Fig. 6). Other examples of SF regions with large range of excitation and constant metallicity can be found in the literature (e.g. Pérez-Montero et al. 2011; K13).

Over $\sim$0.30 kpc^2, using the [OIII]λ4363 line flux, we compute T_e[OIII] values between $\sim$15,000-25,000 K (see Figs.7 & 8); it is the first time that T_e[OIII] $>$ 22,000 K are derived for IZw18. Fig. 8 shows that the highest values of T_e[OIII] are not an effect of an overestimation during the measurement of the [OIII]λ4363 flux. If we look at the "BPT" diagram (Fig. 6), we see that all spaxels occupy the SF region, indicating that shocks do not play an important role in the gas excitation in IZw18. Thus, the enhanced T_e[OIII] values derived are expected to be associated primarily with photoionization from hot massive stars, and T_e[OIII] errors due to shocks should be negligible. We note that more than 70% of the higher-T_e[OIII] ($>$ 22,000 K) spaxels are HeIIλ4686-emitting spaxels too. This

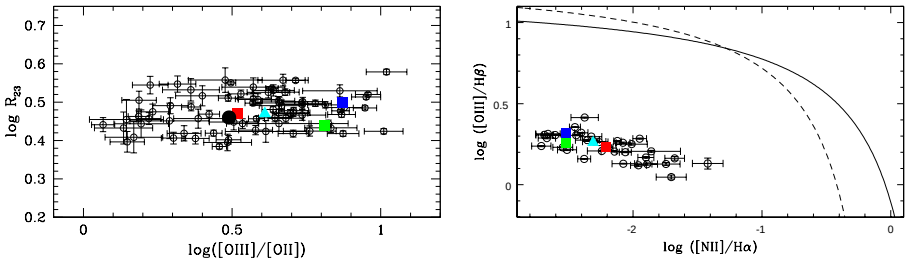

Figure 6. *Left panel*: The relation between log(R_{23}) and log([OIII]/[OII]). Open circles correspond to individual spaxels from the data cube. *Right panel*: The "BPT" diagnostic diagram, showing [OIII]λ5007/Hβ vs. [NII]λ6584/Hα. The [SII]/Hα-BPT and [OI]/Hα-BPT are shown in K16. Blue, red, and green squares are the line ratios measured from the 1D spectra of the NW knot, SE knot and "plume", respectively; the cyan triangle shows the line ratio values from the total integrated spectrum of IZw18; the black circle corresponds to the line ratios from the spectrum of the "halo" of IZw18 (see K16 for details). Figure adapted from K16.

reinforces the existence of a harder ionizing radiation field towards the NW SF knot.

Our statistical analysis shows an important degree of nonhomogeneity for the T_e[OIII] distribution and that the scatter in T_e[OIII] can be larger than that in O/H within the observed [OIII] λ4363-emitting region. We find no statistically significant variations in O/H (derived directly from T_e[OIII]) across the PMAS-IFU aperture, indicating a global homogeneity of the O/H in IZw18 over spatial scales of hundreds of parsecs. The representative metallicity of IZw18 derived here, from individual spaxel measurements, is 12 + log(O/H) = 7.11 $\pm$ 0.01 (error-weighted mean value of O/H and its corresponding statistical error). The prevalence of a substantial degree of homogeneity in O/H over IZw18 can constrain its chemical history, suggesting an overall enrichment phase previous to the current burst.

We took advantage of our IFU data to create 1D integrated spectra for regions of interest in the galaxy. For the first time, we derive the IZw18 integrated spectrum by summing the spaxels over the whole FOV. Physical-chemical properties of the ionized gas were derived from these selected region spectra. We also show that the derivation of O/H and N/O does not depend on the aperture size used. This is a relevant result for studies of high-redshift SF objects for which only the integrated spectra are available.

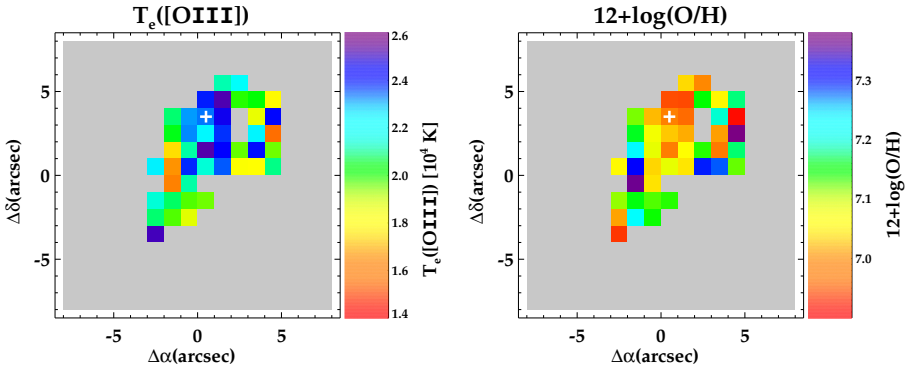

Figure 7. *Left panel*: Map of T_e[OIII] derived directly from the measurement of the [OIII]λ4363 flux above 3σ detection limit. *Right panel*: Map of O/H derived from T_e[OIII]. Figure adapted from K16.

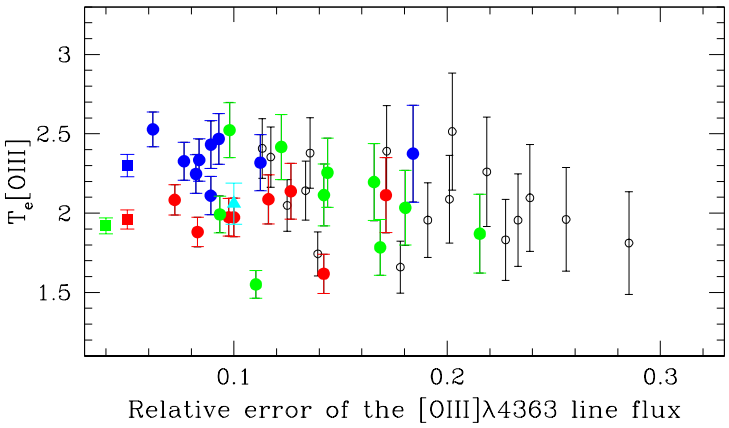

Figure 8. T_e[OIII] derived directly from the [OIII]λ4363 line vs. the relative error of the measurement. Open circles represent individual spaxels; blue, red and green circles indicate the individual spaxels used to create the 1D spectra of the NW knot, SE knot, and plume, respectively. Squares indicate the values measured from the 1D integrated spectra with the same colour-code as used for the individual spaxels. Figure adapted from K16.

PopIII-star siblings: a possible culprit behind the extended nebular HeIIλ4686 emission in IZw18

Narrow HeII emission in SF galaxies has been suggested to be mainly associated with photoionization from WRs, but WRs cannot satisfactorily explain the HeII-ionization in all cases, particularly at lowest metallicities where nebular HeII emission is often seen and observed to be stronger (e.g. Kehrig et al., 2004; Shirazi & Brinchmann, 2012; James et al., 2017). Why is studying the formation of HeII emission relevant? HeII emission indicates the presence of high energy photons (E $\geq$ 54 eV), and so provides essential constraints on the SEDs of hot massive stars. HeII-emitters are apparently more frequent among high-z galaxies than for local objects (Kehrig et al., 2011; Cassata et al., 2013). Actually, narrow HeII emission has been claimed to be a good tracer of PopIII-stars (the first very hot metal-free stars) in distant galaxies (e.g. Schaerer, 2003); these stars are believed to have contributed significantly to the reionization of the Universe, a challenging subject in contemporary cosmology. In fact, searching for PopIII-hosting galaxy candidates is among the main science drivers for next generation telescopes (e.g., JWST; E-ELT). However, we should note that the origin of narrow HeII lines remains difficult to understand in many nearby and distant SF galaxies/regions (e.g. Kehrig et al., 2011; Shirazi & Brinchmann, 2012; Gräfener & Vink, 2015; Pallottini et al., 2015; Hartwig et al., 2016). One of the main reasons why we do not fully understand the physics behind the formation of nebular HeII is the lack of direct probes on HeII-ionizing hot stars. Detailed investigation of the HeII emission at low redshift is needed to better interpret distant narrow HeII-emitters and therefore gaining a deeper understanding of the reionization epoch. IZw18, as the most metal-poor HeII-emitter in the local Universe, is an ideal object to perform this study.

Our IFS data reveal for the first time the entire nebular HeIIλ4686-emitting region (see map of HeIIλ4686 in Fig. 4) and corresponding total HeII-ionizing photon flux [Q(HeII)$_{obs}$] in IZw18. These observations combined with stellar model predictions point out that conventional excitation sources (e.g., single WRs, shocks, X-ray binaries) cannot convincingly explain the total Q(HeII)$_{obs}$ derived for IZw18 (see K15 for details). Other mechanisms are probably also at work. If the HeII-ionization in IZw18 is due to stellar sources, these might be peculiar very hot stars. Based on models of very massive O stars (Kudritzki, 2002), $\sim$ 10-20 stars with 300 M$_\odot$ at Z$_{IZw18}$ [or lower, down to Z$\sim$(1/100) Z$_\odot$] can reproduce our total Q(HeII)$_{obs}$ (see also Szécsi et al., 2015). However, the super-massive star scenario requires a cluster mass much higher than the mass of the IZw18 NW knot (where the HeII region is located), and it would not be hard enough to explain the highest HeII/Hβ values observed. On top of that, the existence of super-massive 300 M$_\odot$ stars remains heavily debated, and an extrapolation of the IMF predicting such massive stars remains unchecked up to now (Vink, 2015).

Considering that the previous scenarios fail in reproducing the observations, and that searches for PopIII-hosting galaxies have been carried out using HeII lines (e.g. Schaerer, 2008; Cassata et al., 2013), we thought that (nearly) metal-free hot stars may hold the key to the HeII ionization in IZw18. To test this hypothesis, as an approximation of (nearly) metal-free stars in IZw18 – the so-called *PopIII-star siblings* – we compared our observations with current models for rotating

Z=0 stars (Yoon et al., 2012), which in fact reproduce our data better: ∼8-10 of such stars with M_{ini}=150 $M_{\odot}$ can explain the total Q(HeII)$_{obs}$ and the highest HeII/Hβ values observed. The PopIII-star sibling scenario, invoked for the first time in IZw18 by K15, goes in line with the results by Lebouteiller et al. (2013). While gas in IZw 18 is very metal-deficient but not primordial, Lebouteiller et al. (2013) have pointed out that the HI envelope of IZw 18 near the NW knot contains essentially metal-free gas pockets. These gas pockets could provide the raw material for making such *PopIII-star siblings* (see also Tornatore et al., 2007).

3. Summary and Conclusions

A brief overview of the first optical IFU observations of two nearby, extremely metal-poor *bursty*-galaxies (Mrk178 and IZw18) is presented. Clues of the early-universe can be found in our cosmic backyard through this class of objects which are excellent primordial analogues, and are key in understanding galaxy evolution. IFS studies of such galaxies enable extended insight into their "realistic" ISM and massive stars, therefore providing constraints on high-redshift galaxy evolution, and on metal-poor stellar models. Our data provide useful testbench for realistic photoionization models at the lowest metallicity regime.
The elusive PopIII-hosting galaxies have been searched through the high-ionization HeII line signature. The HeII line is in comfortable reach of next generation telescopes, like JWST and TMT, which will detect the rest-frame UV of thousands of galaxies during the epoch of reionization. In light of these new observations, a more sophisticated understanding of the high-ionization phenomenon is required to interpret the data in a physically meaningful manner, and to possibly constrain sources responsible for the Universe reionization. Using IFU data, we were able to recover the *total* HeII luminosity and perform a *free-aperture* investigation on the formation of narrow HeII line. Our observations of IZw18 test the current poorly-constrained models for metal-poor massive stars, and suggest that peculiar hot stellar sources, as PopIII-star siblings, might be culprits for the HeII-ionization in this galaxy. This result emphasizes the need to identify extremely metal-poor HeII-emitting targets, such as IZw18, and the power of IFS for such kind of investigation.

Acknowledgments. CK gratefully acknowledges the co-authors and referees from K13, K15 and K16 who made significant contribution to the results presented in this review.

References

Brinchmann J., Kunth D., Durret F., 2008, *A&A*, **485**, 657
Cairós L. M., Caon N., Papaderos P., et al., 2009, *ApJ*, **707**, 1676
Cairós L. M., Caon N., Zurita C., et al., 2010, *A&A*, **520**, A90
Cassata P., Le Fèvre O., Charlot S., et al., 2013, *A&A*, **556**, A68
Crowther P. A., Hadfield L. J., 2006, *A&A*, **449**, 711
Duarte Puertas S., Vílchez J. M., et al., 2017, *A&A*, **599**, A71
Gräfener G., Vink J. S., 2015, *A&A*, **578**, L2

Guseva N. G., Izotov Y. I., Fricke K. J., Henkel C., 2017, *A&A*, **599**, A65
Guseva N. G., Izotov Y. I., Thuan T. X., 2000, *ApJ*, **531**, 776
Hartwig T., Latif M. A., Magg M., et al., 2016, *MNRAS*, **462**, 2184
Hunter D. A., Hoffman L., 1999, *AJ*, **117**, 2789
Izotov Y. I., Guseva N. G., Fricke K. J., Papaderos P., 2009, *A&A*, **503**, 61
Izotov Y. I., Thuan T. X., Lipovetsky V. A., 1994, *ApJ*, **435**, 647
James B. L., Koposov S. E., Stark D. P., et al., 2017, *MNRAS*, **465**, 3977
James B. L., Tsamis Y. G., Walsh J. R. e., 2013, *MNRAS*, **430**, 2097
Kehrig C., Monreal-Ibero A., Papaderos P., et al., 2012, *A&A*, **540**, A11
Kehrig C., Oey M. S., Crowther P. A., et al., 2011, *A&A*, **526**, A128
Kehrig C., Pérez-Montero E., Vílchez J. M., et al., 2013, *MNRAS*, **432**, 2731
Kehrig C., Telles E., Cuisinier F., 2004, *AJ*, **128**, 1141
Kehrig C., Vílchez J. M., Pérez-Montero E., et al., 2015, *ApJL*, **801**, L28
Kehrig C., Vílchez J. M., Pérez-Montero E., et al., 2016, *MNRAS*, **459**, 2992
Kehrig C., Vílchez J. M., Sánchez S. F., et al., 2008, *A&A*, **477**, 813
Kehrig C., Vílchez J. M., Telles E., et al., 2006, *A&A*, **457**, 477
Kudritzki R. P., 2002, *ApJ*, **577**, 389
Lebouteiller V., Heap S., Hubeny I., Kunth D., 2013, *A&A*, **553**, A16
Legrand F., Kunth D., Roy J.-R., et al., 1997, *A&A*, **326**, L17
Leitherer C., Ekström S., Meynet G., et al., 2014, *ApJS*, **212**, 14
Pagel B. E. J., Simonson E. A., Terlevich R. J., et al., 1992, *MNRAS*, **255**, 325
Pallottini A., Ferrara A., Pacucci F., et al., 2015, *MNRAS*, **453**, 2465
Pérez-Montero E., Kehrig C., et al., 2013, *Adv. Astron.*, **2013**, 837392
Pérez-Montero E., Vílchez J. M., Cedrés B., et al., 2011, *A&A*, **532**, A141
Sánchez Almeida J., Filho M. E., Dalla Vecchia C., et al., 2017, *ApJ*, **835**, 159
Schaerer D., 2003, *A&A*, **397**, 527
Schaerer D., 2008, Vol. 255 of *IAU Symposium*, pp 66–74
Shirazi M., Brinchmann J., 2012, *MNRAS*, **421**, 1043
Szécsi D., Langer N., Yoon S.-C., et al., 2015, *A&A*, **581**, A15
Thuan T. X., Izotov Y. I., 2005, *ApJS*, **161**, 240
Tornatore L., Ferrara A., Schneider R., 2007, *MNRAS*, **382**, 945
Vílchez J. M., Iglesias-Páramo J., 1998, *ApJ*, **508**, 248
Vink J. S. (ed.), 2015, *Very Massive Stars in the Local Universe*, Vol. 412 of *ASSL*
Woosley S. E., Bloom J. S., 2006, *ARA&A*, **44**, 507
Yoon S.-C., Dierks A., Langer N., 2012, *A&A*, **542**, A113

Chemical Abundances in Gaseous Nebulae
AAA Workshop Series 10, 2016
G. Hägele, M. Cardaci & E. Pérez-Montero, eds.

Invited Review

The evolution of the radial gradient of oxygen abundance in spiral galaxies

M. Mollá[1], A. I. Díaz[2,3], Y. Ascasibar[2,3], B. K. Gibson[4], O. Cavichia[5], R. D. D. Costa[6], and W. J. Maciel[6]

[1] *CIEMAT, Avda. Complutense 40, 28040, Madrid, Spain*
[2] *Universidad Autónoma de Madrid, 28049, Madrid, Spain*
[3] *Astro-UAM, Unidad Asociada CSIC, Universidad Autónoma de Madrid, 28049, Madrid, Spain*
[4] *E. A Milne Centre for Astrophysics, University of Hull, HU6 7RX, United Kingdom*
[5] *Instituto de Física e Química, Universidade Federal de Itajubá, Av. BPS, 1303, 37500-903, Itajubá-MG, Brazil*
[6] *Instituto de Astronomia, Geofisica e Ciências Atmosféricas, Universidade de Sâo Paulo, 05508-900, Sâo Paulo-SP, Brazil*

Abstract. The aim of this work is to present our new series of chemical evolution models computed for spiral and low mass galaxies of different total masses and star formation efficiencies. We analyze the results of models, in particular the evolution of the radial gradient of oxygen abundance. Furthermore, we study the role of the infall rate and of the star formation history on the variations of this radial gradient. The relations between the O/H radial gradient and other spiral galaxies characteristics as the size or the stellar mass are also shown. We find that the radial gradient is mainly a scale effect which basically does not change with the redshift (or time) if it is measured within the optical radius. Moreover, when it is measured as a function of a normalized radius, show a similar value for all galaxy masses, showing a correlation with a dispersion around an average value which is due to the differences in star formation efficiencies, in agreement with the idea of an universal O/H radial gradient.

1. Introduction

The elemental abundances in spiral and low mass galaxies are lower in the outer regions than in the inner ones, showing a well characterized radial gradient defined by the slope of a least-squares straight line fitted to the radial distribution of these abundances along the galactocentric radius (Shaver et al., 1983; Zaritsky et al., 1994; Henry & Worthey, 1999). These radial gradients seem to correlate with other characteristics defining the galaxies. In this way, they are flatter in the early galaxies than in the late ones. They also seem steeper in the low mass galaxies than in the bright massive disks. The radial gradient is considered as an evolutionary effect, that is, it comes from a difference in the enrichment between

regions more evolved (at the inner parts of disk) compared with the less evolved zones of the outer disks. In this way, a flat gradient implies a more rapid evolution than in disks where the gradient is steeper, as shown by Mollá et al. (1996) for a set of models for some nearby galaxies. These models resulted in a steep radial gradient for NGC 300 or M 33, while M 31 had a flatter gradient than our Milky Way Galaxy (MWG), and other similar galaxies as NGC 628 or NGC 6946. Since the evolution modifies the level of enrichment of a given region or galaxy, it is expected that the radial gradient also changes with time and, therefore, high-intermediate redshift galaxies would have to show a steeper radial gradient than in the present time, at least when measured as $\mathrm{dex\,kpc^{-1}}$. These results were obtained by Mollá et al. (1997), further obtained later by Mollá & Díaz (2005), hereafter MD05, and was also supported by the Planetary Nebulae (PN) O/H abundance data (Maciel et al., 2003) and by open stellar cluster metallicities for different age bins. Results of cosmological simulations for a MWG-like galaxy also obtained a similar behavior (Pilkington et al., 2012).
However, when a correct feedback is included in these simulations, the radial gradient results to have a very similar slope for all times/redshifts (Gibson et al., 2013). In turn, the most recent PN data (Stanghellini & Haywood, 2010; Maciel & Costa, 2013; Magrini et al., 2016) refined to estimate with more precision their ages and distances, give now the same result: there are no evidences of evolution of the radial gradient with time for the MWG nor for other close spiral galaxies, at least until $z = 1.5$. Simultaneously, there are, however, some recent observational data from which the abundances of galaxies at high and intermediate redshift are estimated, and from which a *plethora* of different radial gradients with values as different as -0.30 $\mathrm{dex\,kpc^{-1}}$ or +0.20 $\mathrm{dex\,kpc^{-1}}$ are obtained (Cresci et al., 2010; Yuan et al., 2011; Queyrel et al., 2012; Jones et al., 2013; Genovali et al., 2014; Jones et al., 2015; Xiang et al., 2015; Anders et al., 2017). It is therefore necessary to revise our chemical evolution models and analyze in detail the evolution of this radial gradient not only for the MWG, but also for different galaxies.

2. Chemical evolution model description

We have computed a series of 76 models applied to spiral galaxies with dynamical masses in the range 5×10^{10}–$10^{13}\,\mathrm{M_\odot}$ (with mass step in logarithmic scale of $\Delta \log M = 0.03$) which implies disk total masses in the range 1.25×10^{8}–$5.3 \times 10^{11}\,\mathrm{M_\odot}$, or, equivalently rotation velocities between 42 and 320 $\mathrm{km\,s^{-1}}$. The radial distributions of these masses are calculated through equations from Salucci et al. (2007), based in the rotation curves and their decomposition in halo and disk components.
The scenario is the same as the one from MD05, with the total mass in a spherical region at the time $t = 0$, which infall over the equatorial plane and forms out the disk. The gas infall rates are computed taking into account the relationship between halo and disk masses in order to obtain at the end of the evolution disks as observed, with the adequate mass. They result to be higher in the centers of disks (bulges) and lower in disks, decreasing towards the outer regions, as expected in an inside-out scenario. However, the evolution with the redshift is very similar for all disk regions, only with differences in the absolute values of the infall rates, but with a smooth decreasing for decreasing z, except for the

central regions for which the infall changes strongly with z, more similarly to the cosmological simulations results found for early and spheroidal galaxies. Details about these resulting rates are given in Mollá et al. (2016).
Within each galaxy we assume that there is star formation (SF) in the halo, following a Schmidt-Kennicutt power law on the gas density with an index $n = 1.5$. In the disk, however, we have a star formation law in two steps: first molecular clouds form from diffuse gas, then stars form from cloud-cloud collisions (or by the interaction of massive stars with the molecular clouds surrounding them). In our classical standard models from MD05, we treated these processes as depending on the volume of each region and a probability factor or efficiency for each one. For the halo SF, it is assumed a constant efficiency for all galaxies. The process of interaction of massive stars with clouds is considered as local and we use the same approach for all galaxies. The two other efficiencies defining the molecular clouds and stars formation processes are modified simultaneously from one model to another, with values between 0 and 1.
In this new series of models we have also used an efficiency to form stars from molecular clouds, but to convert diffuse gas into molecular phase we have tried six different methods, two based in the same efficiency method as in MD05, called STD and MOD, and four based in different prescriptions based in Blitz & Rosolowsky (2006), Krumholz et al. (2008, 2009), Gnedin & Kravtsov (2011), and Ascasibar et al. (in preparation), so-called BLI, KRU, GNE, and ASC, respectively. More details about these calculations and their implementation in our code are given in Mollá et al. (2017), where we have applied the models to the MWG and have checked which of these techniques give the best results when comparing with the observational data. Our results indicate that the ASC technique shows a behavior in better agreement with data than the others. In particular those related with the ratio HI/H_2 along radius or as a function of the gas density.
The stellar yields are selected as derived in Mollá et al. (2015) among 144 different combinations with which we calculate a MWG model to see which of them is the best in reproducing the MWG data. We chose the Gavilán et al. (2005, 2006) stellar yields for low and intermediate stars, the ones from Limongi & Chieffi (2003) and Chieffi & Limongi (2004) for massive stars, and the Kroupa (2002) Initial Mass Function (IMF). The Supernova type Ia yields by Iwamoto et al. (1999) are also used.

3. Results

3.1. Evolution of the O/H radial gradient in MWG

In Fig. 1 we represent the O/H radial gradient as a function of redshift for the six models for the MWG calculated in Mollá et al. (2017) with the different prescriptions of the HI to H_2 conversion as explained. In top panels we show these gradients as $\mathrm{dex\,kpc^{-1}}$, computed in panel a) with the whole radial range for which we have calculated the models. In panel b) we have the gradients calculated with regions for which $R \leq 2.5\,R_{\rm eff}$. We may see that in this last case the gradient is basically constant along z with very small differences among models. In both panels we have included the MWG data which give this evolution along z, PN from Stanghellini & Haywood (2010) and Maciel & Costa (2013);

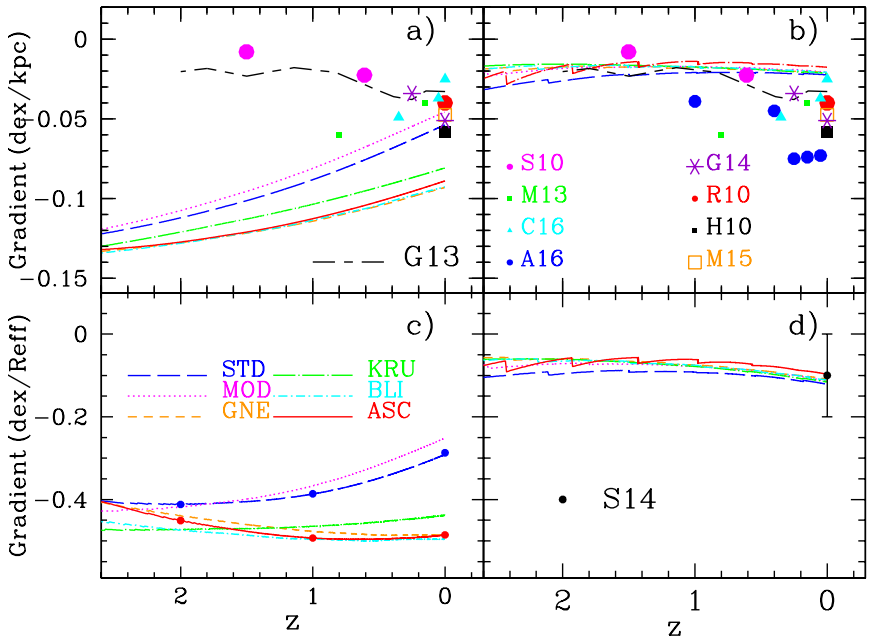

Figure 1. Evolution of the O/H radial gradient with redshift z for the MWG, measured as: $\mathrm{dex\,kpc^{-1}}$ (top panels) and as $\mathrm{dex\,R_{eff}^{-1}}$ (bottom panels). Solid lines represent our different models as labelled in c). Left panels show gradients for the whole radial range. Right panels show gradients only using regions within $\mathrm{R} \leq 2.5\,\mathrm{R_{eff}}$. Data are from Stanghellini & Haywood (2010, S10), Maciel & Costa (2013, M13), Cunha et al. (2016, C16), Anders et al. (2017, A16), Henry et al. (2010, H10), Rupke et al. (2010, R10), Genovali et al. (2014, G14), Sánchez et al. (2014, S14) and Mollá et al. (2015, M15), as labelled in b) and d). Cosmological simulations result for a MWG-like object from Gibson et al. (2013, G13) is also drawn in a) and b).

open clusters from Cunha et al. (2016); and stellar abundance from Anders et al. (2017). The present time values are from Henry et al. (2010), Rupke et al. (2010), Genovali et al. (2014) and the ones compiled by Mollá et al. (2015), as labelled. We have also shown the cosmological simulation result for a Milly Way-like galaxy from Gibson et al. (2013). We see that, in order to reproduce the data, it is necessary to compute the gradient within the optical radius. In bottom panels we show the gradients obtained using a normalized radius (R/R_{eff}). In panel c), where we use again all radial range, we see a different behavior between STD and MOD models (which use an efficiency to form molecular clouds) and all the others using a prescription to convert HI in H_2 which depends on the gas, stars or total density or/and on the dust through the metallicity. In these last cases the effective radius increases more slowly than in our standard models, thus producing a strong radial gradient when regions out of the optical disk are

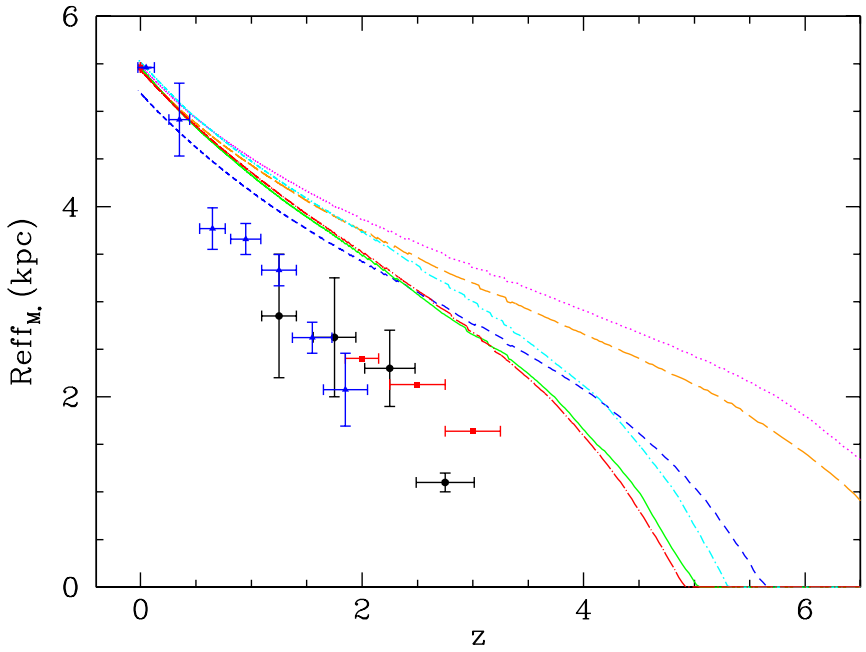

Figure 2. Evolution of the effective radius R_{eff} with redshift z. Data are from Trujillo et al. (2007), Buitrago et al. (2008), and Margalef-Bentabol et al. (2016), as blue triangles, red squares, and black dots, respectively. Figure 12 taken from Mollá et al. (2017).

included for the fit. In panel d), where only regions with $R \leq 2.5\,R_{\rm eff}$ are used, we find again a very constant radial gradient along the redshift. In fact, this value is in very good agreement with the one found by Sánchez et al. (2014) as a common gradient for all the CALIFA survey galaxies.
The grow of the disk in the different models is shown in Fig. 2 with data overimposed labelled. We see, as said before, that ASC model is the one for which the radius increases more slowly while the STD and MOD models started very early to show a large disk. GNE, BLI and KRU show an intermediate behavior. Although the data we show in Fig. 2 refer mainly to bulges and disks from early-type galaxies, it seems clear that ASC is the model closest to the observations.

3.2. Evolution of the O/H radial gradient in spiral and low mass galaxies

In Fig. 3 we show the radial gradients computed for different galaxy masses, as labelled, in a similar way than in Fig. 1. In panel a), as in Fig.1a, the radial gradient computed for all radial regions is shown. It is clear that each galaxy has its own evolution being the smallest one which shows the most different behavior. Each galaxy has a different radial gradient, with the most massive ones showing the flattest distributions ($\sim -0.05\,{\rm dex\,kpc^{-1}}$ for all z), while the smallest has the steepest gradient ($\sim -0.20\,{\rm dex\,kpc^{-1}}$). However, when only

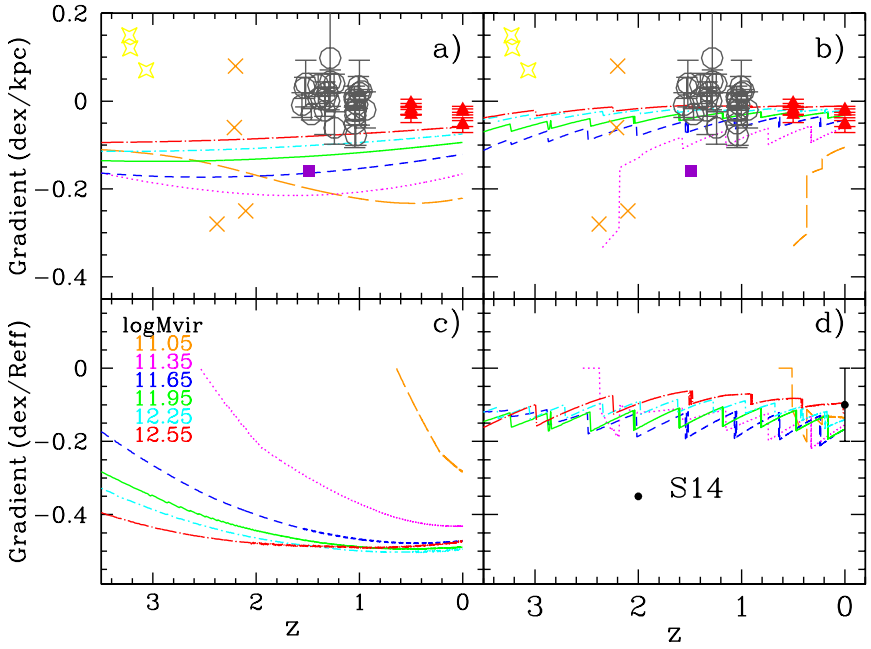

Figure 3. Evolution of the O/H radial gradient with redshift z for several galaxy models with different virial masses ($M_{\rm vir}$), measured as: $\mathrm{dex\,kpc^{-1}}$ (top panels) and $\mathrm{dex\,R_{eff}^{-1}}$ (bottom panels). Left panels show the gradients obtained using the whole radial range available in the simulations. Right panels show gradients computed only using regions within the optical disk defined as $\mathrm{R} \leq 2.5\,\mathrm{R_{eff}}$. Data correspond to the observations by Cresci et al. (2010, yellow stars), Yuan et al. (2011, purple square), Queyrel et al. (2012, grey open dots), Jones et al. (2013, orange crosses), and Magrini et al. (2016, red points with error bars).

radial regions within the optical radius are used to compute the radial gradient a very different behavior arises: all gradients are approximately constant with z for galaxies with $\log(M_{\rm vir}) \geq 11.65$, although with the same behavior than before: the more massive the galaxy, the flatter the gradient. In the lowest masses galaxies, it is evident the moment in which the disk begins to grow: at $z = 2.5$ for $\log M_{\rm vir} = 11.35$ and at $z = 0.5$ for $\log M_{\rm vir} = 11.05$.

When we represent the gradients measured as function of the effective radius, we see that they steepen with decreasing z when all radial regions are used (Fig. 3c) and, again, a very smooth evolution along z for all galaxies appears when only the optical disk is used to fit the gradient (panel d). The average value in this case is $\sim -0.13\,\mathrm{dex\,kpc^{-1}}$, as the value found by Sánchez et al. (2014), supporting their claim that a universal radial gradient appears for all galaxies.

A common radial gradient is easily obtained drawing O/H for the present time as a function of $\mathrm{R/R_{eff}}$ for all galaxy masses and efficiencies (larger than 0.002) in a same plot, as we show in Fig.4. We see that effectively, such as Sánchez

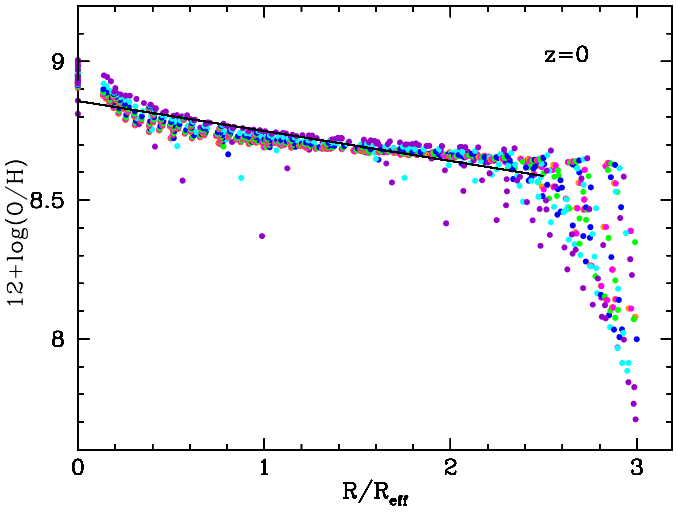

Figure 4. The O/H radial distribution for the present time obtained with our series of models for all galaxy masses and six different efficiencies to form stars with values $\epsilon_* \geq 0.002$, as a function of the normalized radius $R/R_{\rm eff}$. Each color shows a different efficiency ϵ_*.

et al. (2014) found, a same radial gradient is obtained for all models, when $R/R_{\rm eff} \leq 2.5$, with a dispersion given by the differences in the star formation efficiencies around an average radial distribution.
Since it seems quite evident that the radial gradient is a scale effect due to the star formation rate which is measuring the stellar disk growth, we would expect a correlation between this O/H radial gradient measured as dex kpc^1 and the scale length of the disk or any other quantity defining the size of the disk. We plot in Fig. 5, right panel, this correlation for all our models with different galaxy masses and with six different values for the efficiencies to form stars from molecular clouds, which are coded with different colored dots. The correlation is clear for all effective radii larger than 1.25 kpc. If the effective radius is smaller than this value, our code, working with radial regions of 1 kpc wide, is not able to calculate a radial gradient nor an effective radius. This theoretical correlation supports the observational one found by Bresolin & Kennicutt (2015) with the radial gradient and the scale length of the disks (their Fig. 3). These authors claim in that work that all galaxies, even the low surface brightness galaxies, share a common abundance radial gradient when this one is expressed in terms of the exponential disk scale-length (or any other normalization quantity).

4. Conclusions

The conclusions can be summarized as:

- A grid of chemical evolution models with 76 different total dynamical masses in the range 10^{10} to 10^{13} $M_\odot$ is calculated.

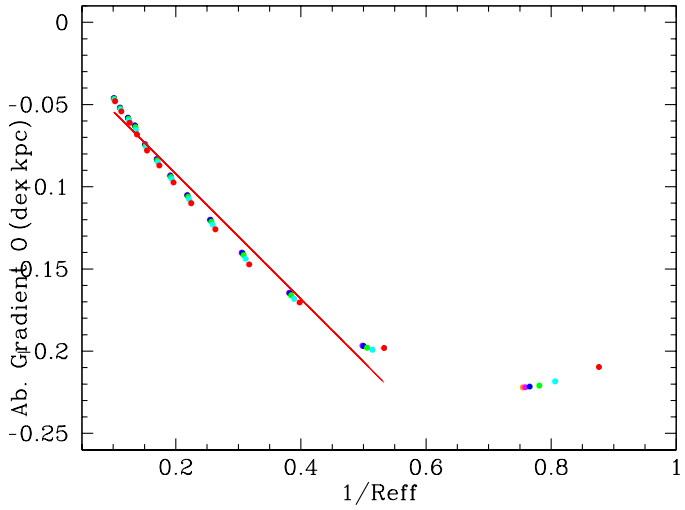

Figure 5. The O/H radial gradient measured as dex kpc^{-1}, as a function of the inverse of the effective radius, $1/R_{eff}$. Each color shows a different efficiency ϵ_*.

- 10 values of efficiencies ϵ_* to form stars from molecular clouds are used with values $0 < \epsilon_* < 1$. But we find that useful values are only the first six-seven of them with $\epsilon_* > 0.002$.
- The best combination IMF from Kroupa (2002) + Gavilán et al. (2006) + Chieffi & Limongi (2004) and Limongi & Chieffi (2003) yields, is used. The stellar yields + IMF may modify the absolute abundances on a disk, but they do not change the radial slope of the abundance distributions of disks.
- Using Shankar et al. (2006) prescriptions for $M_{\rm halo}/M_{\rm disk}$, we obtain the necessary infall rates to reproduce the radial profiles of galaxy disks
- Different prescriptions for the conversion of HI to H_2 are used finding that the ASC model is the best one.
- The slope of the oxygen abundance radial gradient for a MWG-like model when it is measured for $R < 2.5\,R_{\rm eff}$ has a value ~ -0.06 dex kpc^{-1}, which is around -0.10 dex $R_{\rm eff}^{-1}$ when it is measured using a normalized radius.
- This same slope is also obtained for all efficiencies and all galaxy masses in excellent agreement with CALIFA results, supporting the idea of an universal radial gradient for all galaxies when measured as a function of a normalized radius.
- The slope do not changes very much along z when the infall rate is as smooth as we have obtained recently, compared with old models with a stronger evolution.

Acknowledgments. This work has been supported by DGICYT grant AYA2013-47742-C4-4-P. This work has been supported financially by grant 2012/22236-3 from the São Paulo Research Foundation (FAPESP). This work has made use of the computing facilities of the Laboratory of Astroinformatics (IAG/USP, NAT/Unicsul), whose purchase was made possible by the Brazilian agency FAPESP (grant 2009/54006- 4) and the INCT-A. MM thanks the kind hospitality and wonderful welcome of the Jeremiah Horrocks Institute at the University of Central Lancashire, the E.A. Milne Centre for Astrophysics at the University of Hull, and the Instituto de Astronomia, Geofísica e Ciências Atmosféricas in São Paulo (Brazil), where this work was partially done.

References

Anders F., Chiappini C., Minchev I., et al., 2017, *A&A*, **600**, A70
Blitz L., Rosolowsky E., 2006, *ApJ*, **650**, 933
Bresolin F., Kennicutt R. C., 2015, *MNRAS*, **454**, 3664
Buitrago F., Trujillo I., Conselice C. J., et al., 2008, *ApJL*, **687**, L61
Chieffi A., Limongi M., 2004, *ApJ*, **608**, 405
Cresci G., Mannucci F., Maiolino R., et al., 2010, *Nature*, **467**, 811
Cunha K., Frinchaboy P. M., Souto D., et al., 2016, *Astronomische Nachrichten*, **337**, 922
Gavilán M., Buell J. F., Mollá M., 2005, *A&A*, **432**, 861
Gavilán M., Mollá M., Buell J. F., 2006, *A&A*, **450**, 509
Genovali K., Lemasle B., Bono G., et al., 2014, *A&A*, **566**, A37
Gibson B. K., Pilkington K., Brook C. B., et al., 2013, *A&A*, **554**, A47
Gnedin N. Y., Kravtsov A. V., 2011, *ApJ*, **728**, 88
Henry R. B. C., Kwitter K. B., Jaskot A. E., et al., 2010, *ApJ*, **724**, 748
Henry R. B. C., Worthey G., 1999, *PASP*, **111**, 919
Iwamoto K., Brachwitz F., Nomoto K., et al., 1999, *ApJS*, **125**, 439
Jones T., Ellis R. S., Richard J., Jullo E., 2013, *ApJ*, **765**, 48
Jones T., Wang X., Schmidt K. B., et al., 2015, *AJ*, **149**, 107
Kroupa P., 2002, *Science*, **295**, 82
Krumholz M. R., McKee C. F., Tumlinson J., 2008, *ApJ*, **689**, 865
Krumholz M. R., McKee C. F., Tumlinson J., 2009, *ApJ*, **693**, 216
Limongi M., Chieffi A., 2003, *ApJ*, **592**, 404
Maciel W. J., Costa R. D. D., 2013, *RevMexAA*, **49**, 333
Maciel W. J., Costa R. D. D., Uchida M. M. M., 2003, *A&A*, **397**, 667
Magrini L., Coccato L., Stanghellini L., Casasola V., Galli D., 2016, *A&A*, **588**, A91
Margalef-Bentabol B., Conselice C. J., Mortlock A., et al., 2016, *MNRAS*, **461**, 2728
Mollá M., Cavichia O., Gavilán M., Gibson B. K., 2015, *MNRAS*, **451**, 3693
Mollá M., Díaz A. I., 2005, *MNRAS*, **358**, 521
Mollá M., Díaz Á. I., Ascasibar Y., Gibson B. K., 2017, *MNRAS*, **468**, 305
Mollá M., Díaz Á. I., Gibson B. K., et al., 2016, *MNRAS*, **462**, 1329
Mollá M., Ferrini F., Diaz A. I., 1996, *ApJ*, **466**, 668
Mollá M., Ferrini F., Díaz A. I., 1997, *ApJ*, **475**, 519
Pilkington K., Few C. G., Gibson B. K., et al., 2012, *A&A*, **540**, A56

Queyrel J., Contini T., Kissler-Patig M., et al., 2012, *A&A*, **539**, A93
Rupke D. S. N., Kewley L. J., Chien L.-H., 2010, *ApJ*, **723**, 1255
Salucci P., Lapi A., Tonini C., et al., 2007, *MNRAS*, **378**, 41
Sánchez S. F., Rosales-Ortega F. F., Iglesias-Páramo J., et al., 2014, *A&A*, **563**, A49
Shaver P. A., McGee R. X., Newton L. M., et al., 1983, *MNRAS*, **204**, 53
Stanghellini L., Haywood M., 2010, *ApJ*, **714**, 1096
Trujillo I., Conselice C. J., Bundy K., et al., 2007, *MNRAS*, **382**, 109
Xiang M.-S., Liu X.-W., Yuan H.-B., et al., 2015, *Research in Astronomy and Astrophysics*, **15**, 1209
Yuan T.-T., Kewley L. J., Swinbank A. M., et al., 2011, *ApJL*, **732**, L14
Zaritsky D., Kennicutt Jr. R. C., Huchra J. P., 1994, *ApJ*, **420**, 87

Chemical Abundances in Gaseous Nebulae
AAA Workshop Series 10, 2016
G. Hägele, M. Cardaci & E. Pérez-Montero, eds.

Invited Review

Chemical abundances of photoionized nebulae in the Local Group

W. J. Maciel[1], R. D. D. Costa[1] and O. Cavichia[2]

[1]*IAG, University of São Paulo, Rua do Matão 1226, 05508-090, São Paulo SP, Brazil*
[2]*IFQ, Universidade Federal de Itajubá, Av. BPS, 1303, 37500-903, Itajubá MG, Brazil*

Abstract. Photoionized nebulae comprise basically HII regions and planetary nebulae, and their abundances give important clues on the nucleosynthesis and chemical evolution of their host galaxies. There is presently a large amount of data on these objects, especially for the elements He and N, which are strongly affected by the evolution of intermediate mass stars, as well as O, Ne, S, and Ar, which are essentially synthesized in stars with larger masses. The abundances of these elements in several systems in the Local Group are discussed on the basis of distance-independent correlations.

1. Introduction

Planetary nebulae (PN) provide accurate abundances of elements that are not significantly produced by their progenitor stars such as O, Ne, S, and Ar, as well as some elements for which the abundances have been changed, such as He, N, and C. The former can be used to study the chemical evolution of the host galaxies, and the latter can place constraints on the nucleosynthesis of intermediate mass stars. Distance-independent correlations involving O, Ne, S, and Ar can then be compared with the corresponding abundances of young objects, such as HII regions, Blue Compact Galaxies (BCG) and Emission Line Galaxies (ELG). In this paper we intend (i) to compare the abundances of HII regions and PN in different galaxies of the Local Group in order to investigate the differences derived from the age and origin of these objects, (ii) compare the chemical evolution in these systems, and (iii) investigate to what extent the nucleosynthesis contributions from the progenitor stars affect the observed abundances in planetary nebulae. Section 2 describes the data used in this investigation, and Section 3 presents our results and discussion. Further details can be found in Maciel et al. (2017).

2. The Data

We have considered abundance data for PN and HII regions in the following objects: The Milky Way (MW), the Large Magellanic Cloud (LMC), the Small Mag-

ellanic Cloud (SMC), M 31, M 32, M 33, M 51, M 81, M 101, NGC 185, NGC 205, NGC 300, NGC 628, NGC 3109, NGC 5194, and the Sextans galaxy. The uncertainties are typically of 0.2 to 0.3 dex for PN and 0.1 to 0.2 dex for HII regions. The PN sample includes over 1300 objects, while the HII region sample has over 900 objects, as shown in Table 1. We have preferably used the PN data obtained by our own group, but have also considered some recent abundance determinations from the literature, particularly from sources using a similar procedure as our group. For HII regions we have preferably adopted abundances obtained from detailed electron temperatures, instead of the strong line method. Blue Compact Galaxies and Emission Line Galaxies have also been included, as they are essentially low metallicity HII regions. The samples are large enough to compensate for the inhomogeneity of data, as a large number of sources has to be considered, since there is no complete homogeneous sample available. The complete list of sources for each object is given by Maciel et al. (2017).

Table 1. Total samples.

Planetary Nebulae	Number	HII Regions	Number
Milky Way Disk	347	Milky Way	216
Milky Way Bulge	267	Magellanic Clouds	35
Milky Way	614	Other Galaxies	325
Magellanic Clouds	511	BCG, ELG	360
Total External Galaxies	704	Total External Galaxies	720
TOTAL	1318	TOTAL	936

3. Results and Discussion

Fig. 1 shows histograms of the oxygen abundance O/H for planetary nebulae and HII regions in two representative cases: The Milky Way (left panels) and all objects considered here, namely the Milky Way, the Magellanic Clouds and the remaining external galaxies (right panels). Both PN and HII regions have similar distributions, although the HII region distributions are generally broader than in the case of planetary nebulae. Also, it can be noticed that a larger fraction of HII regions have $\log(\mathrm{O/H}) + 12 \geq 9$, which reflects the fact that these younger objects are formed by more enriched material. Similar plots can be obtained for Ne, S, and Ar.

Distance-independent correlations for Ne are shown in Fig. 2. The left panels refer to the Milky Way, while the right panels are for all objects considered. The top figures show the abundances relative to hydrogen (Ne/H), while the bottom figures show the abundances relative to oxygen (Ne/O). The squares represent Milky Way PN, the circles are external PN, the triangles represent HII regions in the Milky Way, and the crosses are external HII regions. We see that for the Ne/H ratio both PN and HII regions present a lockstep variation with O/H, although for HII regions the dispersion is much smaller. This is also reflected in the bottom figure, indicating that the Ne/O ratio is essentially constant with a

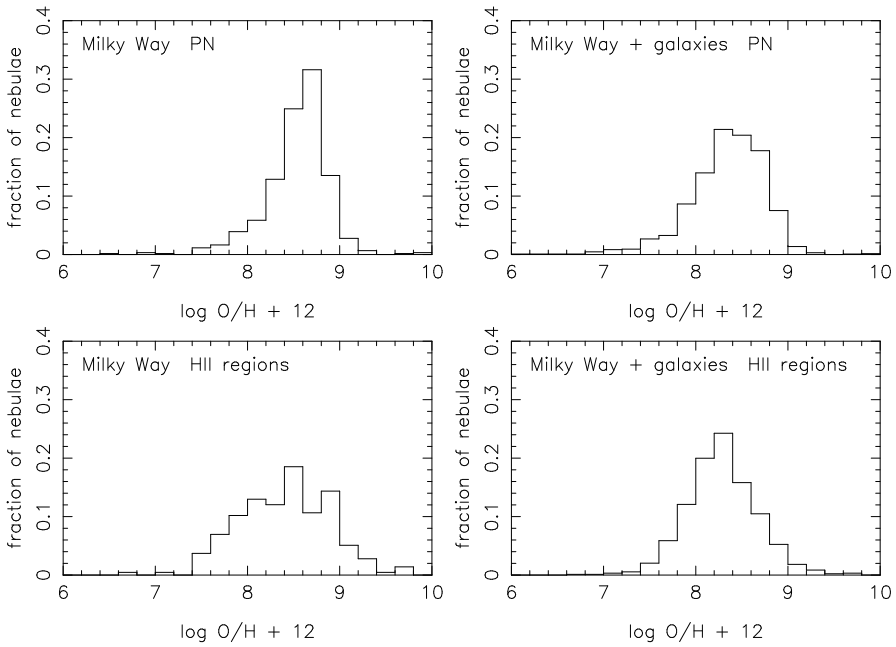

Figure 1. Histograms of the O/H abundances in PN and HII regions. Left: Milky Way; Right: Milky Way and external galaxies.

higher dispersion for PN. The estimated dispersions are about 0.2 dex for PN and 0.1 dex for HII regions.

The same behaviour observed in the Galaxy also holds in other Local Group objects. Despite their different metallicities and morphologies, their nucleosynthetic processes and chemical evolution are apparently very similar. The trend displayed in Fig. 2 (right) shows a very good agreement with the trend found by Izotov et al. (2006) on the basis of ELG only. Similar conclusions were obtained by Richer & McCall (2007, 2008). For the right panel, the fractions of objects within 1σ and 2σ are 0.78 and 0.93, respectively.

It is interesting to notice that in this larger sample the observed ranges of oxygen and neon abundances in PN and HII regions are similar. The similarity essentially reflects the fact that the interstellar metallicities did not change appreciably in the last 5 Gyr approximately, a result that is supported by determinations of the age-metallicity in the Milky Way (see e.g. Rocha-Pinto et al., 2000; Bensby et al., 2004).

The results shown in Fig. 2 can be interpreted assuming that the dispersion in the PN data reflects the fact that the abundances are not as well determined as in the HII regions. However, a larger dispersion would be expected, since PN are older objects than the HII regions and any given sample probably includes objects of different ages, as we have shown elsewhere (Maciel et al., 2010, 2011). It can also be considered that there is some contribution to the Ne abundances from the PN progenitor stars, as suggested in some investigations (see e.g. Peña et al., 2007). It has been argued that the third dredge-up process in AGB stars

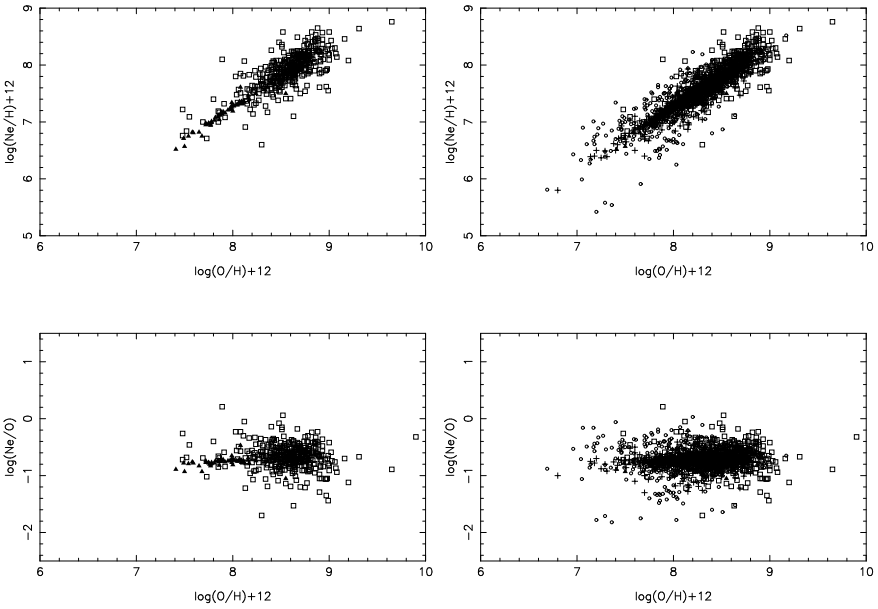

Figure 2. Ne abundances as functions of oxygen abundances. Left: Milky Way, right: Milky Way and external galaxies. Milky Way PN (squares), Milky Way HII regions (triangles); external PN: circles, external HII regions: crosses.

may affect the oxygen abundances observed in PN (see e.g. Karakas & Lattanzio, 2014). ON cycling would also reduce the O/H ratio especially in lower metallicity PN with massive progenitor stars (see e.g. Karakas & Lattanzio, 2007). Our results show that, if present, such contribution should be small compared with the average uncertainties in the PN abundances, so that an average contribution of about 0.1 dex cannot be ruled out. On the other hand, if we compare the expected contributions both to oxygen and neon, it is unlikely that their are equal, which is needed in order to explain the similarity of the PN and HII region trends shown in Fig. 2 (cf. Karakas & Lattanzio, 2003).

In the case of sulphur, as shown in Fig. 3, the general trends with oxygen are similar to neon, but some differences arise. The average dispersions are now 0.3 dex for PN and 0.2 dex for HII regions. For the Milky Way, the HII regions present a very good correlation, and the data extend to higher and lower metallicities compared with neon. The Galactic PN already display what is usually called the "sulphur anomaly", that is, many PN apparently have somewhat lower S/H abundances than expected for their metallicity (see the detailed discussions by Henry et al., 2004, 2012). The sulphur anomaly has been attributed to a deficiency in the sulphur Ionization Correction Factors (ICFs), particularly due to the abundance of the S^{+3} ion, lack of accurate atomic constants, effect of the nucleosynthesis in the progenitor stars, and different chemical evolution of the systems considered.

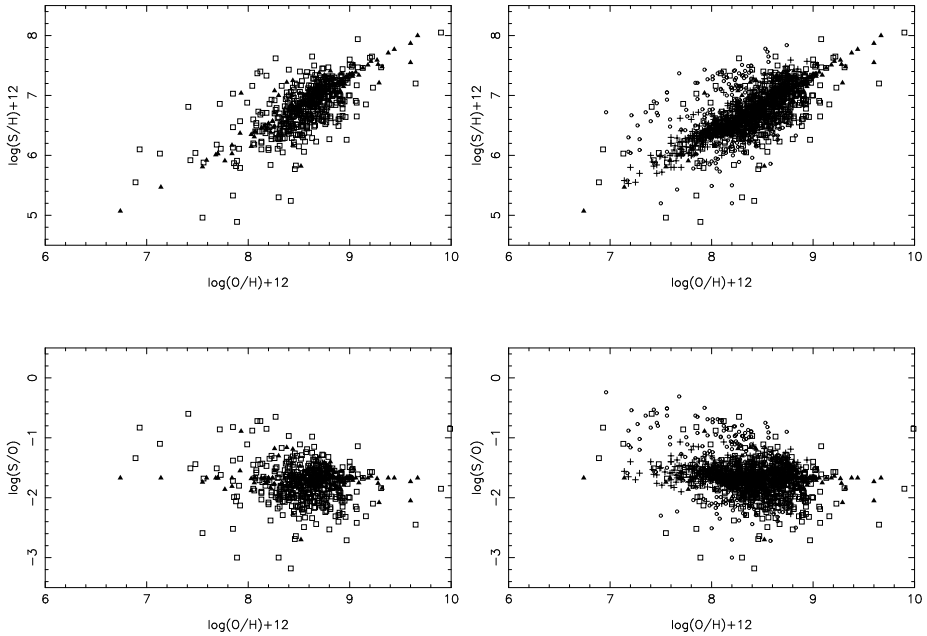

Figure 3. The same as Fig. 2 for Sulphur.

Considering the right panel of Fig. 3, it can be seen that there is still a reasonable number of objects below the HII region curve, but there is a large number of PN in the opposite side, so that the sulphur anomaly is not particularly noticeable. The inclusion of BCG and ELG maintains these conclusions, that is, the sulphur abundances of HII regions apparently do not show the sulphur anomaly, which is then a characteristic of the empirical determination of sulphur abundances in PN.

For argon the observed correlations are similar compared to neon, but the dispersion is higher and is comparable to S/H, as can be seen from Fig. 4. The comparison with HII regions suffers from the lack of data for this element, especially for the Milky Way. The inclusion of BCG and ELG clearly improves the correlation, showing that the correlation defined at higher metallicities for the Milky Way still holds for lower and intermediate oxygen abundances. For PN, the Ar/H dispersion is higher compared with Ne/H, but for HII regions the dispersions in Ne/H, S/H, and Ar/H for the whole sample are similar to each other, and always smaller than the PN data. Therefore, the HII regions are clearly more homogeneous than the PN, which reflects their very low ages, roughly a few million years.

3.1. Elements produced by the PN progenitor stars

Histograms of the N/H abundances for PN and HII regions in our sample are shown in Fig. 5, which can be directly compared with Fig. 1. The PN distribution is similar in the two cases shown, while for HII regions the inclusion of external galaxies (as well as BCG and ELG) shifts the maximum downwards by about 0.5

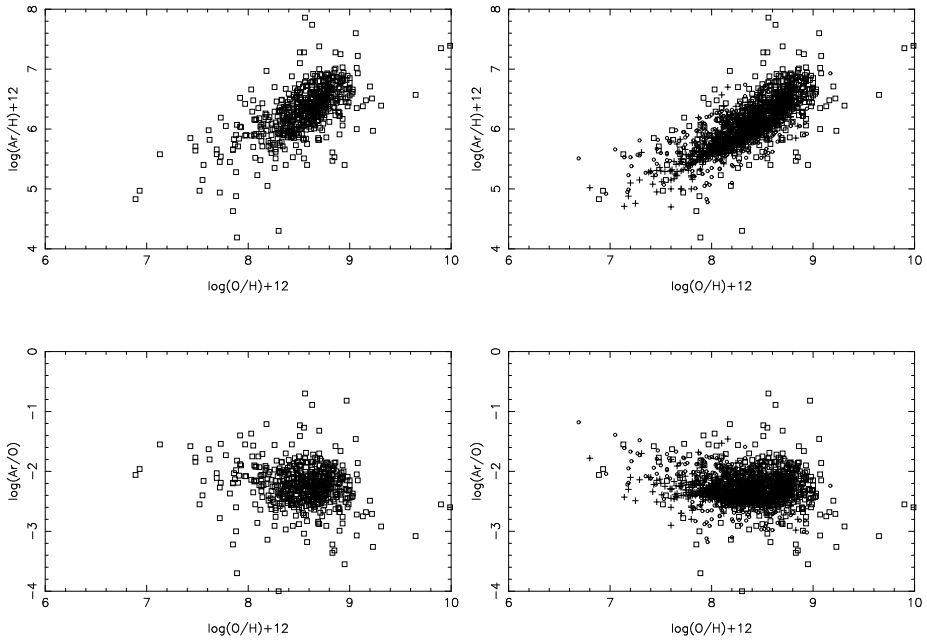

Figure 4. The same as Fig. 2 for Argon.

dex. The main difference between O/H and N/H is that the nitrogen abundances extends to lower metallicities for HII regions compared with PN, which reflects the N production during the evolution of the PN progenitor stars.

Helium abundances in HII regions are frequently affected by the presence of neutral helium, so that in this work we have adopted a lower limit of He/H = 0.03 in order to avoid objects with an important fraction of neutral He.
Fig. 6 shows the N/H and N/O ratios as functions of O/H and He/H, respectively, for the case where all objects are considered. The most striking result is that, as expected, PN show an increase in both N and He compared to most HII regions in the sample. The average dispersions of the nitrogen data are higher, about 0.4 dex for PN and 0.3 dex for HII regions. Therefore, a larger dispersion is also observed for HII regions, so that part of their nitrogen is probably secondary.
Our results clearly reflect the fact that the nitrogen abundances measured in PN include both the pristine nitrogen plus the contribution from the dredge up processes that affect the red giant progenitor stars. Similar trends have also been recently discussed by García-Hernández et al. (2016). Adopting a pregalactic He abundance by mass of about $Y = 0.255$ (cf. Izotov et al., 2014), which corresponds to approximately He/H = 0.09, we conclude from Fig. 6 (bottom) that about 80% of the PN with He excess have abundances up to He/H $\simeq$ 0.141, which is about 57% higher than the pregalactic value. This can be compared with an amount of 50% derived by Richer & McCall (2008) from a smaller sample. More recently, Lattanzio & Karakas (2016) suggested an increase of about 38% in the helium content by mass from the second dredge-up process in AGB stars,

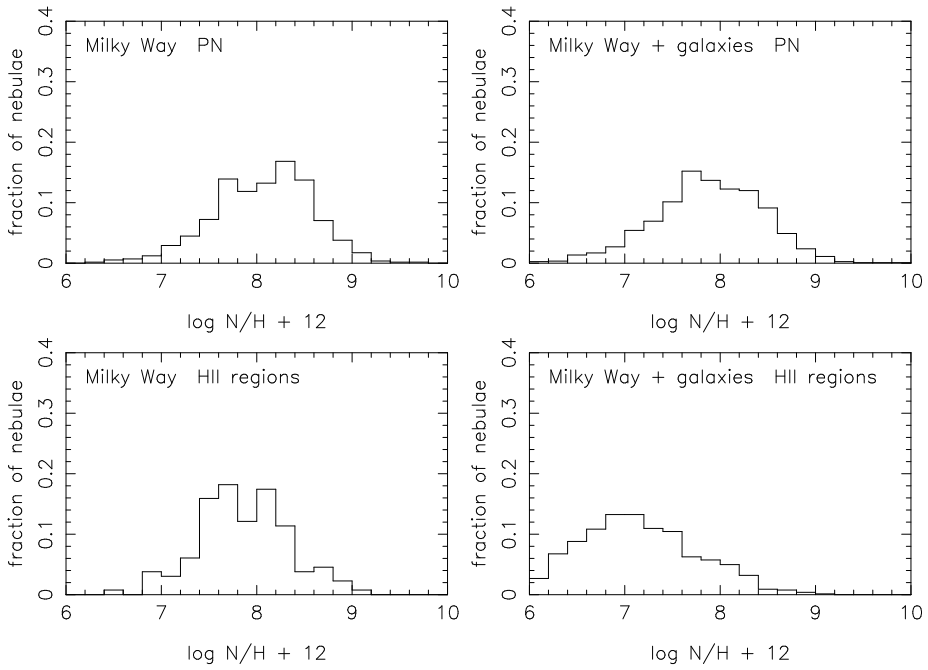

Figure 5. Histograms of the N/H abundances in PN and HII regions. Left: Milky Way, Right: Milky Way and all external galaxies.

which would lead to an increase of about 60% in the He abundance by number of atoms, in excellent agreement with the results shown in Fig. 6.

Also from Fig. 6 we can have an idea of the amount of nitrogen produced by the progenitor stars. Adopting as limit for primary nitrogen the amount produced by type II supernovae (Izotov et al., 2006), corresponding to approximately $\log \mathrm{N/O} = -1.6$, and considering the expected secondary nitrogen enrichment, which corresponds to about $\log \mathrm{N/O} = -1.2$, Fig. 6 (bottom) implies that about 80% of the PN present an enrichment ratio up to factor of 13.3, comparable with the factor of 10 found by Richer & McCall (2015).

In Fig. 6 (bottom) we include a comparison with some recent theoretical models by Karakas (2010) with $Z = 0.02$, 0.004, and 0.008, while the dashed lines represent models by Marigo et al. (2003) with $Z = 0.019$. According to these models, progenitors having 0.9 to 4 $M_{\odot}$ and solar composition can explain the "normal" abundances, $\mathrm{He/H} < 0.15$, while for objects with higher enhancements ($\mathrm{He/H} > 0.15$), masses of 4 to 5 $M_{\odot}$ are needed, plus an efficient HBB. Recent models by Pignatari et al. (2016) with $Z = 0.01$ and 0.02 are also consistent with these results, as can be seen in the discussion by Delgado-Inglada et al. (2015). For intermediate mass stars, agreement with theoretical models is fair, but abundance determinations should be improved and expanded.

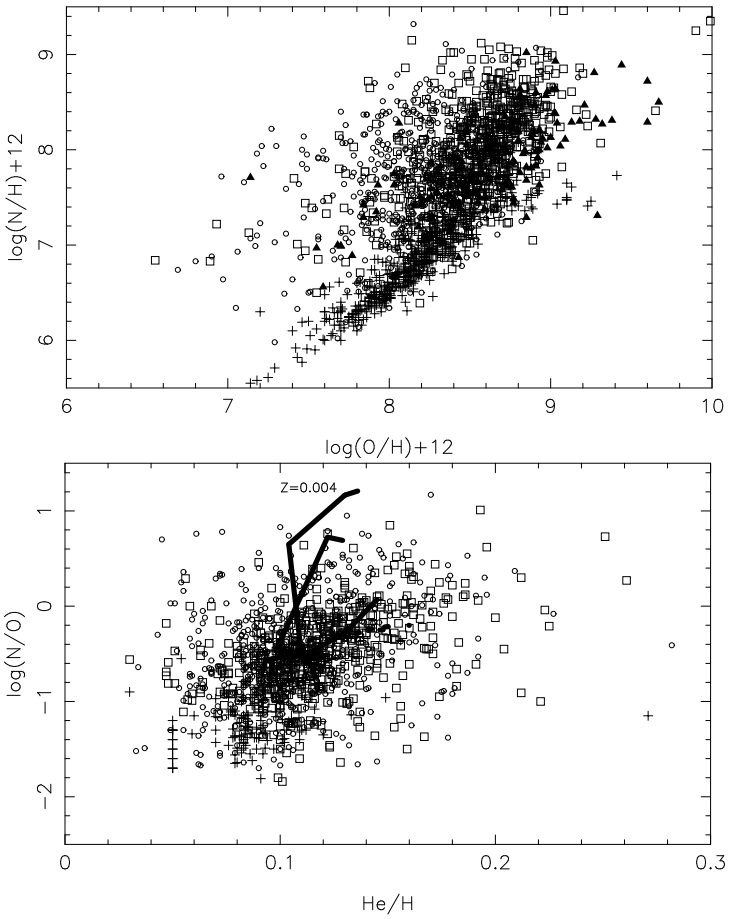

Figure 6. N abundances as functions of O/H (top) and He/H (bottom) for the Milky Way and external galaxies. MW PN (squares), MW HII regions (triangles), external PN (circles), external HII regions (crosses). The lines are models by Karakas (2010, solid lines) and Marigo et al. (2003, dashed line).

Acknowledgments. This work was partially supported by FAPESP, CNPq, and CAPES.

References

Bensby T., Feltzing S., Lundström I., 2004, *A&A*, **421**, 969
Delgado-Inglada G., Rodríguez M., Peimbert M., et al., 2015, *MNRAS*, **449**, 1797
García-Hernández D. A., Ventura P., et al., 2016, *MNRAS*, **461**, 542
Henry R. B. C., Kwitter K. B., Balick B., 2004, *AJ*, **127**, 2284
Henry R. B. C., Speck A., Karakas A. I., et al., 2012, *ApJ*, **749**, 61
Izotov Y. I., Stasińska G., Meynet G., et al., 2006, *A&A*, **448**, 955
Izotov Y. I., Thuan T. X., Guseva N. G., 2014, *MNRAS*, **445**, 778
Karakas A., Lattanzio J. C., 2007, *PASA*, **24**, 103
Karakas A. I., 2010, *MNRAS*, **403**, 1413
Karakas A. I., Lattanzio J. C., 2003, *PASA*, **20**, 393
Karakas A. I., Lattanzio J. C., 2014, *PASA*, **31**, e030
Lattanzio J., Karakas A., 2016, *Journal of Physics Conference Series*, Vol. 728b, p. 2002
Maciel W. J., Costa R. D. D., Cavichia O., 2017, *RevMexAA*, **53**, 151
Maciel W. J., Costa R. D. D., Idiart T. E. P., 2010, *A&A*, **512**, A19
Maciel W. J., Rodrigues T. S., Costa R. D. D., 2011, *RevMexAA*, **47**, 401
Marigo P., Bernard-Salas J., Pottasch S. R., et al., 2003, *A&A*, **409**, 619
Peña M., Stasińska G., Richer M. G., 2007, *A&A*, **476**, 745
Pignatari M., Herwig F., Hirschi R., et al., 2016, *ApJS*, **225**, 24
Richer M. G., McCall M. L., 2007, *ApJ*, **658**, 328
Richer M. G., McCall M. L., 2008, *ApJ*, **684**, 1190
Richer M. G., McCall M. L., 2015, P. Benvenuti (ed.), *Proceedings of the XXIX IAU General Assembly*, Vol. 11, Cambridge University Press (arXiv:1509.08537)
Rocha-Pinto H. J., Maciel W. J., Scalo J., Flynn C., 2000, *A&A*, **358**, 850

Chemical Abundances in Gaseous Nebulae
AAA Workshop Series 10, 2016
G. Hägele, M. Cardaci & E. Pérez-Montero, eds.

Invited Review

Chemical abundances in Galactic planetary nebulae from faint emission lines

J. García–Rojas[1,2]

[1]*Inst. de Astrofísica de Canarias, E-38200, La Laguna, Tenerife, Spain*
[2]*Dept. de Astrofísica, Universidad de La Laguna, E-38206, La Laguna, Tenerife, Spain*

Abstract. Deep spectrophotometry has proved to be a fundamental tool to improve our knowledge on the chemical content of planetary nebulae. With the arrival of very efficient spectrographs installed in the largest ground-based telescopes, outstanding spectra have been obtained. These data are essential to constrain state-of-the-art nucleosynthesis models in asymptotic giant branch stars and, in general, to understand the chemical evolution of our Galaxy. In this paper we review the last advances on the chemical composition of the ionized gas in planetary nebulae based on faint emission lines observed through very deep spectrophotometric data.

1. Introduction

Huggins & Miller (1864) obtained the first spectrum of a planetary nebula (The Cat's Eye Nebula), where they detected a bright emission line coming from a mysterious element that Huggins (1898) called "nebulium". Several decades after, Bowen (1927) showed that this emission was produced by doubly ionized oxygen (O^{2+}). The first "deep" spectra of planetary nebulae (hereinafter, PNe) were obtained by Wyse (1942), who detected for the first time very faint metal recombination lines of CII and OII in the spectrum of several PNe and in the Orion nebula.

Since these early achievements in spectrophotometry of PNe, the amount of deep optical and near-infrared spectrophotometric data of PNe has increased significantly. This has been possible thanks to both the development of more efficient instruments and of ground-based telescopes with large collecting areas. In Table 1 we show some of the deepest optical spectra ever taken for Galactic PNe in the last 25 years with the purpose of obtaining chemical abundances. Although this list does not intend to be complete, it is quite representative of the last advances in the field. To progress in the field of chemical abundances in ionized nebulae we need to obtain very deep spectra to detect the weakest lines and, additionally, we need the spectra to be of high resolution to properly measure important faint emission lines which are blended with other features. As it can be seen in Table 1, the deepest spectra of PNe (those of NGC 7027 and NGC 7009) have been taken at relatively low-resolution. However, the authors of these works did a very careful work of deblending using "ad-hoc" atomic physics. On the other hand, high-resolution spectra can reveal the kinematical structure

Table 1. Deep spectra of PNe.

Reference[a]	Telescope	Objects	Wavelength range (nm)	Number of lines	R∼$\lambda/\Delta\lambda$
1	OHP 1.93m	NGC 7027	399–1050	∼680	<4000
2	Lick 3m	IC 4997	360–1005	∼470	∼30000
3	ESO 1.52m	NGC 6153	304–743	∼380	<4000
4	CTO 4m	IC 418	350–987	∼800	∼20000
5	VLT 8.2m	NGC 5315	300–1040	∼550	∼9000
6	WHT 4.2m	NGC 7027	331–916	∼1170	<5000
7	KPNO 4m	NGC 7027	460–920	∼750	∼15000
	LCO 6.5m	3 PNe	328–758	∼2330	22000–28000
8	WHT 4.2m	NGC 7009	304–1100	∼1200	<5000
	ESO 1.52m				
9	LCO 6.5m	12 PNe	335–940	>3000	22000–28000
10	VLT 8.2m	NGC 3918	300–1040	∼750	∼40000

[a](1) Péquignot & Baluteau (1994); (2) Hyung et al. (1994); (3) Liu et al. (2000); (4) Sharpee et al. (2004); (5) Peimbert et al. (2004); (6) Zhang et al. (2005); (7) Sharpee et al. (2007); (8) Fang & Liu (2011); (9) García-Rojas et al. (2012); (10) García-Rojas et al. (2015).

of the nebula, resulting in different profiles depending on the excitation of the emitting ion (Sharpee et al., 2003; García-Rojas et al., 2015, see e.g.). This makes line identification easier and allows one to deblend important emission lines. Additionally, the distinct line profiles provide a valuable tool to identify the physical region where individual lines are formed (e.g. Richer et al., 2013; Peña et al., 2017). In Fig. 1 we show a portion of the deep, high-resolution (R∼15000) spectra of several PNe, where it is clear that only at such a high-resolution the OII lines can be properly deblended from other N and C emission features (see Sect. 2).

In the following sections, we discuss recent advances in chemical abundances in PNe from the analysis of very deep optical and near-infrared spectra.

2. The abundance discrepancy problem

The *abundance discrepancy problem* is one of the major unresolved problems in nebular astrophysics and it has been around for more than seventy years (since Wyse, 1942). It consists in the fact that in photoionized nebulae –both HII regions and PNe– optical recombination lines (ORLs) provide abundance values that are systematically larger than those obtained using collisionally excited lines (CELs). Solving this problem has obvious implications for the measurement of the chemical content of nearby and distant galaxies, because this task is most often done using CELs from their ionized interstellar medium.

For a given ion, the abundance discrepancy factor (ADF) is defined as the ratio between the abundances obtained from ORLs and CELs, i.e.,

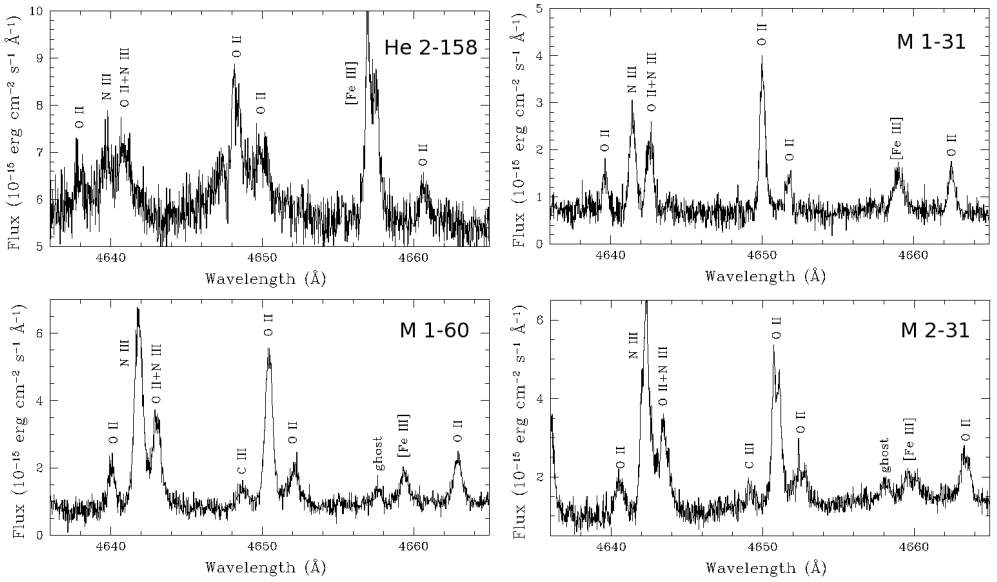

Figure 1. Portion of the high-resolution (R∼15000) spectra showing the zone where the multiplet 1 OII lines lie. As it can be shown the quality of the spectra allows one to detect several other permitted lines of C, O, and N, to deblend several very close emission lines. Figure based on Fig. 4 of García-Rojas et al. (2018).

$$\mathrm{ADF}(\mathrm{X}^{i+}) = (\mathrm{X}^{i+}/\mathrm{H}^{+})_{\mathrm{ORLs}}/(\mathrm{X}^{i+}/\mathrm{H}^{+})_{\mathrm{CELs}}, \quad (1)$$

and is usually between 1.5 and 3 in HII regions and the bulk of PNe (see García-Rojas & Esteban, 2007; McNabb et al., 2013), but in PNe it has a significant tail extending to much larger values.

The reason for this discrepancy has been discussed for many years and three main scenarios have been proposed: i) the existence of temperature fluctuations over the observed volume of the nebula (Peimbert, 1967; Torres-Peimbert et al., 1980), b) the presence of cold and dense H-poor droplets as the origin of the bulk of the ORL emission (e.g. Liu et al., 2000; Stasińska et al., 2007; Henney & Stasińska, 2010), c) the departure of the free electron energy distribution from the Maxwellian distribution (κ-distribution, see Nicholls et al., 2012). However, in the last years, several works have argued against the κ-distribution as being responsible for the abundance discrepancy in PNe (see Mendoza & Bautista, 2014; Storey & Sochi, 2014; Ferland et al., 2016). Unfortunately, there are so far not direct observational evidences that can favor any of these scenarios.

In the last 20 years the group led by Prof. X. –W. Liu (U. Beijing) have developed deep medium-resolution spectrophotometry of dozens of PNe (and high-resolution of a few PNe, see McNabb et al., 2016) to compute the physical and chemical properties of these objects from ORLs. In one of the most detailed and comprehensive studies of this group, Wang & Liu (2007) showed that the values

of the ADF deduced for the four most abundant second-row heavy elements (C, N, O and Ne) are comparable (see their Fig. 18). However, they also computed abundances from ORLs from a third-row element (Mg) and they found that the ORL abundance of magnesium is compatible with the solar photospheric value (even taking into account the small depletion expected for this element onto dust grains - less than 30%). Finally, these authors also showed that, regardless of the value of the ADF, both CEL and ORL abundances yield similar relative abundance ratios of heavy elements such as C/O, N/O and Ne/O . This has important implications, especially in the case of the C/O ratio, given the difficulties of obtaining this ratio from CELs (see Sect. 3).

The Liu's group have strongly argued in favor of the inhomogeneous composition of PNe and against pure temperature fluctuations. Some of their arguments are the following: i) far-IR [OIII] CELs, which in principle, have a much lower dependence on electron temperature than optical CELs, provide abundances that are consistent with those derived from optical CELs (see e.g. Liu et al., 2000); ii) the analysis of the physical conditions using H, He, O and N ORLs yields electron temperatures that are much lower than those computed from classical CEL diagnostic ratios (see Zhang et al., 2004, 2009; Tsamis et al., 2004; Fang et al., 2011); additionally, ORL density diagnostics provide densities that are higher than those derived from CEL diagnostics; iii) chemically homogeneous photoionization models do not reproduce the required temperature fluctuations to match CEL and ORL abundances, while bi-abundance photoionization models including an H-poor (i.e. metal-rich) component of the gas successfully reproduce the observed intensities of both CELs and ORLs (e.g. Yuan et al., 2011). All these arguments strongly favor the presence of a low-mass component of the gas that is much colder and denser than the "normal" gas, and that is responsible for the bulk of the ORL emission. However, we cannot rule out the possibility that different physical phenomena can contribute simultaneously to the abundance discrepancy in PNe.

Some physical phenomena have been proposed to explain the abundance discrepancy in the framework of temperature fluctuations or chemical inhomogeneities scenarios (Peimbert & Peimbert, 2006; Liu, 2006). Some recent works on the Orion nebula have observationally linked the abundance discrepancy to the presence of high velocity flows (Mesa-Delgado et al., 2009) or to the presence of high density clumps, such as protoplanetary disks (Mesa-Delgado et al., 2012; Tsamis et al., 2011). On the other hand, Liu et al. (2006) found a very extreme value of the ADF for the PN Hf 2–2 (ADF$\sim$70) and, for the first time, speculated with the possibility that this large ADF could be related to the fact that the central star of the PN, which is a close-binary star, has gone through a common-envelope phase.

By means of spectroscopic observations at the 4.2m William Herschel Telescope (WHT) in La Palma, Spain, Corradi et al. (2015) recently confirmed the hypothesis proposed by Liu et al. (2006) that the largest abundance discrepancies are reached in PNe with close-binary central stars, the most extreme object being the PN Abell 46, where we have found an ADF(O^{2+})$\sim$120, and as high as 300 in its inner regions. Their spectroscopic analysis supports the previous interpretation that, in addition to "standard" hot ($T_e\sim10^4$ K) gas, a colder ($T_e\sim10^3$ K), metal-rich, ionized component also exists in these nebulae. Both the origin of

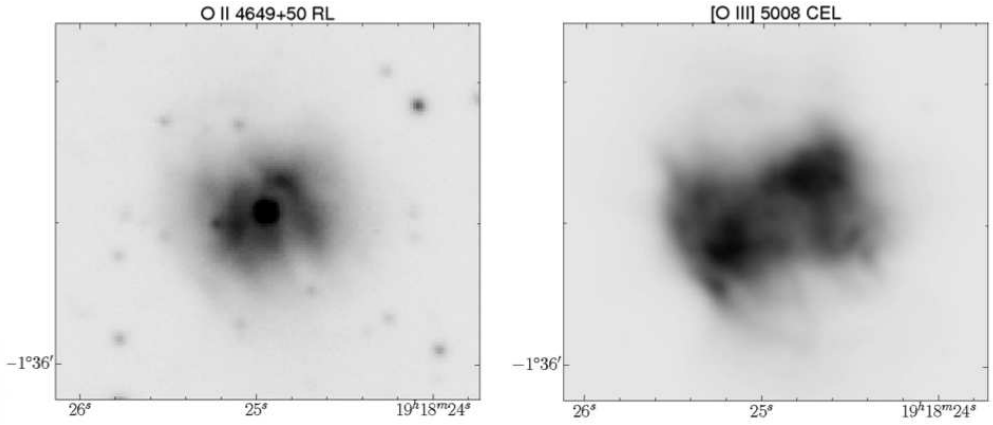

Figure 2. OSIRIS-GTC tunable filter image of NGC 6778 in the OII $\lambda\lambda$4659+51 ORLs (left) and ALFOSC-NOT image of Guerrero & Miranda (2012) in the [OIII] λ5007 CEL (right). Figure adapted from figure 2 of García-Rojas et al. (2016).

the metal-rich component and how the two gas phases are mixed in the nebulae are basically unknown. Moreover, this dual nature is not predicted by mass-loss theories. However, it seems clear that the large-ADF phenomena in PNe is linked to the presence of a close-binary central star. In fact, Wesson et al. (2017) recently completed a survey of the ADFs in seven PNe with known close-binary central stars and they found ADFs larger than 10 for all of them, confirming the strong link between large ADFs and close-binary central stars. On the other hand, several spectroscopic studies have shown that the ORL emitting plasma is generally concentrated in the central parts of the PNe. This occurs in PNe with known close-binary central stars and large ADFs (e.g. Corradi et al., 2015; Jones et al., 2016), in PNe with low-to-moderate ADFs and no indication of binarity (e.g. Liu et al., 2001; Garnett & Dinerstein, 2001) and in PNe with relatively large ADFs but no known close-binary central star (e.g. M 1–42, see Climent, 2016; García-Rojas et al., 2017).

García-Rojas et al. (2016) recently obtained the first direct image of the PN NGC 6778 (a PN with ADF$\sim$20) in OII recombination lines, taking advantage of the tunable filters available at the OSIRIS instrument in the 10.4m Gran Telescopio Canarias (GTC). They found that in NGC 6778, the spatial distribution of the OII $\lambda\lambda$4649+50 ORL emission does not match that of the [OIII] λ5007 CEL (see Fig. 2). García-Rojas et al. (2017) found the same behavior in Abell 46 using direct tunable filter images centered at $\lambda\lambda$4649+51 Å.

Moreover, García-Rojas et al. (2017) obtained deep 2D spectroscopic observations with MUSE at the 8.2m Very Large Telescope (VLT) of five southern large-ADF PNe, and they confirmed this behavior in at least the PNe Hf 2-2 (ADF$\sim$84), M 1-42 and NGC 6778 (both with ADF$\sim$20).

These results clearly support the hypothesis of the existence of two separate plasmas, at least in these large-ADF PNe, with the additional indication that they are not well mixed, perhaps because they were produced in distinct ejec-

tion events related to the binary nature of the PN central star. Wesson et al. (2017) propose that a nova-like outburst from the close-binary central star could be responsible for ejecting H-deficient material into the nebulae soon after the formation of the main nebula.

3. The C/O ratio from recombination lines

The determination of accurate C/H and C/O ratios in HII regions is of paramount importance to constrain chemical evolution models of galaxies. Moreover, C/O determinations in PNe can also constrain nucleosynthesis processes in low-to-intermediate mass stars. However, the determination of C abundances in photoionized nebulae is difficult because, traditionally, C abundances have been derived from the semi-forbidden CIII] λ1909 and CII] λ2326 CELs in the UV, which can only be observed from space and whose intensity is strongly affected by interstellar reddening and extremely dependent on the electron temperature. Alternatively, there is a method to derive C abundances in ionized gas based on the faint CII λ4267 RL. Thanks to the new CCDs with improved efficiency in the blue and the use of large telescopes, several high-quality observations of the CII λ4267 RL in PNe have been achieved in the last years (e.g. Peimbert et al., 2004; Liu et al., 2004; Wesson et al., 2005; Sharpee et al., 2007; Wang & Liu, 2007; García-Rojas et al., 2009, 2013; Fang & Liu, 2013).

C/O ratios derived from RLs combined with other abundance ratios as N/O or He/H, can set strong constraints to the initial mass of PNe progenitors. This is owing to different processes occurring at the interior of AGB stars (third dredge-up episodes, hot bottom burning process) activates at different masses and can strongly modify C/O and N/O ratios (see e.g. Karakas & Lugaro, 2016, and references therein). Additionally, C/O ratios can be used to obtain information about the efficiency of dust formation in C-rich or O-rich environments (see below) and to learn about different dust-formation mechanisms (see García-Hernández et al., 2016).

4. Faint emission lines of refractory elements

Iron emission lines are relatively faint in the spectra of Galactic PNe. Delgado-Inglada et al. (2009) computed detailed Fe abundances for a sample of 28 PNe and found that more than 90% of Fe atoms are condensed on dust grains. These authors did not find differences between the iron abundances in C-rich and O-rich PNe, suggesting similar depletion efficiencies in both environments.

Delgado-Inglada & Rodríguez (2014) combined C/O ratios derived from both UV CELs and optical ORLs (as we comment in Sect. 2, they seem to be equivalent) with information obtained from *Spitzer* mid-infrared spectra. They also computed Fe depletions, and found that the highest depletion factors were found in C-rich objects with SiC or the 30 μm feature in their infrared spectra, while the lowest depletion factors were found for some of the O-rich objects showing silicates in their infrared spectra.

Delgado-Inglada et al. (2016) compiled detections of very faint [NiII] and [NiIII] lines in deep spectra of Galactic PNe and HII regions. They determined the nickel abundance from the [NiIII] lines using an extensive grid of photoionization models

to determine a reliable ionization correction factor (ICF). From the comparison of Fe/Ni ratios with the depletion factor obtained from both [Fe/H] and [Ni/H], they conclude that nickel atoms are more efficiently stuck to dust grains than iron atoms in environments where dust formation or growth is more important.

5. Neutron-capture element abundances in PNe

Nebular spectroscopy of neutron(n)-capture elements (atomic number Z > 30) is a recent field that has seen rapid development in the last 10 years, and holds promise to significantly advance our understanding of AGB n-capture nucleosynthesis. Nebular spectroscopy can reveal unique and complementary information to stellar spectroscopy. Observations of PNe provide the first opportunity to study the production of the lightest n-capture elements (Z $\leq$ 36) and noble gases (Kr and Xe) in one of their sites of origin. Unlike the case of AGB stars, nucleosynthesis and convective dredge-up are complete in PNe, whose envelopes contain material from the last 2−3 thermal pulses. Accurate computations of n-capture elements would shed light on the different scenarios proposed for the production of these elements and would constrain the chemical yields of low- and intermediate-mass stars for these elements.

n-capture elements were not recognized in any astrophysical nebula until Péquignot & Baluteau (1994) identified emission lines of Br, Kr, Rb, Xe, Ba, and possibly other heavy species in the bright PN NGC 7027. Since then, a breathtaking number of n-capture element emission lines have been identified for the first time in near-infrared (Dinerstein, 2001; Sterling et al., 2016, 2017), UV (Sterling et al., 2002) and optical (Sharpee et al., 2007; García-Rojas et al., 2012, 2015) spectra of PNe. The new detections have led to a dedicated effort to produce atomic data needed for abundance determinations (see e.g. Sterling & Witthoeft, 2011; Sterling et al., 2016, and references therein). The new photoionization cross-sections and recombination coefficients have been incorporated in photoionization calculations to compute reliable ICFs (e.g. Sterling et al., 2015). The new collisional strengths have been used for abundance determinations of newly detected ions (see Sterling et al. 2016, for [RbIV], Sterling et al. 2017, for [SeIII] and [KrVI]). Thanks to the fast advances in observations, atomic data determinations and numerical modeling, this field has grown up from just 3 PNe with n-capture element abundances in 2001 to more than 100 Galactic PNe in 2016 (Sharpee et al., 2007; Sterling & Dinerstein, 2008; Sterling et al., 2016; García-Rojas et al., 2012, 2015).

The importance of deep, high-resolution optical spectrophotometry of PNe to detect faint n-capture elements can be understood when comparing the works by Sharpee et al. (2007) and García-Rojas et al. (2015). In the first case, several n-capture emission lines were discovered in the spectra of 5 PNe, but even at a resolution of ∼22000, many features were not unambiguously detected. García-Rojas et al. (2015) took advantage of the very high-resolution (R∼40000) spectrum of NGC 3918 to clearly identify several ions of Kr, Xe, Rb and Se, testing for the first time the complete set of ICFs for Kr created by Sterling et al. (2015). Finally, Madonna et al. (2017) have combined a deep optical spectrum and a near-infrared spectrum of NGC 5315, testing for the first time the complete set of ICFs for Se created by Sterling et al. (2015).

6. Other faint emission lines in optical and IR spectra of PNe

Other faint emission lines have been detected in the optical and mid-IR spectra of PNe and are of great interest for different reasons. I am going to focus on F, Zn and α–elements Ca, K and Na.

Zinc is a useful surrogate element for measuring abundances of the iron group because, unlike iron, it is not depleted onto dust grains. Smith et al. (2014) developed an observational campaign with ISAAC at the VLT in the mid-IR range with the aim of detecting Zn emission lines. These authors successfully detected the faint [ZnIV] at 3.625 μm in seven objects and added other two detections observed by Dinerstein & Geballe (2001). They compute Zn elemental abundances using photoionization models and conclude that assuming $Zn/Zn^{3+}\sim O/O^{2+}$ is a good approximation. The main conclusion of their work was that the majority of the sample exhibit subsolar [Zn/H], and half of the sample show enhancement in [O/Zn].

Fluorine faint emission lines have been detected and measured in deep optical spectra of PNe. This element is very interesting because it only has one stable isotope, ^{19}F, and several possible nucleosynthetic origins in the literature have been proposed: i) explosions of Type II supernovae, ii) stellar winds from massive Wolf-Rayet stars, and iii) the occurrence of the third dredge-up in AGB stars (see Zhang & Liu, 2005). Accurate abundance determinations of fluorine can shed some light on its nucleosynthetic origin. Zhang et al. (2005) performed a survey in the literature looking for detections of the faint [FII] λ4789 and [FIV] λ4060 lines. To compute elemental F abundances, these authors assumed that $F/O=F^+/O^+$ and $F/O=(F^{3+}/Ne^{3+})(Ne/O)$ for low– and high–ionization PNe, respectively. They found that F is generally overabundant in PNe and, that F/O is positively correlated with C/O, which favors the hypothesis of fluorine being produced in thermally pulsing AGB stars. On the other hand, Otsuka et al. (2008)) detected the faint [FIV] $\lambda\lambda$3997, 4060 lines in the extremely metal-poor halo PN BoBn 1. They found a strong enhancement of the F/H ratio and by comparing the abundance pattern of BoBn 1 with carbon-enhanced metal-poor stars abundances, they concluded that the observed behavior could be explained if the nebula evolved from a binary system.

Finally, García-Rojas et al. (2015) reported, for the first time, the detection of faint sodium lines ([NaIV] λ3242 Å and λ3362 Å) in the deep spectrum of NGC 3918. These detections along with the [NaIII] λ7.31 μm by Pottasch et al. (2009) can be used to constrain a grid of photoionization models computed by Delgado-Inglada et al. (2014) to construct, for the first time, an ICF to estimate the total Na abundance (Medina-Amayo et al. in prep.). A similar study can be developed taking advantage of the few detections of potassium and calcium lines in the spectra of PNe.

Acknowledgments. I deeply thank Oli Dors Jr. for inviting me to give this review and for giving me financial support to attend to the workshop. I am indebted to C. Esteban, C. Morisset and G. Stasińska for discussions and a critical reading of this manuscript. I also thank all my collaborators and students for many discussions on the research topics presented in this paper.

References

Bowen I. S., 1927, *Nature*, **120**, 473
Climent J. B., 2016, *M.Sc. thesis*, Universidad de La Laguna
Corradi R. L. M., García-Rojas J., Jones D., et al., 2015, *ApJ*, **803**, 99
Delgado-Inglada G., Mesa-Delgado A., et al., 2016, *MNRAS*, **456**, 3855
Delgado-Inglada G., Morisset C., Stasińska G., 2014, *MNRAS*, **440**, 536
Delgado-Inglada G., Rodríguez M., 2014, *ApJ*, **784**, 173
Delgado-Inglada G., Rodríguez M., Mampaso A., et al., 2009, *ApJ*, **694**, 1335
Dinerstein H. L., 2001, *ApJL*, **550**, L223
Dinerstein H. L., Geballe T. R., 2001, *ApJ*, **562**, 515
Fang X., Liu X.-W., 2011, *MNRAS*, **415**, 181
Fang X., Liu X.-W., 2013, *MNRAS*, **429**, 2791
Fang X., Storey P. J., Liu X.-W., 2011, *A&A*, **530**, A18
Ferland G. J., Henney W. J., O'Dell C. R., et al., 2016, *RevMexAA*, **52**, 261
García-Hernández D. A., Ventura P., et al., 2016, *MNRAS*, **461**, 542
García-Rojas J., Corradi R. L. M., Boffin H. M. J., et al., 2017, X. Liu, L. Stanghellini, and A. Karakas (eds.), *Planetary Nebulae: Multi-Wavelength Probes of Stellar and Galactic Evolution*, Vol. 323 of *IAU Symposium*, pp 65–69
García-Rojas J., Corradi R. L. M., Monteiro H., et al., 2016, *ApJL*, **824**, L27
García-Rojas J., Delgado-Inglada G., García-Hernández D. A., Dell'Agli F., Lugaro M., Karakas A. I., Rodríguez M., 2018, *MNRAS*, **473**, 4476
García-Rojas J., Esteban C., 2007, *ApJ*, **670**, 457
García-Rojas J., Madonna S., Luridiana V., et al., 2015, *MNRAS*, **452**, 2606
García-Rojas J., Peña M., Morisset C., et al., 2012, *A&A*, **538**, A54
García-Rojas J., Peña M., Morisset C., et al., 2013, *A&A*, **558**, A122
García-Rojas J., Peña M., Peimbert A., 2009, *A&A*, **496**, 139
Garnett D. R., Dinerstein H. L., 2001, *ApJ*, **558**, 145
Guerrero M. A., Miranda L. F., 2012, *A&A*, **539**, A47
Henney W. J., Stasińska G., 2010, *ApJ*, **711**, 881
Huggins M. L., 1898, *ApJ*, **8**, 54
Huggins W., Miller W. A., 1864, *Philosophical Transactions of the Royal Society of London Series I*, **154**, 437
Hyung S., Aller L. H., Feibelman W. A., 1994, *ApJS*, **93**, 465
Jones D., Wesson R., García-Rojas J., et al., 2016, *MNRAS*, **455**, 3263
Karakas A. I., Lugaro M., 2016, *ApJ*, **825**, 26
Liu X.-W., 2006, M. J. Barlow and R. H. Méndez (eds.), *Planetary Nebulae in our Galaxy and Beyond*, Vol. 234 of *IAU Symposium*, pp 219–226
Liu X.-W., Barlow M. J., Zhang Y., et al., 2006, *MNRAS*, **368**, 1959
Liu X.-W., Luo S.-G., Barlow M. J., et al., 2001, *MNRAS*, **327**, 141
Liu X.-W., Storey P. J., Barlow M. J., et al., 2000, *MNRAS*, **312**, 585
Liu Y., Liu X.-W., Barlow M. J., Luo S.-G., 2004, *MNRAS*, **353**, 1251
Madonna S., García-Rojas J., Sterling N. C., et al., 2017, *MNRAS*, **471**, 1341
McNabb I. A., Fang X., Liu X.-W., 2016, *MNRAS*, **461**, 2818
McNabb I. A., Fang X., Liu X.-W., et al., 2013, *MNRAS*, **428**, 3443
Mendoza C., Bautista M. A., 2014, *ApJ*, **785**, 91
Mesa-Delgado A., Esteban C., García-Rojas J., et al., 2009, *MNRAS*, **395**, 855
Mesa-Delgado A., Núñez-Díaz M., Esteban C., et al., 2012, *MNRAS*, **426**, 614

Nicholls D. C., Dopita M. A., Sutherland R. S., 2012, *ApJ*, **752**, 148
Otsuka M., Izumiura H., Tajitsu A., Hyung S., 2008, *ApJL*, **682**, L105
Peña M., Ruiz-Escobedo F., Rechy-García J., et al., 2017, X. Liu, L. Stanghellini, and A. Karakas (eds.), *Planetary Nebulae: Multi-Wavelength Probes of Stellar and Galactic Evolution*, Vol. 323 of *IAU Symposium*, pp 60–64
Peimbert M., 1967, *ApJ*, **150**, 825
Peimbert M., Peimbert A., 2006, M. J. Barlow and R. H. Méndez (eds.), *Planetary Nebulae in our Galaxy and Beyond*, Vol. 234 of *IAU Symposium*, pp 227–234
Peimbert M., Peimbert A., Ruiz M. T., Esteban C., 2004, *ApJS*, **150**, 431
Péquignot D., Baluteau J.-P., 1994, *A&A*, **283**, 593
Pottasch S. R., Surendiranath R., Bernard-Salas J., et al., 2009, *A&A*, **502**, 189
Richer M. G., Georgiev L., Arrieta A., Torres-Peimbert S., 2013, *ApJ*, **773**, 133
Sharpee B., Baldwin J. A., Williams R., 2004, *ApJ*, **615**, 323
Sharpee B., Williams R., Baldwin J. A., et al., 2003, *ApJS*, **149**, 157
Sharpee B., Zhang Y., Williams R., et al., 2007, *ApJ*, **659**, 1265
Smith C. L., Zijlstra A. A., Dinerstein H. L., 2014, *MNRAS*, **441**, 3161
Stasińska G., Tenorio-Tagle G., Rodríguez M., et al., 2007, *A&A*, **471**, 193
Sterling N. C., Dinerstein H. L., 2008, *ApJS*, **174**, 158
Sterling N. C., Dinerstein H. L., Kaplan K. F., et al., 2016, *ApJL*, **819**, L9
Sterling N. C., Madonna S., Butler K., et al., 2017, *ApJ*, **840**, 80
Sterling N. C., Porter R. L., Dinerstein H. L., 2015, *ApJS*, **218**, 25
Sterling N. C., Savage B. D., Richter P., et al., 2002, *ApJ*, **567**, 354
Sterling N. C., Witthoeft M. C., 2011, *A&A*, **529**, A147
Storey P. J., Sochi T., 2014, *MNRAS*, **440**, 2581
Torres-Peimbert S., Peimbert M., Daltabuit E., 1980, *ApJ*, **238**, 133
Tsamis Y. G., Barlow M. J., Liu X.-W., et al., 2004, *MNRAS*, **353**, 953
Tsamis Y. G., Walsh J. R., Vílchez J. M., et al., 2011, *MNRAS*, **412**, 1367
Wang W., Liu X.-W., 2007, *MNRAS*, **381**, 669
Wesson R., Jones D., García-Rojas J., et al., 2017, X. Liu, L. Stanghellini, and A. Karakas (eds.), *Planetary Nebulae: Multi-Wavelength Probes of Stellar and Galactic Evolution*, Vol. 323 of *IAU Symposium*, pp 70–73
Wesson R., Liu X.-W., Barlow M. J., 2005, *MNRAS*, **362**, 424
Wyse A. B., 1942, *ApJ*, **95**, 356
Yuan H.-B., Liu X.-W., Péquignot D., et al., 2011, *MNRAS*, **411**, 1035
Zhang Y., Liu X.-W., 2005, *ApJL*, **631**, L61
Zhang Y., Liu X.-W., Luo S.-G., et al., 2005, *A&A*, **442**, 249
Zhang Y., Liu X.-W., Wesson R., et al., 2004, *MNRAS*, **351**, 935
Zhang Y., Yuan H.-B., Hua C.-T., et al., 2009, *ApJ*, **695**, 488

Contributed Talks

Chemical Abundances in Gaseous Nebulae
AAA Workshop Series 10, 2016
G. Hägele, M. Cardaci & E. Pérez-Montero, eds.

Contributed Paper

A quick-start guide to BOND: Bayesian Oxygen and Nitrogen abundance Determinations in HII regions using strong and semistrong lines

N. Vale Asari[1], G. Stasińska[2], C. Morisset[3], and R. Cid Fernandes[1]

[1]*Departamento de Física–CFM, Universidade Federal de Santa Catarina, C.P. 476, 88040-900, Florianópolis, SC, Brazil*
[2]*LUTH, Observatoire de Paris, CNRS, Université Paris Diderot; Place Jules Janssen 92190 Meudon, France*
[3]*Instituto de Astronomía, Universidad Nacional Autónoma de México, Apdo. Postal 70264, México D.F., 04510 México*

Abstract. We present a quick-start guide to BOND, a statistical method to derive oxygen and nitrogen abundances in HII regions. BOND compares a set of carefully selected strong and semistrong emission lines to a grid of photoionization models. The first novelty, in comparison to other statistical methods, is that BOND relies on the [ArIII]/[NeIII] emission line ratio to break the oxygen abundance bimodality. In doing so, we can measure oxygen and nitrogen abundances without assuming any a priori relation between N/O and O/H. The second novelty is that BOND takes into account changes in the hardness of the ionizing radiation field, which can come about due to the aging of HII regions or the stochastically sampling of the IMF. We use the emission line ratio HeI/Hβ, in addition to commonly used strong lines, to constrain the hardness of the ionizing radiation field. Finally, we also stress the pragmatic considerations behind our Bayesian inference.

1. Why a statistical method based on photoionization models

When direct temperature measurements are missing, statistical methods are used to infer abundances in giant HII regions. There are two families of statistical methods. One is based on calibrating samples of objects for which the abundance could be derived from temperature-based methods. The other is based on photoionization model grids. The latter is free from observational biases, but the grid must cover all the configurations that could be found in nature. BOND (Bayesian Oxygen and Nitrogen abundance Determinations) belongs to the second family. BOND infers oxygen and nitrogen abundances using carefully selected strong and semistrong lines by comparing them to a grid of photoionization models. The source code is open and freely available at `http://bond.ufsc.br/`. Full details can be found at Vale Asari et al. (2016). This manuscript is intended to be a quick-start guide to highlight the most important aspects of the method.

2. What sets BOND apart

Common strong line methods based on simple calibrations ([OIII]/[NII], [NII]/Hα, ([OII] + [OIII])/Hβ) assume that emission-line nebulae are a one-parameter family, and that such parameter is the oxygen abundance. The first to realize the importance of introducing a secondary parameter to measure abundances was McGaugh (1991), who considered the effect of the ionization parameter U. Nowadays there is a plethora of methods to measure abundances based on the comparison of observed to theoretical emission lines from a grid of photoionization models (McGaugh, 1991; Kewley & Dopita, 2002; Tremonti et al., 2004; Dopita et al., 2013; Pérez-Montero, 2014; Blanc et al., 2015). We will discuss the difference of our method with respect to others.

One novelty in our grid of photoionization models is that we do not impose any a priori relation between N/O and O/H. The only other method that also does not tie in the nitrogen and oxygen abundances is the one by Pérez-Montero (2014), with the difference that his method uses auroral lines (so it is not a strong line method), and it selects models around the empirical N/O versus O/H relation if auroral lines are not available.

Another novelty in our method is that it uses Bayesian inference to measure abundances, not quite unlike the one by Blanc et al. (2015). The curious reader is referred to Section 4 for the key points; we warn that, although Bayesian inference is part and parcel of our method, it is not the most important aspect of BOND.

The killer features in BOND are: (a) N/O is free to vary, (b) it distinguishes between the lower and upper metallicity branches, and (c) it considers the effect of varying the hardness of the ionizing radiation field. The next section shows how we have tackled (a), (b) and (c), and explains the reasoning behind choosing which emission lines need to be fitted.

3. Input emission lines for BOND

Our grid of photoionization models spans a wide range in O/H, N/O, and U. The ionizing radiation field is provided by the instantaneous starburst models of Mollá et al. (2009) for six different ages. Two nebular geometries are considered (thin shell and filled sphere). We thus have five parameters in our models. Even though we are interested in measuring only two of them, O/H and N/O, we still ought to have good constraints for the other three 'uninteresting' parameters: U, the hardness of the ionizing radiation field, and the density structure. That is why we have chosen a set of emission lines carefully tailored to constrain those five parameters all at once.

In the following we list these emission lines and explain the reason behind each of them. Note that the (reddening-corrected) intensities of *all* of those lines with respect to Hβ are needed to run BOND.

- The strong lines Hβ, [OII]λ3726+λ3729, [OIII]λ5007, and [NII]λ6584. They were chosen because, to first order, the strong line ratios ([OIII]+[OII])/Hβ, [NII]/[OII], and [OIII]/[OII] map into O/H, N/O and U, respectively. We fit line intensities with respect to Hβ, and not the latter strong line ratios

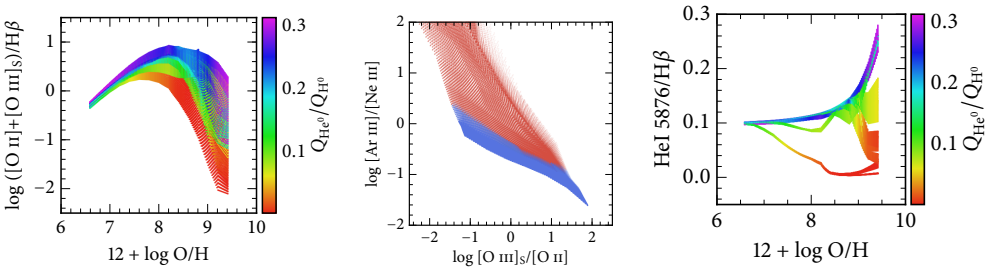

Figure 1. **Left:** ([OIII]$_S$ + [OII])/Hβ versus O/H colored by $Q(He^0)/Q(H^0)$, which traces the hardness of the ionizing radiation field. This represents the two secondary effects considered in BOND. First, for a given $Q(He^0)/Q(H^0)$, ([OIII]$_S$ + [OII])/Hβ maps into two different O/H values. We find the correct metallicity branch by using the [ArIII]/[NeIII] ratio (centre). Second, for high metallicities ([OIII]$_S$+[OII])/Hβ span almost a decade in O/H. We use HeIλ5876/Hβ (right) to find the correct hardness of the ionizing radiation field. **Centre:** [ArIII]/[NeIII] versus [OIII]/[OII], blue for models in the lower metallicity and red for models in the upper metallicity branch. **Right:** HeIλ5876/Hβ versus O/H colored by $Q(He^0)/Q(H^0)$. HeIλ5876/Hβ can be used as a proxy for $Q(He^0)/Q(H^0)$, except for the highest values of $Q(He^0)/Q(H^0)$. All figures are based on our grid of photoionization models and taken from Vale Asari et al. (2016).

directly, because we assume that the intensities with respect to Hβ follow a Gaussian distribution when we calculate likelihood probabilities.

- The semistrong lines [ArIII]λ7135 and [NeIII]λ3869 (plus upper limits for auroral lines of $O^{++}$and N^{+}). The ratio ([OIII]+[OII])/Hβ is bi-valued with respect to the oxygen abundance (see the inverted U shape of the relation in Fig. 1, left). That is why some methods impose a fixed relation between N/O versus O/H in their photoionization models (e.g. Dopita et al., 2013; Blanc et al., 2015). Since we are interested in inferring both N/O and O/H, we did not want to use nitrogen lines to break the bimodality in the oxygen abundance. Restricting our search to emission lines easy to measure in typical optical spectra (though not always reported in the literature), we found an ideal candidate in the emission line ratio [ArIII]/[NeIII]. $Ar^{++}$and $Ne^{++}$are formed in roughly the same zone, but the excitation potentials of [ArIII] and [NeIII] are very different (1.7 and 3.2 eV, respectively), so the ratio of these lines is sensitive to the electronic temperature. Argon and neon are primary elements and their global abundance ratio is expected to be constant. Besides, they are both inert, thus do not suffer dust depletion, so their abundance ratio in the ionized gas phase remains constant. Fig. 1 (centre) shows the line ratio [ArIII]/[NeIII] in our grid as a function of [OIII]/[OII] (the latter traces the ionization parameter U). The points are color-coded as falling in the lower or upper metallicity branch (blue and red, respectively), showing that [ArIII]/[NeIII] can break the bimodality

in the oxygen abundance. An extra help on finding the right metallicity branch can come from *upper limits* in auroral lines.

- The semistrong line HeIλ5876. This is the crucial part of BOND. Since we consider different ionization scenarios, e.g. different spectral energy distributions (SED) of the ionizing radiation, we need to infer which of those scenarios is more appropriate. We expect the SED to be different in different HII regions due to aging (so the most massive stars have disappeared) or due to stochastic effects in low luminosity HII regions when the upper part in the stellar initial mass function of the ionizing cluster is not fully sampled. Fig. 1 (left) shows how the emissivity of ([OIII] + [OII])/Hβ depends not only on the oxygen abundance (abscissa), but also on the hardness of the ionizing radiation field (color code). Note that at high metallicities a single value of ([OIII] + [OII])/Hβ can span 1 dex in oxygen abundance for different ionizing radiation fields. Fig. 1 (right) shows that the HeIλ5876/Hβ line can be used as a proxy of the hardness of the ionizing radiation field.

4. Why go Bayesian

First, let us emphasize that the Bayesian inference is *not* what sets BOND apart. The heart and soul of BOND is the set of carefully selected emission line ratios, tailor-made both to infer the oxygen and nitrogen abundances in HII regions, and to take into account important secondary parameters. As reasoned in the previous section, this allows us to (a) break the bimodality in oxygen abundance without any a priori relation between N/O versus O/H, and (b) consider the (previously neglected) role of the ionizing radiation field in abundance determinations.

That said, we have opted for Bayesian inference for good reasons. Before diving into the most important Bayesian aspects, let us examine the method's acronym. BOND stands for Bayesian Oxygen and Nitrogen abundance Determinations. Our method is not called Oxygen and Nitrogen abundance, Ionization parameter, and Hardness of the ionizing radiation field Determinations (ONIHD). The reason why the letters IH are not in the method's name is the same reason why we have decided to introduce the B for Bayesian in its name: the Ionization parameter and Hardness of the ionizing radiation field are *nuisance* parameters, and the only way to get rid of them respecting dimensional analysis is by going Bayesian.

Let us lay out the problem to see how its resolution points to Bayesian inference. We start with a carefully designed photoionization grid, finely spaced and spanning a wide range in O/H, N/O, and U. It also considers a few values of hardness of the ionizing radiation field mimicked by different SED ages. Even though the latter two parameters (U and ionizing radiation field) are important and need to be well modelled, they are of *secondary* interest. This is why our acronym shifts from ONIHD to OND.

How do we get rid of parameters for which we do not care (a.k.a. *nuisance* parameters)? If we want to consider the probabilities of all models in our grid at the same time, then we can simply *marginalize* over the nuisance parameters. Marginalizing is nothing more than integrating over a parameter. For instance,

for a fixed O/H and N/O, we marginalize over U simply by adding up all the probabilities of all models of a given O/H and N/O for all U. The trick is that to integrate, say, in dU, the probability density function (PDF) in the integrand must have physical units of U^{-1}. Ordinary likelihood PDFs (e.g. $e^{-0.5\chi^2}$ for Gaussian distributions[1]) have units which are the inverse of the observational data being fitted. So, from a *pragmatic* point of view, we are obliged to write out the posterior PDFs, which have the correct physical units when we integrate over a model parameter. For a thorough argument on the dimensional analysis of PDFs, see Hogg (2012), especially the discussion around his equation 3.

In other words, going Bayesian gives us license to kill the nuisance parameters, so we need to add B to OND. To write the posterior PDFs, we need to spell out our priors. This has a two-fold benefit. First, we can plug in an informative prior: if we have empirical evidence that some models are more probable in nature than others, we can give them more weight by setting the prior probabilities just right. In our code so far, we have taken the most conservative approach we can and, following Blanc et al. (2015), we use an uninformative prior (specifically, a Jeffrey's prior that is logarithmic in O/H, N/O and U).

The second benefit of setting a prior is that we have an explicit prescription for making a finer grid. The problem of comparing data to a uniformly spaced grid of models by using a χ^2 likelihood is that most models will be very distant from the observed data as measured by the uncertainties σ_j. If a grid is very very rough, the closest model might even be a few σ_j away from the model with the highest likelihood. An ad hoc prescription to deal with this problem is by setting up cooking factors to increase the observed uncertainties, thus decreasing the distances between observed and computed emission lines. A cooking factor has no real justification and needs to be tailored to work for each new data point. Since we are using a Bayesian prescription, we can do much better than relying on ad hoc prescriptions. We simply interpolate our grid where we need—and interpolation in log N/O, O/H and U is reasonable once the grid is fine enough. The interpolation is informed by posterior probability of each element in the grid: if an element has a high probability, it is worth creating more grid points inside its volume[2].

Just a final note on the Bayesian parlance. The outcome of a Bayesian inference is the posterior PDF for a set of model parameters (say, O/H, N/O, U, hardness of the ionizing radiation field). Since we are interested only in O/H and N/O, we can integrate out all other parameters and obtain the *joint* O/H and N/O posterior PDF. The joint PDF is simply a two-dimensional function that gives the probability of each point in the O/H versus N/O plane, which is the ultimate goal of BOND.

---

[1] $\chi^2 = \sum_j (c_j - o_j)^2/\sigma_j^2$, where o_j and σ_j are the observed line intensity and its uncertainty, and c_j is the computed line intensity.

[2] The algorithm to do importance sampling in BOND is the octree sampling, which is computationally inexpensive. The reader might be more familiar with MCMC samplers, which are more adequate when one has to compute models on the fly and does not have a pre-defined grid. In our case, it is much more sensible to compute many photoionization models a priori and interpolate them on the fly than generating photoionization models on the fly.

However, sometimes it is unpractical to work with the full joint PDF, so we need a summarized description in the form $12 + \log \mathrm{O/H} = 8.35 \pm 0.02$. There are many ways to transform a two-dimensional function into a nominal value and a dispersion. One way is to set the nominal value for N/O and O/H to be the point where the joint PDF is the highest. We call this number the maximum a posteriori (MAP), because it is calculated after (i.e. a posteriori) the marginalization of nuisance parameters. For the dispersion, we can define ellipses of credible regions that encompass, say, 5, 50, 68 or 95% of the total joint PDF.
If we want to marginalize away either O/H or N/O (i.e. if we are interested in one of those parameters alone), we can integrate over the other parameter. Summarizing the fully marginalized PDF also opens up a menu of choices. The nominal value can be taken as the mean, median or mode (that is, its peak) of the PDF. For the dispersion, the usual choices are either the 50, 68, or 95 percent equal-tailed or highest density intervals. Note that the equal-tailed intervals are related to the median. The median is the point in the PDF curve where 50 percent of the probability is to the left and 50 to the right. The equal-tailed 68% interval is the region of a curve where 16 percent of the probability is to the right and 16 percent to the left. The highest density intervals, on the other hand, are related to the mode. The mode is the point in the curve of highest probability. The 68% highest density interval is the region around the mode that adds up to 68 percent of the total probability. A nice visualization tool for those descriptions can be found at `http://www.sumsar.net/blog/2014/10/probable-points-and-credible-intervals-part-one/`.
Another minor nuisance parameter we marginalize away are the uncertainties. For [ArIII]/Hβ, [NeIII]/Hβ and HeI/Hβ, we consider an extra noise source added in quadrature to the observational uncertainties which we allow to vary from 2 to 100 percent of the line intensity. The extra noise source is needed because, in nature, the Ar/O and Ne/O ratios may differ somewhat from the ones assumed in our model grid. Regarding HeI/Hβ, the problem is that our grid is only coarsely meshed as regards the hardness of the ionizing radiation field. We then calculate the marginalized likelihood PDF for those lines by using all values of this extra noise and then marginalizing it away. We do so because we do not expect those lines to be completely correct in our photoionization models, and they are used only to infer secondary parameters.

5. Conclusions

We have highlighted the main characteristics of BOND, a method based on a grid of photoionization models to measure oxygen and nitrogen abundances in giant HII regions using strong and semistrong lines. We show why it is important to consider secondary parameters in abundance determinations, especially the hardness of the ionizing radiation field. The SEDs in HII regions can vary from region to region due to stellar aging or to the stochastically sampling of the IMF. We also show how one can break the metallicity bimodality without recourse either to auroral lines or a fixed relation between N/O and O/H. We use a selective set of emission lines to infer all those parameters. Finally, we argue why using Bayesian inference is the correct way (motivated by the dimensional

analysis of probability density functions) to treat the secondary parameters in abundance determinations.

Acknowledgments. NVA is grateful to Oli Dors for having organized such a useful workshop. NVA acknowledges the support from Programa de Pós-Graduação em Física da UFSC and CAPES/PROAP to attend the workshop. GS and NVA acknowledge the support from the CAPES CsF–PVE project 88881.068116/2014-01. The grid of models has been run on computers from the CONACyT/CB2010:153985, UNAM-PAPIIT-IN107215 and UNAM Posgrado de Astrofísica projects.

References

Blanc G. A., Kewley L., Vogt F. P. A., Dopita M. A., 2015, *ApJ*, **798**, 99
Dopita M. A., Sutherland R. S., Nicholls D. C., Kewley L. J., Vogt F. P. A., 2013, *ApJS*, **208**, 10
Hogg D. W., 2012, *ArXiv e-prints 1205.4446*
Kewley L. J., Dopita M. A., 2002, *ApJS*, **142**, 35
McGaugh S. S., 1991, *ApJ*, **380**, 140
Mollá M., García-Vargas M. L., Bressan A., 2009, *MNRAS*, **398**, 451
Pérez-Montero E., 2014, *MNRAS*, **441**, 2663
Tremonti C. A., Heckman T. M., Kauffmann G., et al., 2004, *ApJ*, **613**, 898
Vale Asari N., Stasińska G., Morisset C., Cid Fernandez R., 2016, *MNRAS*, **460**, 1739

Chemical Abundances in Gaseous Nebulae
AAA Workshop Series 10, 2016
G. Hägele, M. Cardaci & E. Pérez-Montero, eds.

Contributed Paper

Spatial distribution of carbon and oxygen abundances in the Magellanic Clouds

L. Toribio San Cipriano[1,2], C. Esteban[1,2], G. Domínguez-Guzmán[3] and J. García-Rojas[1,2]

[1]*Instituto de Astrofísica de Canarias, E-38200, La Laguna, Tenerife, Spain*
[2]*Departamento de Astrofísica, Universidad de La Laguna, E-38206, La Laguna, Tenerife, Spain*
[3]*Instituto Nacional de Astrofísica, Óptica y Electrónica, Apartado Postal 51 y 216, Puebla, Mexico*

Abstract.
We present chemical abundances of carbon and oxygen in the Large and Small Magellanic Clouds from optical spectra of HII regions. We analyze the behavior of the O/H, C/H and C/O abundances ratios and their spatial distribution inside the galaxies. The results show that the radial gradients can be considered flat for all these elements in both galaxies. In addition, we compare our results with those of other more massive spiral galaxies. We find a correlation between the absolute magnitude, M_V, of the galaxies and the slopes of C/H and C/O gradients. The more massive galaxies show steeper C/H and C/O gradients than the less massive ones.

1. Introduction

A proper knowledge of the spatial distribution of chemical abundances in galaxies is crucial for building up chemical evolution models. In particular, HII regions are used as the best tracers of the current composition of the extragalactic interstellar medium since they can be observed at large distances. After hydrogen and helium, oxygen (O) and carbon (C) are the third and fourth most abundant elements in the Universe, respectively. O abundance of HII regions is the most used proxy of the metallicity of galaxies. Despite the importance of C as a source of opacity in stars and its fundamental role in interstellar dust and organic molecules, C abundance in extragalactic HII regions has been poorly explored. Garnett et al. (1995, 1999) derived C abundances in several extragalactic HII regions of nearby spiral galaxies using the CIII] 1909 Å and CII] 2326 Å collisionally excited lines (hereinafter CELs). Recently, Berg et al. (2016) reported C abundances from UV CELs for 12 HII regions in nearby dwarf galaxies. However, abundances computed from UV CELs have the disadvantage that they are strongly affected by the uncertainty in the choice of UV reddening function. Alternatively, there is another method to derive C abundances in HII regions. Thanks to the arrival of large aperture telescopes and to the more efficient CCDs,

especially in the blue range, reliable measurements of the faint CII 4267 Å recombination line (hereinafter RL) have been achieved. In the last years, several authors (e.g. Peimbert et al., 2005; Esteban et al., 2002, 2009, 2014; López-Sánchez et al., 2007; Toribio San Cipriano et al., 2016) have determined C abundances in Galactic and extragalactic HII regions based on this method.
In this work we present C abundances derived from RLs and O ones from RLs and CELs in the Large Magellanic Cloud (LMC) and the Small Magellanic Cloud (SMC) from deep, high-quality optical spectra of HII regions. We explore the distribution of O/H, C/H and C/O ratios and discuss the results in the framework of the chemical evolution of galaxies.

2. Sample

We used a sample of five HII regions in the LMC and four HII regions in the SMC. Seven of these objects were observed at Cerro Paranal Observatory (Chile) with the Ultraviolet Visual Echelle Spectrograph (UVES) mounted at the Kueyen unit of the 8.2-m Very Large Telescope (VLT). The data of the other two HII regions (one in the LMC and other in the SMC) were taken from Peimbert (2003) and Peña-Guerrero et al. (2012). In order to have an homogeneous data set, in these two cases, we took the measured line fluxes and performed the analysis in the same way than the rest of the sample. The description and analysis of this data set can be found in Domínguez-Guzmán et al. (this proceedings).
We measured the faint CII 4267 Å RL and all or most of the lines of multiplet 1 of the OII RLs at about 4650 Å in all the objects of the sample, allowing the computation of C^{2+} and O^{2+} abundances. In addition, we derived O^{2+} from CELs as well as the total abundances of C and O (from CELs and RLs). The physical conditions used for the determination of the abundances were defined assuming a two-zone scheme. The low-ionization zone, characterized by the electron temperature T_e([NII]) and the weighted mean of the electron density n_e([SII]) and n_e([OII]), was used to calculate the O^+ abundance. The high-ionization zone, characterized by T_e([OIII]) and n_e([ClIII]), was used to derive the C^{2+} and O^{2+} abundances. In order to correct for the unseen ionization stages of the C, we used the ICF by Garnett et al. (1999). In addition, for one of the HII regions which has HeII lines in the spectrum, we corrected the O^{3+} contribution adopting the ICF by Delgado-Inglada et al. (2014).

3. Results

We studied the spatial distribution of O and C abundances in order to explore the presence of radial abundance gradients in the Magellanic Clouds (MCs). We performed least-squares linear fits to the fractional galactocentric distance of the objects, (R/R_{25})[1], for both galaxies. In the case of radial O abundance gradients, we have two different fits whether O^{2+}/H^+ was determined from RLs or CELs.

[1]Defined as the radius where the B-band surface brightness is 25 mag arcsec^{-2}.

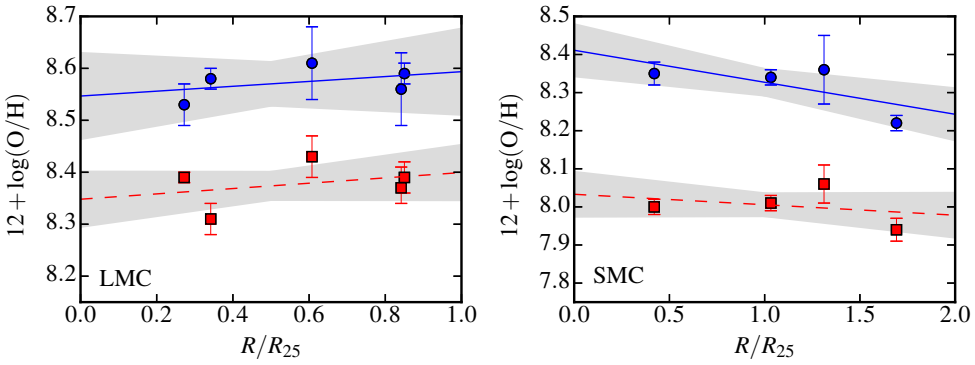

Figure 1. Spatial distribution of the O abundances (blue circles from RLs and red squares from CELs) as a function of R/R_{25} for the LMC (left-hand panel) and the SMC (right-hand panel). The grey areas trace all the radial gradients compatible with the uncertainties of our least-squares linear fits computed through Monte Carlo simulations.

For the LMC:

$$12 + \log(\mathrm{O/H})_{\mathrm{RLs}} = 8.55(\pm0.04) + 0.04(\pm0.07)R/R_{25}, \quad (1)$$

$$12 + \log(\mathrm{O/H})_{\mathrm{CELs}} = 8.35(\pm0.03) + 0.05(\pm0.05)R/R_{25}, \quad (2)$$

and for the SMC:

$$12 + \log(\mathrm{O/H})_{\mathrm{RLs}} = 8.41(\pm0.04) - 0.09(\pm0.04)R/R_{25}, \quad (3)$$

$$12 + \log(\mathrm{O/H})_{\mathrm{CELs}} = 8.03(\pm0.03) - 0.03(\pm0.03)R/R_{25}. \quad (4)$$

Fig. 1 represents the spatial distribution of the O abundances as a function of R/R_{25} and the linear fits for the LMC (left-hand panel) and the SMC (right-hand panel). The blue circles represent the abundances determined from RLs and the red squares those from CELs. The grey areas trace all the radial gradients compatible with the uncertainties of our least-squares linear fits computed through Monte Carlo simulations. The offset between both determinations of O/H ratios (CELs and RLs) for the same object represents the effect known as *abundance discrepancy*. It refers to the difference between the chemical abundances determined from RLs and from CELs of the same ion (see Esteban et al., this proceedings). If we consider the slope of the gradients represented in Fig. 1 and defined in equations 1 and 2 for the LMC and 3 and 4 for the SMC, we can conclude that for both galaxies the slopes from CELs and RLs agree within the errors. In previous works for other galaxies, Esteban et al. (2005, 2009) and Toribio San Cipriano et al. (2016) also reported similar slopes of the O/H gradients independently of the kinds of lines used to derive the abundances. The O/H gradients obtained can be considered rather flat in both galaxies, taking into account the uncertainties computed for the slopes.

Fig. 2 represents the spatial distribution of the C/H (upper panels) and C/O (lower panels) ratios as a function of R/R_{25} for both galaxies (LMC left-hand

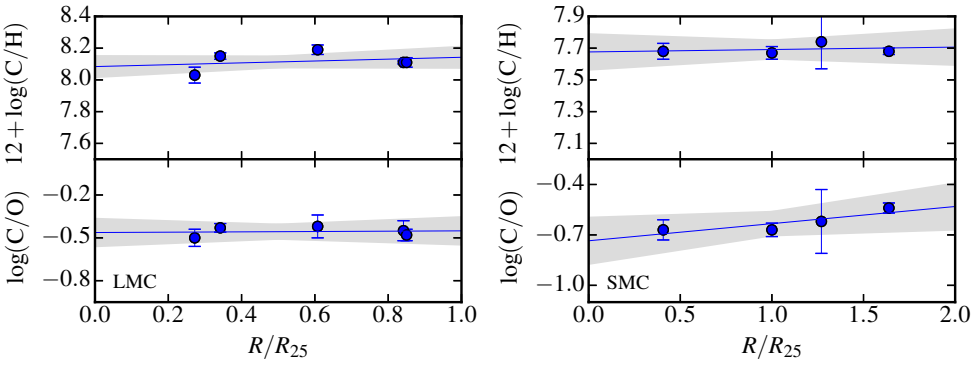

Figure 2. Spatial distribution of the C/H (upper panels) and C/O (lower panels) abundances as a function of the fractional galactocentric distance, R/R_{25}, for the LMC (left-hand panel) and the SMC (right-hand panel). The grey areas trace all the radial gradients compatible with the uncertainties of our least-squares linear fits computed through Monte Carlo simulations.

panel and the SMC right-hand panel). The least-squares linear fits for the LMC are:

$$12 + \log(\mathrm{C/H}) = 8.08(\pm 0.05) + 0.06(\pm 0.07) R/R_{25}, \quad (5)$$

$$\log(\mathrm{C/O}) = -0.46(\pm 0.06) + 0.01(\pm 0.10) R/R_{25}, \quad (6)$$

and for the SMC:

$$12 + \log(\mathrm{C/H}) = 7.68(\pm 0.06) + 0.01(\pm 0.06) R/R_{25}, \quad (7)$$

$$\log(\mathrm{C/O}) = -0.73(\pm 0.07) + 0.09(\pm 0.07) R/R_{25}. \quad (8)$$

We can conclude that the slope of C/H and C/O in both galaxies can be considered practically flat, in contrast with the results we have found in spiral galaxies where the gradients are negative.

Other authors also reported flat radial gradients in the MCs. Pagel et al. (1978) studied the spatial distribution of O abundance in HII regions of both galaxies finding small or flat gradients. Cioni (2009) reported a smooth gradient of the Fe/H ratio in the LMC and a negligible one in the SMC from asymptotic giant branch (AGB) stars. Recently, Choudhury et al. (2016) found a similar slope than ours from a study of red giant branch (RGB) stars in the LMC.

Fig. 3 represents the slope of O/H (violet dashed line/symbols), C/H (red continuous line/symbols) and C/O (cyan dotted line/symbols) radial gradients with respect to the absolute magnitude, M_V, for several galaxies. This figure reinforces the results obtained by Toribio San Cipriano et al. (2016) where the authors found that the slopes of C/H and C/O gradients show a correlation with M_V of the galaxies. The more luminous galaxies as M 31 or M 101 show systematically steeper C/H and C/O gradients than the less luminous ones (e.g. NGC 300 or MCs). According with the results of Fig. 3, the mechanism of C enrichment would be more effective in the more massive galaxies than in the

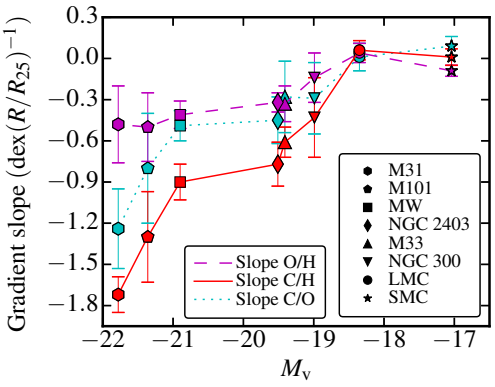

Figure 3. Slope of the O/H (violet dashed line/symbols), C/H (red continuous line/symbols), and C/O (cyan dotted line/symbols) radial gradients versus absolute magnitude, M_V of several spiral galaxies. Figure taken from Toribio San Cipriano et al. (2017).

less massive ones. A deeper analysis of this figure is presented in Toribio San Cipriano et al. (2017).

4. Conclusions

We present the spatial distribution of O/H, C/H and C/O ratios in the Magellanic Clouds through a study of the CII and OII recombination lines in HII regions. We find that radial gradients are practically flat within the uncertainties in both galaxies. Other authors also report flat gradients in the MCs from RGB and AGB stars. We compare our results with those in other galaxies finding that the gradients seem to follow the trend described by Toribio San Cipriano et al. (2016) where the more massive galaxies show steeper C/H and C/O gradients than the less luminous galaxies.

Acknowledgments. This work is based on observations collected at the European Southern Observatory, Chile, proposal numbers ESO 092.C-0191(A) and ESO 60.A-9022(A). LTSC is supported by the FPI Program by the Ministerio de Economía y Competitividad (MINECO) under grant AYA201122614. This project is also partially funded by MINECO under grant AYA2015-65205-P.

References

Berg D. A., Skillman E. D., Henry R. B. C., et al., 2016, *ApJ*, **827**, 126
Choudhury S., Subramaniam A., Cole A. A., 2016, *MNRAS*, **455**, 1855
Cioni M.-R. L., 2009, *A&A*, **506**, 1137
Delgado-Inglada G., Morisset C., Stasińska G., 2014, *MNRAS*, **440**, 536
Esteban C., Bresolin F., Peimbert M., et al., 2009, *ApJ*, **700**, 654
Esteban C., García-Rojas J., Carigi L., et al., 2014, *MNRAS*, **443**, 624
Esteban C., García-Rojas J., Peimbert M., et al., 2005, *ApJL*, **618**, L95

Esteban C., Peimbert M., Torres-Peimbert S., et al., 2002, *ApJ*, **581**, 241
Garnett D. R., Shields G. A., Peimbert M., et al., 1999, *ApJ*, **513**, 168
Garnett D. R., Skillman E. D., Dufour R. J., et al., 1995, *ApJ*, **443**, 64
López-Sánchez A. R., Esteban C., García-Rojas J., et al., 2007, *ApJ*, **656**, 168
Pagel B. E. J., Edmunds M. G., Fosbury R. A. E., Webster B. L., 1978, *MNRAS*, **184**, 569
Peña-Guerrero M. A., Peimbert A., Peimbert M., 2012, *ApJL*, **756**, L14
Peimbert A., 2003, *ApJ*, **584**, 735
Peimbert A., Peimbert M., Ruiz M. T., 2005, *ApJ*, **634**, 1056
Toribio San Cipriano L., Domínguez-Guzmán G., Esteban C., et al., 2017, *MNRAS*, **467**, 3759
Toribio San Cipriano L., García-Rojas J., Esteban C., Bresolin F., Peimbert M., 2016, *MNRAS*, **458**, 1866

Chemical Abundances in Gaseous Nebulae
AAA Workshop Series 10, 2016
G. Hägele, M. Cardaci & E. Pérez-Montero, eds.

Contributed Paper

The systematic uncertainties introduced by atomic data in nebular abundance determinations

L. Juan de Dios[1] and M. Rodríguez[1]

[1]*Instituto Nacional de Astrofísica, Óptica y Electrónica (INAOE), Apdo. Postal 51 y 216, Puebla, Mexico.*
email: leticiajd@inaoep.mx, mrodri@inaoep.mx

Abstract. The calculations of chemical abundances in photoionized nebulae are affected by systematic uncertainties, such as those due to atomic data, whose effects have not been much explored. In this work we present estimates of these uncertainties obtained by calculating the physical conditions and the abundances of different elements using a sample of atomic datasets, and all their possible combinations, for a group of 36 Galactic planetary nebulae and 8 HII regions. We find that the choice of atomic data can introduce differences higher than 0.8 dex in density, 0.25 dex in temperature, and 0.7 dex in some ionic abundances at densities above 10^4 cm^{-3}. The differences in O/H are around 0.1–0.2 dex for low-density nebulae, but are higher than 0.4 dex for objects with $n_e \geq 10^4$ cm^{-3} and low degree of ionization. Other elements show similar or higher differences. We discuss ways to constrain and minimize these uncertainties.

1. Introduction

The study of the chemical abundances in planetary nebulae (PNe) and HII regions provides information on the current composition of the interstellar medium and on how it has been enriched in heavy elements in the past. This helps us to understand the chemical evolution of galaxies. The derived chemical abundances depend, among other things, on the values selected for the transition probabilities and collision strengths for transitions involving the lower energy levels of several ions. Important differences are found among the existing determinations of these atomic data, and the uncertainties are rarely reported because they are very difficult to estimate (Aggarwal & Keenan, 2013). For these reasons, atomic data selection is one important source of systematic uncertainty. Accurately quantifying the uncertainties introduced by atomic data is difficult because a single set of atomic data can affect all the calculations, and different combinations of atomic data will affect the results in complex ways. For example, the atomic data used to derive physical conditions will affect all determinations of chemical abundances. We explore these uncertainties by calculating the impact of different combinations of atomic data in the derived electron densities, n_e, electron temperatures, T_e, and ionic and total abundances.

2. Analysis

We explore the effect that atomic data have in the computations of physical conditions and chemical composition in nebular objects by selecting from the literature a sample of 36 PNe and 8 HII regions with optical spectra that are deep enough to allow the measurement of a large number of emission lines, which can be used to determine the physical conditions using different diagnostics and the chemical abundances of several elements. The objects in the sample cover a wide range in characteristics, such as excitation degree and electron density, and therefore can be considered representative of the population of ionized nebulae.

We use the atomic database available in the software for nebular analysis PYNEB (Luridiana et al., 2015), for the ions O^+, O^{++}, N^+, Cl^{++}, Ar^{++}, Ar^{+3}, Ne^{++}, S^+, and S^{++} (52 atomic datasets in total), and assume that the statistical dispersion among the different determinations of atomic data reflect their uncertainties. For each object we obtain the distributions of results for the values of T_e[NII], T_e[OIII], n_e[SII], n_e[OII], n_e[ClIII], n_e[ArIV], and the ionic and total abundances of O, N, Cl, Ar, Ne and S, implied by the different combinations of atomic data. We calculate the average density obtained from the four density diagnostics, and use T_e[NII] to determine the abundances of the single ionized ions, with the exception of He^+, and T_e[OIII] for the remaining ions. The total abundances of O, Cl, S, Ar, and Ne are obtained using the ionization correction factors (ICFs) proposed by Delgado-Inglada et al. (2014). For N we use the traditional ICF, $N/O = N^+/O^+$.

3. Results

We measure the total widths of the final distributions for the different parameters, which give an indication of the uncertainties introduced by atomic data, and plot them as a function of the median of the average density. Fig. 1 shows the results obtained for the average density, T_e[NII], and T_e[OIII]. The dark symbols in this figure show the results implied by all the available 52 datasets. The uncertainties in the average density are higher than a factor of 4 at $n_e \geq 10^4 cm^{-3}$. Atomic data selection is critical for the ions used to derive electron density, since significant differences are obtained by using one or other atomic dataset. Ultimately, these differences propagate in the calculations of electron temperature and ionic abundances, having a significant impact in the final results. The uncertainties in both T_e[NII] and T_e[OIII] are below 0.05 dex at $n_e \geq 10^4$ cm^{-3}, but reach a factor of 2 for T_e[NII] at higher densities due to the stronger dependence of this diagnostic with density.

The spreads in the ionic abundances reach factors higher than 30 at $n_e \geq 10^4$ cm^{-3} as a result of three causes. The first and main cause is the uncertainty or spread in density, which increases at higher densities. This spread affects mainly those ionic abundances based on lines whose upper levels have low critical densities, like O^+, N^+, S^+, since their emissivities are very sensitive to changes in density. The second cause is the spread in temperature, introduced by the spread in density, which is more important for T_e[NII] and hence affects mostly those ionic abundances where this temperature is used for the calculations. The spreads

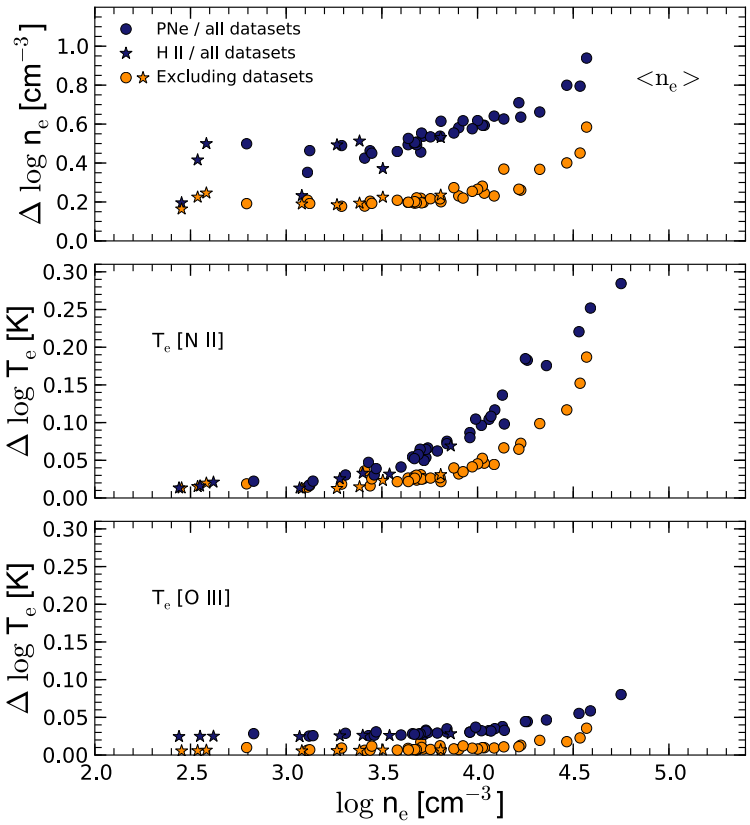

Figure 1. Total widths of the average density, $T_{\rm e}$[NII] and $T_{\rm e}$[OIII] plotted as a function of the median of the average density for all the objects in the sample. The dark symbols show the results implied by all the available datasets; the orange symbols show the results when we exclude the 4 datasets that lead to discordant values of density or temperature. Figures taken from Juan de Dios & Rodríguez (2017).

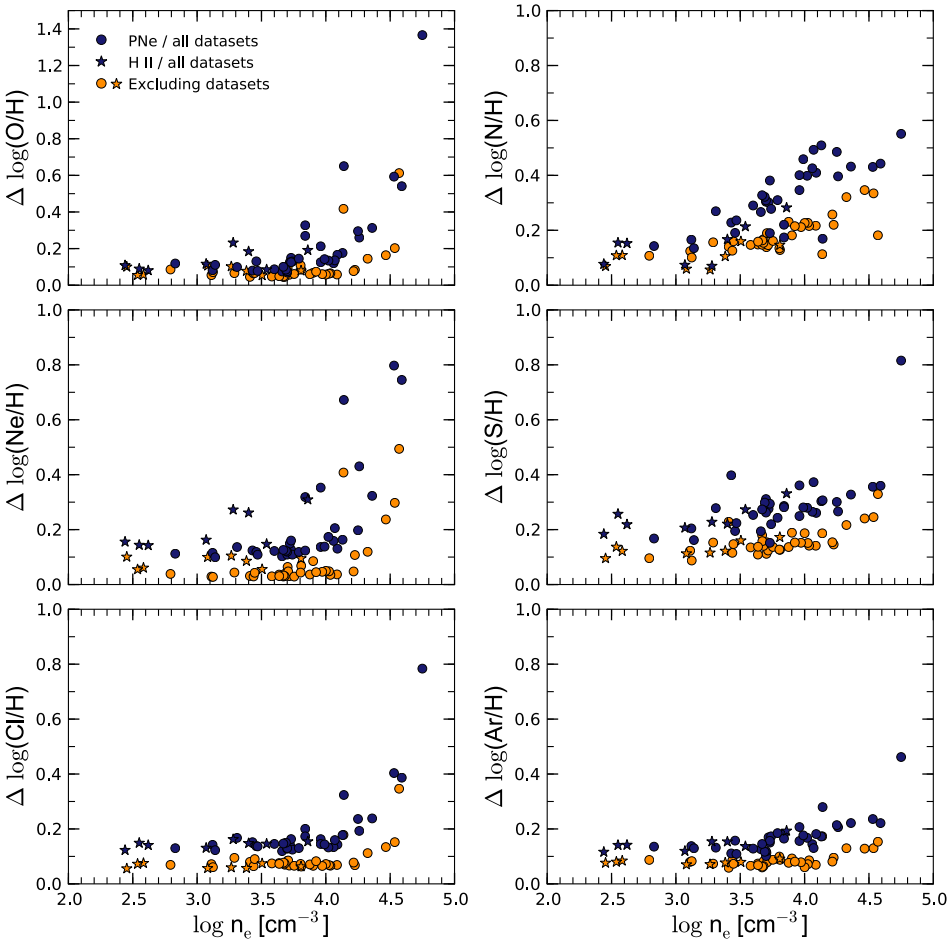

Figure 2. Total widths of the elemental abundances plotted as a function of the median of the average density for all the objects in the sample. The dark symbols show the results implied by all the available datasets; the orange symbols show the results when we exclude the 4 datasets that lead to discordant values of density or temperature. Figures taken from Juan de Dios & Rodríguez (2017).

in ionic abundances introduced by T_e[OIII] for the other ions are smaller and due to changes in all the atomic data for O^{++}. The third cause of the spreads in the ionic abundances is the uncertainties arising from the use of different atomic data for each ion. The spreads in total abundances are ~ 0.2 dex at low densities, but increase to factors of 4–6 or higher at $n_e \geq 10^4$ cm^{-3}, as can be seen in Fig. 2. For O/H we obtain variations of a factor of 2 at $n_e \sim 10^4$ cm^{-3}, that increase to factors of 6–25 at the highest densities.

We have identified four datasets that lead to discordant values of density or temperature: the transition probabilities of Tayal & Zatsarinny (2010) for S^+ and Wiese et al. (1996) for O^+, and the collision strengths of Palay et al. (2012) for O^{++} and Mendoza (1983) for Ar^{+3}. The atomic data of Tayal & Zatsarinny (2010) fail to reproduce some of the observed values of the $\lambda6717/\lambda6731$ intensity ratio. In the case of n_e[OIII], the transition probabilities of Wiese et al. (1996) lead to densities that are generally lower than those implied by the other diagnostics. A similar effect is observed in n_e[ArIV] when using the collision strengths of Mendoza (1983), because the densities obtained are generally much higher than those implied by the other diagnostics. PNe and HII regions might have density inhomogeneities, but we think that the density jumps implied by these atomic datasets are too large to be real. For T_e[OIII], the collision strengths of Palay et al. (2012) lead to systematically lower temperatures in all the objects, and their validity has been questioned by Storey et al. (2014) We have repeated our calculations excluding these four datasets and measured the total widths of the new distributions. By excluding these atomic data the differences are significantly reduced, as can be seen in Figs. 1 and 2, where the orange symbols show the total widths obtained for each parameter.

4. Conclusions

We conclude that the effect of atomic data cannot be disregarded because it can produce great variations in the determinations of physical conditions and chemical abundances, especially in high-density objects. We have identified the atomic data that introduce most of the uncertainty: the transitions probabilities of the ions used to determine density (S^+, O^+, Cl^{++}, and Ar^{+3}) and the collision strengths of Ar^{+3}. Improved calculations of these data will be needed in order to derive more reliable values for the chemical abundances of high-density nebulae. The uncertainties are small for low density objects but can reach factors larger than 6 for high density PNe. The rejection of 4 of the 52 datasets reduces these uncertainties, but high density objects still reach uncertainty factors of 4 for their values of O/H. The complete analysis will be presented in Juan de Dios & Rodríguez (in prep.).

Acknowledgments. We acknowledge support from Mexican CONACYT grant CB-2014-240562. LJdD acknowledges support from CONACYT grant 298356.

References

Aggarwal K., Keenan F., 2013, *ArXiv e-prints 1301.3002*

Delgado-Inglada G., Morisset C., Stasińska G., 2014, *MNRAS*, **440**, 536
Juan de Dios L., Rodríguez M., 2017, *MNRAS*, **469**, 1036
Luridiana V., Morisset C., Shaw R. A., 2015, *A&A*, **573**, A42
Mendoza C., 1983, D. R. Flower (ed.), *Planetary Nebulae*, Vol. 103 of *IAU Symposium*, pp 143–172
Palay E., Nahar S. N., Pradhan A. K., Eissner W., 2012, *MNRAS*, **423**, L35
Storey P. J., Sochi T., Badnell N. R., 2014, *MNRAS*, **441**, 3028
Tayal S. S., Zatsarinny O., 2010, *ApJS*, **188**, 32
Wiese W. L., Fuhr J. R., Deters T. M., 1996, *Atomic transition probabilities of carbon, nitrogen, and oxygen. Journal of Physical and Chemical Reference Data, Monograph 7. National Institute of Standards and Technology (NIST).*

Chemical Abundances in Gaseous Nebulae
AAA Workshop Series 10, 2016
G. Hägele, M. Cardaci & E. Pérez-Montero, eds.

Contributed Paper

Strong-line methods, observational uncertainties, and the T_e[NII] - T_e[OIII] temperature relation

K. Z. Arellano-Córdova[1] and M. Rodríguez[1]

[1]*Instituto Nacional de Astrofísica, Óptica y Electrónica (INAOE), Apdo. Postal 51 y 216, Puebla, Mexico*

Abstract. We explore two sources of uncertainty in the determinations of chemical abundances in HII regions: errors in the measurement of the line intensity ratios and the use of the T_e[NII]-T_e[OIII] temperature relation. In order to explore the first problem we analyze the dispersions introduced by the direct method and by strong-line methods in the metallicity gradient in the galaxy M81. We find that a large part of the dispersion can be attributed to the sensitivity of each method to line ratios that are susceptible to observational problems. In the second part of our work we use a compilation of 125 HII regions that have measurements of both T_e[NII] and T_e[OIII] to study the effect of using the T_e[NII]-T_e[OIII] temperature relation in the calculation of the metallicity. We confirm that this temperature relation depends on the degree of ionization of the studied objects and provide a new set of relations that consider this parameter.

1. Introduction

The chemical abundances in HII regions are generally calculated using the relative intensities of emission lines found in the optical spectral range. The oxygen abundance is easily measured and, because of the large relative abundance of this element, it can be considered as representative of the metallicity of the medium. There are different methods to calculate the metallicity, such as the direct method, that is based on measurements of the electron temperature, and the strong-line methods, that use the most intense lines in the optical spectra of HII regions. Although all these methods are easily applied, we must take into account that the measurements of the line intensity ratios can be affected by uncertainties related to several observational problems which are very difficult to constrain. On the other hand, when applying the direct method, sometimes it is only possible to measure one electron temperature (usually T_e[OIII] or T_e[NII]), which characterizes either the zone of high- or low-degree of ionization in the nebula. This implies the necessary use of temperature relations in order to estimate the other electron temperature, and it is important to know how the use of these relations affects the abundance determinations. We explore these issues using two samples of HII regions observed by different authors, one of them for HII regions in M81 and the other for HII regions in different galaxies whose spectra allow the determination of both T_e[OIII] and T_e[NII].

2. The robustness of abundance determinations

We use the spiral galaxy M81 as a case study to explore the sensitivity of the direct method and some strong-line methods to potential observational problems, like those related to the flux calibration of the observed spectra, the extinction correction of the line intensities, or to the effects of atmospheric differential refraction. The emission line ratios used by the different methods will be affected by these problems in different amounts. We explore the performance of these methods when they are used to estimate the metallicity gradient in M81. We have a sample of HII regions that is composed by our own observations, which were obtained with the Gran Telescopio Canarias (GTC)[1], and data collected from the literature (see Arellano-Córdova et al., 2016). The spectra observed by different authors will be affected in different ways by observational problems, and we will consider that a method is more robust than the others when it shows less dispersion around the metallicity gradient. Fig. 1 shows the metallicity gradients obtained using the oxygen abundances calculated by the direct method, the P method Pilyugin & Thuan (2005), the C method Pilyugin et al. (2012) and the N2 method (Marino et al., 2013).

We find that the direct method and the P method show the largest dispersions around the metallicity gradient, $\sigma \sim 0.25$ and $\sigma \sim 0.15$, respectively; while the C and N2 methods show lower dispersions, $\sigma \sim 0.06$. The dispersions around the gradients obtained with the different methods can be qualitatively explained by considering their sensitivity to the two most critical line ratios: [OIII] $\lambda3727/\mathrm{H}\beta$ and [NII] $(\lambda6548+\lambda6584)/\lambda5755$ (Arellano-Córdova et al., 2016). These low dispersions with the C and N2 methods suggest that O/H, N/O, and the ionization degree vary smoothly along the disc of M81, although we caution that the robustness of these methods does not imply that they provide reliable estimates of the oxygen abundances.

3. The T_e[NII]-T_e[OIII] temperature relation

We have gathered a sample of 125 HII regions with measurements of T_e[NII] and T_e[OIII], which allows us to use the direct method to calculate their metallicities. The physical conditions and chemical abundances were calculated using the line intensities reported by the authors with the use of the software PYNEB (Luridiana et al., 2015). We adopted a two-zone ionization structure with T_e[NII] characterizing the [OII] emitting region and T_e[OIII] the [OIII] emitting region. Fig. 2 shows the values of T_e[NII] and T_e[OIII] for our sample, color-coded according to the value of P (related to the hardness of the ionizing radiation). We show in this figure the generally used temperature relation of Campbell et al. (1986) represented by a dashed line. The results in Fig. 2 show that the temperature relation has a dependence with the degree of ionization. This was previously reported for a smaller sample of objects by Pilyugin (2007), who proposed a temperature relation that depends on this parameter, but this relation has been barely used.

[1]Installed in the Spanish Observatorio del Roque de los Muchachos of the Instituto de Astrofísica de Canarias, in the island of La Palma.

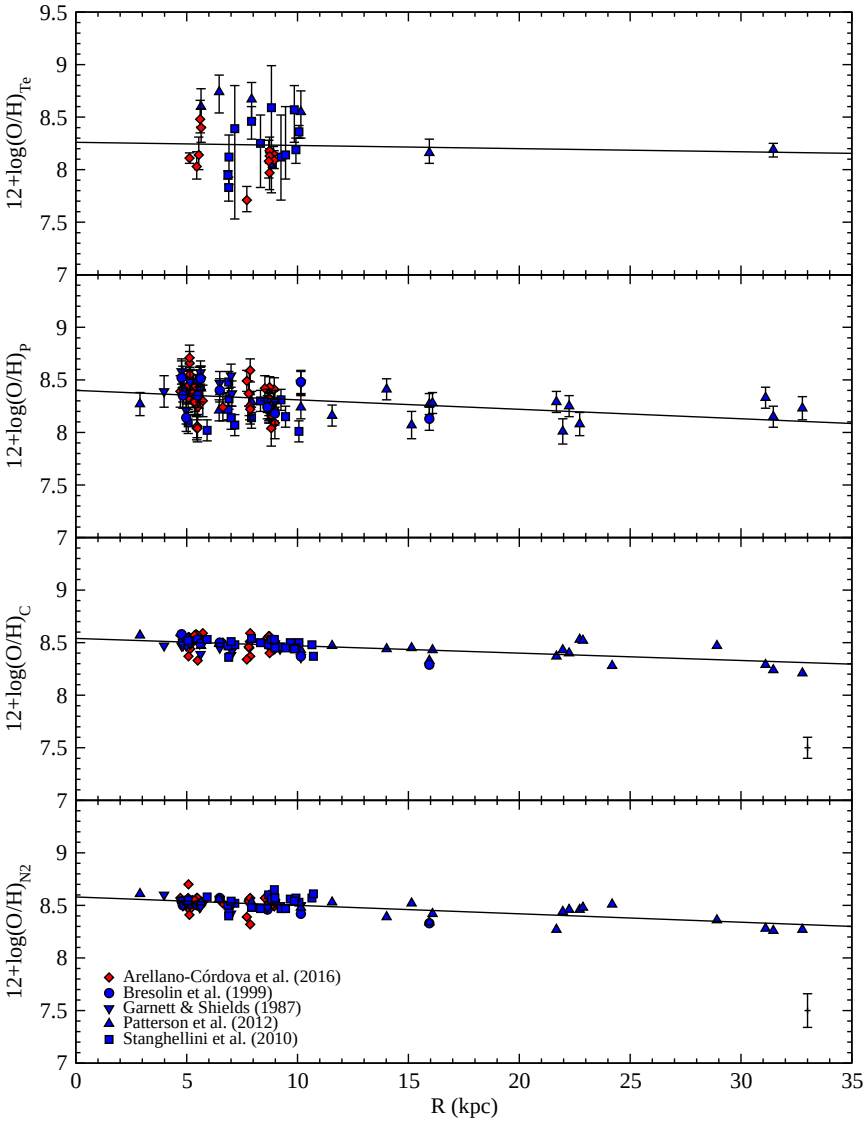

Figure 1. Oxygen abundances in HII regions of M81 as a function of their galactocentric distances and the abundance gradients resulting from our fits. The panels show from top to bottom the results for the direct method and the methods P, C and N2, respectively. The different symbols identify the references for the observational data we used. Note that all panels are in the same scale.

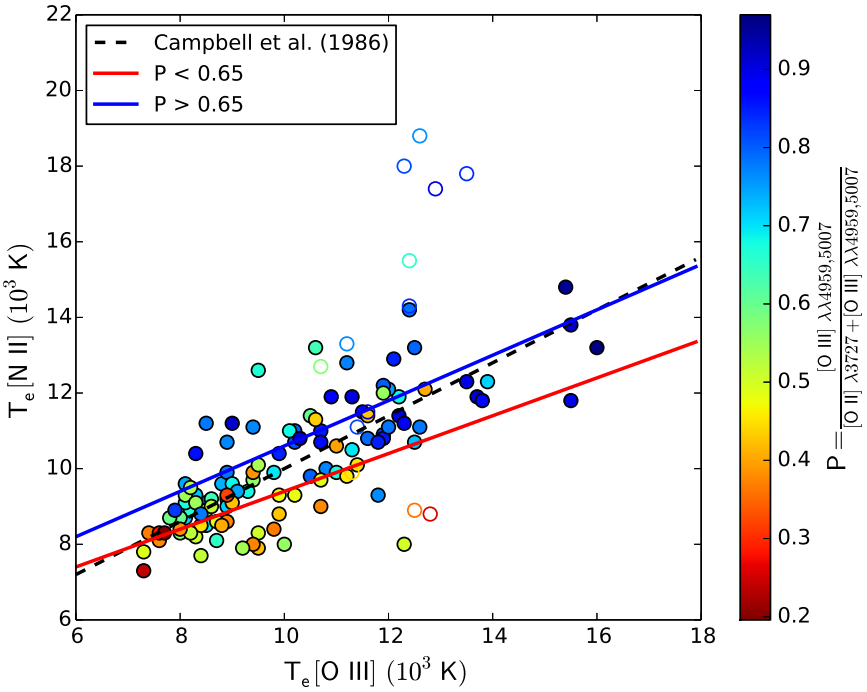

Figure 2. T_e[NII] as a function of T_e[OIII] for a sample of HII regions belonging to different galaxies gathered from the literature. The HII regions are color-coded according to the value of the P parameter. The dashed line shows the temperature relation by Campbell et al. (1986). The continuous lines are the fits we obtain, in blue for objects with $P > 0.65$, and in red for $P < 0.65$.

In this study we propose two new temperature relations, shown with blue and red continuous lines in Fig. 2, that are based on fits to the results found for two ranges in P. For our fits we remove objects with very high values of T_e[NII] and those objects whose temperature uncertainties exceed 30 percent (represented with empty symbols in Fig. 2). Our final sample is composed by 112 HII regions. The two ranges in P were selected to include a comparable number of objects with similar behaviour. For $P > 0.65$, we find:

$$T_e[\mathrm{N\,II}] = 0.6\,T_e[\mathrm{O\,III}] + 4600\,\mathrm{K}, \quad (1)$$

and for $P < 0.65$:

$$T_e[\mathrm{N\,II}] = 0.5\,T_e[\mathrm{O\,III}] + 4400\,\mathrm{K}. \quad (2)$$

These are the fits plotted in Fig. 2 in blue and red continuous lines, respectively. We have compared the differences between the oxygen abundances calculated using both electron temperatures, T_e[NII] and T_e[OIII], and those calculated using our temperature relations and the one derived by Campbell et al. (1986). The temperature relation by Campbell et al. (1986) leads to differences in metallicity of up to 0.6 dex with a dispersion of 0.10 dex. On the other hand, the temperature relations provided by equations 1 and 2 imply differences of up to 0.4 dex, although most objects have differences below 0.2 dex. The dispersion in this case is 0.09 dex, a value similar to the one obtained with the temperature relation by Campbell et al. (1986). The complete analysis will be presented in Arellano-Córdova et al. (in preparation).

Acknowledgments. We acknowledge support from Mexican CONACYT grant CB-2014-240562. K.Z.A.-C. acknowledges support from CONACYT grant 351585.

References

Arellano-Córdova K. Z., Rodríguez M., Mayya Y. D., et al., 2016, *MNRAS*, **455**, 2627
Campbell A., Terlevich R., Melnick J., 1986, *MNRAS*, **223**, 811
Luridiana V., Morisset C., Shaw R. A., 2015, *A&A*, **573**, A42
Marino R. A., Rosales-Ortega F. F., Sánchez S. F., et al., 2013, *A&A*, **559**, A114
Pilyugin L. S., 2007, *MNRAS*, **375**, 685
Pilyugin L. S., Grebel E. K., Mattsson L., 2012, *MNRAS*, **424**, 2316
Pilyugin L. S., Thuan T. X., 2005, *ApJ*, **631**, 231

Chemical Abundances in Gaseous Nebulae
AAA Workshop Series 10, 2016
G. Hägele, M. Cardaci & E. Pérez-Montero, eds.

Contributed Paper

Distribution and kinematics of molecular and ionized gas in nearby AGNs: inflows, outflows and stellar populations

R. A. Riffel[1]

[1] *Departamento de Física, Centro de Ciências Naturais e Exatas, Universidade Federal de Santa Maria, 97105-900, Santa Maria, RS, Brazil*

Abstract. Since 2006 our group has been using near-infrared integral field spectroscopy to map the gas and star distribution and kinematics in the inner kiloparsec of nearby active galaxies. In this work it is presented a summary of the main results obtained so far, related to the distribution and kinematics of molecular and ionized gas and their relation with the circumnuclear stellar populations. The molecular and ionized gas show distinct flux distributions and kinematics, with the former being restricted to the plane of the galaxy and the later extending to high latitudes above it. Inflows are seen in molecular gas for about half of the galaxies, while ionized gas outflows are observed for 80 % of the objects. Young stellar populations ($\leq$ 100 Myr) seem to be correlated with the H_2 line emission, while the distribution of intermediate-age stars (100 Myr–2 Gyr) is correlated with low stellar velocity dispersion rings.

1. Introduction

The feeding and feedback processes in Active Galactic Nuclei (AGNs) are coupled to the co-evolution of the central super-massive black hole (SMBH) and the host galaxy and they are held as responsible for the observed correlation between the mass of the SMBH and the mass (or velocity dispersion - σ) of the host galaxy (e.g. Kormendy & Ho, 2013). The feeding precesses represent the necessary condition to trigger the nuclear activity, while the feedback processes play a fundamental role in galaxy evolution models: models that do not include the AGN feedback are not able to reproduce properties of massive galaxies (Springel et al., 2005; Fabian, 2012).
Near-Infrared (hereafter near-IR) Integral Field Spectroscopy (IFS) of the central region of active galaxies (inner kiloparsec) using 8-10 meter telescopes is a powerful tool to investigate the AGN feeding and feedback processes. This technique allows the mapping of both the kinematics and distribution of the gas and stars at spatial resolutions of few tens of parsecs. The near-IR bands present emission of gas at distinct phases, allowing the mapping of gas streaming motions towards the center of galaxies (expected to be more important in molecular gas), which provides a gas reservoir in the inner 100 pc, necessary to trigger star formation and nuclear activity. Outflows are expected to be more easily observed in ionized gas, associated to the emission of the Narrow-Line Region (NLR).

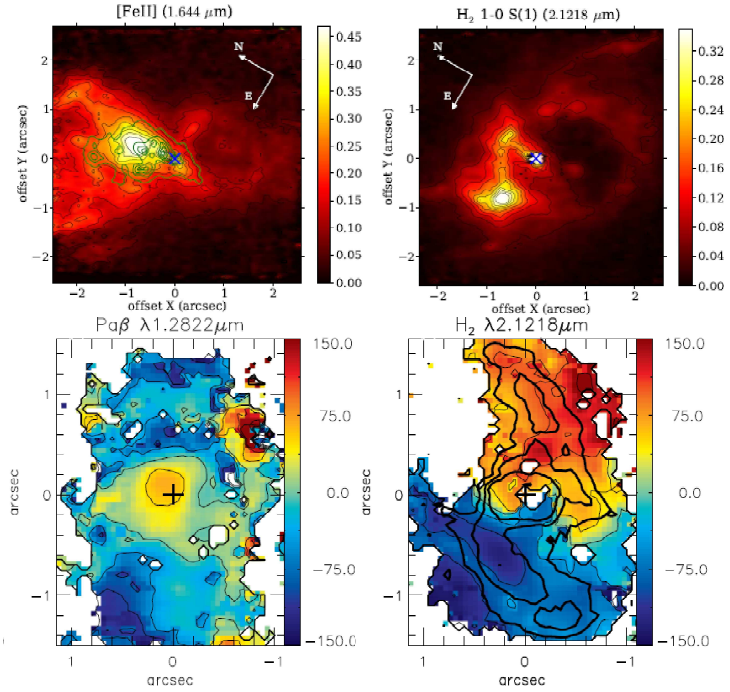

Figure 1. Top: [FeII]λ1.64μm (left) and $H_2\lambda$2.12μm (right) emission-line flux distributions for NGC 1068 obtained with Gemini NIFS (Riffel et al., 2014b). The fluxes are shown in units of 10^{-15} erg s^{-1} cm^{-2}. Bottom: Paβ (left) and $H_2\lambda$2.12μm (right) velocity fields for Mrk 79 (Riffel et al., 2013). The color bars show the line of sight velocities in units of km s^{-1}, after the subtraction of the systemic velocity of the galaxy.

Our group has been using near-IR IFS to map the kinematics and distribution of gas and stars in the inner kiloparsec of AGNs for about a decade (e.g. Riffel et al., 2006, 2009, 2010, 2011, 2014a, 2015; Riffel & Storchi-Bergmann, 2011; Barbosa et al., 2014; Storchi-Bergmann et al., 2009, 2010, 2012; Diniz et al., 2015; Ilha et al., 2016; Schönell et al., 2014, 2017; Riffel, 2013; Fischer et al., 2015). In this paper it is presented a summary of the main results obtained by our group, focusing on the distribution and kinematics of the molecular and ionized gas and their relation with circumnuclear stellar populations and nuclear activity.

This work is organized as follows: Section 2 presents a discussion about the distribution and kinematics of molecular and ionized gas in the inner kiloparsec of nearby AGNs, results for the stellar populations distribution and their relation with molecular gas emission and stellar kinematics are presented in Section 3 and a summary of the results is presented in Section 4.

2. Distribution and kinematics of ionized and molecular gas

Fig. 1 shows in the top panels the [FeII]λ1.64μm (left) and $H_2\lambda$2.12μm (right) emission-line flux distributions for the Seyfert galaxy NGC 1068, obtained from IFS using the Gemini Near-infrared Integral Field Spectrograph (NIFS - McGregor et al., 2003). The fluxes are shown in units of $10^{-15}\,\mathrm{erg\,s^{-1}\,cm^{-2}}$. The $H_2\lambda$2.12μm flux distribution shows an off-centered circumnuclear ring with a radius of $\sim$100 pc and is originated by thermal excitation, while the ionized gas (as traced by the [FeII]λ1.64μm emission) show flux distributions outlining the ionization bi-cone and its kinematics is consistent with outflows from the nucleus of the galaxy (Riffel et al., 2014b; Barbosa et al., 2014).
The bottom panels of Fig. 1 show the line-of-sight velocity fields for Paβ and $H_2\lambda$2.12μm emission lines of the inner $3'' \times 3''$ of the Seyfert galaxy Mrk 79, using Gemini NIFS data. The color bars show the velocities in $\mathrm{km\,s^{-1}}$ units relative to the systemic velocity of the galaxy, white regions correspond to locations where the signal-to-noise ratio was not high enough to obtain good fits of the line profiles, contours of the $H_2\lambda$2.12μm flux are overlaid at the right panel and the central + sign represents the location of the nucleus of the galaxy, defined as the location of the peak near-IR continuum emission. The kinematics of the ionized and molecular gas of Mrk 79 is discussed in details in Riffel et al. (2013), where we conclude that the H_2 kinematics is consistent with two components: a rotating disk and inflows across nuclear spirals at the plane of the disk (seen in the H_2 flux distribution) at a mass inflow rate of $\dot{M}_{H_2} \approx 4 \times 10^{-3} \mathrm{M_\odot yr^{-1}}$, which is one order of magnitude smaller than the mass accretion rate necessary to power the AGN of Mrk 79. On the other hand, the ionized gas emission is well correlated with the radio jet and its kinematics presents both rotation and outflows to the north and south of the nucleus. The estimated outflow rate through a cross-section with a radius of ~ 320 pc located at a distance of ~ 450 pc from the nucleus is $\dot{M}_{\rm out} \approx 3.5 \mathrm{M_\odot yr^{-1}}$, being one order of magnitude larger than the accretion rate, indicating that the outflowing gas is originated in the NLR.
NGC 5929 is another interesting case in which gas outflows are observed perpendicularly to the radio jet (Riffel et al., 2014a, 2015). A clear correlation between the radio and line emission is observed and in Riffel et al. (2014a) we report evidences of interaction of the radio jet with the NLR gas, as for example the presence of wings in the line profiles co-spatial with the radio hotspots. The σ map for [FeII]λ1.25μm shows enhanced values at locations next to the radio hotspots, suggesting an interaction of the radio jet with the ambient gas. However, the highest σ values are observed perpendicular to the radio jet (SE–NW direction) along a strip of 50 pc wide crossing the nucleus and extending by 300 pc from it. Along this structure, the line profiles present two kinematic components, interpreted in Riffel et al. (2014a) as being originated by an equatorial outflow, as predicted in recent accretion disk and torus wind models (e.g. Hönig et al., 2013; Elitzur, 2012).
For NGC 2110 we mapped both gas outflows and inflows in H_2 (Diniz et al., 2015) using Gemini NIFS observations. Fig. 2 shows the $H_2\lambda$2.12μm emission-line flux map (left) and velocity field (right). The $H_2\lambda$2.12μm velocity field shows three distinct kinematic components: (i) a rotating disk with major axis oriented along position angle $\Psi_0 \sim 160°$, (ii) inflows along kinematic spirals as indicated

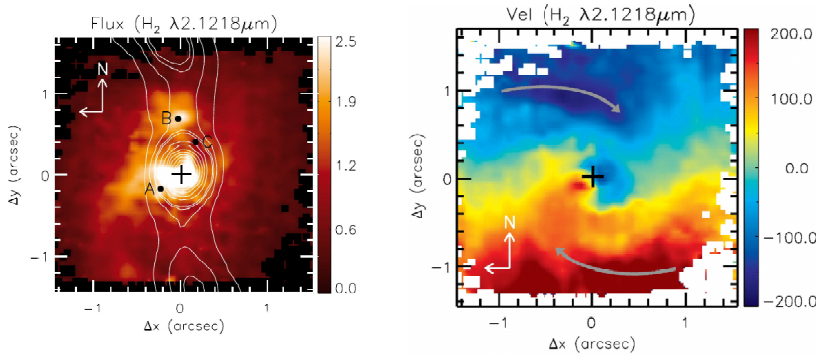

Figure 2. $H_2\lambda2.12\mu$m emission-line flux map (left) in units of $10^{-17}\,\mathrm{erg\,s^{-1}\,cm^{-2}}$ and velocity field (right) in units of $\mathrm{km\,s^{-1}}$ for NGC 2110. The white contours are from the radio image of Ulvestad & Wilson (1989).

by the arrows shown in the figure, with an inflow rate of $\sim 4.6 \times 10^{-4} M_\odot yr^{-1}$ in warm molecular gas and (iii) a bipolar nuclear outflow oriented along the E-W direction, with a mass outflow rate of $\sim 4.3 \times 10^{-4} M_\odot yr^{-1}$ – this component is also observed at optical bands (Schnorr-Müller et al., 2014).
So far, our group has analyzed near-IR datacubes of 15 nearby Seyfert galaxies, mostly of them obtained Gemini NIFS and we detect gas outflows for 80% of the galaxies, while inflows are seen only for 45 % of them. However, the bulk of the inflowing material may be associated to cold molecular gas and the warm H_2 (that produces the near-IR lines) represents only a hot skin of the total inflowing material.

3. Star formation and stellar populations

The presence of gas inflows, as described in previous Section, results in a gas reservoir in the inner tens to few hundreds of parsecs of active galaxies, providing the conditions necessary to form new stars. Circumnuclear star formation is commonly observed in the inner kiloparsec of galaxies, as in the case of NGC 4303 shown in the top panels of Fig. 3. These panels show equivalent width (EqW) maps for [FeII]$\lambda1.64\mu$m, $H_2\lambda2.12\mu$m and Brγ emission lines and show that regions with higher Brγ EqW values show the smallest EqW values for the [FeII]$\lambda1.64\mu$m and $H_2\lambda2.12\mu$m emission lines, suggesting distinct origin of the gas emission, possible with additional contribution of post-starburst stars to the excitation of the [FeII] and H_2 lines. A gradient in the Brγ EqW values is observed, with the highest values observed for the region identified as "A" and the smallest ones for the region identified as "H", suggesting an age gradient for the star-forming regions of NGC 4303. In Riffel et al. (2016), we discuss in more details properties of the circumnuclear star formation in NGC 4303.
The influence of post-starburst stars to the H_2 emission is also supported by a correlation found between the $H_2\lambda2.12\mu$m flux map and young stellar popu-

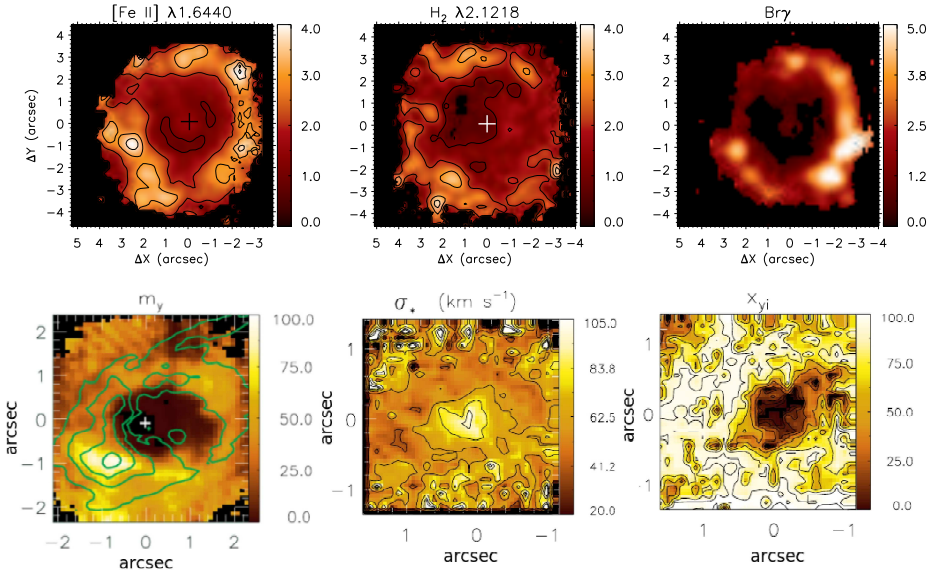

Figure 3. Top: Equivalent width maps for [FeII]λ1.64μm, $H_2\lambda$2.12μm and Brγ emission lines for NGC 4303 obtained using VLT-SINFONI IFS (Riffel et al., 2016). Bottom: Left panel: Contribution of the young stellar populations (ages$\sim$ 30Myr) to the stellar mass with contours of the H_2 flux map (Fig. 1) overlaid (Storchi-Bergmann et al., 2012). Velocity dispersion (middle) and percent contribution to the flux at 2.1μm (right) of intermediate-age stellar populations (100–700 Myr) for Mrk 1066 (Riffel et al., 2010).

lations (ages$\sim$30 Myr), as observed for NGC 1068 in Fig. 3 and discussed by Storchi-Bergmann et al. (2012). Finally, we observed a correlation between the intermediate-age stellar populations (100 Myr – 2 Gyr) with rings of low stellar σ ($\sim$ 50 km s^{-1}), as for example for Mrk 1066 (Fig. 4 – Riffel et al., 2010) and Mrk 1157 (Riffel et al., 2011). This result has been interpreted as the low-σ structures being originated by stars that still preserve the "cold kinematics" of the gas that they were formed.

4. Summary

Recently our group has defined a sample of nearby AGNs selected from the Swift BAT 60-Month Hard X-ray Survey in order to obtain statistically significant results about AGN feeding and feedback (Riffel et al. in prep.). Most of the galaxies observed so far by our group with near-IR IFS are part of this sample and the main results are summarized below.

The molecular and ionized gas have distinct flux distributions and kinematics, with the former more restricted to the plane of the disk and the latter extending to high latitudes above it. The H_2 kinematics is usually dominated by rotation, but inflows of gas are observed associated to nuclear spirals/bars for about 45% of the observed galaxies at total mass inflow rate ranging from 10^{-2} to 10 M$_\odot$ yr^{-1}.

Gas outflows are seen for most of the galaxies at outflow rates between 0.1 to $10\,M_\odot\,yr^{-1}$ in ionized gas.
The mass inflow rates are larger than the accretion rate necessary to power the central AGN and in 10^7 – 10^8 yr can accumulate enough gas to form new stars in the inner kiloparsec. Indeed, recent star formation is seen for some objects as circumnuclear and nuclear star forming regions and results from spectral synthesis suggest that intermediate age stars (100 Myr – 2 Gyr) dominates the continuum emission in the near-IR, possible due to the contribution of TP-AGB stars. These stellar populations are seen in association with low stellar σ rings for some galaxies, suggesting that these stellar populations are still not in orbital equilibrium.

Acknowledgments. I acknowledge support from FAPERGS (project N0. 2366-2551/14-0) and CNPq (project N0. 470090/2013-8 and 302683/2013-5).

References

Barbosa F. K. B., Storchi-Bergmann T., et al., 2014, *MNRAS*, **445**, 2353
Diniz M. R., Riffel R. A., Storchi-Bergmann T., et al., 2015, *MNRAS*, **453**, 1727
Elitzur M., 2012, *ApJL*, **747**, L33
Fabian A. C., 2012, *ARA&A*, **50**, 455
Fischer T. C., Crenshaw D. M., Kraemer S. B., et al., 2015, *ApJ*, **799**, 234
Hönig S. F., Kishimoto M., Tristram K. R. W., et al., 2013, *ApJ*, **771**, 87
Ilha G. d. S., Bianchin M., Riffel R. A., 2016, *Ap&SS*, **361**, 178
Kormendy J., Ho L. C., 2013, *ARA&A*, **51**, 511
McGregor P. J., Hart J., Conroy P. G., et al., 2003, M. Iye and A. F. M. Moorwood (eds.), *Instrument Design and Performance for Optical/Infrared Ground-based Telescopes*, Vol. 4841 of *Proc. SPIEJ*, pp 1581–1591
Riffel R., Riffel R. A., Ferrari F., et al., 2011, *MNRAS*, **416**, 493
Riffel R. A., 2013, *BAAA*, **56**, 13
Riffel R. A., Colina L., Storchi-Bergmann T., et al., 2016, *MNRAS*, **461**, 4192
Riffel R. A., Storchi-Bergmann T., 2011, *MNRAS*, **411**, 469
Riffel R. A., Storchi-Bergmann T., Dors O. L., et al., 2009, *MNRAS*, **393**, 783
Riffel R. A., Storchi-Bergmann T., Riffel R., 2014a, *ApJL*, **780**, L24
Riffel R. A., Storchi-Bergmann T., Riffel R., 2015, *MNRAS*, **451**, 3587
Riffel R. A., Storchi-Bergmann T., Riffel R., et al., 2010, *ApJ*, **713**, 469
Riffel R. A., Storchi-Bergmann T., Winge C., 2013, *MNRAS*, **430**, 2249
Riffel R. A., Storchi-Bergmann T., Winge C., et al., 2006, *MNRAS*, **373**, 2
Riffel R. A., Vale T. B., Storchi-Bergmann T., et al., 2014b, *MNRAS*, **442**, 656
Schnorr-Müller A., Storchi-Bergmann T., et al., 2014, *MNRAS*, **437**, 1708
Schönell A. J., Riffel R. A., et al., 2014, *MNRAS*, **445**, 414
Schönell A. J., Storchi-Bergmann T., et al., 2017, *MNRAS*, **464**, 1771
Springel V., Di Matteo T., Hernquist L., 2005, *MNRAS*, **361**, 776
Storchi-Bergmann T., Lopes R. D. S., McGregor P. J., et al., 2010, *MNRAS*, **402**, 819
Storchi-Bergmann T., McGregor P. J., Riffel R. A., et al., 2009, *MNRAS*, **394**, 1148
Storchi-Bergmann T., Riffel R. A., Riffel R., et al., 2012, *ApJ*, **755**, 87
Ulvestad J. S., Wilson A. S., 1989, *ApJ*, **343**, 659

Chemical Abundances in Gaseous Nebulae
AAA Workshop Series 10, 2016
G. Hägele, M. Cardaci & E. Pérez-Montero, eds.

Contributed Paper

Tracing polycyclic aromatic nitrogen heterocycles through the $6.2\mu m$ band.

C. M. Canelo[1], A. C. S. Friaça[1], D. A. Sales[2], M. G. Pastoriza[3] and D. Ruschel-Dutra[3]

[1]*Institute of Astronomy, Geophysics and Atmospheric Sciences, USP, São Paulo, Brazil*
[2]*Federal University of Rio Grande, Rio Grande do Sul, Brazil*
[3]*Federal University of Rio Grande do Sul, Rio Grande do Sul, Brazil*

Abstract. The polycyclic aromatic hydrocarbons (PAHs), together with other aromatic macromolecules such as the polycyclic aromatic nitrogen heterocycles (PANHs), are among the most abundant molecular species that must have been transported to the planets for meteorite and comet crash and interstellar dust deposition. Therefore, the detailed study of the PAHs formation and distribution enables a better comprehension of the PAHNs role in the origin of life on Earth and other astrophysical environments. Analyses of the PAHs features profiles, especially the $6.2\mu m$ feature, could indicate the presence of nitrogen incorporated to the rings. For this work, the $6.22\mu m$ profiles of 206 starburst and ULIRG galaxies, extracted from the Spitzer/IRS ATLAS project, have been fitted. A total of 125 galaxies presented emission with a central wavelength of $6.22\mu m$, which has only been explicated by carbon replaced by nitrogen, despite other attempts of explanation. According to these results, PAHs and PANHs are very significant sources of infrared luminosity and very meaningful for the origin of life on Earth and maybe on other planets as well.

1. Introduction

A considerable fraction of the carbon in the interstellar medium (ISM), 20% or more, is in the form of Polycyclic Aromatic Hydrocarbons (PAHs; Joblin et al., 1992). In addition, the mid-infrared (MIR) spectral range is dominated by bands of a molecular class, that includes PAHs, known as the Aromatic Infrared Bands (AIBs; Joblin et al., 1992). All other classes of organics and inorganics represent only a tiny fraction of the emitting material that contributes to the AIBs (Allamandola et al., 1999). Up to 50% of the luminosity emitted in the MIR can be due to PAHs, the most prominent bands emit at 3.3, 6.2, 7.7, 8.6, 11.3 and $12.7\mu m$ (Li, 2004).
Because of their robustness, PAHs are the dominant material in space (Ehrenfreund et al., 2006) and, together with other aromatic macromolecules, they are the most abundant molecular species that must have been transported to the planets by comets, meteorites and interplanetary dust deposition (Ehrenfreund

et al., 2002). When a PAH incorporates nitrogen, this substitutes a carbon atom, it becomes a polycyclic aromatic nitrogen heterocycle (PANH). These molecules must be also present in the ISM and a substantial part of them would be formed on ices deposited on grains. PANHs could provide the missing link between the abundant PAH chemistry at the ISM and the nucleobases that compose all living beings.
Analyses of the PAH feature profiles, especially the $6.2\mu m$ band, could indicate the presence of nitrogen incorporated to their rings. Peeters et al. (2002) have suggested the division of spectrum into three class – A, B and C – depending on the variation's interpretation of the profile peak positions. The class A, corresponding to a central wavelength at $6.22\mu m$, has only been well reproduced by carbon replaced by nitrogen into the aromatic rings, despite other attempts of explanation such as size and charge of PAHs (Hudgins et al., 2005).
Identification of the feature class can show if PANHs are present and how important they are for such emission. In this work, we analysed and classified 206 objects according to the Peeters' classes for the $6.2\mu m$ feature, searching for the PANHs contribution to this PAH band.

2. Procedure

For a better understanding of the PANHs distribution in the Universe, first we decided to concentrate our efforts in starbursts galaxies, which present strong PAH emission in the MIR. We selected sources from the MIR starburst sample of the Spitzer/IRS ATLAS project (Hernán-Caballero & Hatziminaoglou, 2011), which contains 257 already reduced spectra from galaxies with emission classified as starburst-dominated by these authors. From these data, 206 objects had the $6.2\mu m$ feature observed and were used for this work, including 10 other ULIRGs (Ultra Luminous Infrared Galaxies) with strong PAH features observed by Yan et al. (2007).
Before the $6.2\mu m$ feature profile fitting the spectral contributions of the continuum, silicate absorption and line emissions were subtracted. They all were previously fitted by PAHFIT (Smith et al., 2007) routines, created to decompose Spitzer IRS spectra of PAH emission sources. Although PAHFIT also recovers dust features, the central wavelengths of the bands are all fixed in the program. This inflexibility prevents the observation of the peak position variations and the fits of PAH bands obtained with this tool were ignored in this work.
In order to evaluate the PAHFIT results, it was applied the root mean square (RMS) deviation to the best-fit data obtained by the tool. As the PAHs bands are stronger for wavelengths lower than $12\mu m$, a partial RMS corresponding to this range was also made and preferred to this approach. As most of the partial values are lower than 40%, the PAHFIT results were used in the next analysis.
Finally, for the study of the behavior of the $6.2\mu m$ profile in these sources, we constructed a python based script to estimate its central wavelength. The optimization algorithms used are listed bellow and the initial guesses for the peak position and FWHM were selected from Smith et al. (2007). For the classification of the objects, the range used was: Class A – $\lambda_{central} < 6.23$, Class B – $6.23 < \lambda_{central} < 6.29$ and Class C – $\lambda_{central} > 6.29$.

3. Results

Initially, the submodule *scipy.optmize.curve_fit* was chosen to fit the data by a Lorentzian profile, usually used for this band, and the uncertainties were propagated by the tool itself. An example of this fit can been seen in Fig. 1 (left). The asymmetry of this specific feature, with a profile composed of a sharp blue rise and a red tail (Peeters et al., 2002), caused a deviation of the fitted central wavelength to the red for some galaxies. In order to resolve this issue, we have excluded the red tails from the range of the profile fit for these objects (Fig. 1, right).

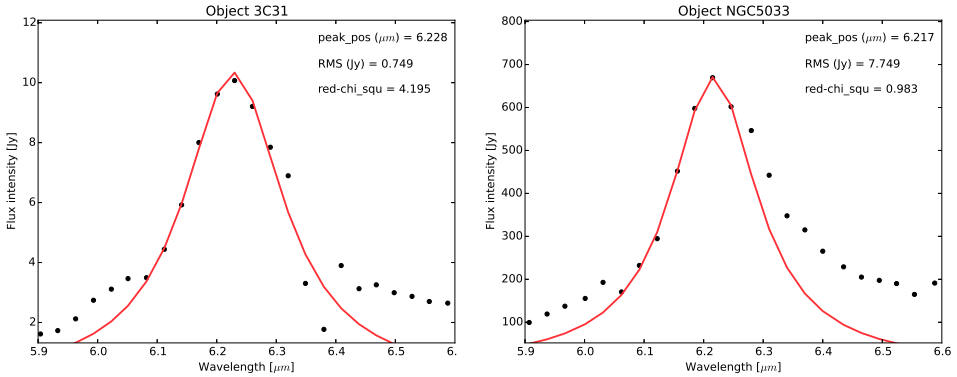

Figure 1. Band profile of 6.2μm fitted with *curve_fit* for the objects 3C31 (left) and NGC5033 (right). In each panel the values of the peak position, rms and reduced χ^2 are shown. In the case of NGC5033, the red tail was not considered for the fit.

We also realized the presence of another emission near 6.35μm in some sources and we performed the fitting adding a new profile after the first one. As this second emission possess wider wings, we opted Drude profile to fit it more properly and we changed the previous submodule for *scipy.optmize.minimize* to better constraint the fit. Unfortunately, it does not compute the uncertainties and, to decide which situation to use for each galaxy, the RMS was calculated for both fitting and the lower value was chosen.

The inclusion of the second feature also improved the fit for high asymmetric profiles by reproducing their red tail, previously ignored. Even so, in these situations, there is no real indication of the second feature's presence and the asymmetry could be just a characteristic of the anharmonic profile (Tielens, 2008). Fig. 2 shows an example of the fit with a second emission (left) and with a probable asymmetry effect (right). The peak position of the second feature varied from 6.246 to 6.471μm and there are a few possibilities that could give an insight into its nature. According to Pino et al. (2008), bands in 6.3μm are related to aliphatic features. On the other hand, the 6.4μm band observed in the reflection nebula NGC7023 was attributed to the C_{60}^{+} (Berné et al., 2015). Finally, this could be the emission of pure PAHs in the sources.

Table 1 presents the classification of the 169 well-fitted objects. The remaining 37 galaxies have no sufficient data points for a trustful fit or the profiles were peculiar

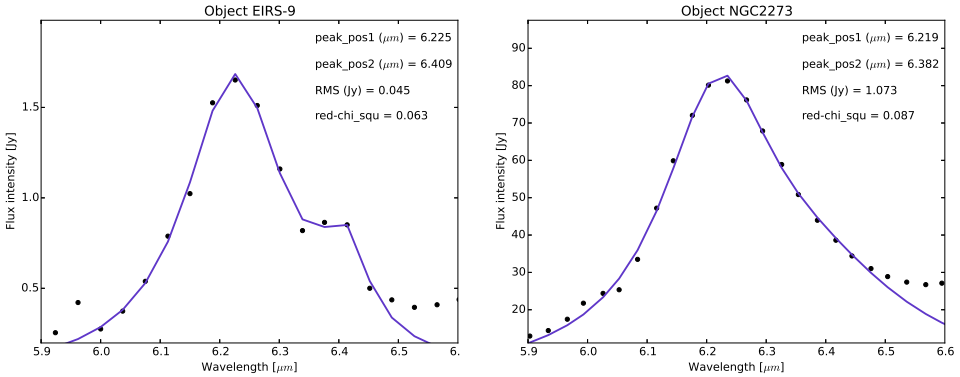

Figure 2. Band profile of 6.2μm fitted with *minimize* for the objects EIRS-9 (left) and NGC2273 (right). In each panel the values of the peak positions, rms and reduced χ^2 are shown.

for a starburst source, and they all were not included in the final analysis. An overview of the results is showed in Fig. 3, with the starburst-dominated sources divided into their common classification. In this figure, both fits are present and the objects without errorbars are those fitted with the *scipy.optmize.minimize* tool.

Table 1. Number of well-fitted galaxies categorized into each Peeters' classes.

Module	Galaxies	Class A	Class B	Class C
curve_fit	61	31	27	3
minimize	108	93	15	0
Total	**169**	**124**	**42**	**3**

4. Conclusions

Pino et al. (2008) have already notice that class A objects are the most common in the Universe and embrace several astrophysical sources, while class C objects are minority. Our results point to same direction, specially for starburst-dominated sources whose class A members is up to 73.4% in this study. This evidence is pronounced at lower redshifts, as can be realized in Fig. 3. In addition, if we consider class B as a mixture between PANH and PAH emissions (Peeters et al., 2002), we can verify that PANHs dominate these galaxies for the 6.2μm band. Regarding the class C, just three objects do not allow us to distinguish patterns. Apparently, they may be expected at higher redshifts, which also would imply an evolutionary timescale of PAHs.

Starbursts seem to be the most affected by PANHs, but higher percentages of class A in ULIRGs and Seyferts may also indicate the strong influence of these

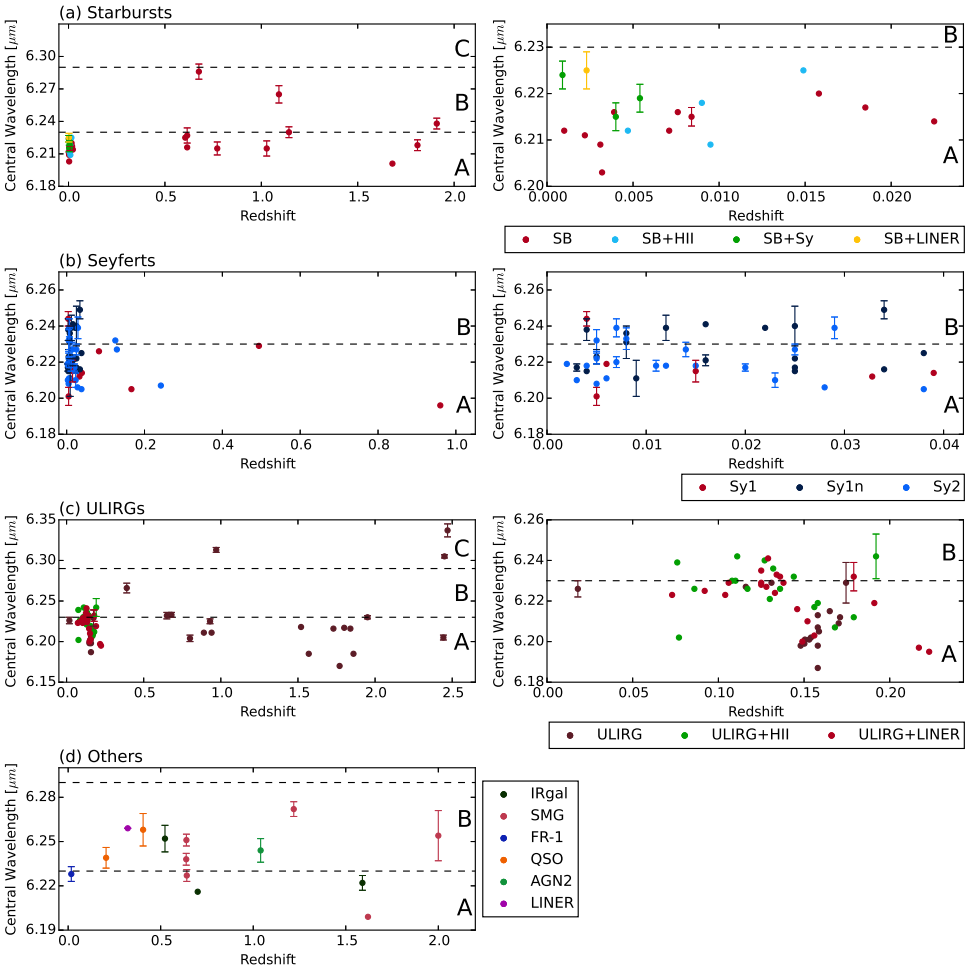

Figure 3. Left panels: plots of the 6.2μm central wavelength for the redshift of the sources: **(a)** Starbursts (SB) and contributions of HII regions (HII), Seyferts (Sy) and low ionization emission-line region (LINER); **(b)** Seyferts 1 (Sy), intermediate (Sy1n) and 2 (Sy2); **(c)** ultra-luminous infrared galaxies (ULIRGs) and contributions of HII regions and LINERs; **(d)** Other types – infrared galaxy (IRgal), submillimeter galaxy (SMG), Fanaroff-Riley galaxy (FR), quasi-stellar object (QSO), active galactic nucleus (AGN) and LINER. Right panels: zoom for lower redshifts of the left panel plots.

molecules in these objects. If these elevate statistics can be explained by the dominance of starburst emission in all the sources or by the ubiquity of PANHs in galaxies, there is still no sufficient data to confirm it. Studies with other kind of objects, such as AGNs, could help to clarify this question. However, the prevalence of class A upon these distinct galaxies for the 6.2μm band is clear. Therefore, these spectra suggest a significant presence of PANHs, what could indicate another reservoir of nitrogen in the Universe, with density and temper-

ature conditions that differ from those of gas phase and ices. These results also strength the idea of their relevant contribution to the origins of life on Earth and elsewhere.

Acknowledgments. Special acknowledgements to the creators of the PAHFIT routine (Smith et al., 2007), used in this work, and to A. Hernan-Caballero and E. Hatziminaoglou for provide the data of the sources already reduced.

References

Allamandola L. J., Hudgins D. M., Sandford S. A., 1999, *ApJL*, **511**, L115
Berné O., Montillaud J., Joblin C., 2015, *A&A*, **577**, A133
Ehrenfreund P., Irvine W., Becker L., et al., 2002, *Reports on Progress in Physics*, **65**, 1427
Ehrenfreund P., Rasmussen S., Cleaves J., Chen L., 2006, *Astrobiology*, **6**, 490
Hernán-Caballero A., Hatziminaoglou E., 2011, *MNRAS*, **414**, 500
Hudgins D. M., Bauschlicher Jr. C. W., Allamandola L. J., 2005, *ApJ*, **632**, 316
Joblin C., Leger A., Martin P., 1992, *ApJL*, **393**, L79
Li A., 2004, A. N. Witt, G. C. Clayton, and B. T. Draine (eds.), *Astrophysics of Dust*, Vol. 309 of *Astronomical Society of the Pacific Conference Series*, p. 417
Peeters E., Hony S., Van Kerckhoven C., et al., 2002, *A&A*, **390**, 1089
Pino T., Dartois E., Cao A.-T., et al., 2008, *A&A*, **490**, 665
Smith J. D. T., Draine B. T., Dale D. A., et al., 2007, *ApJ*, **656**, 770
Tielens A. G. G. M., 2008, *ARA&A*, **46**, 289
Yan L., Sajina A., Fadda D., et al., 2007, *ApJ*, **658**, 778

Chemical Abundances in Gaseous Nebulae
AAA Workshop Series 10, 2016
G. Hägele, M. Cardaci & E. Pérez-Montero, eds.

Contributed Paper

The abundances of O, N, S, Cl, Ne, Ar, and Fe in HII regions of the Magellanic Clouds

G. Domínguez-Guzmán[1], M. Rodríguez[1], C. Esteban[2,3] and J. García-Rojas[2,3]

[1]*Instituto Nacional de Astrofísica, Óptica y Electrónica, Apdo. Postal 51 y 216, Puebla, Mexico*
[2]*Instituto de Astrofísica de Canarias, E-38200, La Laguna, Tenerife, Spain*
[3]*Departamento de Astrofísica, Universidad de La Laguna, E-38206, La Laguna, Tenerife, Spain*

Abstract. We use very deep spectra obtained with the Ultraviolet-Visual Echelle Spectrograph in the Very Large Telescope in order to determine the physical conditions, the chemical abundances and the iron depletion factors of four HII regions of the Large Magellanic Cloud and four HII regions of the Small Magellanic Cloud. The spectral range covered is 3100-10400 Å with a resolution of $\Delta\lambda \sim \lambda/8800$. We measure the intensity of up to 200 emission lines in each object. Electron temperature and electron density are determined using different line intensity ratios. The ionic and total abundances are derived using collisionally excited lines for O, N, S, Cl, Ne, Ar, and Fe. The uncertainties are calculated using Monte Carlo simulations. This is the largest available set of high quality spectra for HII regions in the Magellanic Clouds. Thus, we can derive chemical abundances and depletion factors and constrain their variations across each galaxy with better accuracy than previous studies. In particular, we find that the amount of Fe depleted on to dust grains in the HII regions of the Magellanic Clouds is similar to that found in Galactic HII regions.

1. Introduction

The Magellanic Clouds (MCs) are ideal laboratories to study HII regions with lower metallicities than those in the Milky Way. In particular, deep optical spectra of HII regions in these galaxies allow us to detect and measure relatively faint iron lines and thus, to study the properties of dust in ionized nebulae through the analysis of the iron depletion factor. This factor is defined as the ratio between the expected abundance of iron and the one measured in the gas phase. The study of dust in ionized nebulae of the MCs will provide clues on the processes responsible for the formation and evolution of the grains and the role played by metallicity in the efficiency of these processes. Rodríguez & Rubin (2005) and Delgado-Inglada et al. (2011) found that ionized nebulae with lower

metallicities show lower depletions factors. We extend the sample of HII regions in the MCs in order to better understand this behavior.

2. Observational data

We obtained echelle spectra of 8 HII regions in the MCs, 4 in the Small Magellanic Cloud (SMC) and 4 in the Large Magellanic Cloud (LMC). The data were taken with the Ultraviolet-Visual Echelle Spectrograph (UVES) in the Very Large Telescope (VLT) in Chile. The spectral range covered was from 3100 Å to 10400 Å with a spectral resolution of $\Delta\lambda \sim \lambda/8800$. The atmospheric dispersion corrector was used to keep the same observed region within the slit since the MCs are observed at relatively high airmass (between 1.35 and 1.88). The slit positions and widths for each object were chosen carefully in order to get enough spectral resolution and a high signal-to-noise.

The data reduction was performed using the public UVES pipeline under the GASGANO graphic user interface through the standard procedure of bias and aperture subtraction, flat fielding and wavelength calibration. For flux calibration we used the available tasks in the IRAF[1] software package using the standard stars HR 718, HR 3454 and HR 9087. Fig. 1 shows part of the spectrum of N 81 where we identify several iron emission lines. Line intensities were measured by integrating the flux above the continuum defined by two points on each side of the emission lines. Flux uncertainties were computed taking into account the uncertainties in the measurement of the line intensities, in the flux calibration, and in the reddening coefficient.

3. Results

The calculations of physical conditions and ionic and total abundances were carried out with PyNeb (Luridiana et al., 2015). The uncertainties were obtained through Monte Carlo simulations. We used four diagnostics for the electron density, n_e, which are based on lines of sulfur, oxygen, chlorine, and argon. We decided to use the average electron density of n_e([OII]) and n_e([SII]) since n_e([ClIII]) and n_e([ArIV]) are more uncertain at the low densities that we find for our objects. We computed electron temperature, T_e, using five diagnostics: T_e([NII]), T_e([OII]), T_e([OIII]), T_e([SIII]) and T_e([ArIII]). We used T_e([NII]) as the representative temperature for the low-ionization-degree zone because the emission lines used to determine T_e([OII]) are affected by recombination and density variations. For the high-ionization-degree zone we used T_e([OIII]) because some of the emission lines used to determine T_e([SIII]) are affected by telluric absorption and T_e([ArIII]) has higher uncertainties than T_e([OIII]).

The ionic abundances were calculated for all the available ions assuming the two-zone scheme. The total oxygen abundance was calculated by adding O^+/H^+ and

[1] IRAF is distributed by the National Optical Astronomy Observatories, which are operated by the Association of Universities for Research in Astronomy, Inc., under cooperative agreement with the National Science Foundation.

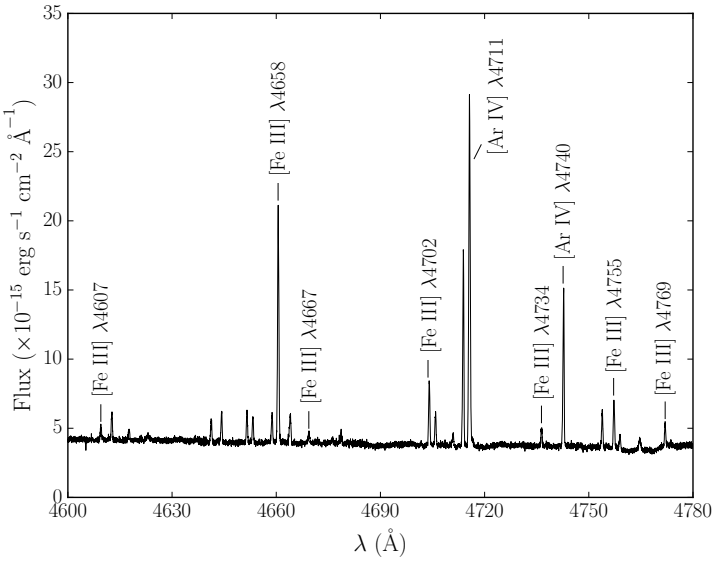

Figure 1. Part of the spectrum of the HII region N 81 in the SMC.

O^{++}/H^{+} when HeII lines were not observed; otherwise we used the ionization corrector factor (ICF) given by Delgado-Inglada et al. (2014). For nitrogen, we used the classical ICF, $N/O = N^{+}/O^{+}$, as suggested by Delgado-Inglada et al. (2015). For iron, we used the two ICFs given by Rodríguez & Rubin (2005), since they provide extreme values of the total iron abundance that can be used to constrain the real value. For the rest of the elements we used the ICFs given by Delgado-Inglada et al. (2014). The uncertainties introduced by the ICFs are not considered in our final results.

Fig. 2 shows the oxygen abundance as a function of the ionization degree for all our observed objects (filled symbols). The orange squares are HII regions from the LMC and the blue stars are HII regions from the SMC. We include other objects from the literature as empty symbols (Tsamis et al. 2003; Nazé et al. 2003; and Peimbert 2003). We can see that the O abundance is higher for the LMC than the SMC by ~ 0.38 dex. In Fig. 3 we plot the abundance ratios N/O, S/O, Cl/O, and Ar/O with respect to oxygen as a function of the ionization degree. The S/O, Cl/O, and Ar/O abundance ratios are similar in both clouds within the uncertainties. There might be a difference in the S/O ratio between the two MCs, but the dispersion is too large to reach a definitive conclusion. The N/O ratio is clearly different in the two MCs, probably due to differences in the chemical evolution of each galaxy. For Ar, there seems to be a problem with the ICF, since the abundances show a trend with the ionization degree.

Fig. 4 shows the values of the depletion factors for Fe derived with the two ICFs as a function of the oxygen abundance for all the objects. The colored and gray symbols are based on the ICFs from equation (2) and (3) of Rodríguez & Rubin (2005), respectively. We include in the figure several Galactic HII regions (green

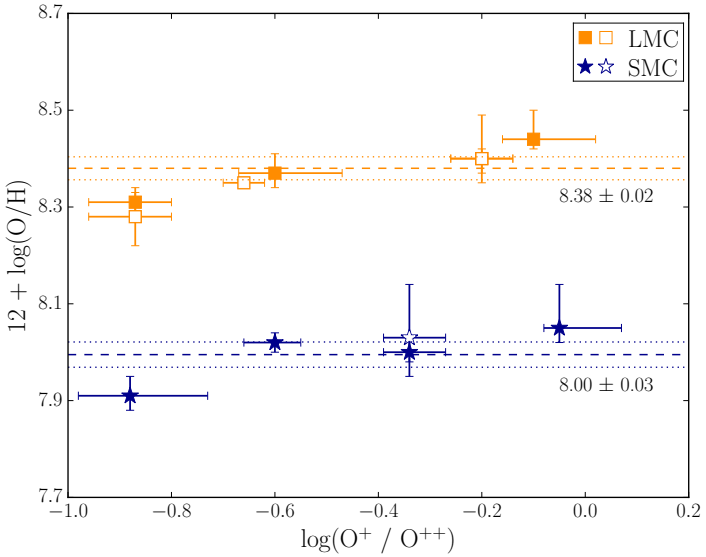

Figure 2. Oxygen abundances as a function of the ionization degree. The orange squares are HII regions in the LMC and the blue stars are HII regions in the SMC. The filled symbols represent our observed sample and the empty ones are based on spectra collected from the literature. The orange and blue dashed lines show the mean oxygen abundances in the LMC and the SMC, respectively; the dotted lines show the standard deviation of the mean.

diamonds), HII galaxies (purple circles), and irregular galaxies (cyan triangles) from the literature. We performed the analysis in the same way as for the main sample. We see that the iron depletions into dust grains in HII regions of the LMC are similar to those found in Galactic nebulae. The SMC also shows this behavior but with a wider range of iron depletions.

4. Conclusions

We present new determinations of chemical abundances of 8 HII regions in the MCs, 4 in the LMC and 4 in the SMC, using deep echelle spectra taken at the VLT. The main conclusions are:

- O/H is higher in the LMC by ~ 0.38 dex.
- Cl/O and Ar/O are similar in both clouds within the uncertainties.
- S/O shows a large dispersion, but it might be higher in the LMC.
- N/O is higher by $\sim$0.2 dex in the LMC.

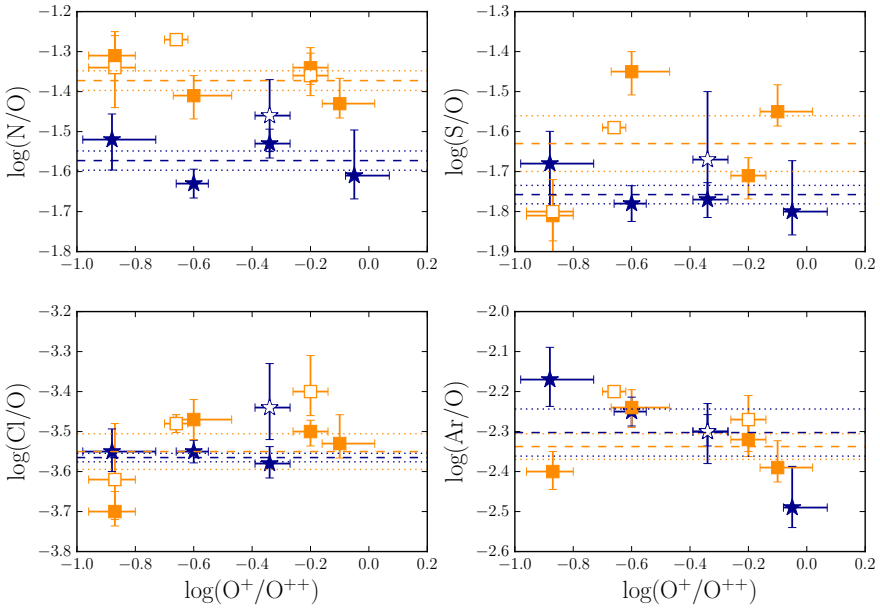

Figure 3. N/O, S/O, Cl/O, Ar/O abundance ratios as a function of the ionization degree. The color code is the same as in Fig. 2.

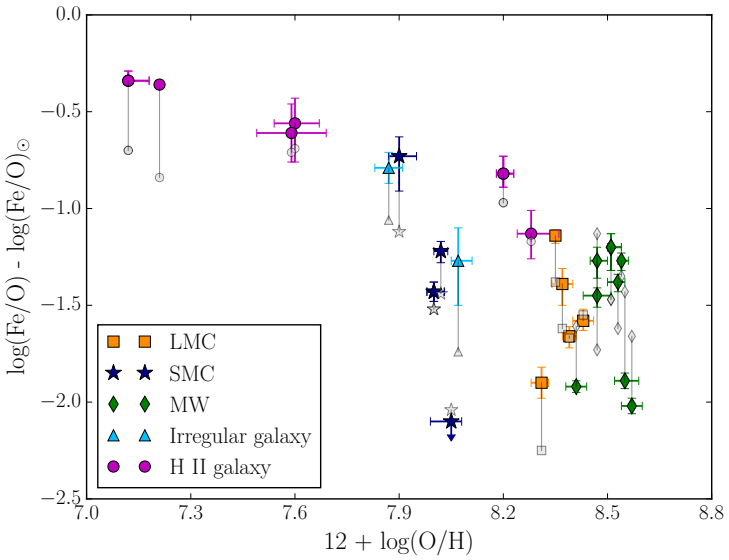

Figure 4. The depletion factor for iron as a function of the oxygen abundance. The colored symbols are for the ICF from equation (2) of Rodríguez & Rubin (2005); the gray ones use the ICF from their equation (3).

• The amount of iron depletion into dust grains in HII regions of the MCs is similar to that found in Galactic HII regions.

Acknowledgments. We acknowledge support from Mexican CONACYT grant CB-2014-240562 and from MINECO under grant AYA2015-65205-P. G.D.-G. acknowledges support from CONACYT grant 297932.

References

Delgado-Inglada G., Morisset C., Stasińska G., 2014, *MNRAS*, **440**, 536
Delgado-Inglada G., Rodríguez M., García-Rojas J., et al., 2011, *Revista Mexicana de Astronomia y Astrofisica Conference Series*, Vol. 40, pp 165–166
Delgado-Inglada G., Rodríguez M., Peimbert M., et al., 2015, *MNRAS*, **449**, 1797
Luridiana V., Morisset C., Shaw R. A., 2015, *A&A*, **573**, A42
Nazé Y., Rauw G., Manfroid J., et al., 2003, *A&A*, **408**, 171
Peimbert A., 2003, *ApJ*, **584**, 735
Rodríguez M., Rubin R. H., 2005, *ApJ*, **626**, 900
Tsamis Y. G., Barlow M. J., Liu X.-W., et al., 2003, *MNRAS*, **338**, 687

Chemical Abundances in Gaseous Nebulae
AAA Workshop Series 10, 2016
G. Hägele, M. Cardaci & E. Pérez-Montero, eds.

Contributed Paper

Giant star-forming regions in interacting galaxies

V. Firpo[1,2], G.F. Hägele[3,4], G. Bosch[3,4], S. Torres-Flores[1],
F. Campuzano-Castro[3,4]

[1]*Departamento de Física y Astronomía, Universidad de La Serena, Chile*
[2]*Gemini Observatory*
[3]*FCAG-Universidad Nacional de La Plata, Argentina*
[4]*Instituto de Astrofísica de La Plata-CONICET, Argentina*

Abstract. The most violent processes of star formation can be found in interacting galaxies, where gas compression can trigger the formation of giant star-forming regions. Using high-resolution spectroscopic information from MIKE/Magellan and multi-slit data from GMOS/Gemini-South, we propose to improve our knowledge in the chemodynamics of extragalactic star-forming regions. The current analysis is based on a sample of star-forming regions located in strongly interacting galaxies. A detailed study of the ionized gaseous component in these regions reveals a complex internal kinematics, which can be identified by asymmetric line profiles and multiple components. The kinematic information suggests that these star-forming objects correspond to giant complexes. Future estimations of physical properties such as the electron densities, temperatures and chemical abundances of the different kinematical components will allow us to determine the chemodynamical state of these star-forming objects. This information will be extremely useful to understand the evolution of these systems in interacting galaxies.

1. Introduction

Giant star-forming regions are extended and luminous objects. They are observed on the discs of spiral, irregular, and dwarf galaxies. They have L(Hα)$\sim$10^{40} erg s^{-1} due to the presence of a young star cluster containing hundreds of massive stars, and the typical sizes are $\sim$100 pc in diameter. In general, they are multiple regions which may be resolved into several components and they are places of very active star formation-(recent or ongoing massive SF). The overall objective in this work is to study Giant HII Region candidates and their impact on the host galaxy evolution (in spiral, compact and interacting galaxies).
The work consists in analyzing the gaseous component, through the study of kinematical and physical properties for the global and different kinematical components. We analyse the line profile asymmetries and multiple components, and determine the radial velocities and the velocity dispersion in all emission line profiles (Firpo et al., 2005, 2010, 2011). In order to verify the nature of our Giant HII

Region candidates, we obtain high-resolution spectra to measure the emission-line profile widths and estimate if the velocity dispersion is indeed supersonic. Then, we estimate electron densities and temperatures, chemical abundances, reddening and ionization structure for these regions (Hägele et al., 2012).

2. Observations

We obtained high-resolution spectroscopic data from MIKE/echelle at the 6.5-m Magellan II (Clay) Telescope (LCO), and echelle and longslit spectroscopic of 100-inch du Pont telescope (LCO). The spectral range covered by MIKE observations was 3300-9200Å by echelle/du Pont was 3400-10000Å and by longslit/du Pont was 3800-9300Å. These spectral ranges guarantee the simultaneous measurement of the nebular emission lines from [OII]3727,29Å to [SIII]9069,32Å. The resolution for MIKE data is ∼25000 (at 6000Å ∼11 km s^{-1}), echelle/du Pont is R∼25000 (at 6000Å ∼12 km^{-1}), and for longslit/du Pont R∼900.

3. Chemodynamics

Chemodynamics (Esteban & Vílchez, 1992) is a detailed analysis after merging chemical and kinematical information obtained from the gaseous component. The analysis is done using the global emission and for the different kinematical components present in the emission-line profiles. In Firpo et al. (2011), we presented a detailed study of the internal kinematics of the nebular material in multiple regions of the galaxy Haro 15 from echelle spectroscopy. We performed a thorough analysis of its emission lines, including multiple-component fittings to the profiles of their strong emission lines. Our results show that the giant HII regions of Haro 15 present a complex structure in all their emission profiles, detected both in recombination and forbidden lines. In Hägele et al. (2012), we performed a chemodynamical analysis of the physical characteristics of the ionized gas in Haro 15, distinguishing among individual components and global line fluxes. Electron temperatures and densities were estimated and used to derive ionic and total abundances for all the different species such as O, S, Ne and Ar. We derived abundances using the temperatures calculated using the direct method or from model-based and empirical temperature relationships (see Fig. 1).

In knot B of Haro 15 galaxy, we carried out a chemodynamical analysis applying the direct method to the kinematical components. We were able to estimate Te([OIII]) and Te([SIII]) using the direct method through the deconvolution of the emission profile for the different kinematical components of the [OIII]4363Å and [SIII]6312Å auroral emission lines (Fig. 2 shows the [OIII]4363Å emission line in the flux-velocity plane with its kinematical decomposition).

Finally, we compared the total oxygen abundances for the global measure and for different kinematical components in each regions with derived abundances using the different strong-line empirical calibrators. In general, the estimated abundances using the empirical calibrators are consistent with the derived abundances using the temperatures calculated from the direct method or from model-based and empirical temperature relationships.

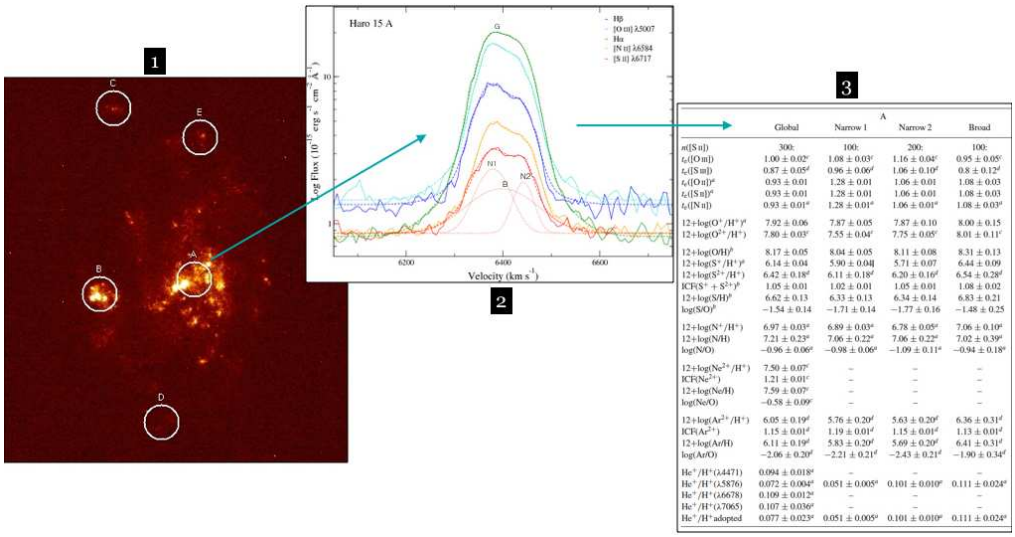

Figure 1. *Image 1:* Example of the chemodynamical analysis in the region Haro 15 A (Fig. 3 from Firpo et al., 2011). *Image 2* show the validity of the profile multiplicity and broadening is checked over the different emission lines, becoming more evident in the strongest emission line such as Hα and [OIII]. *Image 3* shows the table with the derived physical parameters (part of Table 8 from Hägele et al., 2012).

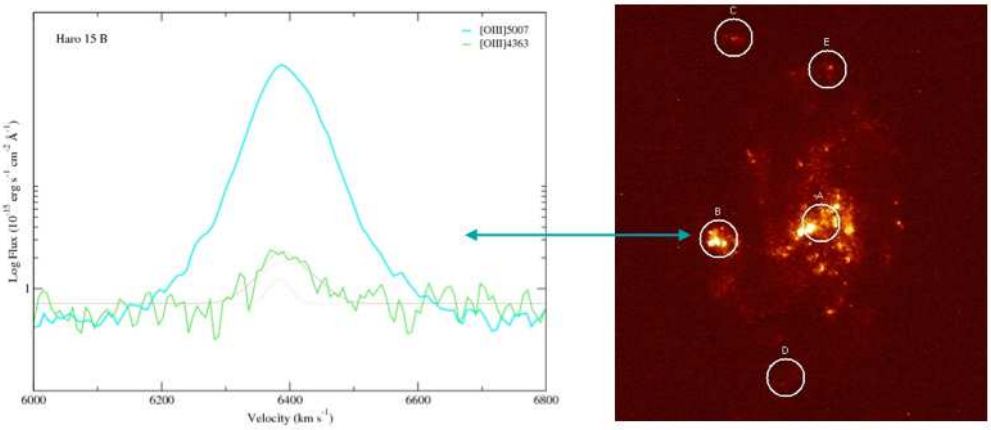

Figure 2. O[III]4363Å auroral emission line in the flux-velocity plane with its kinematical decomposition.

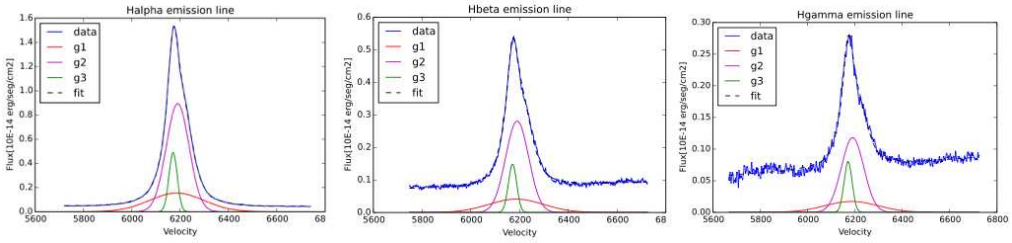

Figure 3. Multiple component fittings to the recombination emission line profiles in a region of NGC 6845 A galaxy. *Left to Right:* Hα, Hβ, Hγ.

4. Chemodynamics in interacting galaxies

In 2014, as part of a collaboration with Torres-Flores, we obtained MIKE/echelle (Magellan Telescope at LCO) high-resolution spectroscopic observations of six star-forming regions located in a sample of three interacting and merging galaxies. In one of these galaxies, NGC 6845 A, which is part of a compact group of galaxies, we started the analysis of the emission line profiles in two star-forming regions. Recombination emission line profiles revel a complex internal kinematics in which we can distinguish and resolve multiple kinematical components (see Fig. 3). Our next work is to improve the multiple component fits in the different emission profiles, and to obtain a chemodynamical analysis for these star-forming regions.

Acknowledgments. This work was supported by CONICYT + Programa de Astronomía + Fondo GEMINI-CONICYT, convocatoria Research Fellow 2015.

References

Esteban C., Vílchez J. M., 1992, *ApJ*, **390**, 536
Firpo V., Bosch G., Hägele G. F., et al., 2011, *MNRAS*, **414**, 3288
Firpo V., Bosch G., Hägele G. F., Morrell N., 2010, *MNRAS*, **406**, 1094
Firpo V., Bosch G., Morrell N., 2005, *MNRAS*, **356**, 1357
Hägele G. F., Firpo V., Bosch G., et al., 2012, *MNRAS*, **422**, 3475

Chemical Abundances in Gaseous Nebulae
AAA Workshop Series 10, 2016
G. Hägele, M. Cardaci & E. Pérez-Montero, eds.

Contributed Paper

Gas metallicity of polar ring galaxies as a probe of their formation scenario

O. Egorov[1] and A. Moiseev[1,2]

[1]*Sternberg Astronomical Institute, Lomonosov Moscow State University, Universitetsky pr. 13, Moscow 119234, Russia*
[2]*Special Astrophysical Observatory, Russian Academy of Sciences, Nizhnii Arkhyz 369167, Russia*

Abstract. We estimated oxygen abundance of polar structures in the sample of 15 polar ring galaxies using the long-slit spectral observations made with 6-m SAO RAS telescope. The measured values of the gas metallicity are sub-solar and consistent with the luminosity in B band for each galaxy from our sample. We did not detect a metal-poor gas in their disk. The results of this study were used to constrain the formation history of polar components in each galaxies. We ruled out scenario of the polar rings formation due to cold accretion from cosmic filaments for these galaxies.

1. Introduction

Polar ring galaxies (PRGs) are the most famous type of so-called multi-spin galaxies, which represent the systems with an external disks or rings rotating at the plane nearly perpendicular to the host galaxy (usually early type galaxy). First catalogue of PRGs candidates selected from photographic plates was compiled by Whitmore et al. (1990). It includes 157 objects. Second catalogue, SDSS-based Polar Rings Catalogue (SPRC), was presented by Moiseev et al. (2011). It contains 275 objects, 185 of them were classified as a good and best candidates. Thus, currently we know several hundreds PRGs candidates; several tens of them are kinematically confirmed.

Despite the large amount of known PRGs, they are still relatively poor studied. In particular, mechanism of the formation of polar components in PRGs is a topic of hot debates. Several scenarios were proposed: a major merging scenario (Bekki, 1997; Bournaud & Combes, 2003); tidal accretion from a disrupted small companion on a polar orbit or from a gas-rich donor galaxy (Schweizer et al., 1983; Reshetnikov & Sotnikova, 1997); cold accretion from cosmic filaments (Macciò et al., 2006). Among them the last one seems to be a most intriguing. It is believed that the accretion of gas along filaments is a very common process and it should take place even at low redshifts (Dekel et al., 2009), but due to chemical and dynamical evolution of galaxies it is very hard to find a tracer of this process. Steiman-Cameron & Durisen (1982) showed that polar orbits around a host galaxy in the case of oblate or triaxial gravitational potential are very stable and slowly evolved. Because of that, if the cold accretion is

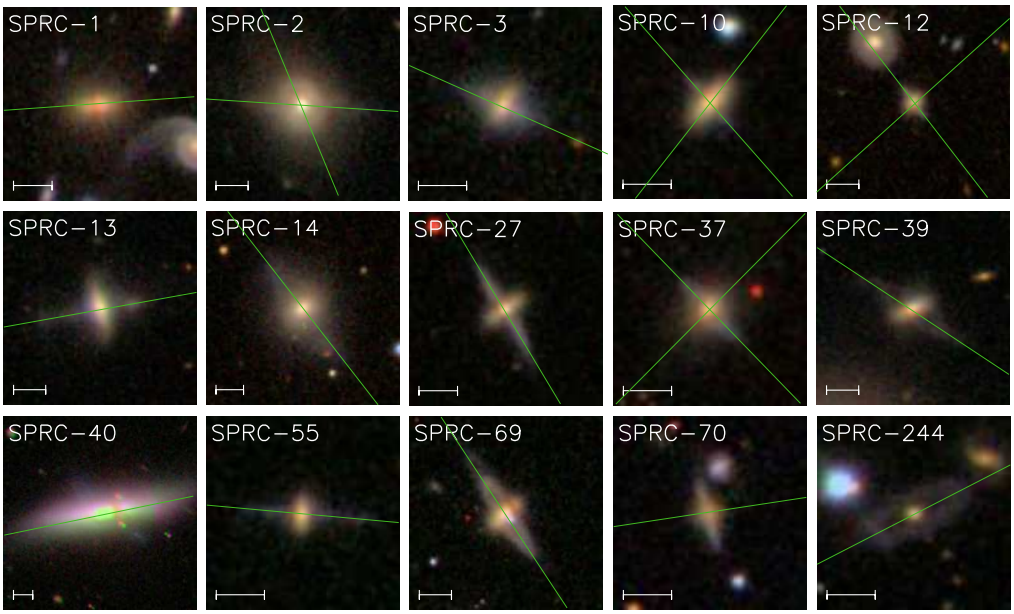

Figure 1. A color combination of SDSS images of the sample galaxies in g, r, i filters. Slit position used during the observations is shown by green line. The scale bar corresponds to the angular size of 10 arcsec.

indeed responsible for polar rings formation, then PRGs should still represens of this process. The important clue to distinguish between different scenarios should be a measuring of chemical abundances of the PRGs.

Up to now, the metallicity measurements were made only for the few PRGs. For some of them authors indeed obtained a low gas metallicity values, which are consistent with the hypothesis of a cold accretion from a cosmic filament Spavone et al. (see, e.g., 2010, 2015, and references therein). Unfortunately, many of these results have a very large uncertainties or correspond to unrealistic physical values, so they might be unreliable. Therefore, new measurements of gas metallicity in large samples of PRGs are still needed to disentangle between possible evolution scenarios of their formation.

Here we present some basic findings of our work aimed to study the ionization conditions in PRGs and to increase a number of PRGs with a known gas metallicity values. Complete results as well as detailed description of the performed observations and data analysis will be published in a forthcoming paper Egorov & Moiseev (in preparation). First results of our metallicity analysis for SPRC-10,14 and 39 galaxies were presented in Moiseev et al. (2014).

2. Observations and data analysis

We have selected 15 galaxies (see Fig. 1) from SPRC catalogue for current analysis. Their observations were made at the prime focus of the 6-m telescope of SAO RAS using the SCORPIO-2 multi-mode focal reducer (Afanasiev & Moiseev, 2011) operating in the long-slit spectrograph mode with a 6 arcmin ×

1 arcsec slit. The scale along the slit was 0.36 arcsec per pixel. A total exposure time was varied from 2700 to 7200 sec and a seeing – from 1.0 to 2.9 arcsec for different objects. The observations were performed with VPHG1200@540 grism, which provides a spectral resolution $\delta\lambda \sim 4.5$Å (estimated by the FWHM of air glow lines).
Initial data reduction was performed in a standard way using the IDL software package written for reducing long-slit spectroscopic data obtained with SCORPIO-2. Before analysing the emission spectrum we have subtracted the stellar population models from each spectrum. These models were recovered from the observed spectra using the ULYSS package (Koleva et al., 2009). Because of possible differences between the chemical abundances and excitation mechanisms of the host galaxies and their polar components, we analyzed the regions where a slit crossed the polar component and both polar ring and host galaxy separately. Each emission line observed in the spectra was fitted by a single Gaussian.
We used several published methods to measure the oxygen abundance of polar rings in the sample PRGs. Here we report the estimates obtained using O3N2 (Marino et al., 2013) and "counterpart" (C; Pilyugin et al., 2012) methods. Both of them are empirical, i.e. calibrated by HII regions with known metallicity calculated by direct T_e method. Other empirical methods we used during the analysis show the same results, whereas theoretical methods (i.e. calibrated by photoionization models) reveal elevated oxygen abundance.

3. Results and discussion

The results of the gas metallicity of PRGs estimation are summarized in Table 1, where different columns mean the galaxy name (according to SPRC catalogue), its absolute magnitude M_B calculated from the reported SDSS photometry made by Reshetnikov & Combes (2015), the oxygen abundances $12 + \log(\mathrm{O/H})$ of polar ring obtained using O3N2 and C methods.
We found that each galaxy from our sample have sub-solar gas metallicity $Z = 0.4 - 0.7Z\odot$. Despite that, we can present a couple of arguments against the scenario of polar rings formation due to cold gas accretion from cosmic filaments, for which the low gas metallicity is expected:

- First of all, in the case of cold accretion we may expect the gaseous polar disk to be more metal poor than the host galaxy. For several galaxies from our sample the signal-to-noise ratio was good enough to trace the oxygen abundance variations along the polar disk. We found that they reveal flat metallicity gradient and that the metallicity of the outer parts of polar ring and of the regions where it overlaps with the host galaxy are the same within the errors for each PRG in out sample. We were able to estimate the gas metallicities for the few host galaxies of PRG systems: they reveal the same values as in their polar rings (but with larger uncertainties). Thus, we do not see any difference of the oxygen abundance between host galaxies and their polar components.

- In Fig. 2 we show the Luminosity–Metallicity relation for spiral galaxies taken from Pilyugin et al. (2004). On the left panel we overlaid points

Table 1. Oxygen abundance of the studied galaxies

Galaxy	M_B, mag	$12+\log(\mathrm{O/H})_{\mathrm{O3N2}}$	$12+\log(\mathrm{O/H})_{\mathrm{C}}$
SPRC-1	-20.86^*	8.32 ± 0.05	8.25 ± 0.13
SPRC-2	-20.84	8.49 ± 0.27	–
SPRC-3	-18.95	8.40 ± 0.05	–
SPRC-10	-18.53	8.50 ± 0.10	8.45 ± 0.14
SPRC-12	-18.37	8.42 ± 0.08	8.43 ± 0.15
SPRC-13	-19.04	8.37 ± 0.08	8.39 ± 0.09
SPRC-14	-19.71	8.44 ± 0.06	8.45 ± 0.09
SPRC-27	-18.88	8.44 ± 0.05	8.40 ± 0.07
SPRC-37	-19.96	8.39 ± 0.05	–
SPRC-39	-18.17	8.42 ± 0.09	8.37 ± 0.12
SPRC-40	-17.88^*	8.46 ± 0.03	8.44 ± 0.06
SPRC-55	-19.39	8.38 ± 0.04	–
SPRC-69	-18.83	8.47 ± 0.05	8.51 ± 0.09
SPRC-70	-18.91^*	8.43 ± 0.07	8.49 ± 0.07
SPRC-244	-19.33^*	8.39 ± 0.03	–

* Taken from HyperLeda database

corresponding to our oxygen abundance estimates (different colors mean different methods) and to the total absolute magnitude M_B of the sample galaxies. In this figure we also overlaid measurements found in the literature (among all available metallicity estimates we have excluded several very uncertain with reported errors more than 0.5 dex). As it follows from this figure, the oxygen abundance of the galaxies from our sample is consistent with their total luminosity.

We used the total luminosity of the galaxies to prepare the plot shown on left panel of Fig. 2, but probably it would be better to use the luminosity of the polar ring only. If chemical abundance of the gas in polar rings are regulated mostly by the evolution of the whole galaxy, then the total luminosity reflects the physics in luminosity-metallicity relation. On the other hand, if the polar structures were formed by external processes like a tidal accretion and the majority of metals in the gaseous disk were presented in the donor galaxy, then the luminosity of the polar ring only (which is a lower limit of donor galaxy luminosity) should be related with the metallicity. On right panel of Fig. 2 we show the luminosity-metallicity relation for that case.

It is clearly seen in Fig. 2 (especially on right panel) that the metallicity of polar rings in the galaxies from our sample almost do not depend on the galaxy (or polar ring) luminosities. This fact might be easily explained in the frame of the formation of polar component by the tidal accretion scenario. The chemical abundance of the polar ring in that case corresponds to the values typical for the donor galaxy, but only a fraction of its gas was accreted onto the host galaxy and built the polar ring. Hence, the mass of gas and the luminosity of the polar ring could be significantly lower for their metallicity.

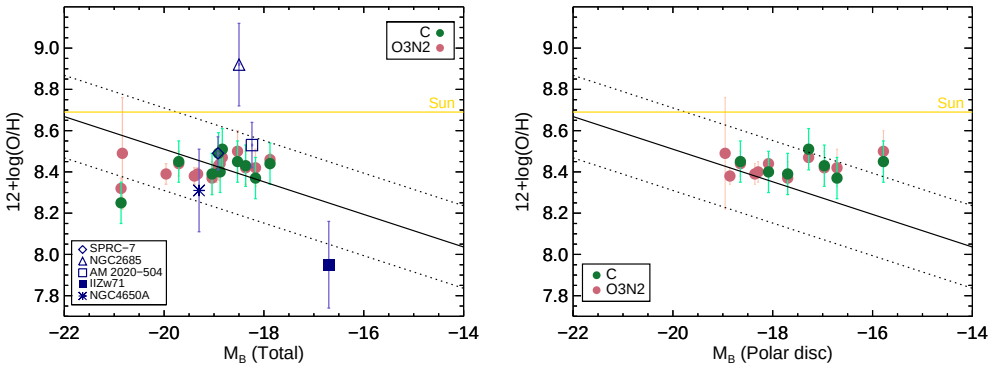

Figure 2. Luminosity–Metallicity relation for our sample galaxies. All points correspond to the total absolute magnitude of galaxy on the left panel and to the magnitude of the polar component only on the right panel. The circles of different color correspond to different calibrators used for metallicity estimation. Other symbols denote the values taken from the literature: SPRC-7 (Brosch et al., 2010), NGC 2685 (Eskridge & Pogge, 1997), AM 2020–504 (Freitas-Lemes et al., 2012), IIZw 71 (Pérez-Montero et al., 2009), NGC 4650A (Spavone et al., 2010). Black solid line shows the O/H – M_B relationship for spiral galaxies (Pilyugin et al., 2004); dashed lines correspond to its uncertainty (±0.2 dex).

4. Conclusions

Using the spectral observations performed with the 6-m SAO RAS telescope we estimated the gas metallicity in 15 PRGs from SPRC catalogue. Our results significantly increase the number of available measurements of chemical abundance in PRGs.

Despite the spread of absolute magnitudes M_B from about -20.9^m to -17.9^m, all galaxies from our sample have similar sub-solar oxygen abundance $12 + \log(\mathrm{O/H}) \sim 8.3 - 8.5$ dex. The estimated metallicities for these galaxies are consistent with their luminosities. Hence, we do not observe the low metallicity gas expected in the case of the cold accretion scenario of polar rings formation. We observe an absence of a clear dependence of metallicity on luminosity, as well as the oxygen overabundance of some galaxies in comparison with metallicities typical for luminosity of their polar rings. It might be easily explained if the PRGs were formed as a result of tidal accretion of the gas from another galaxy.

Acknowledgments. This work is based on observations obtained with the 6-m telescope of the Special Astrophysical Observatory of the Russian Academy of Sciences carried out with the financial support of the Ministry of Education and Science of the Russian Federation (agreement No. 14.619.21.0004, project ID RFMEFI61914X0004). The study was supported by the Russian Science Foundation, project No. 14-22-00041.

References

Afanasiev V. L., Moiseev A. V., 2011, *Baltic Astronomy*, **20**, 363
Bekki K., 1997, *ApJL*, **490**, L37
Bournaud F., Combes F., 2003, *A&A*, **401**, 817
Brosch N., Kniazev A. Y., Moiseev A., Pustilnik S. A., 2010, *MNRAS*, **401**, 2067
Dekel A., Birnboim Y., Engel G., et al., 2009, *Nature*, **457**, 451
Eskridge P. B., Pogge R. W., 1997, *ApJ*, **486**, 259
Freitas-Lemes P., Rodrigues I., Faúndez-Abans M., et al., 2012, *MNRAS*, **427**, 2772
Koleva M., Prugniel P., Bouchard A., Wu Y., 2009, *A&A*, **501**, 1269
Macciò A. V., Moore B., Stadel J., 2006, *ApJL*, **636**, L25
Marino R. A., Rosales-Ortega F. F., Sánchez S. F., et al., 2013, *A&A*, **559**, A114
Moiseev A., Egorov O., Smirnova K., 2014, E. Iodice and E. M. Corsini (eds.), *Multi-Spin Galaxies*, Vol. 486 of *Astronomical Society of the Pacific Conference Series*, p. 71
Moiseev A. V., Smirnova K. I., Smirnova A. A., Reshetnikov V. P., 2011, *MNRAS*, **418**, 244
Pérez-Montero E., García-Benito R., Díaz A. I., et al., 2009, *A&A*, **497**, 53
Pilyugin L. S., Grebel E. K., Mattsson L., 2012, *MNRAS*, **424**, 2316
Pilyugin L. S., Vílchez J. M., Contini T., 2004, *A&A*, **425**, 849
Reshetnikov V., Combes F., 2015, *MNRAS*, **447**, 2287
Reshetnikov V., Sotnikova N., 1997, *A&A*, **325**, 933
Schweizer F., Whitmore B. C., Rubin V. C., 1983, *AJ*, **88**, 909
Spavone M., Iodice E., Arnaboldi M., 2015, *MNRAS*, **450**, 998
Spavone M., Iodice E., Arnaboldi M., et al., 2010, *ApJ*, **714**, 1081
Steiman-Cameron T. Y., Durisen R. H., 1982, *ApJL*, **263**, L51
Whitmore B. C., Lucas R. A., McElroy D. B., et al., 1990, *AJ*, **100**, 1489

Chemical Abundances in Gaseous Nebulae
AAA Workshop Series 10, 2016
G. Hägele, M. Cardaci & E. Pérez-Montero, eds.

Contributed Paper

The two faces of low-ionization knots in Planetary Nebulae

S. Akras[1,2]

[1] *Observatório do Valongo, Universidade Federal do Rio de Janeiro, Ladeira Pedro Antonio 43, 20080-090, Rio de Janeiro, Brazil*
[2] *Observatório Nacional/MCTIC, Rua Gen. José Cristino, 77, 20921-400, Rio de Janeiro, Brazil*

Abstract. Some planetary nebulae possess, in addition to large-scale structures such as rims, shells and haloes, various small-scale structures like knots, jets and filaments bright in low-ionization lines ([NII], [OII], [OI], and [SII]). Here, I present the first study on these structures using emission line ratios and kinematic characteristics. New diagnostic diagrams are used for distinguishing shock-excited from photo-ionized structures. These diagrams seems to offer insights into the basic processes of excitation mechanism. The shock-excited regions have $\log(f_{shocks}/f_\star)>-1$, the photo-ionized regions have $\log(f_{shocks}/f_\star)<-2$, whereas both mechanisms are important in a narrow transition zone with $-2< \log(f_{shocks}/f_\star)<-1$. Moreover, H_2 emission has also been detected in the LISs of two PNe, namely K 4-47 and NGC 7662. The H_2 1-0 S(1)/2-1 S(1) and H_2 1-0 S(1)/Br-γ line ratios indicate shock heated LISs in K 4-47 and a mixture of UV radiation and shock heating mechanisms in the LISs of NGC 7662.

1. Introduction

Several planetary nebulae (PNe) have been found to possess, in addition to large-scale structures such as rims, shells and haloes, various small-scale structures like knots, jets (Balick, 1987; Balick et al., 1998; Corradi et al., 1996; Gonçalves et al., 2001). The typical spectrum of these structures is dominated by low-ionization emission lines such as [OI], [NII], [SII], [OII] with a weak emission from doubly ionized ions (e.g. [OIII]). Because of their strong emission in low-ionization lines the acronym LISs (Low Ionization Structures) has been given (Gonçalves et al., 2001).
The first interpretation of the strong [NII] emission was an overabundance of nitrogen in these structures (Balick et al., 1994). It is now well known that this is not a necessary condition. It has been shown by several authors that there is no difference in chemical composition or electron temperature between the LISs and the surrounding medium (e.g. Gonçalves et al., 2009; Akras & Gonçalves, 2016). Akras & Gonçalves (2016) show that the enhancement of low ionization lines is the result of different degree of ionization in LISs. What alters the ionization structure in the LISs but not in the rest of the nebula?

2. Expansion velocities

LISs cover a wide range of expansion velocities from a few ten of km s^{-1} up to a few hundreds km s^{-1} and because of that the acronyms FLIERs (Fast Low Ionization Emission; Balick et al., 1993) and SLOWERs (Slow moving Low Ionization Emitting Regions; Perinotto et al., 2004) have been given in order to distinguish them based on their expansion velocities. Are FLIERs shocked-excited structures and SLOWERs photo-ionized structures? To answer that question we have to be able to classify and disentangle the shock-excited from the photo-ionized regions.

There is a number of PNe that have emission line ratios (e.g. [NII]/Hα and [SII]/Hα) similar to those of young supernova remnants (see Fig. 7 in Sabin et al., 2013), in which the main excitation mechanisms is shock interactions. Highly-evolved PNe is a subgroup that show strong [NII] $\lambda\lambda$ 6548,6584 and [SII] $\lambda\lambda$ 6716, 6731 lines as well as strong [OI] λ 6300 and [NI] λ 5200 (Akras et al., 2016b). The central stars of that group of PNe have already entered the white dwarf cooling track forming low-excitation nebulae. Pure photo-ionization models have adequately reproduced the [NII], [OII], [SII] emission lines but not the neutral lines [OI], [NI] (Ali et al., 2015; Akras et al., 2016a). Adding a low velocity shock of 25 km s^{-1} to the pure photoionization model of the highly-evolved PN G342.0-01.7, Ali et al. (2015) could reproduce all the emission lines simultaneously and they explain that low velocity shock as the result of the interaction between the expanding nebula and the interstellar medium. This signify that even low-velocity shocks are important on the ionization structure of PNe, but when these shocks become important?

Parameters such as the distance from the central star, T_{eff}, luminosity, N_e and expansion velocity are crucial to answer that question and have to be taken into account. The optical diagnostic diagrams proposed by Akras & Gonçalves (2016) explain the enhancement of low-ionization lines as the result of shock interactions in an ionized environment, with either low or high velocity (see also Raga et al., 2008).

Fig. 1 shows two diagnostic diagrams between the [SII]/Hα and [NII]/Hα emission line ratios with the $\log(f_{shocks}/f_\star)$ parameter (Akras & Gonçalves, 2016) for a sample of PNe with LISs and a number of model by Raga et al. (2008). Three distinct regions can be defined in these plot: (a) the shock-excited region at the upper-right corner of the plots with $\log(f_{shocks}/f_\star) > -1$, (ii) the photo-ionized region at the lower-left corner with $\log(f_{shocks}/f_\star) < -2$ and (iii) the transition zone with $-2 < \log(f_{shocks}/f_\star) < -1$, where both mechanism are equally important. Most of the LISs are found to be located in (or close to) the region of shock-excited without being necessarily FLIERs.

3. Electron density

It is well known that the electronic density, N_e, is systematically lower (or equal at least) in LISs than in the surrounding medium (e.g. Gonçalves et al., 2009; Akras & Gonçalves, 2016). This result is found to be inconsistent with the formation models of LISs, which predict the exact opposite result (e.g. Dopita, 1997; Steffen et al., 2001; García-Segura et al., 2005; Soker & Livio, 1994). It

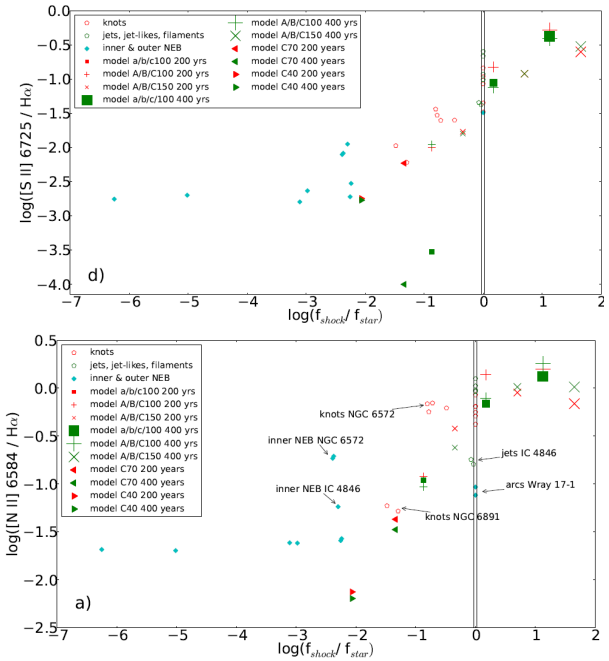

Figure 1. Plots of [SII]/Hα (upper panel), [NII]/Hα (lower panel) vs. log($f_{shocks}/f_{\star}$).

should be noted that the formation models usually refer to the total density (dust, atomic and molecular) and not only to the N_e. Therefore, the question that rises is: Are LISs also made of molecular/atomic gas?

Despite several PNe have been found to exhibit strong H_2 lines, very little work has been done on the H_2 emission in LISs, except those by Matsuura and collaborators on the cometary knots of Helix (Matsuura et al., 2008, 2009). The strong [OI] emission line usually detected in LISs may indicate the presence of molecular H_2 gas. A linear relation between the fluxes of H_2 v=1-0 and the [OI] λ 6300 lines was presented by Reay et al. (1988). More recently, high-angular-resolution adaptic optics H_2 images unveiled a highly knotty and filamentary structure in the bipolar nebula NGC 2346 (Manchado et al., 2015).

To test the scenario of H_2 gas in LISs, two PNe were observed with the NIRI instrument at the Gemini-North telescope. The narrow-band G0216, G0218 and G0220 filters, centered at 2.1239, 2.1686 and 2.2465 μm respectively, were applied to isolate the H_2 v=1-0 S(1), Brγ and H_2 v=2-1 S(1) lines, respectively. In Fig. 2, we present the continuum-subtracted images of K 4-47 and NGC 7662. This is the first observational confirmation of molecular gas in LISs.

K 4-47 is a highly collimated young PN with a pair of fast-moving knots bright in [NII] and [OI] emission lines (Corradi et al., 2000). The radiation field of its central star alone cannot provide an explanation for such bright emission lines. High-velocity shocks of 250-300 km s^{-1} have been proposed to explain these lines (Gonçalves et al., 2004). The R(H_2)=H_2 1-0 S(1)/2-1 S(1) and R(Brγ)=H_2 1-0 S(1)/Br-γ line ratios of these knots strongly indicate shock interactions.

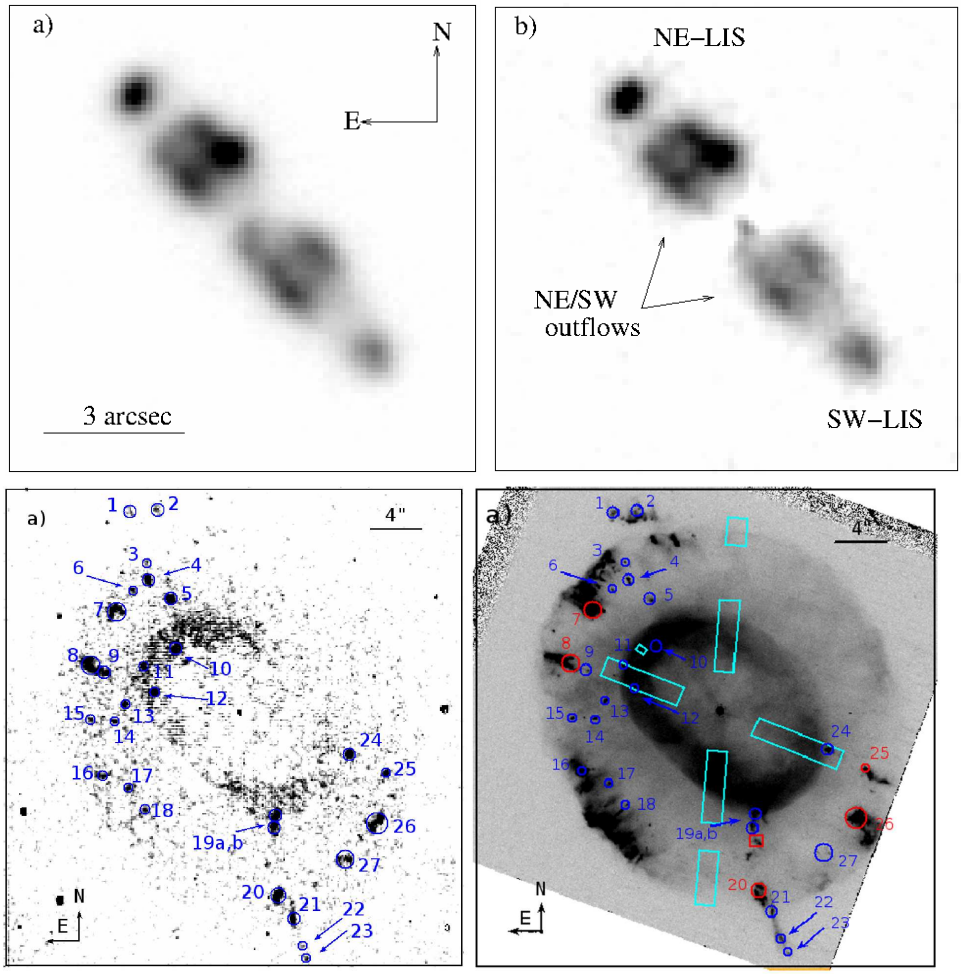

Figure 2. Emission line images of K 4-47 (left panels): H_2 v=1-0 S(1) (panel a), H_2 v=2-1 S(1) (panel b). Emission line images of NGC 7662 (right panels): H_2 v=1-0 S(1) (panel a), HST N/O line ratio image (panel b). The circles (in both lower panels) refer to the low-ionization emission lines (LISs) detected in H_2. The red circles and cyan boxes in panel (b) indicate LISs and nebular regions with available optical spectra. The box size is 35×37 arcsec^2.

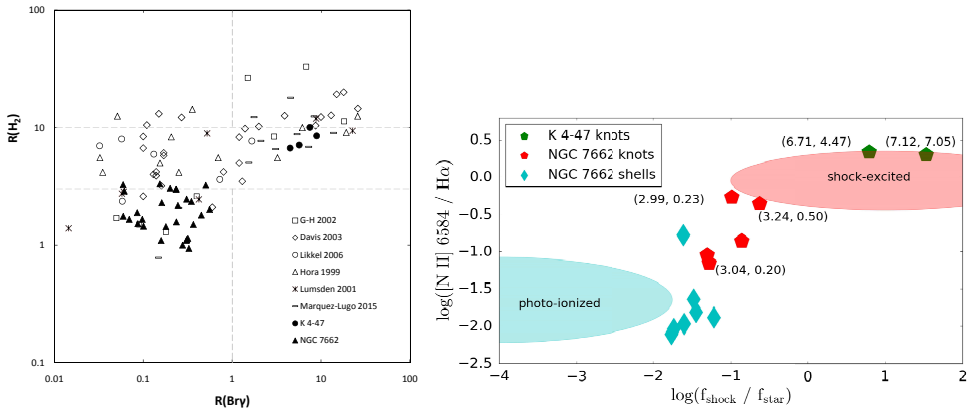

Figure 3. Left panel: R(H_2) vs. R(Br-γ) line ratio diagram from Marquez-Lugo et al. (2015) including the values of K 4-47 (filled circles) and NGC 7662 (filled triangles). Right panel: The optical diagnostic diagram from Akras & Gonçalves (2016). The numbers in the parenthesis refer to the R(H_2) and R(Br-γ) line ratios.

Regarding the elliptical PN NGC 7662, several LISs are found to be H_2 emitters. UV-photons from the central star is likely the main heating mechanism in these structure, as their expansion velocities are very low. The R(H_2) and R(Brγ) line ratios also imply that these LISs are predominantly photo-ionized structures.
Fig. 3 (left panel) displays the R(Brγ) versus R(H_2) plot for K 4-47 and NGC 7662 including a number of PNe (Marquez-Lugo et al., 2015). It is clear that the dominant heating mechanism is different. The optical diagnostic diagram illustrates that the knots of K 4-47 are well placed in the region of shock-excited regions, whereas the knots of NGC 7662 are found in the transition zone, where both heating mechanisms are important (Fig. 3, right panel). By comparing the knots and nebular regions (cyan symbols in Fig. 3), it is apparent that the LISs of NGC 7662 have an extra heating by shocks.

4. Conclusions

Shocks, either of high or low velocities, are an important mechanism in the ionization structure of LISs and of course in PNe, providing an extra source of heating for their thermal gas, which results in increasing the intensity of low-ionization emission lines. New diagnostic diagrams, between the emission line ratios and the $\log(f_{shocks}/f_\star)$ parameter, seem to distinguish well the shock-excited from the photo-ionized regions.
The small number of LISs with confirmed H_2 emission lines compels to continue observing these structure in order to cover a wider range of stellar parameters, N_e, expansion velocities and distances from the central star and better understand the excitation and heating mechanisms.

Acknowledgments. Based on observations obtained at the Gemini Observatory, which is operated by the Association of Universities or Research in

Astronomy, Inc., under a cooperative agreement with the NSF on behalf of the Gemini partnership. This work was partially supported by FAPERJ's grant E-26/111.817/2012 and CAPES's grant A035/2013.

References

Akras S., Clyne N., Boumis P., et al., 2016a, *MNRAS*, **457**, 3409
Akras S., Gonçalves D. R., 2016, *MNRAS*, **455**, 930
Akras S., Gonçalves D. R., Ramos-Larios G., 2016b, *Journal of Physics Conference Series*, Vol. 728, p. 032003
Ali A., Amer M. A., Dopita M. A., et al., 2015, *A&A*, **583**, A83
Balick B., 1987, *AJ*, **94**, 671
Balick B., Alexander J., Hajian A. R., et al., 1998, *AJ*, **116**, 360
Balick B., Perinotto M., Maccioni A., et al., 1994, *ApJ*, **424**, 800
Balick B., Rugers M., Terzian Y., Chengalur J. N., 1993, *ApJ*, **411**, 778
Corradi R. L. M., Gonçalves D. R., Villaver E., et al., 2000, *ApJ*, **535**, 823
Corradi R. L. M., Manso R., Mampaso A., Schwarz H. E., 1996, *A&A*, **313**, 913
Dopita M. A., 1997, *ApJL*, **485**, L41
García-Segura G., López J. A., Franco J., 2005, *ApJ*, **618**, 919
Gonçalves D. R., Corradi R. L. M., Mampaso A., 2001, *ApJ*, **547**, 302
Gonçalves D. R., Mampaso A., Corradi R. L. M., et al., 2004, *MNRAS*, **355**, 37
Gonçalves D. R., Mampaso A., Corradi R. L. M., Quireza C., 2009, *MNRAS*, **398**, 2166
Manchado A., Stanghellini L., Villaver E., et al., 2015, *ApJ*, **808**, 115
Marquez-Lugo R. A., Guerrero M. A., Ramos-Larios G., Miranda L. F., 2015, *MNRAS*, **453**, 1888
Matsuura M., Speck A., Smith M., et al., 2008, *The Messenger*, **132**, 37
Matsuura M., Speck A. K., McHunu B. M., et al., 2009, *ApJ*, **700**, 1067
Perinotto M., Patriarchi P., Balick B., Corradi R. L. M., 2004, *A&A*, **422**, 963
Raga A. C., Riera A., Mellema G., et al., 2008, *A&A*, **489**, 1141
Reay N. K., Walton N. A., Atherton P. D., 1988, *MNRAS*, **232**, 615
Sabin L., Parker Q. A., Contreras M. E., et al., 2013, *MNRAS*, **431**, 279
Soker N., Livio M., 1994, *ApJ*, **421**, 219
Steffen W., López J. A., Lim A., 2001, *ApJ*, **556**, 823

Chemical Abundances in Gaseous Nebulae
AAA Workshop Series 10, 2016
G. Hägele, M. Cardaci & E. Pérez-Montero, eds.

Contributed Paper

Improving the determination of chemical abundances in planetary nebulae

O. Cavichia[1], R.D.D. Costa[2], W.J. Maciel[2] and M. Mollá[3]

[1]*Instituto de Física e Química, Universidade Federal de Itajubá, Av. BPS, 1303, 37500-903, Itajubá-MG, Brazil*
[2]*Instituto de Astronomia, Geofísica e Ciências Atmosféricas, Universidade de São Paulo, 05508-900, São Paulo-SP, Brazil*
[3]*Departamento de Investigación Básica, CIEMAT, Avda. Complutense 40, E-28040 Madrid, Spain*

Abstract.
Planetary nebulae are the products of the evolution of low and intermediate mass stars. The chemical property studies of these objects give important information about the elemental abundances as He, O, Ne, Ar, S and their modifications associated with the evolution of the progenitor stars. The determination of accurate abundances in planetary nebulae is important from the perspective of the stellar evolution as well as the formation and chemical evolution of galaxies. Recently, new HeI emissivities and Ionization Correction Factors (ICFs) were published in the literature. In this work, these new parameters are used in a code for the determination of chemical abundances in photoionized nebulae. This code is used for the recompilation of the chemical abundances of planetary nebulae from the Galactic bulge observed previously by our group and also for the determination of new chemical abundances of a sample of planetary nebulae located near the Galactic center. The new emissivities and ICFs slightly modified the elemental abundances of He, N, O, Ar and Ne. On the other hand, S abundances are higher than previous determinations. The new ICFs can contribute to solve partially the sulfur anomaly.

1. Introduction

The determination of accurate chemical abundances in planetary nebulae (PNe) is very important, since these objects can contribute to studies regarding stellar evolution as well as the chemical evolution of galaxies. Recently, new HeI emissivities have become available in the literature through the work by Porter et al. (2012) and subsequently corrected by Porter et al. (2013), hereafter PFSD13. These are the most recent HeI emissivities, and collisional effects are already included in the emissivities calculation. In this work the emissivities of PFSD13 are adopted in order to calculate the HeI abundances and provide accurate HeI abundances. Usually, the spectral range of the observations is not sufficient to observe all the necessary lines of a given ion, and it is not possible to calcu-

late the total abundance of a particular element by the direct sum of the ionic abundances of all the ions present in a nebula. Instead, it must be calculated by means of the ionization correction factors (ICFs). One of most frequently used ICFs in the literature are those from Kingsburgh & Barlow (1994), hereafter KB94. However, recently Delgado-Inglada et al. (2014), hereafter DMS14, have published new ICFs formulae based on a grid of photoionization models and they have computed analytical expressions for the ICFs of He, O, N, Ne, S, Ar, Cl and C. These new ICFs incorporate more recent physics and are derived using a wider range of parameters of photoionization models than the previous ICFs from KB94. Another advantage of the new ICFs provided by DMS14 is the possibility to compute the errors in the elemental abundances introduced by the adopted ICF approximation. They provide analytical formulae to estimate error bars associated with the ICFs, something not possible until their work. According to DMS14, the oxygen abundances are not expected to be very different from those calculated with the ICFs of KB94. On the other hand, the abundances of N, S, Ar, Ne calculated with the new ICFs show significant differences. However, a direct comparison between the abundances of N, S, Ar and Ne calculated with both ICFs is missing in DMS14. The aim of this work is to use these ICFs and new emissivities to derive chemical abundances of a PNe sample located in the Galactic bulge and also near the Galactic Center (GC).

2. The sample and abundance determinations

The new emissivities and ICFs were used to recalculate the elemental abundances of PNe located in the Galactic bulge from Cavichia et al. (2010), hereafter CCM10. We followed the same procedures described in CCM10, nonetheless using the new emissivities from PFSD13 and ICFs from DMS14. The H^+ emissivities are from Aver et al. (2010) and HeII emissivities are from Osterbrock & Ferland (2006). Also, in 2009 we started an observational program aimed to carrying out a spectroscopic follow-up of high-extinction GBPNe located within 2 degrees of the GC from the catalog of Jacoby & Van de Steene (2004). The Goodman spectrograph at the 4.1 m SOAR telescope at Cerro Pachón (Chile) was used to perform spectroscopic follow-up of 33 objects located within 2 degrees of the GC, in a region of a very high-level of reddening. From those objects, 15 had spectra with acceptable quality to derive physical parameters and chemical abundances. The optical spectra of the GBPNe near the GC suffer for high-level of extinction caused by the material near the Galactic plane and also in the central regions of the Galaxy. As a result, important diagnostic lines as [OIII] λ4363 Å and [NII] λ5755 Å do not have enough S/N ratio to obtain the electron temperature from the temperature diagnostic diagrams. Other important temperature-sensitive lines are those from S^{+3}. In order to observe the near infrared (NIR) [SIII] lines, we started an observational program in 2012 at the Observatório Pico dos Dias (OPD) of National Laboratory for Astrophysics (LNA, Brazil) with the 1.6 m Perkin-Elmer telescope and a Cassegrain Boller & Chivens spectrograph was used. The details of the observations, data reduction, abundances determinations and results can be seen in Cavichia et al. (2017), hereafter C17.

3. Results

The abundances derived using the new HeI emissivities from PFSD13 are compared in Fig. 1 (left panel) with those from Pequignot et al. (1991), hereafter PPB91. The PNe sample used for the comparison is that one from CCM10. As can be seen, some small differences arise when using the new emissivities. From now on, the emissivities from PFSD13 will be used to analyze the differences in the ICFs. A direct comparison between the ICFs from DMS14 and KB94 is provided for N in Fig. 1 (right panel). Most of the abundances are compatible, however for a few objects the N abundance is higher than the one obtained by using the previous ICF. This is regarded as the new ICFs formulae use a wider range of parameters of photoionization models than the previous ICFs .

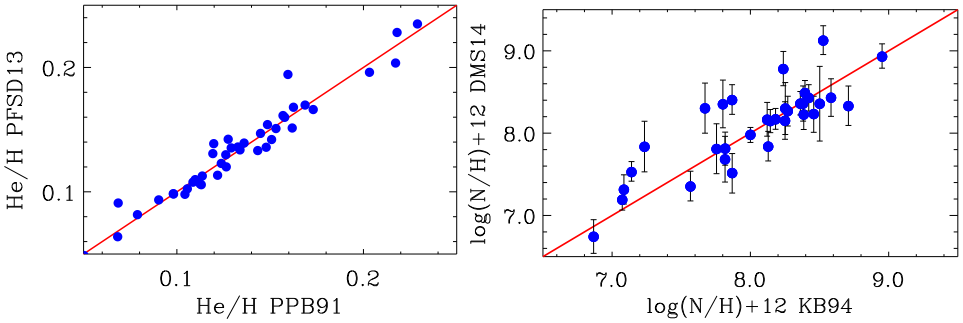

Figure 1. Left: Comparison between He/H abundances from CCM10 (outer bulge PNe) calculated using the emissivities from PFSD13 and PPB91. Error bars include only the errors in the ICFs. The red continuous line is the one to one relation. Right: The same as left panel but for $\log(N/H) + 12$.

In Fig. 2 the same confrontation is done for O, Ar, S, and Ne. Small differences are noted for O, Ar and Ne for both ICFs. However, In the case of S the new ICFs provide higher abundances than the previous ones from KB94. The new ICFs from DMS14 can, at least partially, solve the "sulfur anomaly problem" in PNe.

The behavior of Ar/H vs. O/H and S/H vs. O/H are presented Fig. 3. In this figure both samples from CCM10 (outer bulge PNe) and C17 (PNe near the GC) are included. A correlation is found for these elemental abundances for both samples, although the S/H vs. O/H correlation for CCM10 data is not as tight as in the case of our data. S abundances of C17 were determined using both S^+ and S^{++} ions, contributing to reduce the uncertainties in the S abundances. The predictions of evolution models by Karakas (2010) with $Z = 0.004$, 0.008 and 0.02 are displayed in the graph for S/H vs. O/H. Clearly, models show that S is not modified by stellar nucleosynthesis, independently of the initial stellar mass. On the contrary, O is expected to be modified in progenitor stars heavier than 4 $M_\odot$ at low-metallicity environments. In the case of Ar, the models by Karakas (2010) do not give predictions for these elements, so that the abundances could not be compared with theoretical results.

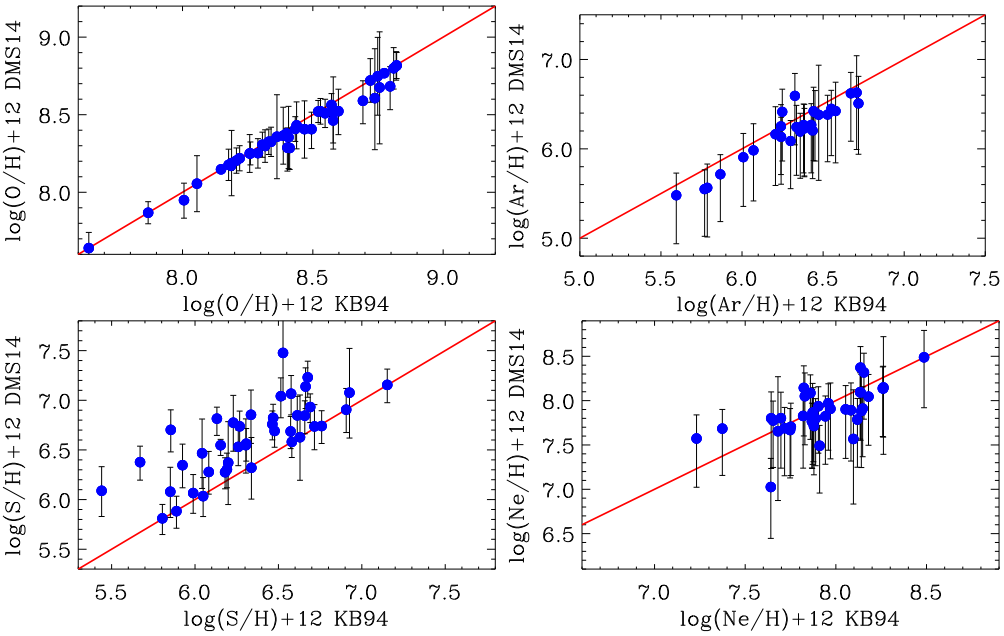

Figure 2. Left: The same as Fig. 1 for log(O/H) + 12 (top left), log(Ar/H)+12 (top right), log(S/H)+12 (bottom left) and log(Ne/H)+ 12 (bottom right).

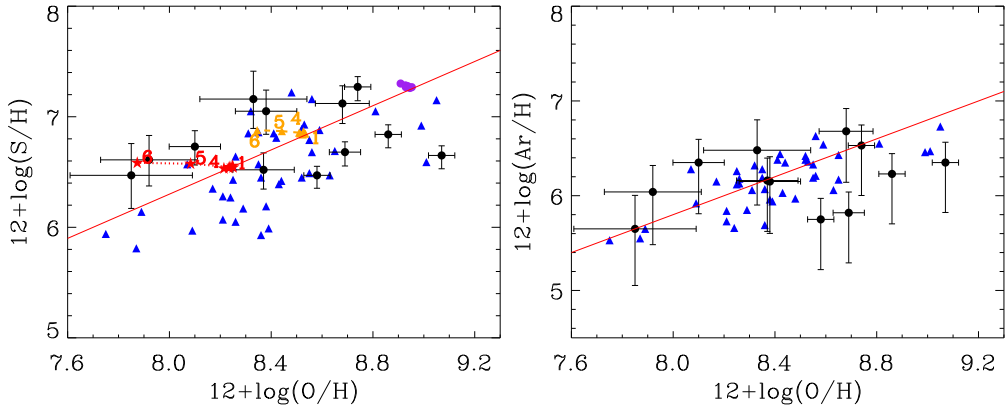

Figure 3. Left: 12 + log(S/H) vs. 12 + log(O/H); Right: 12 + log(Ar/H) vs. 12 + log(O/H). Filled circles with error bars are data from C17 (PNe near the GC), while filled blue triangles are the data from CCM10 (outer bulge PNe). The symbols with numbers represent the results of the models from Karakas (2010) for a given value of Z: red stars joined by dotted line for $Z = 0.004$; yellow triangles joined by dashed line for $Z = 0.008$; purple circles joined by dash-dotted line for $Z = 0.02$. The numbers give the initial masses of the individual models in $M_\odot$ units. The red continuous lines are straight lines with slopes equal to one.

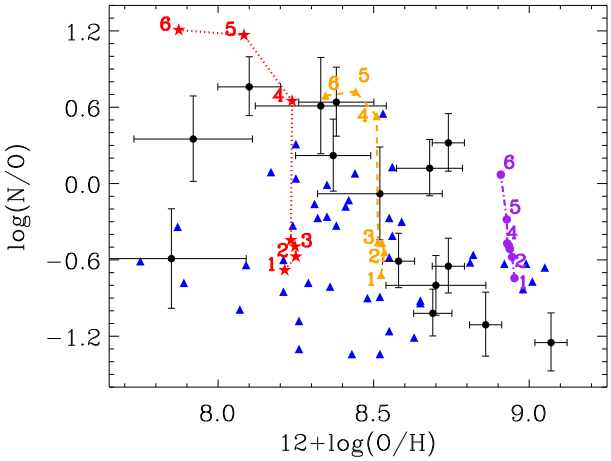

Figure 4. N/O ratio as a function of oxygen abundances. Symbols are as in Fig. 3.

Fig. 4 shows the N/O ratio as a function of O abundances. We can observe a fair agreement between the data and the models by Karakas (2010) for models with $Z = 0.008$ and 0.02. An important difference between the samples of C17 and CCM10 is observed in this figure: in CCM10 some points are compatible with the lower metallicity model ($Z = 0.004$) by Karakas (2010) and also lower initial masses ($< 4M_{\odot}$). In the sample of C17 (PNe near the GC) the majority of PNe have abundances compatible with models at higher metallicities. This can indicate a faster chemical enrichment taking place at the GC, compared with the outer regions of the Galactic bulge. However, this result should be interpreted with some caution, since due to the high interstellar extinction in the direction of the GC it is very difficult to define a metallicity-unbiased sample.

4. Conclusions

We have implemented the new ICFs from DMS14 for the elemental abundances determination and also the new HeI emissivities from PFSD13. The abundances of CCM10 were recalculated with the new emissivities and ICFs. A direct comparison between the He abundances using the new HeI emissivities and those from PPB91 resulted in small differences. The new ICFs from DMS14 were compared with those from KB94. The results show that N, O, Ar and Ne abundances are compatible within the uncertainties. However, S abundances derived with the new ICFs are higher by 0.2 dex in average. The new ICFs from DMS14 can, at least partially, solve the "sulfur anomaly problem" in PNe.

We have performed spectrophotometric observations with the 4.1 m SOAR (Chile) and the 1.6 m OPD/LNA (Brazil) telescopes to obtain physical parameters and chemical abundances for a sample of 15 planetary nebulae located within 2 degrees of the GC (see details in C17). S abundances were derived using optical and NIR lines, reducing the uncertainties associated with S ICFs. The abundances predicted by Karakas (2010) for stars of different initial masses and metallicities were used to constrain the masses and initial metallicity of the

progenitor stars. An important difference between the sample located near the GC and PNe located in the outer parts of the bulge is observed. In our previous work (CCM10) some points are compatible with the lower metallicity model ($Z = 0.004$) by Karakas (2010) and also lower initial masses ($< 4M_{\odot}$). In the PNe located near the GC, the majority of PNe have abundances compatible with models at higher metallicities. This can indicate a faster chemical enrichment taking place at the GC, compared with the outer regions of the Galactic bulge.

Acknowledgments. This work was partially supported by CAPES, FAPESP and CNPq.

References

Aver E., Olive K. A., Skillman E. D., 2010, *J. Cosmology Astropart. Phys.*, **5**, 3
Cavichia O., Costa R. D. D., Maciel W. J., 2010, *RevMexAA*, **46**, 159
Cavichia O., Costa R. D. D., Maciel W. J., Mollá M., 2017, *MNRAS*, **468**, 272
Delgado-Inglada G., Morisset C., Stasińska G., 2014, *MNRAS*, **440**, 536
Jacoby G. H., Van de Steene G., 2004, *A&A*, **419**, 563
Karakas A. I., 2010, *MNRAS*, **403**, 1413
Kingsburgh R. L., Barlow M. J., 1994, *MNRAS*, **271**, 257
Osterbrock D. E., Ferland G. J., 2006, *Astrophysics of gaseous nebulae and active galactic nuclei*
Pequignot D., Petitjean P., Boisson C., 1991, *A&A*, **251**, 680
Porter R. L., Ferland G. J., Storey P. J., et al., 2012, *MNRAS*, **425**, L28
Porter R. L., Ferland G. J., Storey P. J., et al., 2013, *MNRAS*, **433**, L89

Posters

Chemical Abundances in Gaseous Nebulae
AAA Workshop Series 10, 2016
G. Hägele, M. Cardaci & E. Pérez-Montero, eds.

Poster

Physical properties of embedded stellar clusters in W 31 complex

M. Bianchin[1], E. F. Lima[2], R. A. Riffel[1], E. Bica[3], C. Bonatto[3] and R. K. Saito[4]

[1] *Universidade Federal de Santa Maria, Departamento de Física, CCNE, 97105-900 Santa Maria, RS, Brazil*
[2] *Universidade Federal do Pampa, Campus Uruguaiana, 97508-000 Uruguaiana, RS, Brazil*
[3] *Universidade Federal do Rio Grande do Sul, Instituto de Física, 91501-970 Porto Alegre, RS, Brasil*
[4] *Universidade Federal de Santa Catarina, Departamento de Física, 88040-900 Florianópolis, SC, Brasil*

Abstract. Embedded stellar clusters are associated with star formation episodes in a Giant Molecular Cloud (GMC). Usually these objects can be found physically correlated with HII regions, indicating the presence of ionizing OB stars. The aim of this work is to determine physical parameters, such as age, distance and reddening, for the star forming complex W 31, through the photometric analysis of two of its embedded clusters (W 31-CL, BDS 112). We used the VVV and 2MASS infrared photometry (at J, H and K_S bands), field-star decontamination and isochrone fitting to determine the physical parameters for the clusters. We found that W 31-CL is located at the distance $d_\odot = 4.5 \pm 0.2$ kpc, has an age in the range 0–1 Myr and foreground extinction $A_V = 8.72 \pm 0.06$ mag. BDS 112 is located at $d_\odot = 4.83 \pm 0.23$ kpc, is younger than 2 Myr and $A_V = 13.37 \pm 0.06$ mag.

1. Introduction

Giant Molecular Clouds (GMC) are the largest physical structures within the Milky Way and where the star formation processes occur. Within these regions, embedded stellar clusters can be formed, which are usually related with OB stars that ionize the interstellar medium and originate HII regions. These stellar associations cannot reach ages older than ∼3 Myr (Lada & Lada, 2003).
The W 31 star forming region was discovered through radio observations by Westerhout (1958). It has two infrared clusters, W 31-CL (Blum et al., 2001) and BDS 112 (Bica et al., 2003), and three well-known HII regions (G 10.2-03, G 10.3-0.1 and G 10.0-0.3). The distance to the complex is still an open issue in the literature, with values varying from 3.4 kpc (Blum et al., 2001) to 6 kpc (Wilson, 1974).
Associated with the HII region G 10.0-0.3 there is a Soft Gamma-ray Repeater (SGR), which is taken as the *far* component of the W 31 complex. Due to the high

Figure 1. VVV near-IR image of the W31 complex.

extinction (~ 30 mag) associated with the complex, authors assumed distances between 8.7 kpc (Bibby et al., 2008) and 15.1 kpc (Corbel & Eikenberry, 2004). In addition, SGR 1806-20 is associated with an infrared cluster, one Luminous Blue Variable (LBV) candidate and 4 Wolf Rayet (WR) stars (Bibby et al., 2008). In this context, W 31 represents an unique opportunity to study such rare association of diverse astrophysical objects. A detailed analisys of SGR 1806-20 will be given elsewhere.

The VVV and 2MASS photometric data provide the ideal combination for studying embedded stellar cluster in the near-infrared. We were able to photometrically characterize three embedded clusters in W 31 (Fig. 1), and determine physical parameters such as age, distance and reddening. We apply the method used by Lima et al. (2014) to study the stellar clusters in the W 31 complex. In Section 2 we describe the method, Section 3 some preliminary results for W 31 region are shown and Section 4 presents a short discussion and main conclusions of this work.

2. Data Analysis

The VISTA Variables in the Vía Láctea Survey (VVV) was designed to study variability in the Milky Way through multiband ZYJHKs near-IR observations (Minniti et al., 2010). VVV is deeper than previous IR surveys, reaching the pre-main sequence (PMS) faint stars of embedded stellar clusters near the Galactic center. On the other hand, bright OB stars at these distances are saturated in VVV, thus in order to build our clusters CMDs we replaced the photometry of these star by 2MASS data, considering a spatial separation smaller than 0,5".

In order to determine the physical parameters of W31 embedded clusters we apply the field star decontamination (FSD) algorithm developed by Bonatto &

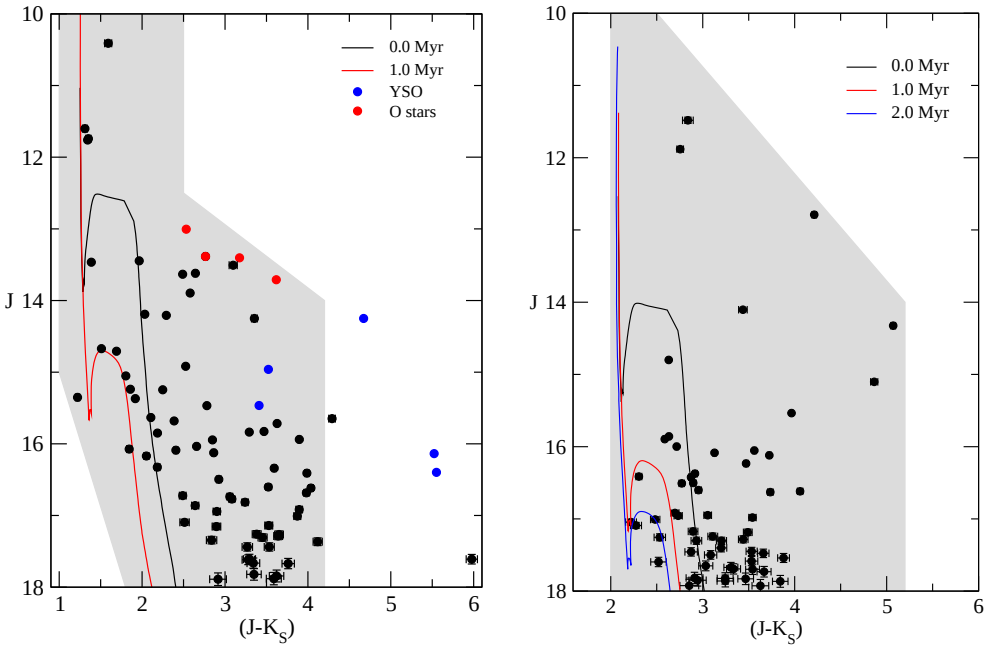

Figure 2. *Left:* Decontaminated CMD for W 31-CL with the PARSEC isochrone fitting. The gray area is the color-magnitude filter, indicating the most likely cluster members and radius is $R = 1.2'$. *Right:* The same for BDS 112, but with a cluster radius $R = 0.8'$.

Bica (2007). In this method we provide the observed color-magnitude diagram (CMD) related to the cluster radius and a comparison field CMD. The algorithm compares each color-magnitude cell in the observed CMD with corresponding field in order to remove the similar stars. This extraction provides an adequate contrast (in terms of density of stars between CMD sequences of the object and offset field.

The age and distance are obtained through the PARSEC isochrones (Bressan et al., 2012) fitted to the field-decontaminated CMD. The fitting procedure is done *by eye*, considering the expected position for the Main Sequence and PMS stars. This method was successfully applied recently to determine the physical properties of NGC 6357 stellar clusters (Lima et al., 2014).

3. Results

Based on radial density profiles (RDPs) and visual inspection we have determined a radius of $R = 1.2'$ for W 31-CL and $R = 0.8'$ for BDS 112. These values were used to define the cluster area in the FSD process.

The field star decontaminated CMD for W 31-CL and BDS 112 are shown in Fig. 2. W 31-CL and BDS 112 have CMDs covering the same range in magnitudes and colors, which indicates that both are physically associated. The age and

distance determination was done considering two or three possible isochrones for each CMD, as both clusters are embedded.
For W 31-CL we determined ages from Zero Age Main Sequence (ZAMS) to 1 Myr, $A_V = 8.72$ and a distance of $d_\odot = 4.51 \pm 0.21$ kpc, while for BDS 112 we obtained that it can be 1 Myr older than the former, has $A_V = 13.37$ and $d_\odot = 4.83 \pm 0.23$ kpc.

4. Conclusions

We used VVV and 2MASS photometries to study the stellar clusters associated to the W 31 star forming complex. The physical parameters of two stellar clusters are listed below:

- W 31-CL: $d_\odot = 4.51 \pm 0.21$ kpc, age of 0–1 Myr and $A_V = 8.72 \pm 0.06$ mag;
- BDS 112: $d_\odot = 4.83 \pm 0.23$ kpc, age of 0–2 Myr and $A_V = 13.37 \pm 0.06$ mag;

These parameters were obtained with the method described in Section 2. A detailed description of the methods and data analysis, as well as results for SGR 1806-20 will be presented in Bianchin et al. (in preparation).
The VVV and 2MASS photometries represent a complete data set for studying both embedded stellar clusters. They provide infrared photometry covering both MS and PMS stars.

Acknowledgments. We thank the Brazilian institutions CAPES and CNPq for the financial support to this work.

References

Bibby J. L., Crowther P. A., Furness J. P., Clark J. S., 2008, *MNRAS*, **386**, L23
Bica E., Dutra C. M., Barbuy B., 2003, *A&A*, **397**, 177
Blum R. D., Damineli A., Conti P. S., 2001, *AJ*, **121**, 3149
Bonatto C., Bica E., 2007, *MNRAS*, **377**, 1301
Bressan A., Marigo P., Girardi L., Salasnich B., et al., 2012, *MNRAS*, **427**, 127
Corbel S., Eikenberry S. S., 2004, *A&A*, **419**, 191
Lada C. J., Lada E. A., 2003, *ARA&A*, **41**, 57
Lima E. F., Bica E., Bonatto C., Saito R. K., 2014, *A&A*, **568**, A16
Minniti D., Lucas P. W., Emerson J. P., et al., 2010, *New Astron.*, **15**, 433
Westerhout G., 1958, *Bull. Astron. Inst. Netherlands*, **14**, 215
Wilson T. L., 1974, *A&A*, **31**, 83

Chemical Abundances in Gaseous Nebulae
AAA Workshop Series 10, 2016
G. Hägele, M. Cardaci & E. Pérez-Montero, eds.

Poster

Ionized gas excitation of Seyfert galaxies mapped with optical Integral Field Spectroscopy

C. Brum[1], R.A. Riffel[1], T. Storchi-Bergmann[2], A. Robinson[3], A. Schnorr–Müller[2] and D. Lena[4,5]

[1] *Universidade Federal de Santa Maria, Departamento de Física/CCNE 13, 97105-900, Santa Maria, RS, Brasil*
[2] *Universidade Federal do Rio Grande do Sul, Instituto de Física, CP 15051, Porto Alegre 91501-970, RS, Brasil*
[3] *Rochester Institute of Technology, 54 Lomb Memorial Drive Rochester, NY 14623, USA*
[4] *SRON, Netherlands Institute for Space Research, Sorbonnelaan 2, NL-3584 CA Utrecht, the Netherlands*
[5] *Department of Astrophysics/IMAPP, Radboud University, Nijmegen, PO Box 9010, NL-6500 GL Nijmegen, the Netherlands.*

Abstract. We present a study of gas excitation and distribution for a sample of four active galaxies composed by NGC 3982, NGC 4501, NGC 2787 and NGC 4450 using optical integral field spectroscopy of the central kpc, obtained with Gemini Multi-Object Spectrograph (GMOS) at Gemini-North telescope. We present the integrated flux distributions for the Ha, [N II]λ6583 and [S II]λ6730 emission lines. All objects show extended emission with the emission peak for all lines being observed at the nucleus. For NGC 3982, the Hα map presents a ring of enhanced emission with radius 6" around of the nucleus, NGC 4501 shows a small region with enhanced emission to the south and NGC 4450 shows a spiral structure. These structures are consistent with the presence of H II regions as suggested by the observed line ratios. The [N II]/Hα line ratio presents its highest values at the nucleus of all galaxies, consistent with gas excitation by the AGN, but some high values of up to 8 are also seen away from the nucleus for NGC 3982 and NGC 4501. For all galaxies the electron density maps, derived from the [S II] line ratio, show a broad range of values, from 100 to 3000 cm^{-3}.

1. Introduction

The study of the accretion of material onto a central supermassive black hole (SMBH) and the triggering of an active galactic nucleus (AGN) is a problem still under investigation. Many theoretical studies and simulations (Shlosman et al., 1990; Maciejewski et al., 2002; Emsellem et al., 2003; Knapen, 2005; Emsellem et al., 2006) have sought understand the mechanism by which the material is dragged to the nuclear regions to feed the AGN. Simões Lopes et al. (2007) reported a strong correlation between the presence of nuclear dust structures (fil-

aments, spirals and discs) and activity in galaxies, suggesting that these nuclear dust structures can be tracers of inflows to transport gas from kiloparsec scales down to the SMBH.
In previous studies with integral field spectroscopy, our group (e.g. Fathi et al., 2006; Storchi-Bergmann et al., 2007; Schnorr Müller et al., 2011; Schnorr-Müller et al., 2014b,a) found kinematic features consistent with gas inflowing along bars and nuclear spirals to the inner tens of parsecs of active galaxies. In this work we have mapped the gaseous kinematics and distribution of four low-luminosity nearby AGNs (NGC 3982, NGC 4501, NGC 2787 and NGC 4450) that show dusty nuclear spirals in structure maps from Simões Lopes et al. (2007), with the goal of looking for correlations between these spirals and the gas kinematics.
This work is organized as follows. Section 2 describes the observations, data reduction and analysis, while Section 3 shows our results. In Section 4 we present our conclusions.

2. Observations and Data Reduction

The observations of the four galaxies were done using the Gemini Multi-Object Spectrograph (GMOS) Integral Field Unit (IFU) at the Gemini North Telescope in 2007, 2008 and 2011. Data reduction was performed using the IRAF[1] packages provided by the Gemini Observatory and specifically developed for the GMOS instrument and followed the standard procedure of spectroscopic data reduction. The spatial resolution of the final data cubes are in the range 30–65 pc as obtained from the full width at half maximum (FWHM) of continuum images for the standard stars.

3. Results

In order to measure the emission-line flux distributions and gas kinematics, we fitted the line profiles of Hα+[N II] $\lambda\lambda$ 6548,6583, [S II] $\lambda\lambda$ 6717,6731 and [O I]λ6300 by single Gaussian curves using a modified version of the PROFIT routine (Riffel, 2010). An example of the resulting maps is shown in Fig. 1. This figure shows flux maps for NGC 4501. Extended emission for Hα and [N II] is observed to up to $\sim$500 pc (6″) from the nucleus. The [S II] flux map is more concentrated, with emission seen only within the inner 160 – 240 pc (2-3″). All maps show the most extended emission along the northwest-southeast direction, approximately along the the major axis of the galaxy. In addition, the Hα map presents a small region with enhanced emission at $\sim$480 pc (6″) south-west of the nucleus attributed to an H II region. Extended emission for these lines up to the borders of the IFU field of view is observed for the other galaxies of our sample.
To better investigate the gas excitation mechanism we constructed the WHAN diagram (Cid Fernandes et al., 2010). The left panel of Fig. 2 shows the corresponding diagram for NGC 4501 and the right panel presents the spatially

[1]IRAF is distributed by National Optical Astronomy Observatories, which are operated by the Association of Universities for Research in Astronomy, Inc., under cooperative agreement with the National Science Foundation

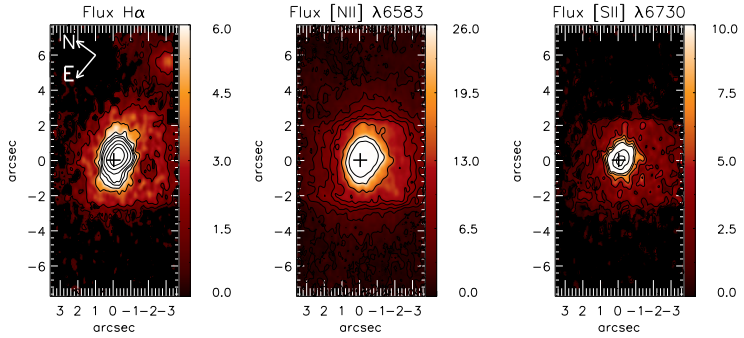

Figure 1. Flux distributions for Hα, [N II] λ6583, [S II] λ6730 and [O I]λ6300 emission lines for NGC 4501. The color bars show the flux scale in units of 10^{-17}erg s^{-1}cm^{-2} and the central cross marks the position of the nucleus. Black regions are masked regions and correspond to locations where no good fits of the line profiles could be obtained. Figure adopted from Brum et al. (2017).

resolved excitation map, identifying regions of each excitation class. This galaxy is cataloged as harboring a Seyfert 2 nucleus (Véron-Cetty & Véron, 2006), while according to our WHAN diagram its nuclear emission is identified at location where weak AGNs are observed. In addition, at 6" west of the nucleus, the WHAN diagram suggests a contribution of shocks (possible due to SNe explosions) as strong AGN signature is seen. For all galaxies, points at several locations of the WHAN diagram are observed, suggesting that the AGN is not the only responsible for the gas excitation.

4. Conclusions

We have mapped the ionized gas kinematics and flux distributions in the inner kiloparsec of NGC 3982, NGC 4501, NGC 2787 and NGC 4450 using GMOS IFS at a velocity resolution of $\sim$ 120 km s^{-1} and spatial resolution from 30–60 pc. The four galaxies show extended emission for Hα, [N II] and [S II] emission lines, while [O I] extended emission was observed only for NGC 3982, to up to 2" from the nucleus. Details about the gas and stellar kinematics will be presented in Brum et al. (in preparation), but we list the main conclusions below:

- The Hα equivalent width ($W_{H\alpha}$) vs. [N II]/Hα (WHAN) diagrams show a wide range of values, with the nuclear emission of NGC 3982 and NGC 4450 showing a signature of Seyfert, while for NGC 2787 and NGC 4101 a LINER signature is seen.

- For all galaxies the electron density maps, derived from the [S II] line ratio, show a broad range of values, from 100 to 3000 cm^{-3}.

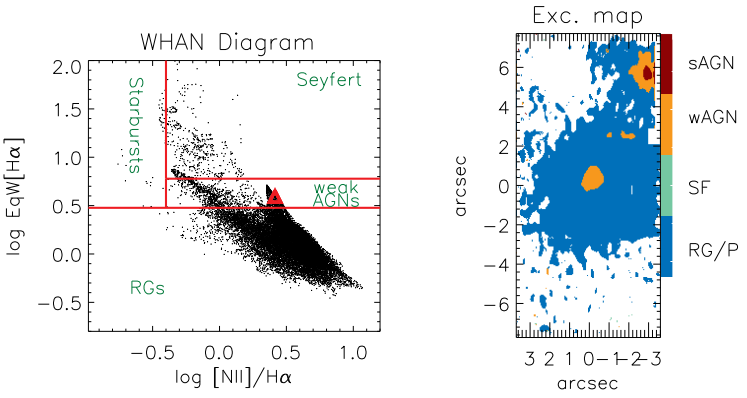

Figure 2. From left to right: the WHAN diagram with distinct excitation classes identified and the Hα EqW shown in Å, where the red triangle corresponds to the nucleus; spatially resolved mask, identifying regions of each excitation class. Figure adopted from Brum et al. (2017).

- The velocity field of all galaxies are dominated by rotation and reproduced by a rotating disk model, under the assumption that the gas rotates in the plane of the galaxy at circular orbits.
- NGC 3982 shows a clear circumnuclear star-formation ring surrounding the nucleus at 4-6 arcsec, as seen in the flux maps and in the WHAN diagram.
- A star forming region was detected at 6 arcsec west of the nucleus of NGC 4501. The WHAN diagram shows values typical of Seyfert galaxies for this region and we interpret it as being originated by emission enhanced due to shocks from supernovae explosions.

Acknowledgments. This work was partially supported by Brazilian institutions CNPq and FAPERGS.

References

Brum C., Riffel R. A., Storchi-Bergmann T., Robinson A., Schnorr Müller A., Lena D., 2017, *MNRAS*, **469**, 3405
Cid Fernandes R., Stasińska G., et al., 2010, *MNRAS*, **403**, 1036
Emsellem E., Fathi K., Wozniak H., et al., 2006, *MNRAS*, **365**, 367
Emsellem E., Goudfrooij P., Ferruit P., 2003, *MNRAS*, **345**, 1297
Fathi K., Storchi-Bergmann T., Riffel R. A., et al., 2006, *ApJL*, **641**, L25
Knapen J. H., 2005, *Ap&SS*, **295**, 85
Maciejewski W., Teuben P. J., Sparke L. S., et al., 2002, *MNRAS*, **329**, 502
Riffel R. A., 2010, *Ap&SS*, **327**, 239
Schnorr-Müller A., T., et al., 2014a, *MNRAS*, **437**, 1708
Schnorr Müller A., Storchi-Bergmann T., et al., 2011, *MNRAS*, **413**, 149

Chemical Abundances in Gaseous Nebulae
AAA Workshop Series 10, 2016
G. Hägele, M. Cardaci & E. Pérez-Montero, eds.

Poster

Chemodynamics of Blue Compact Dwarf galaxies

F. Campuzano-Castro[1,2], G. F. Hägele[1,2], G. Bosch[1,2], V. Firpo[3,4], N. Morrell[5], M. Cardaci[1,2]

[1] *Facultad de Ciencias Astronómicas y Geofísicas, Universidad Nacional de La Plata (FCAG-UNLP)*
[2] *Instituto de Astrofísica de La Plata (IALP-CONICET)*
[3] *Universidad de La Serena*
[4] *Gemini Observatory, Chile*
[5] *Las Campanas Observatory, Chile*

Abstract. This work presents a brief summary of the analysis we are performing on the physical and chemical properties of the ionizing gas in star-forming regions belonging to two Blue Compact Dwarf galaxies (BCDs), using high resolution echelle spectra. Our aim is to perform a detailed study of the Chemodynamics on BCDs. To do that, we use our own Python code using the LMFIT (Non-Linear Least-Squares Minimization and Curve-Fitting for Python) package. We deconvolve the emission-line profiles fitting several gaussians to the different kinematical components to be able to estimate the properties and the nature of the ionized gas. Our next step is to use the kinematical information to perform the chemical abundance analysis and to infer the physical properties of the gas (the chemodynamical study) by using the methodology published in Hägele et al. (2008, 2012).

1. Introduction

Giant Extragalactic HII Regions (GHIIRs) are extended objects, very luminous and located in the discs of spirals and in irregular galaxies. They are formed due to the presence of young and massive stars whose strong ultraviolet flux ionizes their surrounding gas. The observed emission line spectra of HII galaxies and Blue Compact Dwarf galaxies (BCDs) are similar to those shown by Giant HII Regions (Sargent & Searle, 1970; French, 1980), therefore, we are able to use similar analysis techniques to study the physical properties (electron densities and temperatures) and chemical abundances of the emitting gas of the star-forming regions (see e.g. Hägele et al., 2006) belonging to these low metallicity galaxies (Terlevich et al., 1991). BCDs present strong star formation easily identified through their intense Hα emission and narrow emission lines, low metallicity environments and complex star formation history. Due to these characteristics they are interesting objects to study metallicity effects in galaxies (Kunth & Östlin, 2000).

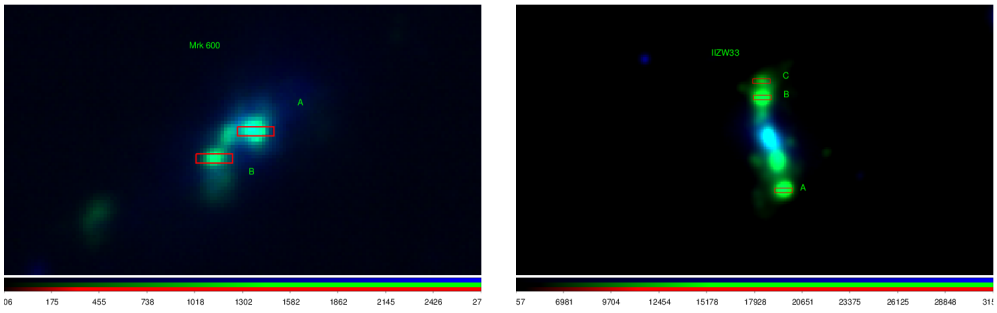

Figure 1. Composite images of Mrk 600 (left panel) and IIZw 33 (right panel). Green and blue are Hα and R band, respectively, images acquired with the 1.8 telescope at Monte Palomar (images taken from NED). The echelle slits are overimposed.

Many BCDs that used to be considered compact objects, currently show a complex spatial structure thanks to the improvement and enlargement of telescopes and instruments (Hägele et al., 2011). For example, Haro 15, currently classified as a spiral galaxy, were included in BCDs catalogues (see discussion in Firpo et al., 2011; Hägele et al., 2012).

2. Observations

Our data were acquired in 2005 and 2006, using the high resolution echelle spectrograph mounted at the Clay Magellan Telescope (6.5m) at Las Campanas Observatory (LCO), Chile. The spectrograph uses a dichroic to separate the light in 2 different spectral ranges. The 1x4 arcsec^2 slit was used with a blue and red spectral resolutions of R 28000 and R 22000, respectively. The blue and red spectral ranges were 3300-5100 Å and 4850-9300 Å, respectively. We used IRAF[1] routines in the usual manner to reduce the data. GD108 was used as standard star. We observed 5 star-forming knots: 2 belonging to Mrk 600 and 3 to IIZw 33. Each studied star-forming region was also divided in sub-components accordingly to the spatial components identified in its spatial profile (see the procedure description in §3). In total we have observations of 11 regions: 4 in Mrk 600 (2 components for each knot, A and B; see left panel of Fig. 1) and 7 for IIZw 33 (3 sub-components for Knot A, and 2 for knots B and C; see right panel of Figs. 1).

3. Results

Spatial components

Analyzing the spatial profile around the Hβ emission line in the 2D echelle spectra we identified more than one different spatial components for each studied

[1]IRAF: the Image Reduction and Analysis Facility is distributed by the National Optical Astronomy Observatories, which is operated by the Association of Universities for Research in Astronomy, Inc. (AURA) under cooperative agreement with the National Science Foundation (NSF).

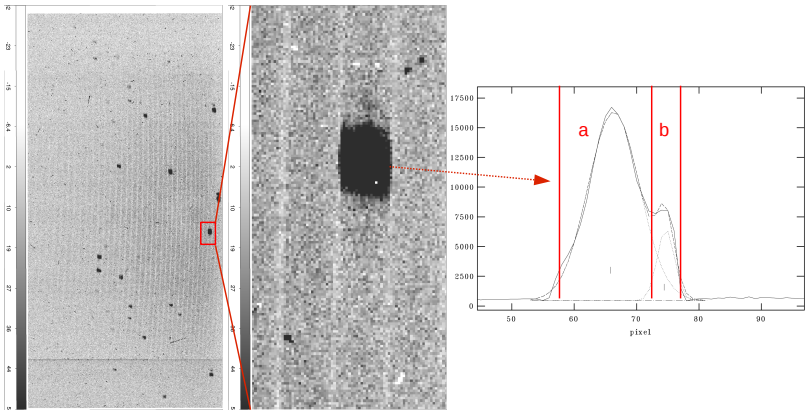

Figure 2. Left: 2D echelle spectrum corresponding to Mrk 600-B, showing different emission lines and orders. Middle: zoom of the 2D echelle spectrum around the Hβ emission line. Right: spatial profile at the position of the Hβ emission line. It can be seen two spatial components and the performed spatial-Gaussian fitting.

star-forming region (see an example of the 2D echelle spectra together with the Hβ spatial profile and the performed fitting in Fig. 2). We performed an extraction for each of the identified spatial components. We are able to perform the chemodynamical study for each of these spatial components.

Kinematical components

Following the methodology proposed, developped and used in Hägele et al. (2007, 2009, 2010, 2012, 2013); Firpo et al. (2010, 2011) we deconvolve the emission line profiles in different kinematical components. We performed the analysis of the strong emission lines detected in our regions using our own Python code based on the use of the LMFIT (Non-Linear Least-Squares Minimization and Curve-Fitting for Python) package. We proposed a model composed by a linear function and "n" Gaussians or normal distributions, to fit the local continuum and the emission-line profile, respectively. We started our analysis modeling the strongest emission-lines: Hα and [OIII]λ5007Å. Then, we used these kinematical results, line positions (velocities) and widths, as the initial approximations for the other emission-lines with similar ionization state. For [OI], [OII], [SII] and [NII] emission-lines we used the solution found for the Hα recombination line. While for HeI, [SIII], [NeIII], [ArIII] and [ArIV], we used the solution found for the [OIII]λ5007A emission-line. It must be noted that for the very weak temperature sensitive auroral emission-lines: [OIII] λ 4363Å, [OII] $\lambda\lambda$ 7319,7330Å, [NII] λ5755Å, [SIII] λ 6312Å, and [SII] λ 4068Å, we used the kinematical solution obtained for the strong emission-line of the same atomic ion since the kinematical solution must be the same (or very similar) and therefore we only varied their amplitudes (see a complete discussion about this point in Hägele et al. (2012). In Fig. 3 some examples of the results of the fittings to the emission-line profiles of Knot A of IIZw 33 are shown.

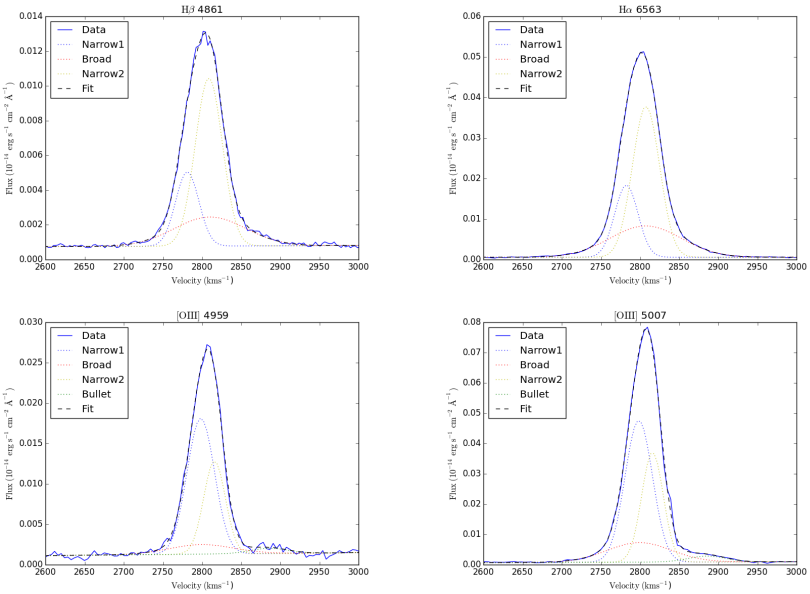

Figure 3. Some results of the fittings performed to the emission-line profiles of Knot A of IIZw 33.

4. Conclusions

We observed 11 star-forming knots belonging to 2 BCDs using high resolution echelle spectroscopy that will allow us to carry on a chemodynamical study of their physical conditions and chemical abundances. We used our own Python code base on the LMFIT package to perform the kinematical decomposition of the emission lines profiles. Our near future objectives are to derive for each kinematical component: (i) the reddening constant from the hydrogen recombination lines in all the regions; (ii) the electron density in the low excitation zone from the emission-line ratios of [SII]λ6717Å/λ6731Å and [OII]λ3727Å/λ3729Å; (iii) the electron temperatures Te ([OII]), Te ([OIII]), Te ([SII]), Te ([SIII]), and Te ([NII]) using the auroral emission lines present in the spectra of several of our regions and applying the direct method (see e.g. Hägele et al., 2008) or empirical relations and photo-ionization models (see e.g. Pérez-Montero & Díaz, 2005; Hägele et al., 2006); (iv) ionic abundances of He+, O+, O2+, S+, S2+, N+, Ne2+, Ar2+ and Ar3+; (v) the total chemical abundances of He, O, S, N, Ne and Ar; (vi) the ionization degree of the nebular gas from the η and η' parameters (Vílchez & Pagel, 1988); and (vii) the relationship between the luminosities and velocity dispersion: L vs. σ (see e.g. Bosch et al., 2002).
We also have observations of other 5 BCDs acquired using the echelle spectrograph mounted at the du Pont telescope at LCO, for which will continue our chemodynamical study.

Acknowledgments. This research has made use of the NASA/IPAC Extragalactic Database (NED) which is operated by the Jet Propulsion Laboratory, California Institute of Technology, under contract with the National Aeronautics and Space Administration.

References

Bosch G., Terlevich E., Terlevich R., 2002, *MNRAS*, **329**, 481
Firpo V., Bosch G., Hägele G. F., et al., 2011, *MNRAS*, **414**, 3288
Firpo V., Bosch G., Hägele G. F., Morrell N., 2010, *MNRAS*, **406**, 1094
French H. B., 1980, *ApJ*, **240**, 41
Hägele G. F., Díaz A. I., Cardaci M. V., et al., 2007, *MNRAS*, **378**, 163
Hägele G. F., Díaz A. I., Cardaci M. V., et al., 2009, *MNRAS*, **396**, 2295
Hägele G. F., Díaz A. I., Cardaci M. V., et al., 2010, *MNRAS*, **402**, 1005
Hägele G. F., Díaz A. I., Terlevich E., et al., 2008, *MNRAS*, **383**, 209
Hägele G. F., Díaz A. I., Terlevich R., et al., 2013, *MNRAS*, **432**, 810
Hägele G. F., Firpo V., Bosch G., et al., 2012, *MNRAS*, **422**, 3475
Hägele G. F., García-Benito R., Pérez-Montero E., et al., 2011, *MNRAS*, **414**, 272
Hägele G. F., Pérez-Montero E., Díaz A. I., et al., 2006, *MNRAS*, **372**, 293
Kunth D., Östlin G., 2000, *A&A Rev.*, **10**, 1
Pérez-Montero E., Díaz A. I., 2005, *MNRAS*, **361**, 1063
Sargent W. L. W., Searle L., 1970, *ApJL*, **162**, L155
Terlevich R., Melnick J., Masegosa J., et al., 1991, *A&AS*, **91**, 285
Vílchez J. M., Pagel B. E. J., 1988, *MNRAS*, **231**, 257

Chemical Abundances in Gaseous Nebulae
AAA Workshop Series 10, 2016
G. Hägele, M. Cardaci & E. Pérez-Montero, eds.

Poster

Emission-line flux distributions in IRASF23199+0123 observed with Gemini Integral Field Spectroscopy

Carpes Hekatelyne[1], Rogemar A. Riffel[1], Dinalva Sales[2], Thaisa Storchi-Bergmann[3] and Andrew Robinson[4]

[1] *Universidade Federal de Santa Maria, 97010-900, Santa Maria, Brazil*
[2] *Instituto de Matemática, Estatística e Física, Universidade Federal do Rio Grande, Rio Grande 96203-900, Brazil*
[3] *Universidade Federal do Rio Grande do Sul, 91501-970 Porto Alegre, RS, Brazil*
[4] *School of Physics and Astronomy, Rochester Institute of Technology, 84 Lomb Memorial Drive, Rochester, NY 14623-5603, USA*

Abstract. In this paper we describe the results of a spectroscopic study for IRASF23199+0123. The data were obtained using Gemini Multi-Object Spectrograph (GMOS) in the Integral Field Unit (IFU) mode. Our aim is to map the kinematics and distribution of the gas. The maps provide information about flux distribution, velocity fields and velocity dispersion fields. These maps were obtained by fitting gaussian curves to the line profiles. The flux maps were similar for both [NII] and Hα emission lines. Moreover, the narrow line kinematics suggests that the emitting gas is located in the plane of the galaxy. Velocity fields presents a clear rotation pattern and ratio lines maps in addiction to diagnostic diagrams reveals a Seyfert nucleus.

1. Introduction

Ultra luminous infrared galaxies (ULIRGs) are between the most luminous objects in the universe and are believed to represent a key stage on the evolution process of the galaxies in which tidal torques associated with mergers drive gas into the galaxy core, leading to the feeding/triggering starbursts and fueling and embedded Active Galactic Nucleus (AGN). ULIRGs are probably the result of advanced stage of merging, with huge quantity of molecular gas in their nucleus (Sanders & Mirabel, 1996; Kim et al., 2002). The causative agents of all this infrared emission are not well defined and hypotheses are on debate. The two phenomena pointed as the main agents are the presence of an AGN or intense star formation. ULIRGs can host both Starburst and AGN and in some cases the phenomena occur simultaneously in the same system. Beyond this scenario, becomes interesting investigate what is the gas ionization source.
Integral Field Spectroscopy (IFS) can be used to investigate the nature of the gas emission of ULIRGs in details, as it provides information about both gas kinematics and excitation. In this work, we present Gemini Multi-Object Spectrographs (GMOS) IFS of IRASF23199+0123, which is an interacting pair of ULIRGs

galaxies with confirmed OH megamaser emission with a redshift z=0.13569 (Darling & Giovanelli, 2006). Our data comprise observations of the central region of one galaxy of this pair and our aim is to map the distribution and kinematics of the optical line emitting gas and investigate the excitation mechanism of the nuclear emission.
This work is organized as follows. Section 2 describes the observations and data reduction procedure, while Section 3 shows our preliminary results and in Section 4 we present our conclusions.

2. Observations and data reduction

The observations of IRASF23199+0123 were done using the Integral Field Unit (IFU) of the GMOS instrument on Gemini North telescope on the night of August, 29, under the observation Programme GS-2013B-Q-86. The total on source exposure time was 1200s. The GMOS-IFU was used in the one slit mode, with the B600 grating in combination with GG455 filter giving an angular coverage of 5"×3.5" and covering the spectral range from 5000 to 7500 Å.
The data reduction process was done using routines of the GEMINI package in IRAF (Image Reduction and Analysis Facility) software and followed the standard procedure of spectroscopic data reduction (Lena, 2014). Datacubes for each individual exposures were created at an angular sampling of 0.1"×0.1" and then median combined using the IRAF gemcombine task to obtain one single data cube for the object.
At most locations of the object, the signal-to-noise ratio at the emission lines was too small to allow the fitting of the line profiles and thus we filtered the final cube using a Butterworth spatial filter to remove high frequency features and thus exclude spurious features. The spectral resolution is 1.7 Å, as obtained from the measurement of the full width at half maximum (FWHM) of typical emission lines of the Ar lamp spectrum used to wavelength calibrate the data.

3. Results

Fig. 1 displays Hubble Space Telescope (HST) images of IRASF23199+0123 that was acquired using the Advanced Camera for Surveys (ACS) with the medium (FR914M) filter and the broad-band (F814W) as a part of a snapshot program of a sample of OHMGs (Program id 11604; PI: D.J. Axon). The total integration time was 600s in the broad band (I) F814W filter, 200s in the medium-band filter and 600s in the narrow band H_α filter. On the left we present a Hα+[NII] narrow-band image and on the right an ACS/HST F814W - I band image. The proposed GMOS IFU fields of view are represented by green boxes and the spatial scale is identified at both panels. North is on the top, and East to the left.
We have constructed bidimensional maps for the emission line fluxes, centroid velocities, velocity dispersion and line intensity ratios. These maps were obtained by fitting the emission line profiles by Gaussian curves using an adapted version of the Emission Line PROfile FITting routine (PROFIT; Riffel, 2010).
We noticed that the [NII] $\lambda\lambda$6548,6583 Å and Hα emission-line profiles are well reproduced by a single Gaussian fitted to each profile at most locations of the

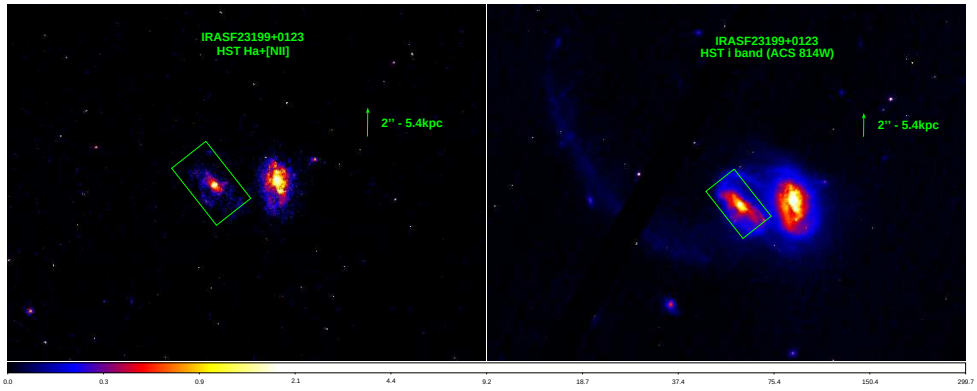

Figure 1. HST images of IRASF23199+0123. Left: Hα+[NII] narrow-band image. Right: ACS/HST F814W - i band image. The green rectangles represent the GMOS field of view and the spatial scale is identified at both panels.

observed field of view. In the inner 0.8" region, the fitting of a single gaussian to each profile does not represent a good model of the [NII]+Hα complex and we tested two possibilities of fitting and both of them resulted in good models. The first possibility is the use of two gaussians for each line. In this scenario, a blue-shifted broad component (FWHM $\sim 700\,\mathrm{km\,s^{-1}}$) is present in all lines, which could be due to gas in outflows from the nucleus of the galaxy. In the second scenario, the [NII] lines are fitted by a single gaussian curve, while the Hα profile is fitted by one narrow component plus two broad components. In this scenario, the origin of the broad Hα components would be due to a double peaked emission of the Broad Line Region. More details about the emission-line profile fitting will be presented in Carpes et al. (in preparation). Here we present an analysis of the narrow components and the choice of one fitting scenario over the other does not affect the flux distributions of the narrow components of the emission lines and consequently their kinematics.

In Fig. 2 we present the flux distributions for the narrow components of Hα (left panel) and [NII] λ6583Å (right panel) emission lines. The color bars show the flux in units of 10^{-17}erg $s^{-1}cm^{-2}$ and the black regions represent masked locations where the signal-to-noise ratio was not high enough to get good fits of the line profiles. The central cross marks the location of the nucleus, defined as the position of the peak of the continuum emission. Both maps show similar flux distributions with emission being observed over the whole field of view. The highest intensity flux levels are observed surrounding the nucleus of the galaxy and at least three knots of emission are observed in extra-nuclear regions, possible due to star forming regions.

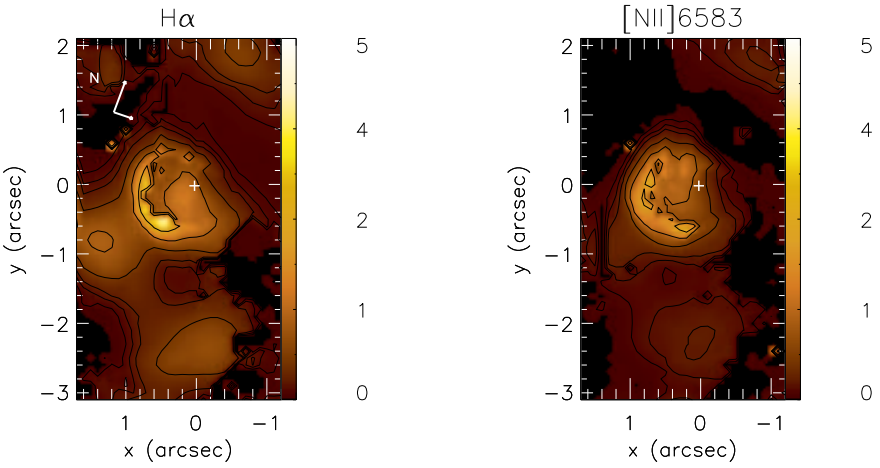

Figure 2. H_α (left) and [NII] λ6583Å flux distributions of the narrow component. Fluxes are shown in units of $10^{-17} ergs^{-1} cm^{-2}$.

4. Conclusions

We used GMOS-IFU observations to map the emission-line flux distributions and kinematics of the inner region the OH Megamaser galaxy IRASF23199+0123. Our main conclusions are:

- [NII] and Hα emission lines are observed over the whole GMOS-IFU field of view. The nuclear emission is attributed to a central AGN, as suggested by the multi-components and line ratios, while the extra-nuclear emission may be due to emission of star forming regions.

- The gas velocity fields show a distorted rotation pattern with velocity amplitude of 170 kms^{-1}.

- The velocity dispersion is small at most locations, suggesting that the gas is located at the plane of the galaxy.

References

Darling J., Giovanelli R., 2006, *AJ*, **132**, 2596
Kim D.-C., Veilleux S., Sanders D. B., 2002, *ApJS*, **143**, 277
Lena D., 2014, *ArXiv e-prints 1409.8264*
Riffel R. A., 2010, *Ap&SS*, **327**, 239
Sanders D. B., Mirabel I. F., 1996, *ARA&A*, **34**, 749

Chemical Abundances in Gaseous Nebulae
AAA Workshop Series 10, 2016
G. Hägele, M. Cardaci & E. Pérez-Montero, eds.

Poster

Emission line morphology and gas excitation in the central kpc of nearby Seyfert galaxies

I. C. Freitas[1], R. A. Riffel[1], T. Storchi-Bergmann[2], M. Elvis[3], M. Crenshaw[4], A. Robinson[5], D. Lena[6,7], H. Schmitt[8], S. Kraemer[9] and N. M. Nagar[10]

[1] *Universidade Federal de Santa Maria, Departamento de Física, Centro de Ciências Naturais e Exatas, 97105-900, Santa Maria, RS, Brazil*
[2] *Universidade Federal do Rio Grande do Sul, Instituto de Física, CP 15051, Porto Alegre, 91501-970, RS, Brazil*
[3] *Harvard-Smithsonian Center for Astrophysics, 60 Garden Street, Cambridge, MA 02138, USA*
[4] *Department of Physics and Astronomy, Georgia State University, Astronomy Offices, One Park Place South SE, Suite 700, Atlanta, GA 30303, USA*
[5] *School of Physics and Astronomy, Rochester Institute of Technology, 84 Lomb Memorial Drive, Rochester, NY 14623-5603, USA*
[6] *SRON, Netherlands Institute for Space Research, Sorbonnelaan 2, NL-3584 CA Utrecht, the Netherlands*
[7] *Department of Astrophysics/IMAPP, Radboud University, Nijmegen, PO Box 9010, NL-6500 GL Nijmegen, the Netherlands*
[8] *Remote Sensing Division, Naval Research Laboratory, 4555 Overlook Avenue, SW, Washington, DC 20375, USA*
[9] *Institute for Astrophysics and Computational Sciences, Department of Physics, The Catholic University of America, Washington, DC 20064, USA*
[10] *Astronomy Department, Universidad de Concepción, Casilla 160-C, Concepción, Chile*

Abstract. We present a study of the Narrow Line Region (NLR) of the nearby Seyfert galaxies Mrk 6, Mrk 79, Mrk 348, Mrk 607 and Mrk 1058. We map the emission-line flux distributions and excitation using Integral Field Spectroscopy (IFS) obtained with GMOS instrument at Gemini-North Telescope covering the inner $3.5'' \times 5.0''$ corresponding to the inner $\sim$ 1.2 kpc x 1.7 kpc at the galaxies. The spectral range covers the strongest NLR emission lines: Hβ, [OIII] $\lambda\lambda$4959,5007 Å, [OI] λ6300, Hα, [NII] $\lambda\lambda$6548,83 Å, [SII] $\lambda\lambda$6716,31 Å. In this contribution we show the range of line ratios covered by the IFS observations, that, although revealing a range of excitation along the NLRs, are all dominated by excitation from the Seyfert nucleus up to $\sim$1 kpc from the nucleus.

1. Introduction

One of the most important questions regarding the study of Active Galactic Nuclei (AGN) is: what is the nature of their Narrow Line Region (NLR)? Early studies of luminous prototypical nearby active galaxies have led to the picture that the NLR is a cone-shaped region reaching $\sim$100 pc from the nucleus where

Table 1. Observation Log: (1) galaxy name, (2) galaxy distance from NED (NASA/IPAC Extragalactic Database), (3) spatial resolution, (4) spectral resolution, (5) exposure time, and (6) nuclear activity class.

Object	D (Mpc)	Spat. R. (pc)	Spec. R. ($km\,s^{-1}$)	Exp. T. (s)	Nuc. A.
Mrk 6	79.5	235	89	7×810	Sy 1
Mrk 79	93.8	278	89	6×810	Sy 1
Mrk 348	63.5	188	84	6×810	Sy 2
Mrk 607	37.7	111	89	7×810	Sy 2
Mrk 1058	71.8	213	83	6×810	Sy 2

the gas is in outflow. However, recent modeling of the NLR using longslit spectroscopy shows that, although conical outflows are observed in 1/3 of the cases, most cases are complex and ambiguous (Fischer & et al., 2014). Recently, Fischer & et al. (2017) used Integral Field Spectroscopy (IFS) of the central region of Mrk 573 and showed that even though there is some outflow in this galaxy most of the NRL is not dominated by the outflow but rather by nuclear ionization. Integral Field Units (IFUs) on large telescopes are the best instruments to map the emission of the NLR, as they provide information about both the kinematics and the gas distribution and excitation (Diniz et al., 2015; Schnorr-Müller et al., 2014).

With the goal of mapping the gas kinematics and excitation along the NLR of Seyfert galaxies, we observed a sample of five nearby Seyfert galaxies using the Gemini Multi-Object Spectrograph (GMOS) operating in the IFU mode. In this contribution we show preliminary results of the gas excitation along the NLR. In Section 2 we describe the observations and data reduction, while Section 3 shows our preliminary results and in Section 4 we present our conclusions.

2. Sample and Observations

Our sample was selected based on the presence of extended [OIII]λ5007 Å emission in Hubble Space Telescope (HST) images (Schmitt & et al., 2003) and is comprised of the five nearby Seyfert galaxies listed in Table 1. The observations were made using the GMOS-IFU on the Gemini North on dates between September 30, 2014 to January 12, 2015. The data reduction process followed the standard procedure for GMOS IFU data reduction (Lena, 2014). Table 1 lists the distance to each object, the spatial and spectral resolutions, total exposure time and nuclear activity class. The spectral and spatial resolutions were obtained from the measurement of the full width at half-maximum (FWHM) of the CuAr calibration lamp lines and of the spatial profile of the flux standard star, respectively.

3. Results

We show in Fig. 1 a large scale image for Mrk 79 obtained from the HST WFPC2 through the F606W filter (Malkan et al., 1998), an [OIII]λ5007 HST narrow-band image (Schmitt & et al., 2003) and the [OIII]λ5007 flux map obtained from the

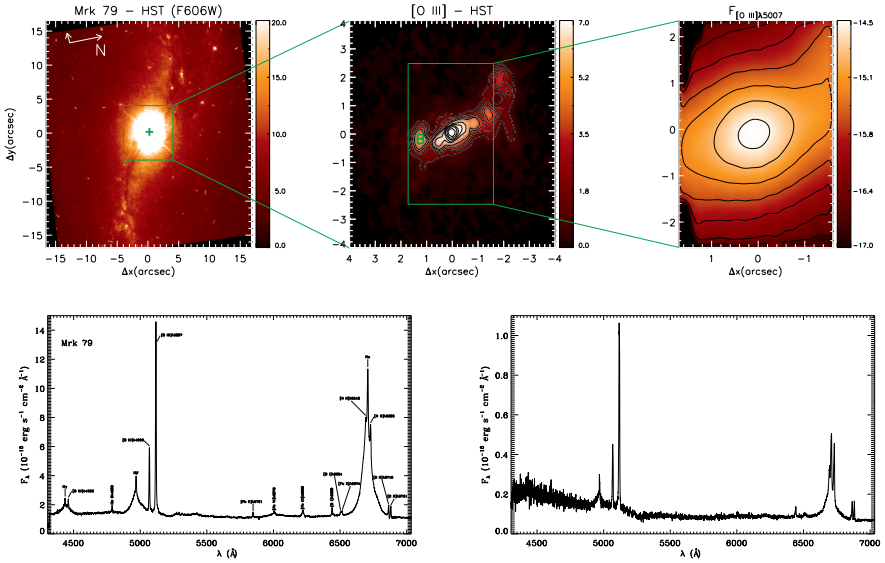

Figure 1. Top left panel: large scale HST image of the galaxy Mrk 79. Top center: [OIII]λ5007 emission-line image from HST. Top right: Log flux map for the [OIII]λ5007 emission line (in units of erg s^{-1}cm^{-2}). The bottom panels show examples of spectra obtained within an aperture of 0.25″×0.25″ centered at the nucleus (left) and at position "B" (right), identified in the top central panel.

GMOS datacube. In the bottom panels, we present spectra extracted within an 0.25″×0.25″ aperture centered at the nucleus (left) and at the position of the [OIII] emission peak. The spectra of the galaxies have been used to map the gas flux distributions, excitation and kinematics. In order to do this, we have fitted the line profiles by Gaussian curves (Riffel, 2010).

Extended emission was observed up to the borders of the field of view for the strongest emission lines (e.g. [OIII]λ5007, Hα, [NII] λ6583 Å), that correspond to average distances from the nuclei in the range 0.5 – 1.2 kpc. In dos Santos et al. (in preparation) we will present the complete results of our study, while here we just show the resolved BPT (Baldwin et al., 1981) diagram [OIII] λ5007 Å/Hβ vs. [NII] λ6583/Hα in Fig. 2. The dashed curves represent the division lines between star-forming (SF) galaxies and AGN from Kauffmann & et al. (2003) and Kewley et al. (2001). The solid line shows the division between Seyfert and LINER nuclei (Cid Fernandes et al., 2010). Different galaxies are shown as distinct colors in this figure. As can be observed, the gas excitation for all galaxies is dominated by the active nucleus, as the line ratios are typical of Seyfert nuclei at all locations of the GMOS field of view.

4. Conclusions

We used GMOS-IFU observations of the inner 3.5"×5.0" (corresponding to average distances at the galaxies of 1.2 kpc – 1.7 kpc) of five nearby Seyfert galaxies to map the optical emission-line flux distributions and excitation. Extended

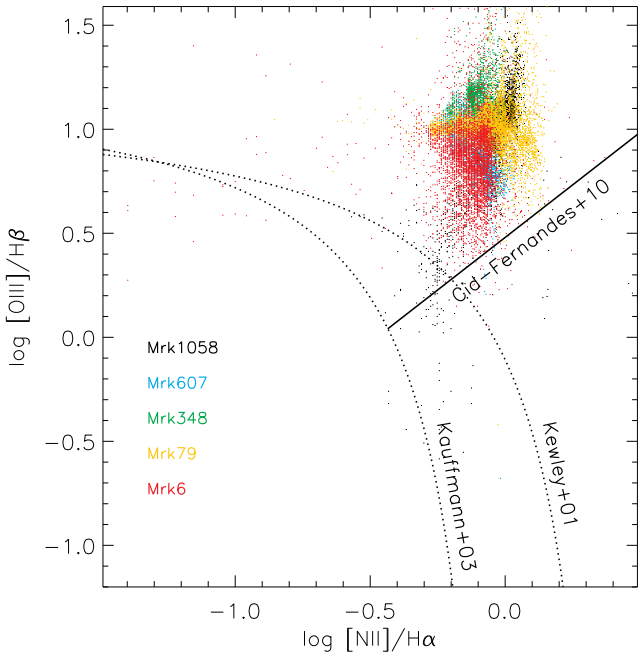

Figure 2. BPT diagram for [OIII] λ5007 Å/Hβ versus [NII] λ6583 Å/Hα line ratios for all the observed galaxies. Figure already published in Freitas et al. (2018).

emission over the whole IFU field of view is observed for most emission lines for all galaxies. The BPT diagram [OIII] λ5007 Å/Hβ vs. [NII] λ6583 Å/Hα shows a range of excitation but all covered positions of the NLR present Seyfert-like excitation. A more complete analysis of the gas excitation, including also its kinematics will be presented in dos Santos et al. (in preparation). The velocity field of all galaxies shows a rotating disk component.

Acknowledgments. We thank Brazilian institutions CNPq and FAPERGS for financial support.

References

Baldwin J. A., Phillips M. M., Terlevich R., 1981, *PASP*, **93**, 5
Cid Fernandes R., Stasińska G., et al., 2010, *MNRAS*, **403**, 1036
Diniz M. R., Riffel R. A., Storchi-Bergmann T., et al., 2015, *MNRAS*, **453**, 1727
Fischer T. C., et al., 2014, *ApJ*, **785**, 25
Fischer T. C., et al., 2017, *ApJ*, **834**, 30
Freitas I. C., Riffel R. A., Storchi-Bergmann T., Elvis M., Robinson A., Crenshaw D. M., Nagar N. M., Lena D., Schmitt H. R., Kraemer S. B., 2018, *MNRAS*, **476(2)**, 2760
Kauffmann G., et al., 2003, *MNRAS*, **346**, 1055
Kewley L. J., Heisler C. A., Dopita M. A., Lumsden S., 2001, *ApJS*, **132**, 37
Lena D., 2014, *ArXiv e-prints 1409.8264*

Chemical Abundances in Gaseous Nebulae
AAA Workshop Series 10, 2016
G. Hägele, M. Cardaci & E. Pérez-Montero, eds.

Poster

Star formation around the Seyfert 1 nucleus of Mrk 42

Moiré G. Hennig[1], Rogemar A. Riffel[1] and Oli Dors[2]

[1] *Universidade Federal de Santa Maria, Departamento de Física, Centro de Ciências Naturais e Exatas, 97105-900, Santa Maria, RS, Brazil*
[2] *Universidade do Vale do Paraíba, Av. Shishima Hifumi 2911, CEP 12244-000, São José dos Campos, SP, Brazil*

Abstract.
We analyzed two-dimensional maps for the emission-line flux distributions, kinematics and equivalent widths of the inner ∼1.5" of the Seyfert 1 galaxy Mrk42. This galaxy shows a ring of circumnuclear star forming regions with radius of 1". The observations were done with the Gemini Near-Infrared Integral-Field Spectrograph (NIFS) at the J, H and K bands at a spatial resolution of 60 pc. For some of the star forming regions we observed absorptions features that may be related to stars in the Thermally Pulsing Asymptotic Giant Branch (TP-AGB) phase, as suggested by simple stellar populations models. At most locations, the [FeII]1.2570μm/Paβ line ratio is smaller than 0.6 indicating that the Seyfert nucleus does not play an important role on the gas excitation, which may be dominated by photoionization by young stars.

1. Introduction

Star formation in the circumnuclear regions of galaxies suggest a scenario in which material flows inwards central region and is accumulated to form a cold gas reservoir in a circumnuclear ring with radius of a few hundreds of parsecs. Two main scenarios have been proposed to explain the origin of rings of Circumnuclear Star-Forming Regions (CNSFRs) in galaxies: the popcorn and the pearls on a string scenarios (Elmegreen, 1994 and Böker et al. 2008). Eventually, the material that is accumulated in the ring can flow towards the nucleus of the galaxy along dust spiral arms as seen for some nearby Seyferts (Riffel et al., 2008) and trigger the nuclear activity of the galaxy, forming an Active Galactic Nucleus (AGN). Another possibility to trigger the nuclear activity would be due to winds from young stars in the CNSFRs, leading to the so-called AGN-Starburst connection, as speculated in Riffel et al. (2009), for example. This connection could play a fundamental role to explain the co-evolution of the central Supermassive Black Hole (SMBH) and the host galaxy (Ferrarese & Merritt, 2000; Gebhardt et al., 2000), as the star formation in the central region leads to the enhancement of the bulge mass, while material accreted by the SMBH increases its mass.
In this work, we present near-infrared Integral Field Spectroscopy (IFS) of the inner $3'' \times 3''$ of the Mrk 42. This galaxy presents a well known circumnuclear star

formation ring at $\sim 1''$ (500 pc) from the nucleus (Muñoz Marín et al., 2007). The IFS allows us to investigate the origin of the near-infrared emission line and map the gas kinematics of the inner 750 pc of the galaxy. This work is organized as follows. In section 2 we describe the observations and data reduction procedure. In section 3 we present and briefly discuss the results for the gas kinematics and distribution. In section 4 we present the conclusions of this study.

2. Observation and data reduction

The J, H and K band spectroscopic data of Mrk 42 were obtained with Gemini Near-infrared Integral Field Spectrograph (NIFS; McGregor et al., 2003) operating with the ALTAIR adaptive optics module on the Gemini North telescope. The observations were done in May 2014 under the programme GN-2014A-Q-28. The NIFS has a $3'' \times 3''$ field of view, which was centered at the nucleus of the galaxy during the observations. The J-band observations were centered at 1.25μm, covering a spectral region from 1.15μm to 1.35μm, at a spectral resolution of ≈ 2.3Å. The H-band observations were centered at 1.65μm and covered the spectral range from 1.48μm to 1.80μm at a spectral resolution of ≈ 2.7Å. The K observations were centered at 2.20μm, covering a spectral range between 2.01μm and 2.42μm at a spectral resolution of ≈ 3.1Å. The total on-source exposure time for each band was 1.15 hours.
The data reduction followed the standard procedure of near-infrared spectroscopic data treatment and the final data cube for each band were created with an angular sampling of 0.05"×0.05", covering the inner 740×740 pc^2 of the galaxy.

3. Results

In the left panel of Fig. 1 we show an optical image of Mrk 42 obtained with the Hubble Space Telescope (HST) using the F606W filter (Malkan et al., 1998), with the NIFS field of view represented by the central square. The symbol "+" marks the location of the nucleus, defined as the peak of the continuum emission. The right panel shows the K-band continuum emission obtained from the NIFS datacube, shown in units of 10^{-17} erg s^{-1} cm^{-2} Å^{-1}.
In order to map the emission-line flux distributions and kinematics, we used the emission-line PROfile FITting (PROFIT) routine (Riffel, 2010) to fit the line profiles of [FeII] $\lambda\,1.25\mu$m, OI $\lambda\,1.12\mu$m, Paβ, [FeII] $\lambda\,1.64\mu$m, Brγ and H_2 $\lambda\,2.12\mu$m at each pixel with Gaussian curves. In Fig. 2 we present the resulting maps for the Equivalent Widths (EW) for the strongest emission lines. The circumnuclear star forming ring is observed for most emission lines, while the individual star forming regions are clearly seen in the map for Paβ. In this map, we have overlaid circles to delineate the star-forming regions and better understand how the star formation is going on in the ring. The spectra for the regions E, F and G (identified in the Paβ map) show absorption features (in particular from VO), characteristic of stars in the Thermally Pulsing Asymptotic Giant Branch (TP-AGB) phase (Maraston, 2005), suggesting that these regions are older than other regions, as indicated also by the lower EW values. Another result is that the H_2 and [FeII] lines show a distinct distribution of EW values, as compared to the

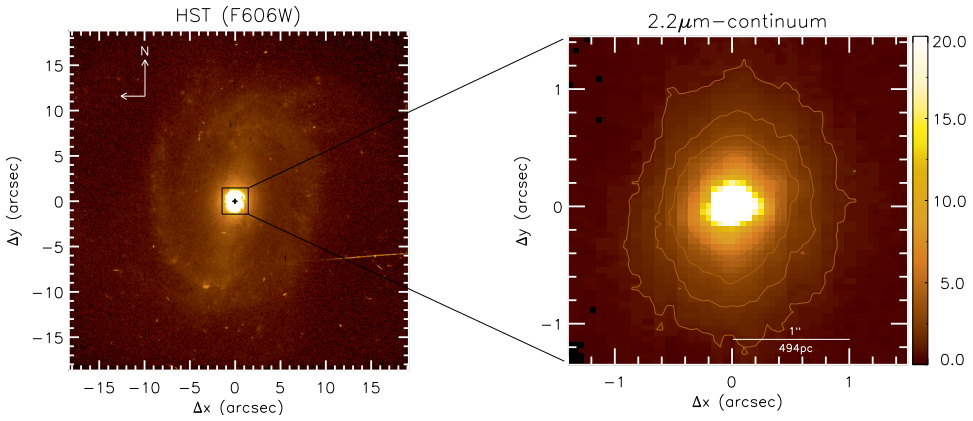

Figure 1. Large scale image obtained with the HST (left) and K-band continuum obtained from NIFS data (right). The continuum fluxes are show in units of 10^{-17} erg s^{-1} cm^{-2} Å^{-1}.

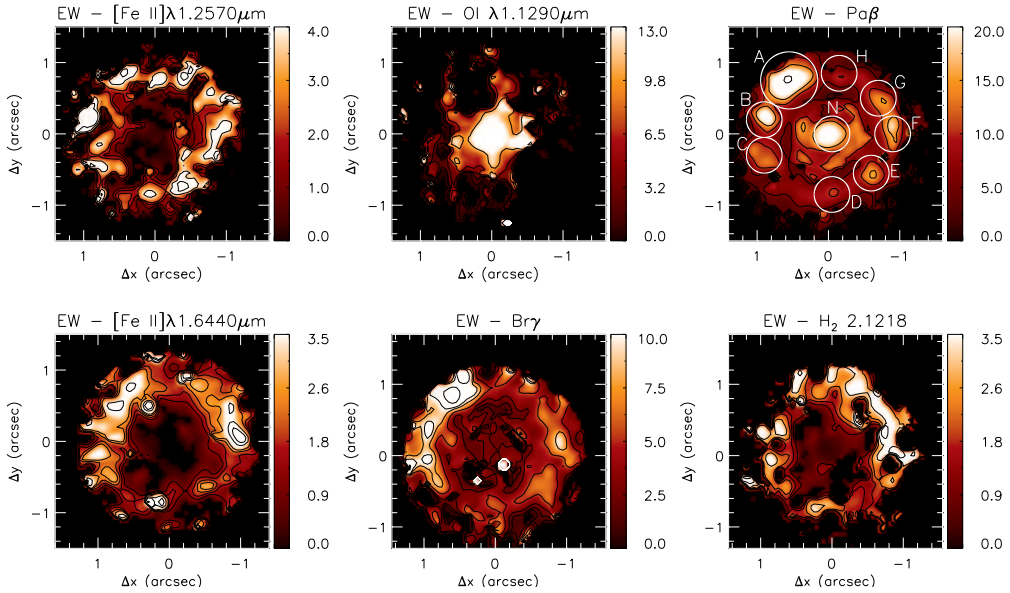

Figure 2. EW maps for [FeII] λ 1.25μm, OI λ 1.12μm, Paβ, [FeII] λ 1.64μm, Brγ and H_2 λ 2.12μm emission-lines

HI recombination lines, suggesting a distinct origin for these lines, possible with additional contribution by shocks to the excitation of the H_2 and [FeII] lines.

4. Conclusions

We presented near-infrared integral field spectroscopy of the inner $3'' \times 3''$ of the Seyfert 1 galaxy Mrk 42 at a spatial resolution of 60 pc. The main conclusions are:

- The flux distributions and EW maps for the [FeII] $\lambda 1.25\mu$m, OI $\lambda 1.12\mu$m, Paβ, [FeII] $\lambda 1.64\mu$m, Brγ and H_2 $\lambda 2.12\mu$m emission-lines show higher values at a ring with $1''$ radius centered at the nucleus. The origin of the emission is consistent with gas excited by young stars, as suggested by flux line ratios.

- The spectra of some star forming regions show spectral features related to stars in the TP-AGB phase.

- The gas velocity fields show a clear rotation pattern and the velocity dispersion maps show small values at extranuclear regions, suggesting that the emitting gas is located at the plane of the galaxy.

Acknowledgments. We thank Brazilian intitutions CNPq and FAPERGS for financial support.

References

Böker T., Falcón-Barroso J., Schinnerer E., et al., 2008, *AJ*, **135**, 479
Elmegreen B. G., 1994, *ApJL*, **425**, L73
Ferrarese L., Merritt D., 2000, *ApJL*, **539**, L9
Gebhardt K., Bender R., Bower G., et al., 2000, *ApJL*, **539**, L13
Malkan M. A., Gorjian V., Tam R., 1998, *ApJS*, **117**, 25
Maraston C., 2005, *MNRAS*, **362**, 799
McGregor P. J., Hart J., Conroy P. G., et al., 2003, M. Iye and A. F. M. Moorwood (eds.), *Instrument Design and Performance for Optical/Infrared Ground-based Telescopes*, Vol. 4841 of *Proc. SPIEJ*, pp 1581–1591
Muñoz Marín V. M., González Delgado R. M., Schmitt H. R., et al., 2007, *AJ*, **134**, 648
Riffel R. A., 2010, *Ap&SS*, **327**, 239
Riffel R. A., Storchi-Bergmann T., Dors O. L., et al., 2009, *MNRAS*, **393**, 783
Riffel R. A., Storchi-Bergmann T., Winge C., et al., 2008, *MNRAS*, **385**, 1129

Chemical Abundances in Gaseous Nebulae
AAA Workshop Series 10, 2016
G. Hägele, M. Cardaci & E. Pérez-Montero, eds.

Poster

The role of shocks in NGC 2440 and NGC 6302

Lago.P.J.A[1] and Costa. R. D. D[1]

[1]*IAG/USP, Rua do Matão, 1226, Cidade Universitária, São Paulo SP, Brazil.*

Abstract. Planetary nebulae (PNe) are the result of the stellar evolution of low mass stars. PNe formation processes are, until now, a challenge to our knowledge, since there are several morphological types of these objects, going from the most regular, with spherical symmetry, to strongly asymmetrical ones. Understanding the physical mechanisms that define the structure and excitation/ionization in PNe is the key to explain their formation. NGC 2440 and NGC 6302 are very well studied PNe; NGC 2440 is a multipolar PN with, at least, two bipolar components, while NGC 6302 is bipolar. Both are rich in small substructures such as knots, displaying a very complex structure. This work aims to investigate, in the light of new diagnostic diagrams, the role of shocks in the excitation/ionization of these nebulae. For this, line ratios and density maps from literature were used; velocity fields were obtained from the literature for NGC 2440, and derived from our data, acquired at Pico dos Dias (OPD) using the Coudé spectroscopy, for NGC 6302. Preliminary results show that the shocks are a very important mechanism of excitation/ionization in both nebulae.

1. Introduction

PNe are the result of evolution of low mass stars; their morphology shaping process is better described by the scenario of interacting winds (Balick, 1987). The morphology is a consequence of the expanding process of the gas shells, taking into account companion stars and interaction with the interstellar medium and older shells in the shaping process.
Recently the shocks in the gas are in evidence, since their role are being revisited using more powerful computational modeling (Riera & Raga, 2007; Raga et al., 2008). The main aspect of shocks in PNe is the increasing of intensity of low ionization lines such as [NII], [OII] and [SII]. These lines are noticeably stronger in Low Ionization Structures (LIS; Gonçalves et al., 2001) and their faster versions, Fast Low-Ionization Emission Regions (FLIERs; Balick et al., 1993, 1994). In these context, Akras & Gonçalves (2016) developed diagnostic diagrams to classify ionization/excitation physical mechanisms of structures in PNe.
The diagnostic diagrams are based on line ratios and photon flux ratios. The low ionization lines are compared with the $H\alpha$ recombination line; the photon flux of the star is compared with the same flux from shocks. The photon flux from shocks depends on the velocity and the density of the medium; the shocks

will be easily detectable in regions of PNe at high velocity regimes far from the central star. In contrast, stars with high luminosity should hide shocks because of the dominance of the radiation field.
NGC 2440 and NGC 6302 are two well studied PNe. NGC 2440 is multipolar, with two bipolar structures and a segmented torus structure around its core (Lago & Costa, 2016), while NGC 6302 is a bipolar one. Both nebulae are classified as type I, being rich in microstructures as knots, rims, arcs and filaments, and at the same time their nitrogen abundances are high.
This work presents our results on the role of shocks in these nebulae. For NGC 2440 we show this for some microstructures in the high velocity regime. For NGC 6302 we performed a complete study along the symmetry axis. Beyond the presence of shocks, we also intent to investigate how they can influence the Ionization Correction Factors (ICFs).

2. Procedure

The study of shocks in NGC 2440 and NGC 6302 was based on our own data and data compiled from the literature (Cuesta & Phillips, 2000; Rauber et al., 2014) to construct the diagnostic diagrams. Using data from Observatório do Pico dos Dias (OPD), Brazil, we obtained the velocity field for NGC 6302, taken into account the projection effect due to the inclination of the nebula, assuming that it has symmetrical lobes. We also derived a distance to the nebulae of 805 ± 143 pc comparing our data with Szyszka et al. (2011).
Rauber et al. (2014) presented detailed maps of NGC 6302, derived with the Southern Astrophysical Research (SOAR) telescope using a long slit spectrograph, sampling the nebula using a large set of parallels slits, and obtaining therefore similar data to those derived with an Integral Field Unit (IFU) instrument. The maps allow us to construct diagnostic diagrams based on the line ratio maps such as the density map along the symmetry axis of the nebula. The main error source for our diagrams is the star luminosity, since there are many different values in the literature. This work assumed a value of $5690\,L_{\odot}$ (Wright et al., 2011), because this value is based on a multi-wavelength observational measure.
Cuesta & Phillips (2000) present maps of NGC 2440 from data obtained using narrow filter images. We used these data in a similar way as those of NGC 6302; the difference is that we built the diagrams for microstructures and not along axis, due to the morphology of nebula. A luminosity of $2100\,L_{\odot}$ was assumed to this nebula, a value accepted in the literature, and the velocities fields are from the model of Lago & Costa (2016).
The diagrams are presented below; all used equations are from the work by Akras & Gonçalves (2016).

3. Results

Figs. 1 and 2 present our results. Vertical lines mark the three different regimes: in the left photo-excitation dominates, the center is a transition zone and at right

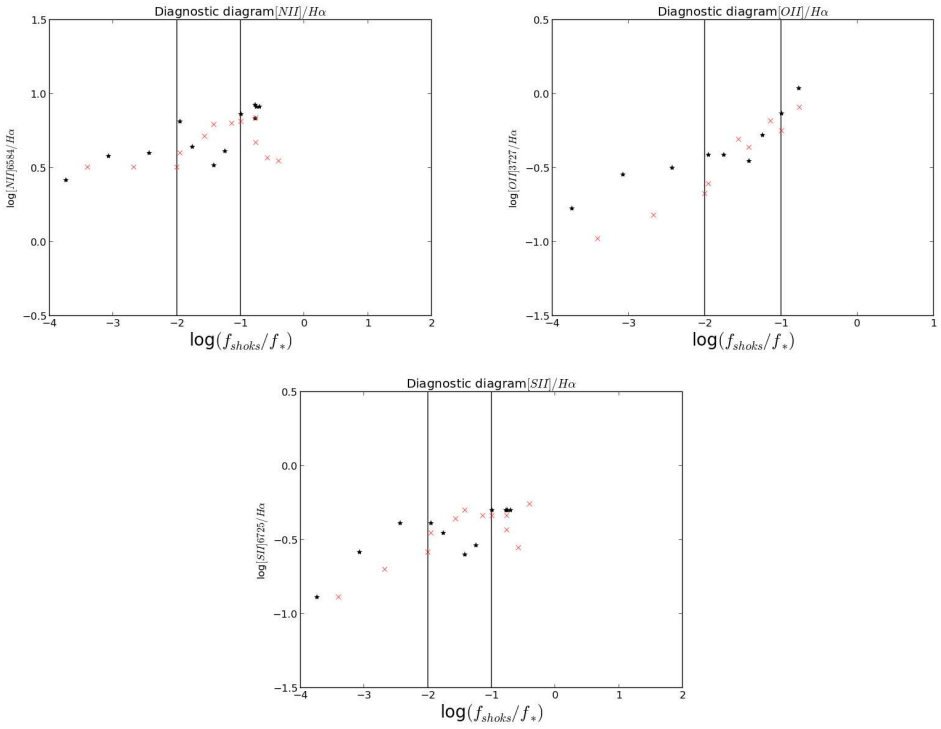

Figure 1. Diagnostic diagrams for NGC 6302. The different symbols refer to each lobe. The black stars and the red crosses represent the east and the west lobe, respectively.

the shocks dominates. Diagrams for NGC 6302 show two different symbols that represent each lobe.

The studied regions of NGC 2440 are all shock-dominated. This result was expected, considering the velocity regimes of the structures and IR observations that shows an outer shell involving all nebula (Ramos-Larios & Phillips, 2009). We suggest, based on visible observations, a kinematic model to this outer shell (Lago at al. 2017 in prep.). We emphasize that the shocks could be a natural consequence, for NGC 2440, of the interaction of the faster inner gas with the outer shell, slower and tenuous.

NGC 6302 shows, in all diagrams, a growing trend of line ratios with the increasing of the photon flux rate, this is a natural consequence of the higher velocities and dilution of radiation field of the central star. Possibly due to the high luminosity of the star, the shocks share their influence with the strong radiation field and most of the points are in the transition zone. Shocks gain relevance far from the star, and therefore the peripheral regions of the nebula are shock-dominated. We could expect an outer shell as in the case for NGC 2440, but data in visible band prevent us to reach this conclusion.

Our diagrams are the first to show the distribution of the nebula parts. They reveal a very important feature: due to the high nitrogen abundance in NGC 6302, it is only significant compare line ratios of one nebula. Comparisons based on line

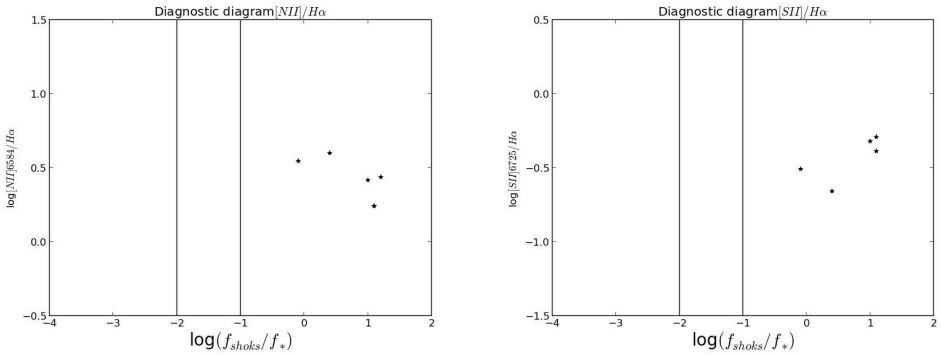

Figure 2. Same as 1 for NGC 2440.

ratios for different objects have no clear meaning. In this case, it would not be possible to separate the increase of line ratios by shocks from an overabundance. A detailed study about the influence of shocks along these nebulae is required. Since it is a problem to distinguish the effects of shocks from abundances, the ICFs could be over or underestimated. The consequence would be errors in the derivation of abundances. Emphasizing: more studies are necessary to quantify the effects of shocks along nebulae, velocity regimes and density changes, in order to suggest a correction to usual ICF's.

References

Akras S., Gonçalves D. R., 2016, *MNRAS*, **455**, 930
Balick B., 1987, *AJ*, **94**, 671
Balick B., Perinotto M., Maccioni A., et al., 1994, *ApJ*, **424**, 800
Balick B., Rugers M., Terzian Y., Chengalur J. N., 1993, *ApJ*, **411**, 778
Cuesta L., Phillips J. P., 2000, *ApJ*, **543**, 754
Gonçalves D. R., Corradi R. L. M., Mampaso A., 2001, *ApJ*, **547**, 302
Lago P. J. A., Costa R. D. D., 2016, *RevMexAA*, **52**, 329
Raga A. C., Riera A., Mellema G., et al., 2008, *A&A*, **489**, 1141
Ramos-Larios G., Phillips J. P., 2009, *MNRAS*, **400**, 575
Rauber A. B., Copetti M. V. F., Krabbe A. C., 2014, *A&A*, **563**, A42
Riera A., Raga A. C., 2007, *Asymmetrical Planetary Nebulae IV*
Szyszka C., Zijlstra A. A., Walsh J. R., 2011, *MNRAS*, **416**, 715
Wright N. J., Barlow M. J., Ercolano B., Rauch T., 2011, *MNRAS*, **418**, 370

Chemical Abundances in Gaseous Nebulae
AAA Workshop Series 10, 2016
G. Hägele, M. Cardaci & E. Pérez-Montero, eds.

Poster

Investigating spatial variation of the physical and chemical conditions of NGC 6778.

H. Monteiro[1], J. García-Rojas[2,3], D. Jones[2,3], R. Corradi[2,3,4] and Rodríguez-Gil[2,3], P.

[1] *Universidade Federal de Itajubá - UNIFEI*
[2] *Instituto de Astrofísica de Canarias (IAC), Vía Láctea s/n, E38200, La Laguna, Tenerife, Spain*
[3] *Departamento de Astrofísica, Universidad de La Laguna, La Laguna, E-38206, Tenerife, Spain*
[4] *GRANTECAN, Cuesta de San José s/n, E-38712 , Breña Baja, La Palma, Spain*

Abstract. A number of planetary nebulae show binary central stars and significant abundance discrepancies between values estimated from collisionally excited lines when compared to the same abundances estimated from recombination lines. One approach to investigate this yet unsolved problem is using spatially resolved images of emission lines in an attempt to detect a possibly distinct metal rich component in the nebula. In this work we present results of spatially resolved abundance analysis of NGC 6778 based on data gathered from VLT VIMOS-IFU. We discuss the spatial variations found as well as possible limitations of the method in answering questions about abundance variations.

1. Introduction

Chemical abundances in planetary nebulae are important as a tool to study stellar evolution, estimate effects of internal stellar nucleosynthesis and mixing, among others issues related to chemical evolution. Because of that PNe are used to study the chemical evolution in the Galaxy and in other nearby galaxies.
It is well known (see e.g. Osterbrock & Ferland, 2006) that in photoionized nebulae – both HII regions and planetary nebulae – optical recombination lines (ORLs) provide chemical abundance values that are systematically larger than those obtained using collisionally excited lines (CELs). The abundance discrepancy factor (ADF) between ORLs and CELs is usually between 1.5 and 3 (see e.g. García-Rojas & Esteban, 2007; Liu, 2012), but in planetary nebulae (PNe) it has a significant tail extending to much larger values. This is generally known as the abundance discrepancy problem. It has been around for more than seventy years (Wyse, 1942), and is one of the major unresolved problems in nebular astrophysics. The problem has far-reaching consequences on the measurement of abundances throughout the Universe, as the chemical content of near and far-away galaxies is most often done using CELs from their ionized gas (e.g. Hamann et al., 2002).

Corradi et al. (2015) have recently shown that the largest abundance discrepancies are reached in planetary nebulae with close binary central stars. For instance, in the PNe Abell 46, Ou5, and NGC 6778, which have binary central stars with orbital periods of a few hours, they found O^{2+}/H^{+} ADFs larger than 40, and as high as 300 in the inner regions of Abell 46. Spectroscopic analysis supports the previous interpretation that two different gas phases coexist in these nebulae (e.g. Liu et al., 2006; Tsamis et al., 2008): hot gas at 10^4 K with standard metallicity where the CELs can be efficiently excited, and a much cooler (10^3 K) plasma with a highly enhanced content of heavy elements (which is likely the cause of the cooling) where only ORLs form. How much each gas component contributes to the total mass, and how they are distributed and mixed, is basically unknown. In this work we show the results for the object NGC 6778 obtained from VLT Integral Field Unit (IFU) data and spatially resolved abundance analysis. The present effort is part of a larger project that aims to understand the large discrepancy in PNe.

2. Observational data

The observations were obtained with the instrument VIMOS-IFU, attached to ESO-VLT-U3 on the 14 of september, 2007. The instrument is composed of 6400 fibers and, has a changeable scale on the sky that was set to 0.33" per fiber, to obtain our data. The image is formed by a matrix of 40x40 fibers, which gave us a coverage of 13.2"x13.2" on the sky. We obtained observations in high-resolution mode, with a pixel scale of 0.6 Å pix^{-1} with a useable range from 3900 Å to 7000 Å, considering both the blue and red grisms of the spectrograph. The object was observed with an exposure time of 300 seconds in both red and blue configurations. The reduction was performed with the VIMOS pipelines available at the instrument website[1].

3. Results

Because we do not deal with integrated fluxes, the typical signal-to-noise ratio in a volumetric pixel (voxel) of the data cube can be significantly lower in comparison to usual long-slit data. In practice, the trade-off of spatial resolution is lower signal to noise ratio (S/N) in a given pixel of the observed map. The limited S/N may result in significant noise when spatially resolved diagnostic ratio maps are computed. To improve the quality of the final maps we applied a median noise filter to remove some of the noise, especially in the low S/N regions.
To work with the emission line maps and derive the nebular properties (internal extinction, electron densities, and temperatures and abundances), we used a set of Python scripts and the NEAT software described in detail in Wesson et al. (2012).
The code computes the extinction coefficient c(Hβ) using the available Balmer lines. The extinction-corrected emission-line maps were used to derive the spatial distribution of the electron density (N_e) and temperature (T_e) of the nebula

[1]http://www.eso.org/sci/facilities/paranal/instruments/vimos/

as well as abundances and abundance discrepancy factors (ADFs). For the calculations we adopted the extinction law of Howarth (1983). The atomic data used for He I abundances is from Smits (1996). The ICF scheme used to correct for unseen ions was that of Delgado-Inglada et al. (2014). In Fig. 1 we show the temperature, abundances and ADFs maps.

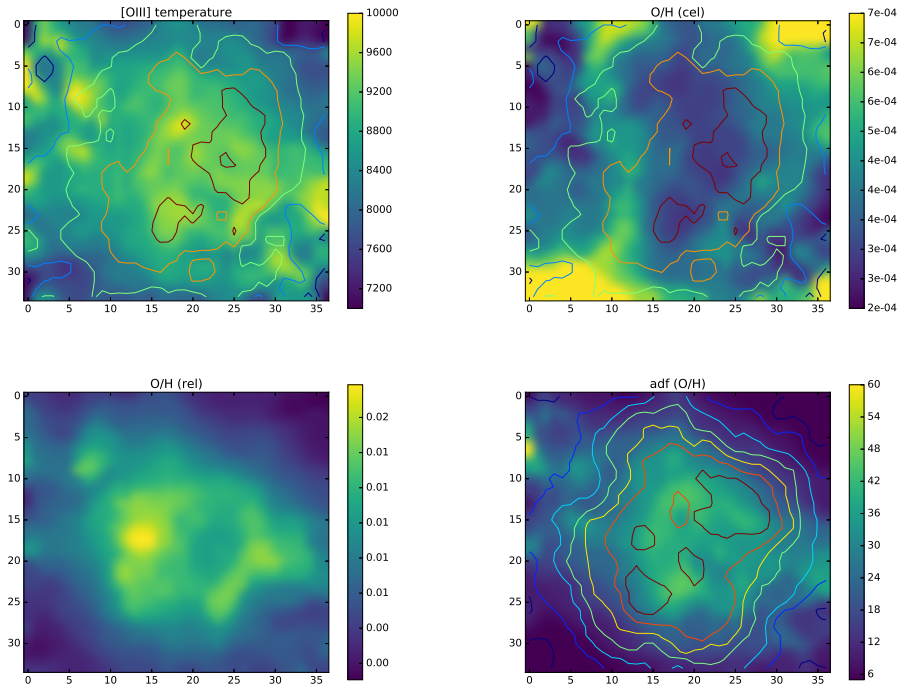

Figure 1. Temperature (upper left), abundances obtained from CELs (upper right), both with the [OIII]4363 contours overlaid, from RELs (lower left) and ADF maps (lower right with the OII 4650 contours overlaid) for NGC 6778.

The results obtained here corroborate previous results from long-slit spectra presented by Jones et al. (2016) and expand on the ones from García-Rojas et al. (2016).

4. Conclusion

The planetary nebula NGC 6778 has been studied with data from the VLT IFU instrument from where we collected high resolution spatially resolved spectra. The nebula shows a density enhanced waist which correlates with the bright emissions regions seen in both [SII] and [NII] lines. The temperature estimated from the low ionization [NII] lines as well as the [OIII] lines, shows hotter regions along the axis perpendicular to the main waist.

The abundance maps also show structural variations that seem to follow the axis perpendicular to the main waist. Interestingly the abundance variations obtained from recombination lines show an increase towards the central region of the nebula while the abundances obtained from collisional lines show increases that are coincident with the higher density waist.
The [OIII]4363 emission resembles the OII recombination emission but not the strong [OIII]5007 emission which may be due to presence of a high-density, H-poor gas component in the inner regions of the nebula. The H-poor component could be the source of the OII emission and the cause of the abundance discrepancy. The ADF maps show larger discrepancies correlated with the axis perpendicular to the waist, consistent with values obtained by Jones et al. (2016). These results may provide important constraints for the existence and formation times of jets (Guerrero & Miranda, 2012). All this information will also help in constraining the role of binaries and their relation to the geometry and ejection mechanism of the metal rich (H-poor) component.

Acknowledgments. This research was performed using the computer cluster **Giskard** and assistance of the Laboratório de Astrofísica Computacional da Universidade Federal de Itajubá (LAC-UNIFEI). The LAC-UNIFEI Giskard cluster was acquired by a Capes Pró-Equipamentos Grant in 2014.

References

Corradi R. L. M., García-Rojas J., Jones D., et al., 2015, *ApJ*, **803**, 99
Delgado-Inglada G., Morisset C., Stasińska G., 2014, *MNRAS*, **440**, 536
García-Rojas J., Corradi R. L. M., Monteiro H., et al., 2016, *ApJL*, **824**, L27
García-Rojas J., Esteban C., 2007, *ApJ*, **670**, 457
Guerrero M. A., Miranda L. F., 2012, *A&A*, **539**, A47
Hamann F., Korista K. T., Ferland G. J., et al., 2002, *ApJ*, **564**, 592
Howarth I. D., 1983, *MNRAS*, **203**, 301
Jones D., Wesson R., García-Rojas J., et al., 2016, *MNRAS*, **455**, 3263
Liu X., 2012, *IAU Symposium*, Vol. 283 of *IAU Symposium*, pp 131–138
Liu X.-W., Barlow M. J., Zhang Y., et al., 2006, *MNRAS*, **368**, 1959
Osterbrock D. E., Ferland G. J., 2006, *Astrophysics of gaseous nebulae and active galactic nuclei*
Smits D. P., 1996, *MNRAS*, **278**, 683
Tsamis Y. G., Walsh J. R., Péquignot D., et al., 2008, *MNRAS*, **386**, 22
Wesson R., Stock D. J., Scicluna P., 2012, *MNRAS*, **422**, 3516
Wyse A. B., 1942, *ApJ*, **95**, 356

Chemical Abundances in Gaseous Nebulae
AAA Workshop Series 10, 2016
G. Hägele, M. Cardaci & E. Pérez-Montero, eds.

Poster

Bar effects on ionized gas chemical abundances in disc galaxies

A. Zurita[1,2], E. Florido[1,2], E. Pérez-Montero[3], I. Pérez[1,2], P. Coelho[4] and D.A. Gadotti[5]

[1]*Dpto. de Física Teórica y del Cosmos. Universidad de Granada, 18071 Granada, Spain*
[2]*Instituto Carlos I de Física Teórica y Computacional, 18071 Granada, Spain*
[3]*Instituto de Astrofísica de Andalucía, CSIC, 18080 Granada, Spain*
[4]*Universidade de São Paolo, R. do Matão, 1226, 05508-090 São Paolo, SP, Brazil*
[5]*European Southern Observatory, 19001 Casilla, Santiago 19, Chile*

Abstract. Bars are considered important agents for the secular evolution of galaxies, as they induce gas inflows towards galaxy centers. According to simulations, bar-induced gas inflow effects include the accumulation of gas in galaxy centers where it can trigger star formation, and the alteration of the physical and chemical properties of the central ionized gas. However observations are not yet conclusive on the impact of bars in galaxy evolution. We have analyzed the ionized gas properties in the central parts of barred and unbarred galaxies in order to study whether these properties are altered by the presence of a bar, and whether the induced changes are related to parent galaxy properties.

1. Galaxy sample and methodology

The galaxy sample is the one used by Coelho & Gadotti (2011) and includes all spiral face-on galaxies ($b/a \geqslant 0.9$) in the Sloan Digital Sky Survey (SDSS) data release 2, with stellar masses larger than 10^{10} $M_{\odot}$, redshift $0.02 \leqslant z \leqslant 0.07$, bulge-to-total luminosity ratio above 0.043 (i.e. earlier than ∼Sd), and with signal-to-noise ratio in their corresponding SDSS spectra greater than or equal to 10 (in the g-band). This sample is made up of 251 barred and 324 unbarred galaxies.

The pre-processing of their SDSS spectra includes Galactic extinction correction, and modelling and subtraction of the stellar component with the spectral synthesis code STARLIGHT (Cid Fernandes et al., 2005). Afterwards, the fluxes of the brightest emission lines (from [O II]$\lambda\lambda$3727,3729 to [S II]$\lambda\lambda$6717,6731) were measured. We refer the reader to Gadotti (2009), Coelho & Gadotti (2011) and Florido et al. (2015) for further details on the sample selection, on the spectra processing and on the emission-line measurements, respectively.

Standard diagnostics based on bright emission-line ratios (Kewley et al., 2001) were then used to separate the galaxies where the dominant mechanism of ioni-

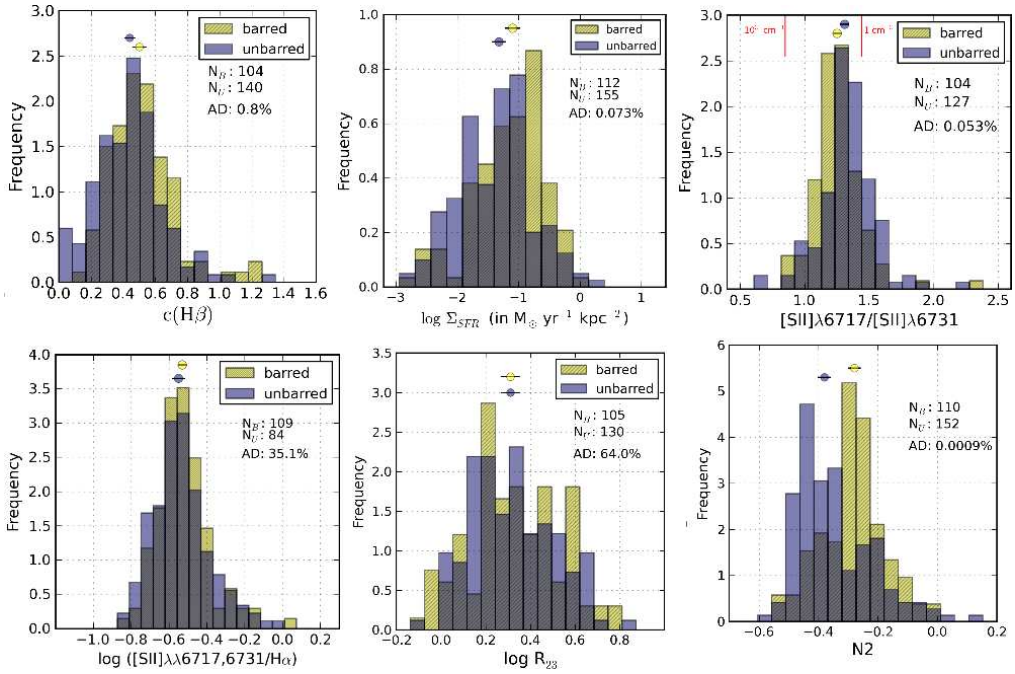

Figure 1. Histograms of the values for different parameters for all non-AGN barred and unbarred galaxies of the sample. From left to right and from top to bottom: internal Balmer extinction at Hβ, star formation rate per unit area, emission-line ratio [S II]λ6717/[S II]λ6731, decimal logarithm of the [S II]$\lambda\lambda$6717,6731/Hα ratio, and oxygen abundance indicators R_{23} and N2. The number of galaxies in each subsample (N_B and N_U) is indicated in each panel, together with the two-sample Anderson-Darling test P-values (AD, in %). Credit: Florido et al., A&A, 584, A88, 2015, reproduced with permission © ESO.

sation is UV radiation from massive stars from those galaxies hosting an active galactic nucleus (AGN). The final non-AGN galaxy sample comprises 173 barred and 265 unbarred galaxies. The total galaxy stellar mass and redshift distributions are similar for barred and unbarred galaxies with two-sample Anderson-Darling (AD) P-values larger than 35%.

2. Comparison barred/unbarred

We have analyzed the distributions of internal Balmer extinction at Hβ [c(Hβ)], star formation rate per unit area (Σ_{SFR}), empirical abundance tracers (R_{23} and N2), electron density sensitive emission-line ratio [S II]λ6717/[S II]λ6731, and shock- and/or AGN sensitive emission-line ratios [S II]$\lambda\lambda$6717,6731/Hα and the [O I]λ6300/Hα, for barred and unbarred galaxies separately. These are shown in Fig. 1, except for [O I]λ6300/Hα (available in Florido et al., 2015). The distributions of all the parameters analyzed are different in barred and unbarred galaxies,

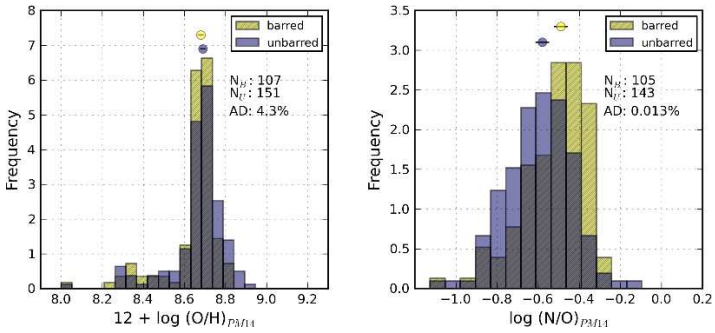

Figure 2. Histograms of the oxygen abundance (*left*) and nitrogen-to-oxygen abundance ratio (*right*) for barred and unbarred galaxies separately. Credit: Florido et al., A&A, 584, A88, 2015, reproduced with permission © ESO.

except for the R_{23} parameter and the [S II]$\lambda\lambda$6717,6731/Hα and [O I]λ6300/Hα emission-line ratios. The most striking result appears in the [N II]λ6583/Hα line ratio that is, on average, ∼25% higher in barred galaxies, with an AD P-value of 0.0009%, much lower than the 5% value normally adopted, below which the null hypothesis that both sub-samples are drawn from the same parent distribution can be discarded. The fact that shock- and/or AGN sensitive emission-line ratios are similar for barred and unbarred galaxies, implies that the most plausible explanation for the [N II]λ6583/Hα enhancement in barred galaxies is a larger nitrogen-to-oxygen abundance in the centers of these galaxies compared to the unbarred ones.

2.1. Chemical abundances

Given that there is no difference between barred and unbarred galaxies in terms of the R_{23} parameter, any empirical calibration of this parameter would yield the same average oxygen abundance for both types of galaxies. The opposite would happen with calibrations of the N2 parameter, except for those including a correction for the N/O abundance ratio (e.g. Pérez-Montero & Contini, 2009). We have estimated 12+log(O/H) and log(N/O) with the grids of photoionisation models by Pérez-Montero (2014), the so called HII-CHI-mistry method.

Fig. 2 shows the resulting distributions for barred and unbarred galaxies separately. The N/O abundance ratio is enhanced in the centers of barred galaxies by ∼0.1 dex. However, we do not find differences in central 12+log(O/H) in barred and unbarred galaxies. This is in contrast with previous work by Ellison et al. (2011), who find a larger O/H in barred galaxies. However, these authors use the [N II]/[O II] empirical calibration by Kewley & Dopita (2002) to derive oxygen abundances without correction for N/O, which could be masking a larger N/O in barred galaxies under a fake larger oxygen abundance.

We have investigated whether the observed barred/unbarred differences depend on parent galaxy properties, finding that these increase towards lower mass galaxies or later types. As an example of this, Fig. 3 shows a boxplot for the N/O

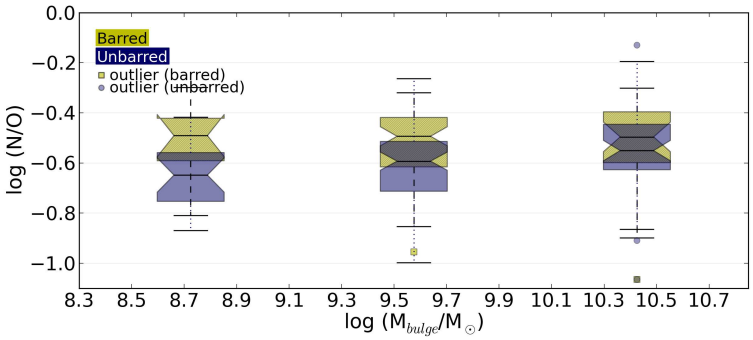

Figure 3. Boxplot showing the median values for the nitrogen-to-oxygen abundance for barred and unbarred galaxies for three different bins in bulge stellar mass. Credit: Florido et al., A&A, 584, A88, 2015, reproduced with permission © ESO.

abundance ratio as a function of the bulge stellar mass. We do not find any clear dependence on bar parameters (e.g. ellipticity or bar length).

3. Conclusions

Our main conclusion from the analysis of the ionized gas in the center of barred and unbarred galaxies is that bars do modify the properties of central ionized gas, in particular the internal extinction, electron density, Σ_{SFR}, and more notably the [N II]λ6583/Hα line ratio. The latter implies a larger N/O abundance ratio in the centers of barred galaxies. In general, the barred/unbarred differences are larger in galaxies with lower mass bulges (or lower total stellar mass or later types). The enhancement in N/O abundance ratio can be qualitatively interpreted as being the result of a different star formation history in the center of barred galaxies, caused by the gas flow induced by the bar (Florido et al., 2015).

Acknowledgments. We acknowledge support from the Spanish "Ministerio de Economía y Competitividad" via grants AYA2014-53506-P (AZ, EF, IP), FPA2010-16802 (EF) and AYA2010-21887-C04-01 (EPM), and from the Junta de Andalucía through the FQM-108 project.

References

Cid Fernandes R., Mateus A., Sodré L., et al., 2005, *MNRAS*, **358**, 363
Coelho P., Gadotti D. A., 2011, *ApJL*, **743**, L13
Ellison S. L., Nair P., Patton D. R., et a., 2011, *MNRAS*, **416**, 2182
Florido E., Zurita A., Pérez I., et al., 2015, *A&A*, **584**, A88
Gadotti D. A., 2009, *MNRAS*, **393**, 1531
Kewley L. J., Dopita M. A., 2002, *ApJS*, **142**, 35
Kewley L. J., Dopita M. A., Sutherland R. S., et al., 2001, *ApJ*, **556**, 121
Pérez-Montero E., 2014, *MNRAS*, **441**, 2663

List of Authors

The purpose of this workshop was to gather scientists and students to address crucial questions related to the chemical abundances in gaseous nebulae. It covered all major theoretical and observational aspects of the study of chemical abundance in HII regions and Planetary Nebulae as well as in Active Galactic Nuclei. For three days, extensive discussion about specific issues in the areas covered by the workshop were provided.

ISBN 978-987-24948-5-8

AAA Workshop Series Vol. 10